Departament d'Enginyeria Electrònica
(Escola Tècnica Superior d'Enginyeria)

PHD THESIS

MONOLITHIC CMOS-MEMS RESONANT BEAMS FOR ULTRASENSITIVE MASS DETECTION

JAUME VERD MARTORELL

2008

Memòria presentada per optar al
Grau de Doctor en Enginyeria Electrònica
per la Universitat Autònoma de Barcelona.
Directora: Prof. Núria Barniol Beumala

La Dra. Núria Barniol Beumala, Catedràtica d'Electrònica del Departament d'Enginyeria Electrònica de la Universitat Autònoma de Barcelona,

CERTIFICA

que la memòria "Monolithic CMOS-MEMS Resonant Beams for Ultrasensitive Mass Detection" que presenta Jaume Verd Martorell per optar al grau de Doctor en Enginyeria Electrònica, ha estat realitzada sota la seva direcció.

Bellaterra, febrer de 2008

Dra. Núria Barniol Beumala

A na Maria

AGRAÏMENTS

Per portar a terme qualsevol projecte en la vida, com pugui esser la realització d'una tesis, sempre necessitem l'ajuda d'altres des de moltes vessants diferents. En aquestes línies voldria agrair a totes les persones que d'una manera o altre m'han ajudat i han fet possible aquesta tesis.

Primerament voldria agrair a na Núria Barniol tot el seu immens esforç i dedicació en la direcció d'aquesta tesis. Els seus consells, propostes, optimisme i especialment la seva empenta en moments crítics han estat claus. Na Núria Barniol em va permetre integrar-me en el seu grup (ECAS) participant molt activament en els projectes Nanomass i Nanosys. A més li voldria agrair totes les facilitats que em va donar des del principi per a que pogués realitzar també tasques de docència.

Igualment vull agrair a nen Francesc Pérez-Murano i a nen Gabriel Abadal, dels quals he après moltíssim, totes les seves rellevants aportacions i discussions mantingudes que han fet que esdevinguessin per mi uns quasi directors d'aquesta tesis. Agrair-los especialment el seu ajut en la caracterització funcional del dispositius desenvolupats.

Voldria agrair a tots i cadascun dels altres integrants o ja ex integrants del grup ECAS, que he tingut el plaer de conèixer, pel bon ambient tant personal com laboral que hi ha hagut sempre al grup. Per ordre d'antiguitat, en Xevi Borrisé, n'Arantxa Uranga, na Maria Villarroya, en Jordi Teva, en Francesc Torres, i en Joan Lluís López. A nen Xevi voldria agrair-li tot el seu suport rebut durant el projecte Nanomass. Per una altre part, durant l'etapa del Nanosys la col·laboració amb n'Arantxa, en Jordi, en Francesc i en Joan Lluís ha esdevingut molt estreta i fructífera. Sense la col·laboració de tots i cada un d'ells no hauria estat possible obtenir els resultats presentats en aquesta tesis. Agrair especialment a n'Arantxa la seva inestimable ajuda en el disseny dels xips i en la caracterització elèctrica, a nen Jordi el seu suport en el disseny i fabricació dels ressonadors, i a nen Francesc la "seva" càmera de buit i imatges SEM.

A l´Institut de Microelectrònica de Barcelona (CNM-CSIC) agrair-li l'oportunitat que m'han donat de desenvolupar la primera part de la meva recerca en les seves instal·lacions i agrair a tot el seu personal pel bon ambient de treball que hi vaig trobar i per tota la seva ajuda. A través de diferents projectes he tingut l'oportunitat de treballar més estretament amb algunes persones

d'aquest centre, com en Jaume Esteve, na Francesca Campabadal i n'Edurd Figueras. Especialment vull agrair a nen Jaume les seves lliçons magistrals de tecnologia i tot el seu gran suport en el post procés CMOS. La seva col·laboració ha estat fonamental pel bon èxit dels ressonadors presentats en aquesta tesis. En aquest sentit, he d'agrair moltíssim la predisposició i la bona feina desenvolupada per na Marta Duch i na Marta Gerbolés en el post processat dels xips. Vull agrair també a n'en Xevi Formatje, Paco Serra i Jordi Sacristan el seu suport en temes de CAD durant la meva estada al CNM.

Al Departament d'Enginyeria Electrònica de la UAB agrair l'oportunitat de realitzar tasques de docència com a professor associat. Agrair especialment a na Mari Carmen i a na Toñi el seu suport logístic durant tot aquest temps.

Thanks a lot to Anja Boisen, from the Mikroelektronik Centret of Denmark, for providing me the opportunity to stay at that research center and to Zach Davis for introduce to me the fabrication process of cantilevers, a world really unknown for me before. Thanks also to Esko Forsen (from MIC) and Sara Nilsson (from LUND University) for their cantilevers and their affability.

Per una altra part, voldria expressar la meva gratitud a nen Jaume Segura del grup de Tecnologia Electrònica de la UIB per haver-me donat l'oportunitat d'incorporar-me a aquest grup. Des del primer moment em va donar tot el seu suport i facilitats per a que pogués realitzar bona part de la meva tesis des de la UIB. La seva desinteressada col·laboració també ha estat clau perquè aquesta tesis sigui una realitat. Durant aquest temps, he començat a participar en qualque projecte de recerca d'en Jaume. En aquest sentit agrair a les diferents persones amb les que he tingut el plaer de col·laborar; Sebastià Bota, Tomeu Alorda, i Pep Lluís Rosselló. Agrair especialment a n'en Sebastià la seva gran eficiència, tot el seu suport desinteressat en temes de CAD així com per la seva companyia en els desplaçaments diaris de Pollença a la UIB. A nen Tomeu i a nen Pep lluís agrair-los el seu companyerisme i la seva bona tasca realitzada sobretot en les estretes col·laboracions mantingudes en temes docents. Fer extensiva aquesta gratitud als altres companys del despatx #13, Vicenç, Kay, Salva i Biel, pel gran ambient que hi ha. A nen Vicenç i a n'Ivan agrair-los també el seu ajut logístic i tècnic sempre que els hi he demanat. Agrair així mateix a tota la resta del grup de Tecnologia Electrònica les facilitats que m'han donat per a treballar com a professor associat a la UIB. Amb alguns d'ells he tingut el plaer de col·laborar i planificar alguna que altre assignatura sempre en un molt bon ambient. Expressar el meu agraïment en aquest sentit a nen Rodrigo, Carol, Miquel i a tota la resta del grup, també per les més d'una celebració que hem compartit.

Finalment però amb tot la meva estimació vull agrair a na Maria, a la que vaig conèixer en una de les escapades a "neu" meu poble i que ara afortunadament és la meva dona, tot el seu recolzament i sobretot la paciència que ha tingut amb mi ja que ella ha patit com ningú aquesta tesis. Agrair als meus pares, Jaume i Joana, i al meu germà Miquel per tot el suport i ànims que m'han donat des de sempre. Sense l'ajut inestimable de tot tipus dels meus pares segur que mai hagués realitzat ni aquesta tesis ni cap dels meus estudis. Així mateix agrair, al meu sogre Jaume i de forma molt emotiva a la meva sogra Maria, que malauradament mos va deixar ja fa quasi un any, pel seu acolliment i confiança des del primer dia.

Jaume,
Febrer 2008

SUMMARY

Resonant beams structures are very attractive transducers for physical, chemical and biological sensors based on micro-/nanoelectromechanical systems (M-/NEMS) due to its simplicity, wide range of sensing domains, and extremely high sensitivity. This Ph.D. thesis is focused on the design, fabrication and characterization of monolithic CMOS-MEMS based on sub-micrometer scale resonant beams for its application in ultrasensitive mass detection with a portable device. The resonators operate in dynamic mode where the mass is measured as a change of its resonant frequency which is electrostatically induced and capacitive readout by means of a monolithically integrated CMOS circuitry.

Two different technological approaches are considered to fabricate sub-micrometer scale resonant beams on pre-processed CMOS chips allowing a monolithic integration: (i) nano post-processing of the CMOS chip to obtain the resonant beams or (ii) definition of the resonant beams at the same time that the CMOS circuits. From both approaches, metal and polysilicon devices exhibiting unprecedented mass sensitivities (for monolithic CMOS sensors) in the atto-/zeptogram range are reported. Comparison of the results following both approaches is given.

High-sensitivity readout CMOS circuits are specifically designed to amplify the capacitive current with transimpedance gains (using a commercial 0.35-μm CMOS technology) up to 120 dBΩ at 10 MHz allowing to detect the resonator displacement with resolutions up to ~10 fm/√Hz which are similar than the best reported optical readout systems without the need of a bulky setup.

Electrical characterization, in air and in vacuum conditions, of fabricated CMOS-MEMS devices is presented corroborating the ability of the presented monolithic approach in measuring the frequency characteristics of sub-micrometer scale beam resonators. Optimal electrostatic transduction is achieved measuring electrical frequency responses with high peaks (up to 20 dB or more) and large phase shifts (up to 160º) around the resonance frequency. Measurements showing soft/hard-spring effect and hysteretic performance due to nonlinearities are also reported as well as the detection of intrinsic Brownian motion demonstrating the noise-matching between the resonator and the readout circuit.

Results from calibration, real time mass measurements, and resolution analysis on fabricated devices obtaining values down to ~30 zg/√Hz (equivalent to ~6 pg/cm^2√Hz) in vacuum conditions

are also reported indicating the improvement from previous works in terms of sensitivity, resolution, and fabrication process.

A specific CMOS Pierce oscillator circuit adapted to work with ~10 MHz beam resonators showing motional resistance up to 100 MΩ is presented and tested demonstrating the feasible attogram detection with a completely portable sensor device.

RESUM EN CATALÀ

Estructures ressonants en forma de biga (p.e. ponts o palanques) són molt interessants com a element transductor en sensors físics, químics i biològics basats en sistemes micro-/nanoelectromecànics (M-/NEMS) degut a la seva simplicitat, al gran rang de dominis que poden sensar, i a la seva extremada alta sensibilitat. Aquesta tesis està focalitzada en el disseny, fabricació i caracterització de CMOS-MEMS monolítics basats en bigues ressonants a escala sub-micromètrica per a la seva utilització en la detecció ultra sensible de massa amb un dispositiu portable. Els ressonadors operen en mode dinàmic on la massa es mesurada com un canvi de la seva freqüència de ressonància que és induïda electrostàticament i llegida d'una forma capacitiva mitjançant un circuit CMOS integrat monolíticament.

Dues aproximacions tecnològiques diferents són considerades per tal de fabricar bigues ressonants a escala sub-micromètrica sobre xips CMOS prèviament processats, possibilitant una integració monolítica: (i) post processant els xips CMOS amb tècniques de nano fabricació per obtenir les estructures ressonants o (ii) definint els ressonadors al mateix temps que els circuits CMOS. Per les dues aproximacions, es presenten dispositius de metall i de polysilici amb sensibilitats de massa sense precedents (per a sensors CMOS monolítics) dins el rang dels atto-/zeptograms. Es presenta una comparativa dels resultats aconseguits mitjançant les dues aproximacions tecnològiques.

Es dissenyen circuits de lectura CMOS d'alta sensibilitat per amplificar el corrent capacitiu amb guanys de transimpedància (utilitzant una tecnologia comercial CMOS 0.35-μm) de fins a 120 dBΩ a 10 MHz possibilitant la detecció del desplaçament del ressonador amb resolucions de fins a ~10 fm/√Hz semblants a les obtingudes pels millors sistemes de detecció òptics reportats i sense la necessitat d'un equipament complexa.

Es presenta la caracterització elèctrica, a l'aire i al buit, de dispositius CMOS-MEMS fabricats que corroboren la capacitat de l'aproximació monolítica presentada per mesurar la característica freqüencial de ressonadors a escala sub-micromètrica. S'aconsegueix una transducció electrostàtica òptima i es mesuren respostes freqüencials elèctriques amb pics elevats (fins a 20 dB o més) i grans canvis de fase (fins a 160º) al voltant de la freqüència de ressonància. També es reporten mesures on s'observen efectes de *softening/harderning* de la constant de molla i

d'histèresis produïts per les no linealitats així com la detecció del moviment Brownià intrínsec demostrant el bon *matching* de soroll entre el ressonador i el circuit de lectura.

També es presenten els resultats de calibració, de mesures en temps real, i d'anàlisi de la resolució dels dispositius fabricats obtenint valors de fins a ~30 zg/√Hz (equivalent a ~6 pg/cm^2√Hz) en condicions de buit que indiquen la millora respecte a treballs anteriors en termes de sensibilitat, resolució i procés de fabricació.

Es presenta i es testeja un circuit oscil·lador Pierce CMOS adaptat per a treballar amb ressonadors de ~10 MHz i amb resistències mecàniques equivalents de fins a 100 MΩ demostrant que és factible la detecció d'attograms amb un dispositiu sensor completament portable.

CONTENTS

CHAPTER 1

THESIS OVERVIEW

This chapter gives an overview of the thesis. First, a brief description of MEMS topics including main applications and fabrication technologies is presented. Next section introduces the mass sensors based on resonant beams including the state-of-the-art of these ultra-sensitive sensors. The Nanomass and Nanosys research projects that constitute the framework of this thesis are also introduced. Finally the main objectives of this thesis and the chapters outline are described.

This PhD dissertation has been carried out at the Electronics Circuits and Systems (ECAS) group of the Department of Electronic Engineering of the *Universitat Autònoma de Barcelona*. Prof. Dra. Núria Barniol is the ECAS group leader and the supervisor of this PhD work. The activity of this group is related with the development of high-performance microelectronic systems. In particular, the work is focused on the development of sensor/actuator elements as well as on the design of the microsystem interfacing. Nowadays, the group is involved in design of resonant MEMS/NEMS for sensing and RF applications.

1.1 MEMS OVERVIEW

Microsystems are claimed to be the smallest functional machines that are currently engineered by humans [Kor06]. Microsystem technology has borrowed a variety of materials and processes from the integrated circuits (IC) industry. Micro-optics, Micro-machines, MEMS and MOEMS are different aspect of the Microsystem technology.

MEMS is the abbreviation for micro-electromechanical system. As the name indicates, it is a device in the size of microns, containing mechanical moving parts where its movement is electrically excited and/or sensed, thus a transduction between mechanical magnitudes and electrical magnitudes (electromechanical transduction) is present.

The field of MEMS has, over the past 20 years, emerged as a technology that promises to have significant impact on every day living in the near future. MEMS provide inexpensive means to sense and, in a limited way, control physical, chemical and biological interactions with nature.

MEMS cover a wide range of research areas and commercial applications, which include sense, actuation, materials and material properties, process techniques and equipment, computer-aided-design (CAD), packaging and system integration. Because of the nature of MEMS, researchers involved in this area come from all areas of engineering and science.

1.1.1 APPLICATIONS

Typical application of MEMS include: microsensors, optical and micro-mirrors, biomedical applications, RF MEMS and microactuators.

There are quite selections of MEMS-based sensors that have been commercialized. One of the more common applications of microsensors comes in the form of an accelerometer in the deployment of safety airbag in car [Cha96]. Some commercial examples of MEMS sensors include Infineon's pressure sensors [Hie00, Infin], strain gauges and Analog Devices' accelerometers for the measuring of acceleration and gyroscopes for the measurement of rotation [Analo].

The MEMS micro-mirrors can be used in making optical sensors and display both of which involves the controlling and detecting of the light band. In the future, MEMS-based micro-mirror array is a likely candidate to replace cathode ray tubes and liquid crystal displays (LCD) as the dominant form of display technologies. An example of a successful MEMS-based micro-mirror array comes in the form of the Digital Mirror Device (DMD) from Texas Instruments [Mig98, Kes98,].

Another rapidly developing field of MEMS falls under the biomedical category. In this area, MEMS have great potential in biomedical instruments and analysis, and implants and drug delivery. Biomedical MEMS can be used for DNA testing, blood testing and any more [Bas04, Fri00, Ili00, Pei04, Ric04,].

A recent progress of MEMS devices is its application in RF applications [Kri05, Ngu98, Ngu99b, Ngu07]. Among specific devices like tunable micromachined capacitors [Gol99], integrated high-Q inductors [Jia00], micromachined low-loss microwave and millimeter-wave filters [Ban00, Che04, Fed05], low-loss micromechanical switches [Bro98], microscale vibrating high-Q mechanical resonators to implement RF oscillators [Ngu99, Oti03] and miniature antennas are currently developed in order to replace the off-chip components in RF systems.

Finally some MEMS acting as actuators have been developed. An example of a highly successful microactuator is a micro-pump used in the Ink Jet Print Head [Kra95].

1.1.2 SCALING-DOWN

A scaling-down of the mechanical transducer size into the nano-meter range leads to a new generation of systems called Nanoelectromechanical Systems (NEMS) [Eki05]. The size scaling-down give important advantages but at the same time some challenges [Eki05b]. In Table 1.1 we can observe how dimensional scaling acts on different physical variables of the system, these results are valid when a uniform scaling in the three dimensions is performed.

In general, a scaling-down in the three dimensions of the MEMS represents an improvement on

sensitivity, energy efficiency and response time. The transducer miniaturization produces a lowering of the output signals (i.e., force, capacity, current) making necessary an improvement of the detection/sensing techniques.

Also, we can observe that uniform scaling produces an increasing of the resonance frequency of the system; this may be an advantage for RF applications but sometimes may be a disadvantage in sensor applications. This inconvenient can be overcome if the scaling is not uniform in the three dimensions.

Table 1.1 Scaling factor for several magnitudes assuming an uniform scaling in the three dimensions ($\lambda<1$).

Parameter	Scaling Factor
Mass (m)	λ^3
Electrostatic force (F_E)	λ^2
Resonance frequency (f_o)	λ^{-1}
Response time (τ)	λ
Power consumption (P)	λ^2
Electrostatic capacity (C_o) *	λ^2
Spring constant (k)	λ
Capacitive current (I_C)	λ
Mass sensitivity (S_m)	λ^4

1.1.3 MICROSYSTEMS TECHNOLOGY AND NANOTECHNOLOGY

MEMS are fabricated using two basic techniques; bulk micromachining and surface micromachining. **Bulk micromachining** covers all techniques that remove significant amounts of the substrate (bulk) material and the bulk is part of the micromachined movable structure. In general silicon has been used as optimal structural material. Silicon etching can be performed using wet (or liquid) etchants or etchants in vapor and plasma states (dry etching) both in an anisotropic or isotropic way. **Surface micromachining** basically involves depositing thin films on the wafer surface and selectively removing one or more of these layers (sacrificial layers) to leave free-standing structures.

In Fig 1.1.1, a simplified scheme of the bulk micromachining and surface micromachining is presented. The structures obtained from bulk micromachining have better mechanical properties than the structures obtained from surface micromachining. Nevertheless, the bulk process is more complex since specific techniques for automatic etch-stop cycles are necessary.

Lithography is the fundamental tool used to fabricate any Microsystem or IC by transferring a pattern onto a certain material. The lithographic step becomes the crucial step in order to define structures in the sub-micrometer range. In this sense, some lithographic techniques that can be used to fabricate very small structures are briefly described.

* It is assumed that the gap does not scale in terms of λ.

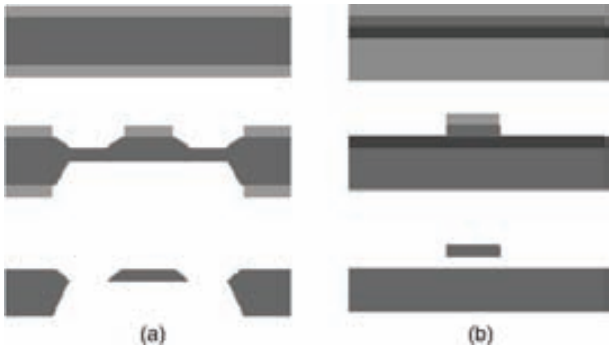

Figure 1.1.1 Simplified scheme of the bulk micromachining (a) and the surface micromachining (b).

Ultra-Violet Photolithography (UVL). Photolithography is the standard process used to fabricate integrated circuits. This is a parallel technique and enable high throughput on a wafer scale. Nowadays, this technique uses ultra-violet light instead of visible light to improve the resolution in pattern transferring. The process sequence is illustrated in Fig. 1.1.2. A mask with the desired pattern is created using electron-beam lithography. A photo-resist layer is spin-coated on to the material to be patterned. Next, the photo-resist layer is exposed to ultraviolet light through the mask. Depending on whether positive or negative photo-resist was use, the expose or the unexposed photo-resist areas, respectively, are removed during the resist development process. The remaining photo-resist acts as a protective mask during the subsequent etching process, which transfers the pattern onto the underlying material. After the etching step, the remaining photo-resist is removed. Using short wavelength light sources, such as ArF lasers (λ=193 nm), innovative materials, and advanced optics, IC circuits with features below 50 nm can readily be achieved.

Electron Beam Lithography (EBL). This is the most used standard nano-lithographic technique and it is based on the scanning electron microscopy (SEM). EBL is a serial lithography technique based on local electron exposure of an electron sensitive polymer film. As the electron beam is scanned over the resist the electrons interact with the polymer resulting in a chemical change similar to photolithography. EBL is also used for production of high quality photolithography masks. The resolution of this technique can be down to 10 nm and normally is around 35-100 nm dependent of the resist and the system used.

Atomic Force Microscopy based Lithography (AFM-L). This technique consists on perform a local oxidation on a metal surface (i.e. aluminum) or directly on silicon by means of the atomic force microscopy (AFM). This local oxidation is obtained by applying a negative voltage between the microscopy tip and the surface. Thus, it is also a serial lithography where the structure motive is defined by means of the oxidation of the surface that acts like a mask. This is a slow technique but resolution les than 10 nm can be achieved.

Direct write Laser Lithography (DWL). In this not standard technique a thin aluminum layer is deposited onto the surface and then it is selectively annealed using a laser beam. The non-annealed aluminum is removed leaving the annealed-Al that acts as the mask. This is a serial

lithography faster than the AFM-L and the resolution is limited by the laser wavelength (i.e. argon ion laser has a λ=488 nm).

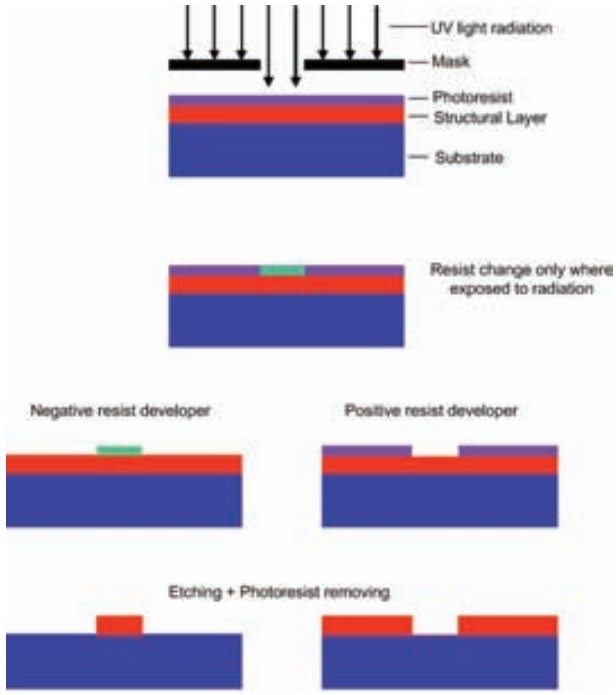

Figure 1.1.2 Schematic of a photolithographic process sequence to structure a thin film layer.

1.1.4 SYSTEM INTEGRATION: CMOS-MEMS

Over the past few years, progress in silicon planar technologies has allowed miniaturized sensors (microsensors) to be performed by exploiting the sensing properties of IC materials (silicon, polysilicon, aluminum, silicon oxide, and nitride) or additional deposited materials (such as piezoelectric zinc oxide, sensitive polymers, or additional metallization layers). When microsensors are fabricated using IC technologies and materials, it is possible to integrate the interface circuit and several sensors on the same chip or in the same package, leading to sensing systems-on-chip (SSoCs) [Bra06]. The potential advantages of this approach are numerous: the cost is reduced due to batch fabrication of both the sensors and the interface circuits; its size and interconnections are minimized; and its reliability is improved. Different approaches have been developed over the years for the system integration. Basically they can be divided into two groups: hybrid integration and monolithic integration.

In the **monolithic integration**, the MEMS and the IC are integrated on the same chip. The whole system is implemented using a fabrication process optimized for integrated circuits with a

few compatible post-processing steps when necessary. The MEMS must be designed by taking into account the material characteristics and design rules given by the standard IC process used. Some advantages of this approach are: the parasitics due to interconnections between the sensors and the interface circuitry are minimized and are well-defined and reproducible; the system assembly is simple, inexpensive, and independent of the number of connections needed; and finally the use of the same technology allows to achieve a good matching between the sensor and the interface circuitry allowing accurate compensation of many parasitic effects.

R.T. Howe and R.S. Muller (UC Berkeley) published in 80's the first fabricated polysilicon microstructures integrated monolithically with NMOS circuitry [How83, How86].

In the **hybrid integration**, the MEMS and the IC are integrated on different chips. They are included in the same package or mounted on the same substrate. The interconnections between the sensor chip and the interface circuit chip can be performed with bonding wires or other techniques, such as flip-chip or wafer bonding. With this approach, the two chips can be fabricated with two different technologies, which are optimized for the sensors and the circuitry, respectively. However this approach have some drawbacks: the assembling can be quite expensive, limited and a source of possible failures; the parasitics due to the interconnections are some orders of magnitude larger, more unpredictable and less repeatable than the monolithic approach, thus destroying in many cases any improvements obtained in sensor performance by technology optimization; finally, matching between MEMS and IC cannot be guaranteed.

In this thesis work, the monolithic approach has been adopted basically for two reasons: the first is that the mechanical structures to fabricate are very simple; the second and more important is that since the mechanical transducers fabricated are in the sub-micrometer range, a reduction of parasitics is compulsory in order to allow operative sensor readout.

CMOS technology has become by far the predominant fabrication technology for integrated circuits. Nowadays, the power of CMOS technology is not only exploited for ICs but also for MEMS fabrication benefiting from well established fabrication technologies and the availability of on-chip circuitry. Pioneering work has been achieved by H. Baltes and co-workers et al. who in 1989 highlighted a new approach based on sensor systems-on-chip integrating MEMS with CMOS by releasing the microstructures from the front of the wafer [Par89].

Although several kinds of microsystems can be completely formed within the regular CMOS process sequence (i.e. magnetic, optical and temperature sensors), MEMS fabrication are produced using CMOS technology in combination with compatible micromachining and thin film deposition steps. These additional fabrication steps can precede (pre-CMOS) or follow (post-CMOS) the standard CMOS steps, or can be performed in-between the standard CMOS steps (intermediate-CMOS).

In the **Pre-CMOS approach**, the MEMS structures or part of them are formed before the CMOS process sequence. In this case, the CMOS IC is not altered by the micromachining process but the MEMS has to be protected during the CMOS process. Also, the pre-micromachined wafers have to meet stringent criteria with respect to contaminations to be able to enter a microelectronics processing line afterwards. An example of this approach is the fabrication of polysilicon structures using the iMEMS technology of Sandia National Laboratories [Smi95] or recently the ModMEMS technology [Yas03].

In the **Intermediate-CMOS approach**, the CMOS process sequence is interrupted for additional thin film deposition or micromachining steps. This approach is commonly exploited to implement surface micromachined polysilicon structures in CMOS technology. As in the Pre-CMOS approach, the MEMS structures has to be also protected. Commercial examples of this approach are Infineon's pressure sensors [Hie00, Infin] and Analog Devices' accelerometers [Cha96, Analo].

In the **Post-CMOS approach**, two general fabrication strategies can be distinguished. In the first strategy, the MEMS structures are completely built on top of a finished CMOS substrate, leaving the CMOS layers untouched. In this case, the microstructures are released by etching a CMOS sacrificial layer. An industrial example is the Texas Instrument' Digital Micromirror Device [Kes98]. Another interesting example of this approach is the technology developed by Prof. Fedder [Fed96] where the MEMS structure is a sandwich of metals and inter-metal oxides. In the second strategy, the MEMS are obtained by machining the CMOS layers after the completion of the regular CMOS process sequence using the variety of CMOS-compatible bulk and surface-micromachining techniques. Piezoresistive pressure sensors were the first commercial devices fabricated using a post-CMOS bulk-micromachined process [Ish87].

In this thesis a post-CMOS approach with surface micromachined techniques in order to fabricate different monolithic mass sensors has been used. The details of the fabrication process will be discussed in Chapter 2.

1.2 HIGH-SENSITIVITY MASS SENSORS

Mass-sensitive sensors detect the change of mass on a sensing layer. Traditionally, the quartz crystal microbalance (QCM) has been used to measure very small masses (in the nanogram range). A QCM is a bulk acoustic wave (BAW) sensor consisting of a piezoelectric resonator which resonant frequency is sensitive to the mass deposited. QCMs usually operate at a frequency less than hundred MHz showing very high quality factors [Osu96]. Commercial QCM-based devices exhibit sensitivities of $\sim 10^{-8}$ g/cm^{2}Hz with resolutions of around 10^{-10} g/cm^2 [Infic, QSen] in air conditions. Since the area of these devices is ~cm^2, they exhibit absolute mass resolution of hundreds of picograms.

Since many physical and chemical processes can be monitored by measuring the associated mass changes, these high-sensitivity mass sensors are used in monitoring chemical reactions, material depositions, biomedical applications and environment control. In particular, relevant works in the study of the immobilization and hybridation of DNA [Car97] and in monitoring of sub-monolayer deposits [Nar98] have been reported.

Recently, thin-film acoustic resonators (FBARs) based sensors have been proven to be a suitable candidate to replace the QCM sensors [Zha05]. Compared with QCM, FBAR is much smaller in thickness and volume showing higher resonance frequencies and better mass sensitivities. Mass sensitivities of $\sim 10^{-14}$ g/cm^{2}Hz have been reported with a 2.29-GHz FBAR [Cam06]. In any case, the quality factors observed ($Q<1000$ in air conditions) are lower than for QCM sensors and the final mass resolution of the FBAR sensor has not been demonstrated to be superior to QCM sensors [Zha05, Cam06].

On the other hand, small cantilever structures have also been proven to be an excellent transducer for a wide range of sensing domains presenting higher resolutions than QCM sensors. Micromachined cantilevers have its origin in the advent of scanning probe microscopy (SPM) where these structures have been used as force sensors in atomic force microscopy (AFM). As a result of more recent advances in several converging areas of science and technology an innovative family of physical, chemical and biological sensors based on cantilever technology has been shaped out [Eki04, Fri00, Illi04, Lan98, Lan99, Lan02, Lav03, Lav04, Ono03, and Tam01]. The operating principle and the state-of-the-art of mass sensors based on cantilever structures is reported in next sections.

1.2.1 Operating Modes for Cantilever Mass Sensors

Depending on the measured parameter of the cantilever (deflection or resonant frequency) the mode of cantilever operation can be referred to as either static or dynamic.

In the **static mode** of operation, the measurand produces a deflection of the cantilever that is detected and converted to an electrical signal (Fig. 1.2.1). The main advantage of this mode is its simplicity since no actuation system is needed.

The **dynamic mode** of operation, also called resonant mode, is inspirited from the original idea of Cleveland et al. where the spring constant of a cantilever is determined by measuring their resonant frequencies before and after adding small end masses [Cle93]. In the dynamic mode the measurand modify any characteristic of the cantilever oscillation (i.e. resonance frequency, resonance amplitude, and phase at resonance or quality factor). In this approach (Fig. 1.2.1), an excitation or actuation system is necessary in order to excite the cantilever at resonance. The merit compared to static mode is that the dynamic mode gives both absolute information regarding the measurand without the need of any careful calibration.

The cost in the higher complexity of the dynamic mode in front of the static mode is compensated with a much better sensitivity of the sensor. Additionally, the dynamic mode is not well suited for measurements in liquid media due to the liquid damping and the consequent lowering of the Q-factor. Improvements on the detection system to overcome this problem must be added like in QCM-based systems [Tam01].

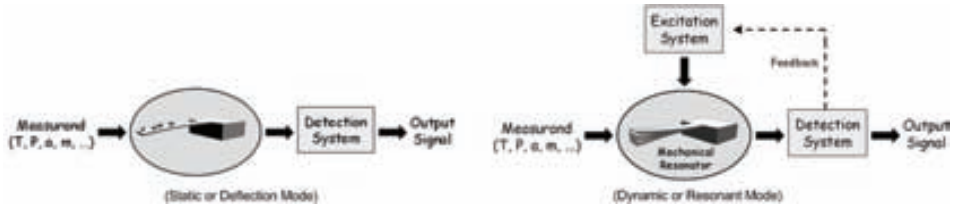

Figure 1.2.1 Schematic representation of the static and dynamic operation modes.

1.2.2 READOUT AND EXCITATION TECHNIQUES

In this section the common techniques for excitation and detection in cantilever-based sensors and MEMS in general are presented. In the case of static sensors only the detection or readout system is needed in order to measure the deflection of the cantilever.

- **READOUT TECHNIQUES**

Next a brief description of the common readout techniques is presented and analyzed in terms of benefits and disadvantages of these techniques.

Optical method. For static and dynamic cantilever-based sensors, this is the most used technique in modern AFM instruments. Such systems use a position sensitive photodetector to detect the reflected laser beam from the apex of the cantilever. This is a simple and sensitive method but critical for small cantilevers since the diffraction limit of the light used. To overcome this limit, another optical technique called fiber-optic interferometry is used [Rug89, Aza07]. Nevertheless, the main disadvantage of the optical method is the need of lasers, photo-detectors or more advanced optics which results in a bulky and non integrated measurement system that is not suitable for system-on-chip applications.

Piezoresistive method. This method is based in the measurements of the resistance that experiments any material shared in common with the cantilever when it is stressed due to any cantilever bending. This is a common method used in CMOS-MEMS since the good piezoresistive properties of the silicon and the polysilicon (at appropriate doping levels). The method enables integration on a single chip but it limits the miniaturization of the cantilever since piezoresistor wiring needs to be fitted on to the cantilever. Another disadvantage of this technique is that it requires current to flow through the cantilever resulting in additional dissipation of heat and associated to thermal drifts. Despite of these constraints, Roukes' group have been reported a 70-nm thick cantilever resonator with an integrated piezoresistance that presents a mass resolution less than 1 attogram [Li07].

Piezoelectric method. This technique requires deposition of piezoelectric material, such as ZnO, on the cantilever. Due to the piezoelectric effect, transient charges are induced in the piezoelectric layer when the cantilever is deformed. The main disadvantage of this technique is that in order to obtain large output signals it requires the thickness of the piezoelectric film to be well above the values that correspond to optimal mechanical characteristics.

Capacitive method. This method is based on measuring the changes of the capacitance constituted by the cantilever and an additional electrode. Capacitive sensing has the advantages of low temperature coefficients, low power dissipation, low noise, low-cost fabrication, and compatibility with VLSI technology scaling. For these reason, capacitive sensing has received the most attention and has been the most used in MEMS products. The main problem of this technique in micro-/nanocantilevers is the very small capacitance to measure. In addition, the use of this technique is limited in non-conductive environments. The capacitive method is the readout approach used in this thesis and it is described in detail in Chapter 2.

In addition of previous techniques, novel transduction techniques for NEMS (not previously used in MEMS) are being developed: magnetomotive, single-electron transistor, quantum or atomic point contact, or a combination of above methods. A good example is the work published in 2003 by Roukes' group where a nanowire resonator with a diameter of 43 nm was fabricated and electrically characterized using magnetomotive driving and detection [Hus03]. In any case, these techniques are not suitable in practical devices due to the extreme conditions necessary for operation: large magnetic fields, very low temperatures, device complexity, etc.

- **EXCITATION TECHNIQUES**

As we previously commented, resonant sensors need an excitation to force the cantilever to oscillation. In this section the most typical excitation techniques are enumerated.

Electrostatic. This method consists on applying an AC-voltage between the two electrodes that constitutes a capacitor (one of these electrodes is the same resonator) that produces an attractive electrostatic force that bends harmonically the resonator towards the other electrode. This is the technique used in this thesis and is described in depth in chapter 2.

Piezoelectric. This method uses the dual property of the piezoelectric material previously described. In this case, the application of an AC-voltage produces a mechanical stress of the piezoelectric material than bends the resonator.

Electrothermal. This method consists on heating the resonator by means of an AC-current through an integrated resistance on the resonator.

Electromagnetic. This method consists in the application of an static magnetic field to the resonator. The force is generated since an AC-current is force to flow through the resonator perpendicularly to the magnetic field.

Photothermal. This method consists on heating the resonator by means of a pulsed diode laser focused onto the resonator.

1.2.3 STATE-OF-THE-ART OF RESONANT N/MEMS-BASED MASS SENSORS

The actual tendency of decrease the size of the mechanical transducer into the submicron domain allows the fabrication of ultra-sensitive mass sensors [Eki05]. Moreover, the use of vibrating cantilevers (resonant mode) allows detecting masses in the attogram range and below. In Table 1.2, the most relevant results, from the point of view of resolution in mass sensing are reported.

The Roukes' group at Caltech (USA) is the leader in the study and developing of ultrasensitive mass sensors based on resonant NEMS devices. Magnetomotive actuation and electromotive actuation is usually applied at nanometer-scale SiC bridges reporting zeptogram resolution in ultrahigh vacuum and cryogenic temperatures [Yan06]. The real time mass sensing is achieved using a complex off-chip electronics based on a frequency-modulated phase-lock loop (FM-PLL).

On the other hand, this group has recently demonstrated a mass resolution less than 1 attogram in air conditions using a 127-MHz SiC cantilever based NEMS with piezoresistive detection [Li07]. In this case, any excitation is system is used and the NEMS resonance frequency is measured from the thermomechanical noise of the cantilever that at the resonance becomes higher than the readout electronics noise.

The Craighead's group at Cornell University (USA) uses the optical interference technique to detect the resonance of cantilevers that are excited photothermally [Ili05] or piezoelectrically [Ili04, Ili04b]. In [Ili05], they reported the detection of a single DNA molecule[†] in vacuum conditions.

Finally, Lavrik and Datskos [Lav03] reported in 2003 femtogram mass detection using a silicon cantilever with photothermal excitation and optical readout in air conditions.

We can appreciate that all these devices need off-chip complex electronics resulting in a bulky system that does not allows their use in system-on-chip applications.

Table 1.2 Main features of the state-of-the-art of resonant mass sensors.

Group or Author, Year [Ref.]	f_o (MHz)	S_m	$\Delta m^{\ddagger}$	δM (ag)	Excitation/ Readout	Resonator	Analyte	Medium
Roukes, 2006 [Yan06]	190	0.86 zg/Hz	0.1 ag	0.02[§]	Magnetomotive/ Electromotive	SiC bridge	N_2	UH vacuum (37ºK)
Roukes, 2007 [Li07]	127	1.43 zg/Hz	1 ag	0.1[¤]	None / Piezoresistive	SiC cantilever	difluorethane	Air
Craighead, 2005 [Ili05]	11	5.1 zg/Hz	1.6 ag	0.05	Photothermal / Optical interference	Silicon nitride cantilever with gold dots	dsDNA	Vacuum
Craighead, 2004 [Ili04]	13.4	---	6.3 ag	0.4	Piezoelectric / Optical interference	Silicon nitride cantilever	Thiolate SAM	Vacuum
Craighead, 2004 [Ili04b]	10	0.4 ag/Hz	2.3 fg	50	Piezoelectric/ Optical interference	PolySi cantilever antibody-coated	BaculoVirus	Vacuum
Lavrik-Datskos, 2003 [Lav03]	2.2	2.8 ag/Hz	5.5 fg	570*	Photothermal / Optical interference	Silicon cantilever gold-coated	11-m acid[**]	Air

[†] 1578 base pair long double-stranded deoxyribonucleic acid (dsDNA) molecule.
[‡] Minimum mass detected.
[§] Resolution obtained for a 1 s averaging time.
[¤] Resolution obtained for a 1 Hz readout bandwidth
[**] 11-mercaptoundecanoic acid.

1.3 NANOMASS AND NANOSYS PROJECTS

In this section a brief description of the Nanomass and Nanosys [NanoS] research projects is given.

1.3.1 NANOMASS PROJECT

Nanomass is a FET-Open Domain project of the IST programme of the V Framework of EU Comission which the first phase was initiated in beginning of the year 2000 [NanoM]. NANOMASS is the acronym of "NANOresonators with integrated circuitry for high sensitivity and high spatial resolution MASS detection". The objective of the project was the development of the technologies for the combination of CMOS circuitry with nanotechnology processes and techniques. The technology is applied to the realization of mass sensors based on resonant small silicon cantilevers integrated monolithically with CMOS signal conditioning circuits. The excitation and detection of the cantilever displacement is performed through the integrated CMOS circuitry.

Mass detection is based on monitoring the resonant frequency shift of the cantilever when micro/nanometer-sized particles or molecules are deposited on the cantilever. The cantilever is electrostatically excited by means of an electrode located at sub-micrometer distance from the cantilever. A change in the cantilever resonance frequency is detected as a capacitance change (capacitive readout). Electrostatic transduction in the sub-micrometer size regime requires the minimization of the parasitic capacitance since the magnitude of the current to be detected is proportional to the coupling capacitance between the cantilever and the driver, which is in the order of 10^{-16} or less. Consequently, the readout circuit used to monitor the cantilever movement has to be "on-chip" integrated in order to minimize the parasitic capacitance introduced by the external bonding pads and wires, which otherwise would drastically reduce the readout signal. CMOS circuitry for excitation and readout of the cantilever movement is integrated together with the cantilever by using a monolithic technology that consists of the combination of standard CMOS processes and novel nanofabrication techniques.

The goal of the project is the development of an ultrasensitive system-on-chip based mass sensor, based on a micro-/Nanoelectromechanical device integrated with readout circuitry (Figure 1.3.1).

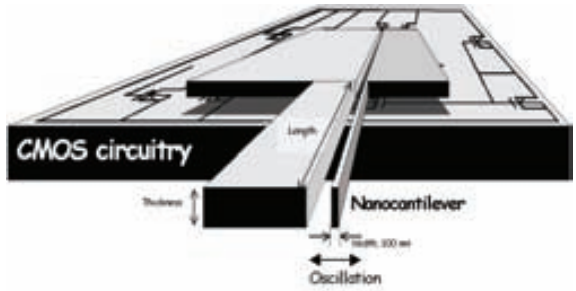

Figure 1.3.1 Conceptual schematic of the NANOMASS project showing a cantilever monolithically integrated with CMOS circuitry.

The Nanomass consortium was constituted by four European research groups. The main tasks of each partner were as follows:

- ECAS group (project leader) at the Electronic Engineering Department of the *Universitat Autònoma de Barcelona* (**UAB**, Spain): CMOS circuit design. MEMS design and modeling. Electrical and functional characterization.

- Mikroelektronik Centret at the Technical University of Denmark (MIC, Denmark): Si-processing, general surface micromachining. MEMS/NEMS fabrication by laser and SFM nanolithography. Functional characterization.

- Institut de Microelectronica de Barcelona at the *Centro Nacional de Microelectrónica* (CNM, Spain): CMOS fabrication.

- Solid State Department at Lund University (LU, Sweeden): MEMS/NEMS fabrication using novel nanolithography techniques such as electron beam lithography and nanoimprint lithography.

1.3.2 NANOSYS PROJECT

Nanosys is the acronym of the national research project "Sistemas micro-nanoelectromecánicos con circuitos CMOS de bajo consumo para la transducción y procesado de señales en aplicacions portables" [NanoS] with the aim of developing micro/nano systems based on micro/nano mechanical structures and low power CMOS circuits. The project includes research on a) the technology of fabrication of micro/nano mechanical resonant structures, and on b) low power integrated circuit design for signal processing and conditioning from the mechanical structures in order to develop integrated micro/nano systems that exploit the properties of the micro/nano mechanical element for transduction and signal processing applications for communication systems. In the design of the systems, special attention was devoted towards optimizing sensitivity for the case of the sensors, and to minimize power consumption for the case of signal processing applications, where decreasing the dimensions from micro to nano represents an important improvement for portable applications.

The activity of the project has been focused in the development of two types of systems: a) systems based on mechanical resonant structures at relative low frequency in applications of ultrasensitive mass sensing and b) systems based on mechanical resonant structures at high frequency for applications in telecommunications receiver systems.

The Nanosys partners and their main tasks were as follows:

- ECAS group at the Electronic Engineering Department at the *Universitat Autònoma de Barcelona* (UAB, Spain): Integrated circuit and MEMS devices design.

- Instituto de Microelectronica de Barcelona at the *Centro Nacional de Microelectrónica* (CNM, Spain): Integrated circuit design. Micro/nano fabrication.

The work developed in this thesis can be included in both projects, being most of the circuits developed for the MEMS interfacing and readout the ones described in this thesis (Chapter 4). Related with the MEMS devices for sensor applications in the Nanosys project, all the MEMS designs are the ones reported in this thesis.

1.4 OBJECTIVES AND CHAPTERS OUTLINE

The main objective of this thesis was the development of a monolithic mass sensor with a very high mass resolution in the attogram range using a CMOS technology.

This general aim of the PhD thesis can be divided in the following specific objectives:

- Design and modeling of the sensor based on a MEMS device with electrostatic excitation and capacitive detection to allow their monolithic integration.
- In order to obtain an attogram resolution, dimensions in the sub-micrometer range will be needed, and in consequence NEMS devices will be developed. In this sense a particular objective will be the evaluation of the capabilities in using sub-micrometer CMOS technologies to obtain the required specifications (this includes for instance the selection of the structural and sacrificial layers).
- The design of an optimal interface between the MEMS and the CMOS circuitry will be one of the main objectives of this thesis. It is important to emphasize that we want to develop a feasible Sensor-System-on-Chip (a CMOS-MEMS), thus it will be necessary to develop a self-excited M/NEMS resonator using a dedicated and specific CMOS circuitry.
- Finally last objective is to characterize the system, in order to state if the SSoC developed achieves the general objective in having an attogram mass resolution. This characterization includes both a full electrical characterization and also a functional characterization in terms of mass.
- The definition, when needed, the dedicated figures of merit in order to compare different approaches (mainly for detection systems) will be also a secondary objective.

These objectives pursuit in this thesis work have been developed in two phases related with the Nanomass and Nanosys projects. In the first phase, the objective was the development of monolithic mass sensors using an in-house 2.5-μm CMOS technology and nanolithography techniques to fabricate sub-micrometer scale cantilevers compatible with CMOS. On the other hand, in the second phase the objective was the improvement of the mass sensors performance and fabrication process by using a commercial sub-micrometer CMOS technology to fabricate sub-micrometer scale cantilevers monolithically integrated with capacitive readout CMOS circuitry without the use of nanolithography techniques. The application possibilities of these sensors are several. Since their ultra-high sensitivity, they can be used in different fields like biochemical or technological for detecting the performance and interactions of molecules on the resonator surface [Lan99] or in mass spectrometry to detect a single molecule. On the other hand, the high spatial resolution that presents these small resonators can be used to monitor or characterize the performance of atom/ion beams in lithography systems (i.e. ABL, FIB) or in thin-film deposition applications replacing the existing QCM based systems.

After this introductory chapter, the dissertation has been divided into six main chapters and two additional appendixes.

Chapter 2: This chapter describes the theory of beam resonators with electrostatic transduction and their performance as mass sensors.

Chapter 3: This chapter presents the fabrication of the MEMS resonators designed for ultra sensitive mass sensing. The two fabrication approaches, Nanomass devices (using an in-house CMOS technology) and Nanosys devices (using a commercial submicron technology) are presented.

Chapter 4: This chapter is dedicated to the design of the CMOS circuitry. The different designed readout circuits are presented and a description of their main parameters as well as CMOS-MEMS system performance is given.

Chapter 5: In this chapter the experimental results related with the electrical and functional characterization of the different mixed CMOS-MEMS sensors are presented.

Chapter 6: This chapter presents the design and characterization of the self-sustaining CMOS-MEMS oscillators implemented.

Chapter 7: The main conclusion and achievements of this thesis are listed in this chapter.

Append. A: This appendix describes the non-linear electromechanical model developed and implemented in Verilog-A to perform system-level electrical simulations.

Append. B: This appendix is a list of the different chips designed during this thesis.

REFERENCES

[Analo] Analog Devices, Norwood, MA. [Online]. Available: http://www.analog.com/imems.

[Aza07] N.O. Azak, M.Y. Shagam, D.M. Karabacak, K.L. Ekinci, D.H. Kim, D.Y. Yang, "Nanomechanical displacement detection using fiber-optic interferometry", *Applied Physics Letters,* vol. 91, pp. 093112, 2007.

[Bal02b] H. Baltes, O. Brand, A. Hierlemann, D. Lange, and C. Hagleitner, "CMOS MEMS – Present and Future", in *Micro Electro Mechanical Systems, 2002. The Fifteenth IEEE International Conference on*, pp. 459-466, 2002.

[Ban00] F.D. Bannon, J.R. Clark, and C.T.-C Nguyen, "High-Q HF Microelectromechanical Filters", *IEEE J. Solid-State Circuits*, vol. 35, no. 4, pp. 512-526, 2000.

[Bas04] R. Bashir, "BioMEMS: state-of-the-art in detection, opportunities and prospects", *Advanced Drug Delivery Reviews*, vol. 56, pp. 1565-1586, 2004.

[Bat01] F. M. Battiston, J. P. Ramseyer, H. P. Lang, M. K. Baller, Ch. Gerber, J. K. Gimzewski, E. Meyer, H. J. Güntherodt, "A chemical sensor based on a microfabricated cantilever array with simultaneous resonance-frequency and bending readout", *Sensors and Actuators (B)*, vol. 77, pp. 122-131, 2001.

[Ber02] R. Berger, Ch. Gerber, H. P. Lang, J. K. Gimzewski, "Micromechanics: A Toolbox for Femtoscale Science: 'Towards a Laboratory on a Tip' , *Microelectronic Enginnering*, vol. 35, pp. 373-379, 1997.

[Bra98] O. Brand, H. Baltes, *Micromachined Resonant Sensors. An Overview*, Wiley-VCH, Sensors vol. 4, 1998.

[Bra05] O. Brand and G.K. Fedder, *CMOS-MEMS, Advanced Micro and Nanosystems*, H. Baltes, O. Brand, G. Fedder, C. Hierold, J.G. Korvink, O. Tabata, Eds. Weinheim, Wiley-VCH, 2005, vol. 2.

[Bra06] O. Brand, "Microsensor Integration Into Systems-on-Chip", *Proceedings of the IEEE*, vol. 94 (6), pp. 1160-1176, 2006.

[Bro98] E.R. Brown, "RF-MEMS switches for reconfigurable integrated circuits", *IEEE Trans. Microw. Theory Tech.*, vol. 46 (11), pp. 1868-1880, 1998.

[Bus98] J. M. Bustillo, R. T. Howe and R. S. Muller, "Surface Micromachining for Microelectromechanical Systems", *Proceedings of the IEEE*, vol. 86, no. 8, pp.1552-1574, 1998.

[Cam06] H. Campanella, J. Esteve, J. Montserrat, A. Uranga, G. Abadal, N. Barniol, A. Romano-Rodriguez, "Localized and distributed mass detectors with high sensitivity based on thin-film bulk acoustic resonators", *Applied Physics Letters*, vol.89, pp. 033507, 2006.

[Car97] F. Caruso, E. Rodda, N. Furlong, K. Niikura, Y. Okahata, "Quartz Crystal Microbalance Study of DNA Immobilization and Hybridization for Nucleic Acid Sensor Development", *Anal. Chem..*, vol. 69, pp. 2043-2049, 1997.

[Cha96] K.H.-L. Chau, S.R. Lewis, Y. Zhao, R.T. Howe, S.F. Bart, R.G. Marcheselli, "An integrated force-balanced capacitive accelerometer for low-g applications", *Sensors and Actuators A.*, vol. 54, pp. 472-476, 1996.

[Che04] W. Ark-Chew and C. T. C. Nguyen, "Micromechanical mixer-filters ("mixlers")," *Journal of Microelectromechanical Systems,* vol. 13, pp. 100-112, 2004

[Cle93] J. P. Cleveland, S. Manne, D. Bocek, P. K. Hansma, "A nondestructive method for determining the spring constant of cantilevers for scanning force microscopy", *Rev. Sci. Instrum.*, vol. 64 (2), pp. 403-405, 1993.

[Des00] M. Despont, J. Brugger, U. Drechsler, U. Dürig, W. Häberle, M. Lutwyche, H. Rothuizen, R. Stutz, R. Widmer, G. Binnig, H. Rohrer, P. Vettiger, "VLSI-NEMS chip for parallel AFM data storage", *Sensors and Actuators (A),* vol. 80, pp. 100-107, 2000.

[Eki04] K.L. Ekinci, X.M.H. Huang, and M.L. Roukes, "Ultransensitive nanoeletromechanical mass detection", *Applied Physics Letters,* vol. 84, pp. 4469, 2004.

[Eki05] K.L. Ekinci, M.L. Roukes, "Nanoelectromechanical systems", *Rev. Sci. Instrum.*, vol. 76, pp. 061101, 2005.

[Eki05b] K.L. Ekinci, "Electromechanical Transducers at the Nanoscale: Actuation and Sensing of Motion in Nanoelectromechanical Systems (NEMS)", *Small*, vol. 1 (8-9), pp.786-797, 2005.

[Fed96] G.K. Fedder, S. Santhanam, M.L. Reed, S.C. Eagle, D.F. Guillou, M.S.-C. Lu, L.R. Carley, "Laminated high-aspect-ratio microstructures in a conventional CMOS process", *Sensors and Actuators A*, vol. 57, pp. 103-110, 1996.

[Fed05] G. Fedder, "CMOS-MEMS Resonant Mixer-Filters", in *Technical Digest of the IEEE International Electron Device Meeting 2005,* pp. 274-277, 2005.

[Fri00] J. Fritz, M. K. Baller, H. P. Lang, H. Rothuizen, P. Vettiger, E. Meyer, H. J. Güntherodt, Ch. Gerber, J. K. Gimzewski, "Translating Biomolecular Recognition into Nanomechanics", *Science* vol. 288, pp. 316-318, 2000.

[Gol99] C.L. Goldsmith, A. Malczewski, Z.J. Yao, S. Chen, J. Ehmke, D.H. Hinzel, "RF MEMS variable capacitors for tunable filters", *Int. J. RF Microw. Comput-Aid. Eng.*, vol. 9 (4), pp. 362-374, 1999.

[Hag01] C. Hagleitner, A. Hierlemann, D. Lange, A. Kummer, N. Kerness, O. Brand, and H. Baltes, "Smart single-chip gas sensor microsystem**"**, *Nature*, vol. 414, pp. 193-296, 2001.

[Hag02] C. Hagleitner, D. Lange, A. Hierlemann, O. Brand, and H. Baltes, "CMOS single-chip gas detection system comprising capacitive, calorimetric and mass-sensitive microsensors**"**, *IEEE J. of Solid-State Circuit*, vol. 37, no. 12, pp. 1867-1878, Dec. 2002.

[Hie00] C. Hierold, "Intelligent CMOS sensors**"**, in *Proc. of the IEEE MEMS 2000*, pp. 1-6, 2000.

[How83] R.T. Howe and R.S. Muller, "Polycrystalline silicon micromechanical beams**"**, *J. Electrochem. Soc.*, vol. 130, pp. 1420-1423, 1983.

[How86] R.T. Howe and R.S. Muller, "Resonant microbridge vapor sensor**"**, *IEEE Trans. Electron Devices*, vol. ED-33, pp. 499-507, 1986.

[Hus03] A. Husain, J. Hone, H.W.Ch. Postma, X.M.H. Huang, T. Drake, M. Barbic, A. Scherer, and M.L. Roukes, "Nanowire-based very-high-frequency electromechanical resonator**"**, *Applied Physics Letters*, vol. 83 (6), pp. 1240, 2003.

[Ili00] B. Ilic, D. Czaplewski, H.G. Craighead, P. Neuzil, C. Campagnolo, C. Batt, "Mechanical resonant immunospecific biological detector", *Appl. Phys. Lett.*, vol. 77 (3), pp. 450-452, 2000.

[Ili04] B. Illic, H. C. Craighead, S. Krylov, W. Senaratne, C. Ober, P. Neuzil, "Attogram detection using nanoelectromechanical oscillators", *J. Appl. Phys.*, vol. 95 (7), pp. 3694-3703, 2004.

[Ili04b] B. Illic, Y. Yang, and H. C. Craighead, "Virus detection using nanoelectromechanical devices", *Appl. Phys. Lett.*, vol. 85 (13), pp. 2604-2606, 2004.

[Ili05] B. Illic, Y. Yang, K. Aubin, R. Reichenbach, S. Krylov, and H. C. Craighead, "Enumeration of DNA Molecules Bound to a Nanomechanical Oscillator", *Nanoletters*, vol. 5 (5), pp. 925-929, 2005.

[Infic] INFICON, USA. [Online]. Available: http://www.inficonthinfilmdeposition.com/en/index.html/.

[Infin] Infineon Technologies, Munich, Germany. [Online]. Available: http://www.infineon.com/sensors/.

[Ish87] T. Ishihara, K. Suzuki, S. Suwazono, M. Hirata, and H. Tanigawa, "CMOS integrated silicon pressure sensor", *IEEE J. Solid-State Circuits*, vol. SSC-22, no. 2, pp. 151–155, 1987.

[Jia00] H.T. Jiang, Y. Wang, J.L.-A. Yeh, N.C. Tien, "On-chip spiral inductors suspended over deep copper-lined cavities", *IEEE Trans. Microw. Theory Tech*., vol. 48 (12), pp. 2415-2423, 2000.

[Kes98] P.F. van Kessel, J.J. Hornbeck, R.E. Meier, and M.R. Douglas, "A MEMS-based projection display", *Proceedings of the IEE*, vol. 86, no. 8, pp.1687-1704, 1998.

[Kor06] J.G. Korvink and O. Paul Eds., *MEMS: a practical guide to design, analysis, and aplications*, William Andrew and Springer-Verlag GmbH, 2006.

[Kov98] G. T. A. Kovacs, N. I. Maluf and K. E. Petersen, "Bulk Micromachining of Silicon", *Proceedings of the IEE*, vol. 86, no. 8, pp.1536-1551, 1998.

[Kra95] P. Krause, E. Obermeir, W. Wehl, "Backshooter-A New Smart Micromachined Single-chip Inkjet Printhead", in *Digest of Technical Papers of Transducers'95*, vol. 2. pp. 325-328, 1995.

[Kri05] K. Sundaresan, G. Ho, S. Pourkamali, and F. Ayazi, "A two-chip, 4-MHz microelectromechanical reference oscillator", in *Proc. of the IEEE International Symposium on Circuits and Systems (ISCAS'05)*, pp. 5461-5464, 2005.

[Lan98] H.P. Lang, R. Berger, F. Battiston, J.-P. Ramseyer, E. Meyer, C. Andreoli, J. Brugger, P. Vettiger, M. Despont, T. Mezzacasa, L. Scandella, H.-J. Guntherodt, Ch. Berger, J.K. Gimzewski, *"*A chemical sensor based on a micromechanical cantilever array for the identification of gases and vapors", *Appl. Phys. A*, vol. 66, pp. S61-S64, 1998.

[Lan99] H.P. Lang, M.K. Baller, R. Berger, C. Gerber, J.K. Gimzewski, F. M. Battiston, P. Fornaro, J. P. Ramseyer, E. Meyer, and H. J. Guntherodt, *"*An artificial nose based on a micromechanical cantilever array*"*, *Analytica Chimica Acta*, vol. 393 (1-3), pp. 59-65, 1999.

[Lan02] D. Lange, C. Hagleitner, A. Hierlemann, O. Brand, and H. Baltes, *"*Complementary Metal Oxide Semiconductor Cantilever Arrays on a Single Chip: Mass-Sensitive Detection of Volatile Organic Compounds", *Anal. Chem.*, vol. 74 (13), pp. 3084-3095, 2002.

[Lav03] N. V. Lavrik, and P. G. Datskos, "Femtogram mass detection using photothermally actuated nanomechanical resonators", *Appl. Phys. Lett.*, vol. 82 (16), pp. 2697-2699, 2003.

[Lav04] N. V. Lavrik, M. J. Sepaniak, P. G. Datskos, "Cantilever transducers as a platform for chemical and biological sensors", *Rev. Sci. Instrum.*, vol. 75 (7), pp. 2229-2253, 2004.

[Lee01] S. Lee, M. U. Demirci, and C. T.–C., "A 10-MHz Micromechanical Resonator Pierce Reference Oscillator for Communication", in *Proc. of Transducers'01*, June 10-14, pp. 1094-1097, 2001.

[Li07] M. Li, H. X. Tang, and M. L. Roukes, "Ultra-sensitive NEMS-based cantilevers for sensing, scanned probe and very high-frequency applications", *Nature nanotechnology*, vol. 2, pp. 114-120, 2007.

[Mad02] M. J. Madou, Fundamentals of Microfabrication: the science of miniaturization, CRC Press, 2nd edition, 2002.

[Mig98] M.A. Mignardi, "From IC's to DMD's", *Texas Instruments Technical J.*, vol. 15 (3), pp. 56-63, 1998.

[NanoM] Nanomass project, reference of the Information Society Technologies of the European Commission 2001-33068.

[NanoS] Nanosys project, reference of the *Ministerio de Ciencia y Tecnologia*, MCYT-TIC2003-0723.

[Nar98] S.S. Narine, A.J. Slavin, "Use of the quartz crystal microbalance to measure the mass of submonolayer deposits: Measuring the stoichiometry of surface oxides", *J. Vac. Sci. Technol. A*, vol. 16 (3), pp. 1857-1862, 1998.

[Ngu98] C.T.-C Nguyen, L.P-B Katehi, G.M. Rebeiz, "Micromachined devices for wireless communications", *Proc. of the IEEE*, vol. 86, no. 8, pp. 1756-1768, 1998.

[Ngu99] C.T.-C Nguyen and R.T. Howe, "An Integrated CMOS Micromechanical Resonator High-Q Oscillator", *IEEE J. Solid-State Circuits*, vol. 34, no. 4, pp. 440-455, April 1999.

[Ngu99b] C.T.-C Nguyen, "Frequency-selective MEMS for minituarized low-power communication devices", *IEEE Trans. Microw. Theory Tech*., vol. 47(8), pp. 1486-1503, 1999.

[Ngu07] C.T.-C Nguyen, "MEMS technology for timing and frequency control", *IEEE Trans. Ultrason. Ferroelectr. Freq. Control*, vol. 54 (2), pp. 251-270, 2007.

[Ono03] T. Ono, X. Li, H. Miyashita, and M. Esashi, "Mass sensing of adsorbed molecules in sub-picogram sample with ultrathin silicon resonator", *Rev. Sci. Instrum.*, vol. 74 (3), pp. 1240-1243, 2003.

[Osu96] C.K. O'Sullivan, G.G. Guilbaut, "Commercial quartz crystal microbalances – theory and applications", *Biosensors and Bioelectronics*, vol. 14, pp. 663-670, 1996.

[Oti03] B.P. Otis, and J.M. Rabaey, "A 300-uW 1.9-GHz CMOS Oscillator Utilizing Micromachined Resonators", *IEEE J. Solid-State Circuits*, vol. 38, no. 7, pp. 1271-1274, 2003.

[Par89] M. Parameswaran, H. P. Baltes, L. Ristic, A.C. Dhaded, and A.M. Robinson, "A New Approach for the Fabrication of Microelectromechanical Structures", *Sensors and Actuators*, vol. 19 (3), pp. 289-307, 1989.

[Pei04] J.H. Pei, F. Tian, and T. Thundat, "Glucose biosensor based on the microcantilever", *Analytical Chemistry*, vol. 76, no. 2, pp. 292-297, 2004.

[Pet82] K. E. Petersen, "Silicon as a mechanical material", *Proc. IEEE*, vol. 70, no. 5, pp. 420-457, April 1999.

[QSen] Q-SENSE, Sweeden. [Online]. Available: http://www.q-sense.com/.

[Ric04] A.C. Richards, R.S. Shawgo, A.M. Johnson, N.T. Flyinn, Y. Li, M.J. Cima, and R. Langer, "A BioMEMS Review: MEMS Technology for Physiologically Integrated Devices", *Proc. IEEE*, vol. 92 (1), pp. 6-21, 2004.

[Rug89] Rugar, D., Mamin, H.J., and Guethner, P., "Improved fiber-opticinterferometer for atomic force microscopy", *Appl. Phys. Lett.*, vol. 55, pp. 2588–2590, 1989.

[Sar94] D. Sarid, Scanning Force Microscopy with applications to electric, magnetic and atomic forces, Oxford University Press, Inc., 1994.

[Smi95] J. Smith, S. Montague, J. Sniegowski, J. Murray, and P. McWhorter, "Embedded micromechanical devices for the monolithic integration of MEMS with CMOS", in *Proc.IEEE IEDM '95*, 1995, pp. 609–612D.

[Tam01] J. Tamayo, A.D.L. Humphris, A.M. Malloy, M.J. Miles, "Chemical sensors and biosensors in liquid environment based on microcantilevers with amplified quality factor", *Ultramicroscopy*, vol. 86, pp. 167-173, 2001.

[Yan06] Y. T. Yang, C. Callegari, X. L. Feng, K. L. Ekinci, and M. L. Roukes, "Zeptogram-Scale Nanomechanical Mass Sensing", *Nanoletters*, vol. 6 (4), pp. 583-586, 2006.

[Yas03] J. Yasaitis, M. Judy, T. Brosnihan, P. Garone, N. Pokrovskiy, D. Sniderman, S. Limb, R. Howe, B. Boser, M. Palaniapan, X. Jiang, and S. Bhave, "A modular process for integrating thick polysilicon MEMS devices with sub-micron CMOS", in *Proc. SPIE*, vol. 4979, pp. 145–154, 2003.

[Zha05] H. Zhang, and E.S. Kim, "Micromachined Acoustic Resonant Mass Sensor", *Journal of Microelectromechanical Systmes*, vol. 14, pp. 699, 2005.

CHAPTER 2

THEORY AND MODELING

This chapter introduces the theory related with beam resonators with electrostatic excitation and capacitive readout. The fundamental parameters and electrical characteristics are revised and analyzed for cantilever and CC-beam resonators in mass sensing applications. Finally, the ultimate limits in mass sensing are exposed and some figures of merit are defined to give some criteria in designing the resonant MEMS transducers.

2.1 ELECTROMECHANICAL TRANSDUCTION WITH BEAMS

In this section the main topics related with resonant beam based transducers with electrostatic excitation and capacitive readout are analyzed. In particular, two beam topologies are explored as mass sensors, the clamped-free beam commonly known as cantilever and the clamped-clamped beam or bridge (Figure 2.1.1).

2.1.1 STATIC AND DYNAMIC CHARACTERISTICS

A profound knowledge of the beam theory is needed in order to design sensor systems based on this type of mechanical structures. In this section the fundamental parameters for cantilevers and clamped-clamped beams (C-C beams) are derived. For further references see [Sar94] and [Tho93].

- **STATIC DEFORMATION (SPRING CONSTANT)**

The spring constant or stiffness (k) of any beam can be defined in terms of Hook's Law who relates the force (F) acting on the beam with the deflection of the beam (x):

$$F = -kx \tag{2.1.1}$$

We assume that this force is produced at the free-end and at the centre of the beam for a cantilever and a C-C beam respectively (see Figure 2.1.1). For a simple cantilever the spring constant is defined as

$$k = \frac{3\mathrm{E}I}{l^3}, \tag{2.1.2}$$

while for a C-C beam is

$$k = \frac{192\mathrm{E}I}{l^3}, \tag{2.1.3}$$

where E is the Young's Modulus of the material, which is concerning with the material elasticity, and I is the moment of inertia that for a rectangular cross-section beam is

$$I = \frac{tw^3}{12}. \tag{2.1.4}$$

Finally, using this value of I in equations (2.1.2) and (2.1.3) the spring constant equations for a cantilever and a C-C beam are respectively:

$$k = \frac{\mathrm{E}tw^3}{4l^3} \tag{2.1.5}$$

$$k = \frac{16\mathrm{E}tw^3}{l^3}. \tag{2.1.6}$$

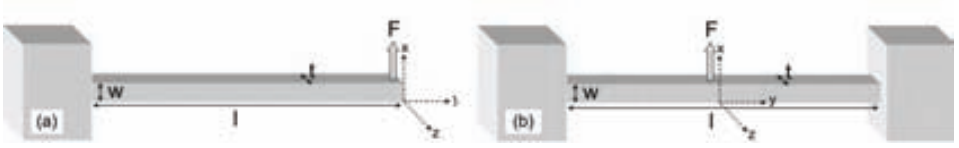

Figure 2.1.1 Schematic showing a clamped-free beam or cantilever (a) and a clamped-clamped beam or bridge (b) showing its dimensions: length (***l***), width (***w***) and thickness (***t***).

- **DYNAMIC BEHAVIOR (RESONANCE FREQUENCIES)**

The one-dimensional Euler-Bernoulli equation for a homogeneous beam is

$$\mathrm{E}I\frac{\partial^4 x}{\partial y^4} + \rho A\frac{\partial^2 x}{\partial t^2} = 0, \tag{2.1.7}$$

where A is the cross-section area ($t \times w$) and ρ is the mass density of the beam. The general solutions of Eq. 2.1.7 under vibration in the x-axis are given by:

$$x(y,t) = x(y)\cos(\omega_n t + \theta), \tag{2.1.8}$$

where ω_n is the resonant frequency of the n mode of vibration mode and θ an arbitrary phase. By defining the parameter κ in the form:

$$\kappa_n^4 = \frac{\omega_n^2 \rho t w}{\mathrm{E}I}, \tag{2.1.9}$$

Equation 2.1.7 is reduced to

$$\frac{\partial^4 x(y)}{\partial y^4} = \kappa_n^4 x(y) \cdot \tag{2.1.10}$$

The general solution of the Equation 2.1.10 is

$$x(y) = A_1 \sin \kappa_n x + A_2 \cos \kappa_n x + A_3 \sinh \kappa_n x + A_4 \cosh \kappa_n x \,. \tag{2.1.11}$$

Boundary conditions are used to find the values of κ_n, which lead to the values of ω_n. For a cantilever, the boundary conditions lead to

$$\cos \kappa_n l \cdot \cosh \kappa_n l = -1, \tag{2.1.12}$$

which when solved numerically, yields the first three Eigen-values $\kappa_n l$ to be: 1.875 for the fundamental vibration mode, 4.694 for the second mode, and 7.855 for the third mode.

For a C-C beam, the boundary conditions lead to

$$\cos \kappa_n l \cdot \cosh \kappa_n l = 1, \tag{2.1.13}$$

which yield the first three $\kappa_n l$ values of 4.730 for fundamental mode, 7.853 for the second mode, 10.996 for the third mode.

Finally, substituting Eq. (2.1.4) in Eq. (2.1.10) a general expression can be obtained for the natural resonant frequencies of beams (Eq. 2.1.14), where the Eigen-values to use will be different for a cantilever or for a C-C beam.

$$f_n = \frac{(\kappa_n \ell)^2}{2\pi} \frac{w}{l^2} \sqrt{\frac{E}{12\rho}} \tag{2.1.14}$$

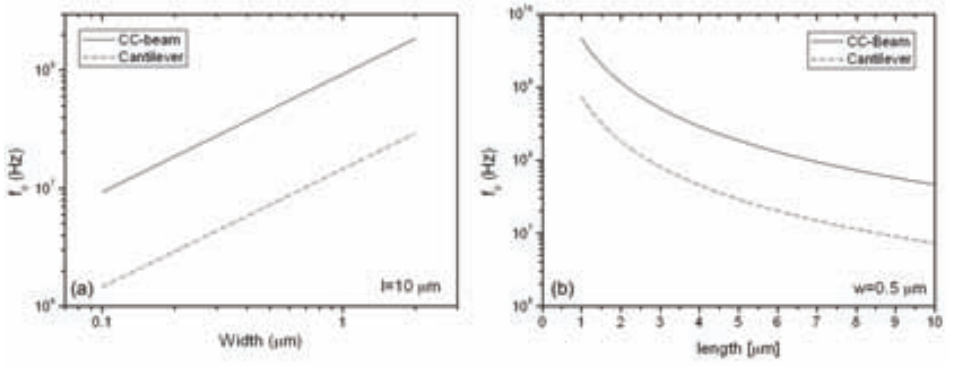

Figure 2.1.2 Fundamental resonant frequency versus width (a) and length (b) for a cantilever and a C-C beam with E=190 GPa and ρ=2330 kg/m^3.

In this case f_n is the natural resonance frequency expressed in Hz of the n mode of resonance. It can be observed that the resonance frequency is independent of the thickness of the beam. In Fig. 2.1.2 the dependence of the fundamental resonance frequency versus the width and the length of the beam are represented for a cantilever beam and a CC-beam.

- **MASS-SPRING SYSTEM (EFFECTIVE MASS)**

The behavior of mechanical resonators can be conceived as a lumped system. In this sense, the resonance frequency can be expressed in terms of the spring constant (k) and the effective mass (m_{eff}) using a mass-spring system model (Figure 2.1.3). In this approach we are considering that all the mass of the beam is concentrated at the free-end of the cantilever or at the middle of the CC-beam. The equation of the beam motion, in one dimension with no damping is:

$$m_{eff}\ddot{x} + kx = 0\,. \tag{2.1.15}$$

A general solution for the corresponding homogeneous equation is $x(t) = A\sin(\omega t + \theta)$ (harmonic oscillator) that allows to find and expression for the resonance frequency:

$$f_o = \frac{\omega}{2\pi} = \frac{1}{2\pi}\sqrt{\frac{k}{m_{eff}}}\,. \tag{2.1.16}$$

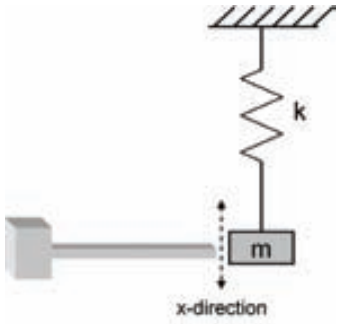

Figure 2.1.3 Mechanical lumped-parameter schematic for an un-dumped beam resonator.

In order to use this equation for beam structures, we need to define its effective mass. Using equations (2.1.5) and (2.1.14) we find that the effective mass for each vibration mode of a cantilever resonator is

$$m_{eff}^{c} = \frac{3\rho wlt}{(\kappa_n l)^4} = \alpha_n^{c} m_B\,, \tag{2.1.17}$$

where $\alpha_n^{c} = 3/(\kappa_n l)^4$ is the effective mass parameter and m_B is the total mass of the beam. For the first resonant mode α_n^{c} value is 0.2427.

With the same analysis, we find that the effective mass for each vibration mode of a CC-beam resonator is:

$$m_{eff}^{c-c} = \frac{192\rho wlt}{(\kappa_n l)^4} = \alpha_n^{c-c} m_B \tag{2.1.18}$$

- **DAMPING AND QUALITY FACTOR**

In any micromechanical system a dissipation of mechanical energy is always present. In these sense, the mass-spring model is modified in order to include a damping element (Fig. 2.1.4). In this case, the dynamic motion of the system can be described by next equation:

$$m_{eff}\ddot{x} + D\dot{x} + kx = 0\,, \tag{2.1.19}$$

where D is the damping coefficient. Last equation can be expressed in terms of the damping factor ζ and the natural resonance frequency $\omega_o=(k/m_{eff})^{1/2}$,

$$\ddot{x} + 2\zeta\omega_0\dot{x} + \omega_0^2 x = 0 \tag{2.1.20}$$

with $\zeta=D/2m_{eff}\omega_o$. When ζ is less than one, the system is under-damped and the damping factor is approximately related to the quality factor by

$$Q = \frac{1}{2\zeta}. \tag{2.1.21}$$

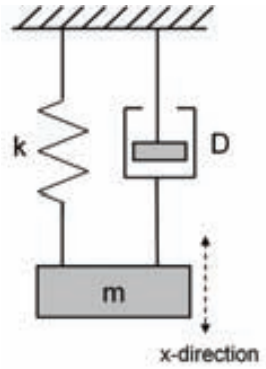

Figure 2.1.4 Mechanical lumped-parameter schematic for a mechanical resonator including losses (dumped system).

The impulsional response of the damped system in the time domain can be expressed as

$$x(t) = Ae^{-\frac{\omega_o}{2Q}t}\sin\left[\sqrt{\omega_o^2 - \left(\frac{\omega_o}{2Q}\right)^2}\,t + \theta\right], \tag{2.1.22}$$

where it is appreciated that as high is the Q-factor as slow is the dynamic response of the system.

By taking the Laplace transform, we can obtain the transfer function of the mass-spring-damper system

$$H(s) = \frac{1/m_{eff}}{s^2 + \omega_o/Q\, s + \omega_o^2}. \tag{2.1.23}$$

In the frequency domain, an under-damped system presents a resonant peak that increases in amplitude with greater quality factor and smaller damping factor. The maximum amplitude corresponds naturally to the resonance frequency ω_r. The resonance frequency is also a function of damping

$$\varpi_r = \varpi_o \sqrt{1 - \frac{1}{2Q^2}}. \tag{2.1.24}$$

The effects of damping on the amplitude and phase performance in the frequency response are presented in Fig. 2.1.5 for different quality factors.

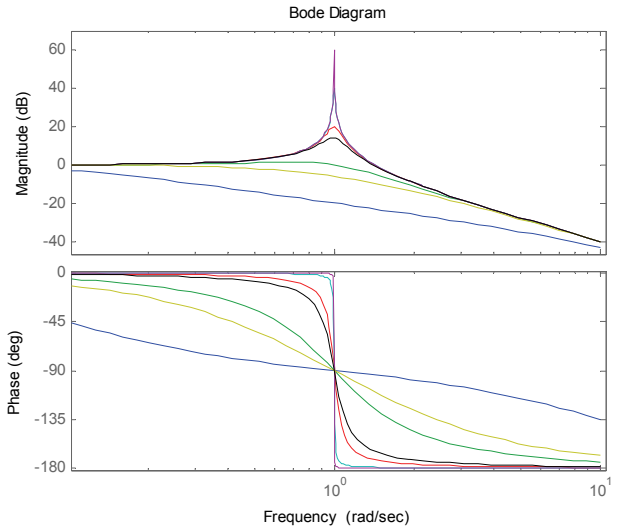

Figure 2.1.5 The effect of damping on the amplitude and phase response on the normalized transfer function (ω_o=m_{eff}=1). The Q-factor is varied between 0.1 (blue line) and 1000 (violet line).

Experimentally the quality factor is measured as $Q \approx f_o/BW_{3dB}$, where f_c is the center frequency of the peak and BW_{3dB} is the half-power, or -3dB, bandwidth of the measured peak.

There are several dissipation mechanisms that contribute to the total damping in MEMS/NEMS resonators. For small resonators working in air, the major components of energy dissipation in order of importance are squeeze force, airflow force, internal friction and support losses [Hos95]. The inverse of the total Q-factor of the device can be expressed as the inverse of the sum of all contributions. In this sense, the final Q-factor is dominated by the small Q-factor component. For

resonators with electrostatic actuation, where there is a rigid wall nearby (i.e. driver electrode), the damping is determined by the squeeze force, which is inversely proportional to the beam length. When the oscillator is used in vacuum, the damping is dominated by internal friction (bulk and surface effects) and support or clamping loss [Yas00].

2.1.2 RESONANT BEAM CHARACTERISTICS AS SENSOR

Since the resonance frequency of any beam depends on its effective mass, it can be used as a mass sensor. The mass sensing principle is based on measuring the resonance frequency shift of the resonator due to the accreted mass to the resonator. In this section, the mass sensitivity for cantilevers and C-C beams is derived and discussed.

- **MASS SENSITIVITY**

For the mass sensitivity analysis we assume that an accreted mass on the beam does not produce any change in the spring constant (i.e. very small amount of deposited mass compared with the beam mass and any stress effect on the beam surface). With this assumption, when a punctual mass is added (Δm) a down shift on the resonance frequency (Δf_n) is produced according with next equation [Cle93]:

$$f_n - \Delta f_n = \frac{1}{2\pi}\sqrt{\frac{k}{\Delta m + m_{eff}}} \tag{2.1.25}$$

The mass sensitivity of any beam (S_m) can be defined as:

$$S_m = \frac{\Delta m}{\Delta f_n} \approx -\frac{2m_{eff}}{f_n} \quad \text{(kg/Hz)}. \tag{2.1.26}$$

The IEEE Standard Dictionary of Electrical and Electronics defines the sensitivity of any sensor as the ratio of the magnitude of its response to the magnitude of the quantity measured [Vig00]. In this sense, in the literature we find a more formal term, called mass responsivity ($\Re$), and defined as [Eki05]:

$$\Re = \left|\frac{\partial f_n}{\partial m}\right| \approx \frac{f_n}{2m_{eff}} \quad \text{(Hz/kg)}. \tag{2.1.27}$$

Since in the mass sensing literature is commonly used the expression (Eq. 2.1.26) to indicate the mass sensitivity, in this dissertation the mass sensitivity is expressed in terms of the inverse of the mass responsivity ($\Re^{-1}$).

The previous equations are valid for punctual mass depositions, where the mass is added at the free-end of the cantilever or at the centre of the CC-beam. When the mass is uniformly distributed on the beam area ($A=l\times w$), the contribution of the total added mass on the mass-spring model is only in terms of its effective mass. In this case, the sensitivity may be given in terms of area using next expression

$$\Re_{area}^{-1} = \frac{\Re^{-1}}{\alpha_n A} \quad (\text{kg/m}^2\text{Hz}). \tag{2.1.28}$$

Using the equations of previous sections, the mass sensitivity of any rectangular cross-section beam can be expressed in terms of its geometrical parameters (l, w, t) as well as of the material characteristics (E, ρ). In Table 2.1 are summarized the main parameters for cantilevers and C-C beams.

Table 2.1 Summary of main parameters for mass sensors based on resonant cantilevers and CC-beams.

Parameter	**Symbol**	**Cantilever**	**CC-Beam**
Resonance frequency	f_n [Hz]	$f_n = \frac{1}{2\pi}\sqrt{\frac{k}{m_{eff}}} = \frac{(\kappa_n \ell)^2}{2\pi}\frac{w}{l^2}\sqrt{\frac{E}{12\varphi}}$	
		$f_o \approx 0.16\frac{w}{l^2}\sqrt{\frac{E}{\varphi}}$	$f_o \approx 1.03\frac{w}{l^2}\sqrt{\frac{E}{\varphi}}$
Spring constant	k [N/m]	$\frac{Etw^3}{4l^3}$	$\frac{16Etw^3}{l^3}$
Effective mass	m_{eff} [kg]	$\frac{3\rho wlt}{(\kappa_n \ell)^4}$	$\frac{192\rho wlt}{(\kappa_n \ell)^4}$
Eigenvalues	$(\kappa_n \ell)$	1.875, 4.694, 7.855, …	4.730, 7.853, 10.996, …
Mass sensitivity	$\Re^{-1}$ [kg/Hz]	$\frac{24\sqrt{3}\pi}{(\kappa_n \ell)^6}\frac{\rho^{3/2}}{\sqrt{E}}l^3 t$	$\frac{1536\sqrt{3}\pi}{(\kappa_n \ell)^6}\frac{\rho^{3/2}}{\sqrt{E}}l^3 t$
		$\approx 3\frac{\rho^{3/2}}{\sqrt{E}}l^3 t$ *(fundamental mode)*	$\approx 0.75\frac{\rho^{3/2}}{\sqrt{E}}l^3 t$ *(fundamental mode)*

From Table 2.1 we can note that the mass sensitivity, for punctual depositions, is proportional to $l^3 t$ and it does not depend on the width of the beam. From this geometrical point of view, we need to work with short beams in order to obtain high mass sensitivities (see Fig. 2.1.6). This means that the mass sensitivity can be improved by scaling down the beam dimensions. On the other hand, the use of materials with a high Young Modulus and low mass density are also indicated to fabricate high-sensitivity mass sensors. However, the effects on the resonance frequency, inversely proportional to the square of the length, have to be considered in order to develop a feasible mass sensor system.

In summary, last results indicate the need to work with short and narrow beams to achieve high mass sensitivities at not too high frequencies. In this case, the technological limitation to fabricate very narrow beams becomes a fundamental challenge.

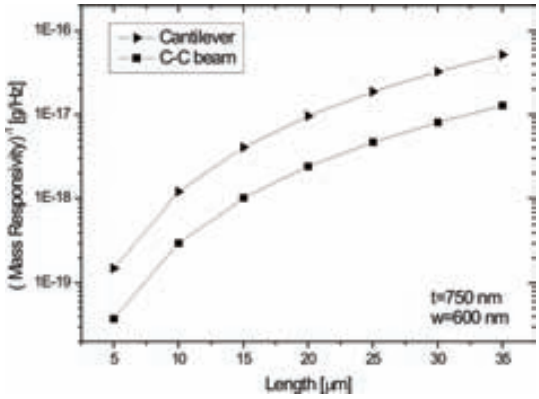

Figure 2.1.6 Punctual mass sensitivity versus length for a cantilever and a CC-beam with E=190 GPa and ρ=2330 kg/m^3.

2.1.3 ELECTROSTATIC ACTUATION AND CAPACITIVE READOUT

In our approach the beam resonator is electrostatically actuated and detected. The oscillation of the beam is electrostatically induced applying an external AC force and is detected as a capacitance change. This electrostatic coupling approach leads to the minimal power consumption.

- **ELECTROSTATIC ACTUATION**

The electrostatic actuation or excitation (F_E) is performed by means of a fixed electrode (called driver) that is placed close and parallel to the beam resonator (Fig. 2.1.7). The dynamic motion of the system with an external force is described by the equation

$$m_{eff}\ddot{x} + D\dot{x} + kx = F_E . \tag{2.1.29}$$

The beam resonator and the driver electrode constitutes a capacitor C which value depends on the gap size s and on the displacement of the moving resonator x,

$$C = \varepsilon \frac{l \cdot t}{s - x} = C_o \frac{s}{s - x}, \tag{2.1.30}$$

where C_o is the capacitance with zero displacement.
The electrostatic energy W stored in the capacitor is

$$W = \frac{1}{2} C V^2, \tag{2.1.31}$$

where V is the effective voltage across the capacitor. The electrostatic force is a negative gradient of energy and can be written using Taylor's series approximation (small variation in x) as

$$F_E = -\frac{dW}{dx} = -\frac{1}{2}V^2\frac{\partial C}{\partial x} \approx -\frac{1}{2}V^2\frac{C_o}{s}\left[1+2\left(\frac{x}{s}\right)+3\left(\frac{x}{s}\right)^2+\ldots+(n+1)\left(\frac{x}{s}\right)^n\right]. \quad (2.1.32)$$

The electrostatic force is proportional to the squared voltage and consequently is always attractive. In this sense, a DC bias voltage (V_{DC}) is also required to produce an electrostatic force that excites the beam resonator exactly at the AC driving voltage (V_{AC}) frequency. Therefore we get

$$V^2 = \left(V_{DC}+V_{AC}\cos\omega t\right)^2 = {V_{DC}}^2 + \frac{1}{2}{V_{AC}}^2 + \frac{1}{2}{V_{AC}}^2\cos 2\omega t + 2V_{DC}V_{AC}\cos\omega t \quad (2.1.33)$$

and

$$F_E = -\frac{1}{2}\frac{\partial C}{\partial x}\left({V_{DC}}^2 + \frac{1}{2}{V_{AC}}^2 + \frac{1}{2}{V_{AC}}^2\cos 2\omega t + 2V_{DC}V_{AC}\cos\omega t\right). \quad (2.1.34)$$

From the previous equations we can see that the electrostatic force may have components at zero frequency, at ω and at 2ω. Since we aim at having the excitation at frequency ω, the DC voltage must be much stronger than the AC voltage ($V_{DC}>> V_{AC}$). In addition, the displacement x is typically small compared with the gap size s (linear region, $x<<s$), which means that the force can be approximated as

$$F_E \approx -\frac{C_o}{2s}\left[1+2\left(\frac{x}{s}\right)\right]V^2 \approx -\frac{C_o{V_{DC}}^2}{2s} - \frac{C_oV_{DC}V_{AC}\cos\omega t}{s} - \frac{C_o{V_{DC}}^2}{s^2}x - \frac{2C_oV_{DC}V_{AC}\cos\omega t}{s^2}x. \quad (2.1.35)$$

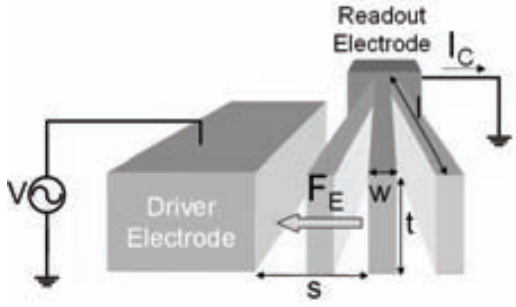

Figure 2.1.7 Schematic showing a cantilever with electrostatic actuation and capacitive readout.

- **ELECTRICAL SPRING SOFTENING**

Equation 2.1.35 indicates that, as a first approximation, the electrostatic force depends linearly on the cantilever position (x). This dependence can be interpreted as an electrical spring constant (k_{el}) which can be expressed as

$$\frac{\partial F_E}{\partial x} = k_{el} = -\left\langle V^2\right\rangle\frac{C_o}{s^2}, \quad (2.1.36)$$

where $\langle V^2 \rangle$ is the square of the effective DC voltage that is corresponding with the first two components in Eq. 2.1.33.

Since as the beam move in one direction, the electrostatic force tends to push the beam further into this direction, the electrical spring constant is negative. This effect can be referred as a change on the spring constant of the lumped system, defining an effective spring constant k_{eff} that is softer than the mechanical spring constant,

$$k_{eff} = k - |k_{el}| . \tag{2.1.37}$$

In this sense, the electrostatic force applied to the resonator alters its sensitivity and resonance frequency. The effective resonance frequency can be expressed in terms of the mechanical and electrical spring constant that takes into account the spring softening effect,

$$f_e = \sqrt{\frac{k_{eff}}{m_{eff}}} = f_o \sqrt{1 - \left|\frac{k_{el}}{k}\right|} = f_o \sqrt{1 - \frac{\langle V^2 \rangle C_o}{ks^2}} . \tag{2.1.38}$$

Therefore, electromechanical coupling can also be used to tune the resonance frequency which is very useful in RF applications (i.e. voltage-controlled oscillators based on MEMS resonators). However, the frequency tuning is limited by a pull-in or snap-in effect.

- **SNAP-IN VOLTAGE**

The snap-in effect occurs when the voltage is so high that the resonator sticks to the driver electrode. The pull-in behavior is observed when the mechanical and electrical forces (and simultaneously also their derivatives) cancel each other. Assuming that the mechanical resonator bends parallel towards the driver electrode, the snap-in voltage and the corresponding snap-in distance x_{si} (in non-resonant case) are [Sen01]:

$$V_{si} = \sqrt{\frac{8s^2 k}{27 C_o}} , \tag{2.1.39}$$

$$x_{si} = s/3 . \tag{2.1.40}$$

So the snap-in voltage of the system depends on the coupling strength and on the spring constant.

In the case of a cantilever resonator, last assumption is not valid and a more accurate value for the snap-in voltage can be found assuming that the cantilever sustains a linear deformation shape deflection [Aba01]:

$$V_{si} = \sqrt{\frac{0.88 s^2 k}{C_o}} , \tag{2.1.41}$$

$$x_{si} = 0.44 s . \tag{2.1.42}$$

In this case the snap-in distance is corresponding with the displacement of the free-end of the cantilever.

- **CAPACITIVE READOUT PRINCIPLE**

The oscillation of the beam can be sensed using the anchor of the resonator as the readout electrode. When the resonator is electrostatically excited by means of a DC-voltage plus an AC-voltage, a capacitive current is generated in the driver-resonator interface according with next equation, assuming $V_{DC}>>V_{AC}$:

$$I_C = \frac{\partial}{\partial t}(C \cdot V) = C\frac{\partial V_{AC}}{\partial t} + (V_{DC} + V_{AC})\frac{\partial C}{\partial t} \approx C_o \frac{\partial V_{AC}}{\partial t} + V_{DC}\frac{\partial C}{\partial t} = I_P + I_M \cdot \quad (2.1.43)$$

The first term is a parasitic current (I_P) since it does not reflect the movement of the resonator and it is generated due to the AC-voltage applied for its excitation. The second term, called motional current (I_M), reflects the oscillation of the beam since it depends on the variation of the driver-resonator capacitance.

To analyze the motional current induced by this oscillation, we assume that the motion is (harmonic) sinusoidal, obtaining:

$$I_M \approx V_{DC}\frac{\partial C}{\partial t} = V_{DC}\frac{\partial C}{\partial x}\frac{\partial(x_o \sin\omega t)}{\partial t} = V_{DC}\frac{\partial C}{\partial x}\omega x_o \cos\omega t = \eta\omega x_o \cos\omega t \cdot \quad (2.1.44)$$

η is the electromechanical coupling factor that express the relation between the AC-voltage applied and the electrostatic force generated at the frequency ω (last term of Eq. 2.1.34):

$$\eta = \frac{F_E(\omega)}{V_{AC}} = V_{DC}\frac{\partial C}{\partial x} \approx V_{DC}\frac{C_o}{s} \cdot \quad (2.1.45)$$

The coupling between the electrostatic and mechanical domains depends on the coupling capacitance and the gap size between electrodes as well as on the DC bias voltage over the gap. Thus narrow gaps (s small) increase strongly the electromechanical coupling.

In addition to the voltage and the vibration amplitude, the motional current depends also on the frequency and the gradient of the capacitance between the driver electrode and the resonator. When the excitation voltage (V_{AC}), and hence the force that it generates, are acting at the resonance frequency of the resonator, the effect of that force is multiplied by the Q factor of the resonator. We are assuming a high-Q resonator, so $QF=kx$. Dividing the force with the spring constant, we get the vibration amplitude at resonance

$$x_r = Q\frac{\eta V_{AC}}{k} \approx Q\frac{C_o V_{DC} V_{AC}}{ks} \cdot \quad (2.1.46)$$

The motional current at resonance can now be written in a form

$$I_{M,r} = Q\frac{\eta^2 V_{AC}\omega}{k} \approx Q\frac{{V_{DC}}^2 V_{AC}\omega {C_o}^2}{ks^2}, \quad (2.1.47)$$

showing that the motional current depends strongly on the electromechanical coupling factor.

- **ONE VERSUS TWO DRIVERS CONFIGURATION**

The capacitive coupling, in particular the configuration of Fig. 2.1.7, has a significant drawback. The capacitance C_o, which drives the resonance of the beam through the V_{AC} applied

voltage, is also in charge of detecting the induced total current: the motional term and the parasitic term. This parasitic current, I_p in Eq. 2.1.43, can constitutes a serious problem, since both currents (motional and parasitic) oscillate at the same frequency and can mask the motional current. The ratio of induced motional current to the parasitic current is

$$\frac{I_{M,r}}{I_P} = \frac{Q\dfrac{V_{DC}{}^2 V_{AC}\omega C_o{}^2}{ks^2}}{\omega V_{AC} C_o} = \frac{QC_o V_{DC}{}^2}{ks^2}. \qquad (2.1.48)$$

Thus, high quality factors, high DC-voltages and narrow gaps help to improve coupling. In addition, we can see that the AC-voltage level has not effect on the current ratio.

Using different electrodes for driving and readout, that is the two-port configuration depicted in Fig. 2.1.8, the current ratio can be improved. In this configuration, the DC-bias voltage is applied directly to the resonator. The AC-voltage is applied to one of the electrodes (driver electrode), and the output capacitive current is detected from the other (readout electrode).

With this scheme, the parasitic current term is theoretically canceled since any direct coupling between the excitation or driver electrode and the readout electrode is present. In practice, some parasitic coupling between these drivers (C_p) is still present and arises from the package and from the bonding wires when the readout electronics is not integrated. In the case of monolithic sensors, this parasitic coupling is still present ought to the fringing field coupling through IC bulk or air. The effect of this parasitic coupling on the frequency response of the resonator is discussed in next section.

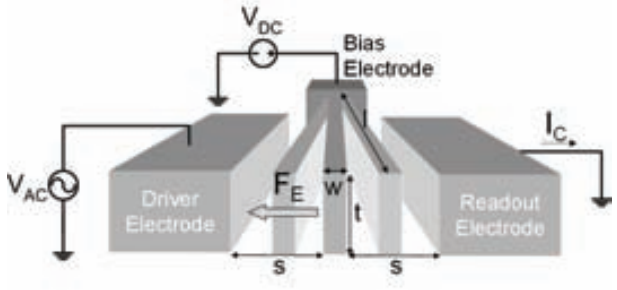

Figure 2.1.8 Schematic showing a cantilever with electrostatic actuation and capacitive readout with two-port configuration.

2.2 ELECTRICAL MODELING

An electrical model of the electromechanical transducer performance is required to perform system level electrical simulations of the MEMS and the interfacing circuitry. The equivalent circuit using lumped constant elements ($R_m L_m C_m$) is shown in Fig. 2.2.1a. All resonators, in the lineal regime, can be modeled in this way. The component values of the equivalent circuit are obtained finding the electrical equivalences with respect to the mass, spring constant and damping of the dynamic system [Ngu99]. The main parameter of the model is the equivalent motional resistance (R_m) of the resonator that is defined as the fraction of the excitation AC-voltage divided by the motional current generated at the resonance (Eq. 2.1.47). In this sense, the equivalent motional resistance can be expressed as

$$R_m = \frac{\sqrt{km_{eff}}}{Q\eta^2} = \frac{1}{Q}\frac{ks^4}{V_{DC}^2\omega_o A^2\varepsilon^2} = \frac{1}{Q}\sqrt{\frac{L_m}{C_m}}, \tag{2.2.1}$$

with $C_m = \frac{\eta^2}{k}$ and $L_m = \frac{m_{eff}}{\eta^2}$. (2.2.2)

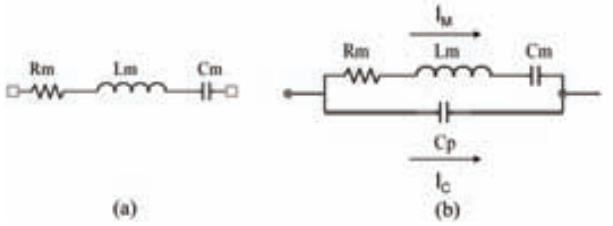

Figure 2.2.1 Small-signal electrical equivalent circuit for the electromechanical resonator without parsitics (a) and including the parasitic feedtrough capacitance (b).

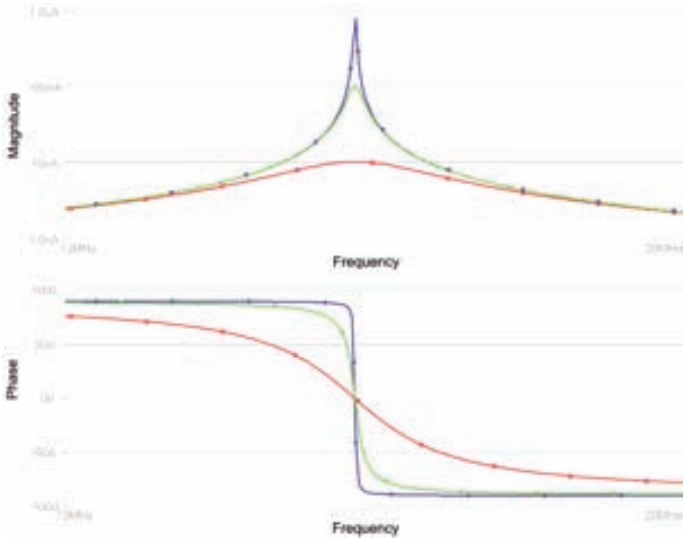

Figure 2.2.2 Electrical frequency response of a MEMS resonator with L_m=10 H, C_m=10 aF and different motional resistances (R_m) values of 1MΩ (blue line), 10MΩ (green line) and 100MΩ (red line).

The admittance of the series *RLC* branch have the maximum at the resonance frequency, where the effects of the L_m and C_m are cancelled and the branch acts as a purely resistor R_m. Large values of R_m tend to decrease the resonance peak magnitude as well as the phase slope around the resonance frequency (Fig. 2.2.2). High values or R_m comes from, among other factors, a low value of the mechanical quality factor of the resonator. The electrical quality factor obtained from the

electrical performance of the series *RLC* branch is corresponding with the mechanical quality factor of the resonator and can be obtained using the equation

$$Q = \frac{f_o}{BW_{3dB}} = f_o \frac{\pi}{360} \frac{\delta\phi}{\delta f} \cdot \tag{2.2.3}$$

- **PARASITIC CAPACITANCE C_P**

The parasitic capacitance C_p present in any system with electrostatic transduction may be incorporated at the electrical model as shown in Fig. 2.2.1b. The admittance of the resonator at resonance is given by

$$Y_{eq} = \frac{1}{R_m} + j\omega_o C_p \cdot \tag{2.2.4}$$

The two components of the admittance are related with the motional current and the parasitic current terms. These two terms are in quadrature (90º out of phase) at resonance and consequently, the square of the admittance magnitude is corresponding with sum of the squares of each component.

For sufficiently large values of $\omega_o C_p$ relative to $1/R_m$, the parasitic capacitance term dominates, resulting in a feedthrough current that effectively masks the motional current derived from R_m. Furthermore, this parasitic capacitance creates a parallel-resonance at the frequency given by

$$f_p = f_o \sqrt{1 + \frac{C_m}{C_p}} \cdot \tag{2.2.5}$$

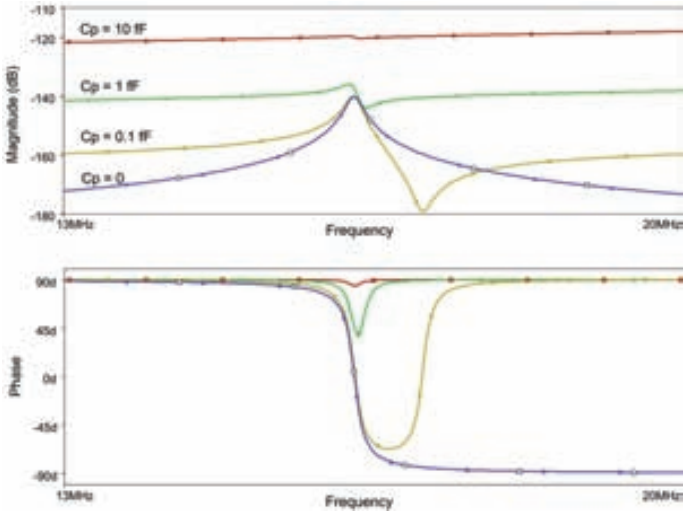

Figure 2.2.3 Effect of parasitic capacitance on the frequency response of a MEMS resonator with R_m=1 MΩ, L_m=10 H and C_m=10 aF.

In Fig. 2.2.3, is observed that as the value of the parasitic capacitance increases, the parallel resonance becomes closer to the series resonance lowering the resonance peak and degrading the electrical quality factor measured that is not corresponding with the intrinsic mechanical quality factor of the resonator (Q).

- **NONLINEARITIES**

The origin of nonlinearities in electrostatically actuated resonators can be electrical and mechanical. The electrical nonlinearity is due to the nonlinearity of the capacitive transduction and the mechanical nonlinearity is due to geometrical and material effects [Kaa04].

Due to the inverse relationship between displacement and parallel plate capacitance, the electrostatic coupling introduces nonlinear terms in the electrostatic force (see. Eq. 2.1.32). As already stated, the first term (independent of the resonator displacement x) of the Eq. 2.1.32 is corresponding with the linear electrical spring constant. The other terms of the series expansion are corresponding with the nonlinear electrical spring constants generating a nonlinear spring softening effect that produces a bending of the resonance peak towards lower frequencies. At large amplitude levels of the resonator the frequency characteristics become hysteretic (Fig. 2.2.4a).

On the other hand, the mechanical nonlinearity is mainly due to the beam elongation effect that produces a cubic spring coefficient, that is, the mechanical spring constant depends on the resonator displacement (x) in a cubic form. In this case, the resonance peak bends to higher frequency (hard-softening effect) and for high amplitudes the frequency response also presents hysteresis (Fig. 2.2.4b). This phenomenon is emphasized for high-Q resonator since the critical amplitude leading to hysteretic behavior is inversely proportional to the Q-factor [Kaa04].

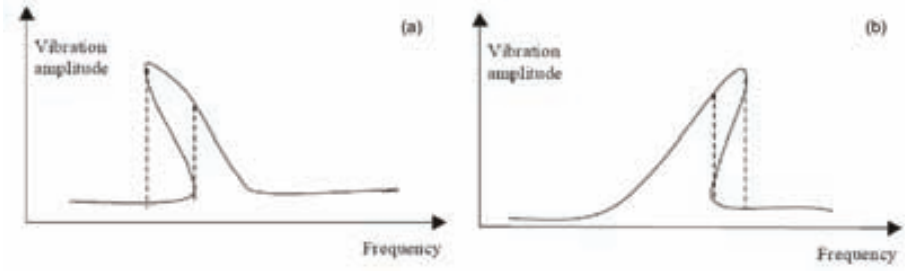

Figure 2.2.4 Illustration of (a) the spring-softening effect in the capacitive transducer and (b) the spring-hardening effect due to the cubic nonlinearity of the spring coefficient.

- **LARGE-SIGNAL MODEL**

The *RLC* model previously presented can be used for modeling beam resonators but it is a linear small-signal approximation that is only valid for small oscillation amplitudes of the resonator. As we have exposed, beam resonators may present a nonlinear performance that can not be modeled by electrical components with linear characteristics (i.e. *RLC*).

In this thesis, a parallel work has been performed in order to develop a non-linear electromechanical model for electrostatically driven resonant beams that can be used to perform

system level electrical simulations. The model takes into account non-linearities from electrostatic transduction, fringing field contributions and real deflection profile of the beam [Tev04]. The model is implemented by using an analog hardware description language (Verilog-A) that allows its use in a common IC CAD environment like CADENCE [Ver05, Ver06].

This model has been used during this thesis work in order to simulate the performance of different cantilevers and C-C beam structures integrated with CMOS circuitry. A description in depth of the model can be found in the Appendix A.

2.3 LIMITS TO MASS SENSING

The resolution of a mass sensor is the minimum increment of mass (δM) that we are able to measure. Although the mass sensitivity depends only on the resonator characteristics (resonance frequency and effective mass), the final resolution of the sensor system is limited by the noise sources of the different elements of the system.

Noise processes in MEMS resonators can be divided into processes intrinsic to the device (for instance, thermomechanical noise or temperature fluctuations) and those extrinsic related to interactions with its environment (for instance, adsorption-desorption noise or momentum exchange noise). In addition, the readout system noise used to detect the MEMS resonance has been also to be considered.

- **INTRINSIC NOISE**

In this section only the thermomechanical noise is analyzed since it is the dominant intrinsic source noise present in our resonators when operating at room temperature. For further references about intrinsic noise source in electromechanical resonators see [Cle02, Dju00, Eki04, Vig99].

The thermomechanical noise is equivalent to Johnson noise, white noise or Brownian motion. Any mechanical structure able to dissipate energy has associated a motional noise for temperatures higher than 0 K. The fluctuation-dissipation theorem gives the energy associated at each vibration mode of the resonator:

$$\frac{1}{2} m_{eff} \omega_o^2 \langle x \rangle^2 = \frac{1}{2} K_B T \cdot \tag{2.3.1}$$

Where $<x>$ is the mean square displacement fluctuations of the resonator, K_B is the Boltzmann's constant and T is the temperature expressed in Kelvin.

The spectral density of these random displacements $N_x(\omega)$ (with units of m^2/Hz), which is shaped by the frequency characteristics of the resonator, is given by [Eki04]

$$N_x(w) = \frac{4K_B T \omega_o}{m_{eff}} \frac{1}{\left(\omega^2 - \omega_o^2\right)^2 + \omega_o^2 \omega^2 / Q^2} \cdot \tag{2.3.2}$$

From Figure 2.3.1 we can observe than the quality factor is an important factor in the distribution of the noise spectral density. The spectral density has the maximum at the resonance frequency since the beam oscillates at higher amplitudes at the resonance. The root mean square displacement at the resonance is

$$N_x(\omega_o) = \frac{4K_BTQ}{m_{eff}\omega_o^3} = \frac{4K_BTQ}{k\omega_o} \quad \rightarrow \quad \langle x(\omega_o)\rangle = \sqrt{\frac{4K_BTQ}{k\omega_o}BW}, \tag{2.3.3}$$

where BW is the readout bandwidth.

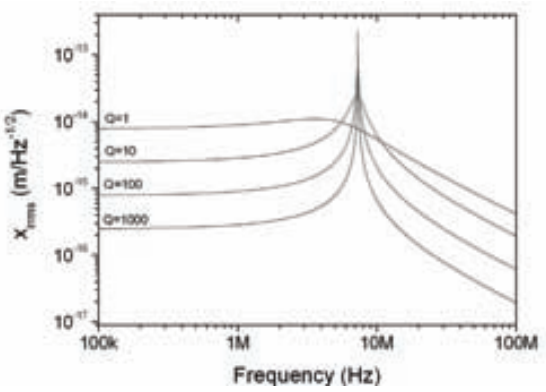

Figure 2.3.1 Thermomechanical noise associated to a polysilicon cantilever resonator (w=0.5 μm, l=10 μm and t=1 μm) for different values of Q.

Thermal displacements fluctuations generate frequency fluctuations on the frequency response of the resonator. The effective spectral density of these frequency fluctuations can be expressed as [Eki04]

$$N_\varpi(w) \approx \frac{\omega_o^5 K_B T}{Q^3 E_c} \frac{1}{\left(\omega^2 - \omega_o^2\right)^2 + \omega_o^2\omega^2/Q^2}. \tag{2.3.4}$$

In this case $E_C = m_{eff}\omega_o^2\langle x^2\rangle$ represents the cinematic energy of the resonator when is forced to oscillate (i.e., electrostatic excitation) with a mean square amplitude of $\langle x^2\rangle$. The resonance frequency fluctuations in Hz, δf_o, for a given readout bandwidth is

$$\delta f_o \approx \sqrt{\frac{K_BT}{E_c}\frac{f_oBW}{2\pi Q}}. \tag{2.3.5}$$

The minimum frequency shift able to measure is limited by Eq. 2.3.5 that with Eq. 2.1.26 set the ultimate limit on the mass resolution

$$\delta M \approx 2m_{eff}\sqrt{\frac{K_BT}{E_c}\frac{BW}{Q2\pi f_o}}. \tag{2.3.6}$$

Figure 2.3.2 plots the ultimate mass resolution imposed by thermomechanical noise for a polysilicon resonator with CC-beam or cantilever configuration for different oscillation amplitudes and two different quality factors. It is observed that for the same conditions, the CC-beam structure is superior in terms of mass resolution.

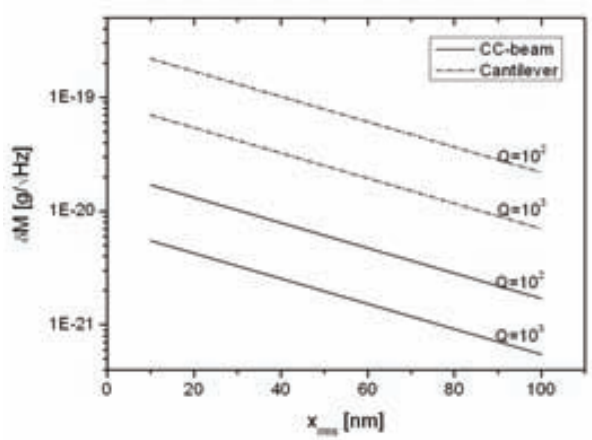

Figure 2.3.2 Limits to mass resolution per unit of the readout bandwidth imposed by thermomechanical fluctuation as a function of the root mean squared oscillation amplitude for a polysilicon cantilever and a C-C beam resonator (w=0.5 μm, l=10 μm and t=1 μm).

- **READOUT SYSTEM NOISE**

In most cases, the readout system noise limits the mass resolution of the sensor system avoiding to achieve the mass resolution set by Eq. 2.3.6. The resonance frequency fluctuations set by the readout system can be expressed as [Eki04b]

$$\delta f_o \approx \frac{f_o}{Q_E}\sqrt{\frac{S_v BW}{D_s\langle x_c\rangle}} = \frac{f_o}{Q_E}\frac{1}{SNR}. \tag{2.3.7}$$

In this case S_V is the spectral density of the voltage noise generated by the readout electronics, and D_S is the displacement sensitivity of the readout system used to detect the movement of the resonator that is expressed in units of V/m. The signal-to-noise ratio, equivalent to the dynamic range, is defined as the amplitude of oscillation divided by the minimum amplitude that the readout system can detect.

Finally, the mass resolution limited by the readout system can be also found using Eq. 2.1.26,

$$\delta M = \frac{2m_{eff}}{f_o}\delta f \approx \frac{2m_{eff}}{Q_E}\frac{1}{SNR}. \tag{2.3.8}$$

- **ACTUATION SYSTEM NOISE**

Due to the spring-softening effect in electrostatic actuation, the frequency stability of the resonator also depends on the noise present in the voltage source used to electrostatically actuate the resonator. By linearization of Eq. 2.1.38 and differentiating it with respect to effective voltage $<V>$, one can deduce the frequency fluctuations due to voltage fluctuations or noise δV according to:

$$\delta f_o = \langle V \rangle \frac{f_o}{2k} \frac{C_o}{s^2} \delta V \cdot \tag{2.3.9}$$

In practice, the electrical noise of voltage suppliers (DC sources) used to bias the resonator is low enough to assure that the frequency noise due to this phenomenon is negligible.

2.4 FIGURES OF MERIT

In this section, some figures of merit (FOM) are defined and analyzed for mass sensors based on resonant MEMS transducers with electrostatic excitation and capacitive readout. Since the transducer has to be integrated with electronics, it can not be conceived only in terms of its mass sensitivity but also in electrical terms. For this purpose, the FOM finally proposed can be used to compare the performance of different mass resonant transducers. In particular, the expressions of these FOMs are expressed for a cantilever and a CC-beam in terms of its physical parameters allowing comparison and giving criteria for its optimization.

From the electrical point of view, an electrical figure of merit (FOM_1) of any resonator can be expressed in terms of the ratio between the parasitic impedance relative to the motional resistance as we have commented in section 2.2. In Table 2.2 this FOM_1 is obtained for a cantilever and a CC-beam showing that for the same parameters the cantilever is superior.

On the other hand, since our purpose is perform mass measurements, it results compulsory to take into account the mass sensitivity of the transducer in the FOM. In Table 2.2, FOM_2 introduces this term and the equations obtained for the CC-beam and the cantilever shows that the CC-beam performance becomes more similar to the cantilever.

In mass sensing applications with readout electronics, a high value of the resonance frequency may be a disadvantage and ones want to minimize it in order to relax the readout circuit specifications. For this purpose the last figure of merit (FOM_3) takes into account the resonance frequency. In this case, the cantilever results two order of magnitude better than the CC-beam.

We have to remark that the performance of the CC-beam can be comparable to the cantilever by using a bias voltage ten times higher. Nevertheless, this option not always can be assumed.

Table 2.2 gives the information to design beam resonators for mass sensing applications taking into account both sensitive and electrical aspects. Note that $FOM_{2\text{-}3}$ indicates that the transducer performance is independent of the thickness. As small is the thickness as lower is the signal generated by the transducer but this is compensated since the sensor is more sensitive (the mass of the beam is reduced).

In Table 2.3 are listed the different criteria and the physical/technological limits to achieve them for an optimal design of beam resonators. For a specific technology, only geometrical parameters of the beam can be defined by the designer. In this sense, it is interesting to design long beams to improve its electromechanical performance but with the limitation that long beams tend to bend out-of-plane and the vertical snap-in becomes critical. On the other hand, the width and the gap have to be minimized in order to increase the mass sensitivity and the electrostatic coupling. In this case, the technology used to fabricate the devices sets the minimum dimensions available. The parasitic coupling is another parameter that the designer can improve by an optimal layout design. For example the use of two driver electrodes minimizes the parasitic coupling.

The use of high bias voltages increases the motional current generated improving the electrical performance. For mechanical transducers with small gaps, the main limitation is set by the snap-in voltage of the resonator towards the driver electrode.

Physical parameters like the Young Modulus and mass density are limited by the characteristics of the CMOS layer used to fabricate the resonator. The quality factor is also limited by the technology since the ultimate limit is set by the internal losses in the material.

Finally, the dielectric used in our resonators is air and consequently its constant value can not be modified. In any case, MEMS resonators fabricated with a solid dielectric (with a higher dielectric constant) have been developed mainly for RF-applications [Lin05, Tev04 and Tev07].

Table 2.2 Summary of main parameters for mass sensors based on resonant cantilevers and CC-beams.

Figure of Merit	Cantilever	CC-Beam	Ratio (FOM_{CANT} / FOM_{CC-B})
$FOM_1 = \frac{\lvert Z_{Cp} \rvert}{R_m}$	$4\frac{Q\varepsilon_o^2 l^5 t V_{DC}^2}{s^4 C_P E w^3}$	$\frac{1}{16}\frac{Q\varepsilon_o^2 l^5 t V_{DC}^2}{s^4 C_P E w^3}$	64
$FOM_2 = \frac{\lvert Z_{Cp} \rvert}{R_m}\Re$	$\frac{1}{3^2}\frac{Q\varepsilon_o^2 l^2 V_{DC}^2 (\kappa_n \ell)^6 \sqrt{12}}{s^4 C_P w^3 2\rho^{3/2}\sqrt{E}}$	$\frac{1}{192^2}\frac{Q\varepsilon_o^2 l^2 V_{DC}^2 (\kappa_n \ell)^6 \sqrt{12}}{s^4 C_P w^3 2\rho^{3/2}\sqrt{E}}$	~16
$FOM_3 = \frac{\lvert Z_{Cp} \rvert}{R_m}\frac{\Re}{\omega_o}$	$\frac{1}{3^2}\frac{Q\varepsilon_o^2 l^4 V_{DC}^2 (\kappa_n \ell)^4}{s^4 C_P w^4 \rho E}$	$\frac{1}{192^2}\frac{Q\varepsilon_o^2 l^4 V_{DC}^2 (\kappa_n \ell)^4}{s^4 C_P w^4 \varphi E}$	~101

Table 2.3 Criteria and limits in designing beam resonators for mass sensing applications.

Parameter	Condition	Limits
Length	high	Snap-in, material stress
Width	small	Fabrication technology
Gap	small	Fabrication technology
Bias voltage	high	Snap-in, dielectric breakdown
Young modulus, Mass density	low	Layers available in the technology
Dielectric constant	high	Air value. For not flexural structures solid dielectrics can be used.
Quality factor	high	Layers available in the technology. Operating conditions (air/vacuum).
Parasitic coupling	low	Layout of the structure (2-driver configuration reduces the parasitic coupling).

REFERENCES

[Aba01] G. Abadal, Z.J. Davis, B. Helbo, X. Borrise, R. Ruiz, A. Boisen, F. Campabadal, J. Esteve, E. Figueras, F. Perez-Murano, and N. Barniol, "Electromechanical model of a resonating nano-cantilever-based sensor for high-resolution and high-sensitivity mass detection", *Nanotechnology,* vol. 12 (2), pp. 100-104, 2001.

[Cle93] J. P. Cleveland, S. Manne, D. Bocek, P. K. Hansma, "A nondestructive method for determining the spring constant of cantilevers for scanning force microscopy", *Rev. Sci. Instrum.*, vol. 64 (2), pp. 403-405, 1993.

[Cle02] A.N. Cleland, M.L. Roukes, "Noise processes in nanomechanical resonators", *Journal of Applied Physics*, vol. 92 (5), pp. 2758-2769, 2002.

[Dju00] Z. Djuric, "Noise sources in microelectromechanical systems", in *Proc. 22nd IEEE International Conference on Microelectronics*, vol. 1, pp. 85-96, 2000.

[Eki04] K.L. Ekinci, Y.T. Yang, and M.L. Roukes, "Ultimate limits to inertial mass sensing based upon nanoelectromechanical systems", *J. Appl. Phys.,* vol. 95, pp. 2682, 2004.

[Eki04b] K.L. Ekinci, X.M.H. Huang, and M.L. Roukes, "Ultransensitive nanoeletromechanical mass detection", *Applied Physics Letters,* vol. 84, pp. 4469, 2004.

[Eki05] K.L. Ekinci, M.L. Roukes, "Nanoelectromechanical systems", *Rev. Sci. Instrum.*, vol. 76, pp. 061101, 2005.

[Hos95] H. Hosaka, K. Itao, S. Kuroda, "Damping characteristics of beam-shaped micro-oscillators", *Sensors and Actuators (A)*, vol. 49, pp. 87-95, 1995.

[Kaa04] V. Kaajakari, T. Mattila, A. Oja, and H. Seppa, "Nonlinear Limits for Single-Crystal Silicon Microresonators", *Journal of Microelectromechanical Systems,* vol. 13 (5), pp. 715-724, 2004

[Ngu99] C.T.-C Nguyen and R.T. Howe, "An Integrated CMOS Micromechanical Resonator High-Q Oscillator", *IEEE J. Solid-State Circuits*, vol. 34, no. 4, pp. 440-455, April 1999.

[Sar94] D. Sarid, *Scanning Force Microscopy with applications to electric, magnetic and atomic forces*, Oxford University Press, Inc., 1994.

[Sar94] S.D. Senturia, *Microsystem design*, Springer Science + Business Media, Inc., 2001.

[Tev04] J.Teva, G.Abadal, Z.J.Davis, J.Verd, X.Borrisé, A.Boisen, F.Pérez-Murano, N.Barniol, "On the electromechanical modelling of a resonating nano-cantilever-based transducer", *Ultramicroscopy*, vol. 100, pp. 225-232, 2004.

[Tev07] J. Teva, "Integration of CMOS-MEMS resonators for radiofrequency applications in the VHF and UHF bands", *PhD thesis,* Universitat Autonoma de Barcelona , Jul. 2007.

[Tho93] William. T. Thomson, "Theory of Vibration with Applications", *Stanley Thornes (Publichers) Ltd*, 4 edition, 1993.

[Ver05] J. Verd, J. Teva, G. Abadal, F. Pérez-Murano, J. Esteve, N. Barniol, "Large-signal model of a resonating cantilever-based transducer for system level electrical simulation", in *Proc. of SPIE's International Symposium on Microtechnologies for the New Millenium 2005*, vol. 5836, pp. 98, 2005.

[Ver06] J. Verd, J. Teva, G. Abadal, F. Torres, F. Pérez-Murano, N. Barniol, "Nonlinear Model for Cantilevers-based MEMS implemented in Verilog-A for System Level Electrical Simulations", in *Proc. of the XXI Conference on Design of Circuits and Integrated Systems (DCIS'06)*, vol. , pp. , 2006.

[Vig99] J.R. Vig and Y. Kim, "Noise in microelectromechanical system resonators", *IEEE Transactions on Ultrasonics, Ferroelectrics, and Frequency Control*, vol. 46 (6), pp. 1558-1565, 1999.

[Vig00] J.R. Vig, F.L. Walls, "A review of sensor sensitivity and stability", in *Proc. of the IEEE/IEA International Frequency Control Symposium and Exhibition*, pp. 30-33, 2000.

[Yas00] K.Y. Yasumura, T.D. Stowe, E.M. Chow, T. Pfafman, T.W. Kenny, B.C. Stipe, and D. Rugar, "Quality Factors in Micron- and Submicron-Thick Cantilevers", *Journal of Microelectromechanical Systems,* vol. 9 (1), pp. 117-125, 2000.

CHAPTER 3

FABRICATION

Fabrication of beam resonators with a width and a gap as small as possible is an important issue for developing MEMS sensors with the most optimal mass sensitivity and capacitive readout performance. In this thesis work, two different technological approaches have been taken into account in order to fabricate CMOS-MEMS resonators for mass sensing applications. These two approaches are related with the NANOMASS and NANOSYS projects where the MEMS resonators are fabricated using post-CMOS processes based on surface micromachining techniques. In this Chapter, a description of the two fabrication approaches and the more representative fabricated resonators are presented.

3.1 NANOMASS APPROACH

In this approach the fabrication of the MEMS is performed as a post-process module on pre-fabricated CMOS chips (Post-CMOS). The CMOS chips have been designed at the UAB being one of the topics of this thesis work. The CMOS fabrication has been performed at the *Institut de Microelectronica de Barcelona* (IMB-CNM-CSIC) using the in-house standard CMOS technology with some slight modifications. Most of the post-CMOS fabrication of the MEMS has been performed at Mikroelektronik Centret of Denmark (MIC) using the laser lithography (DWL) developed at this centre and etching processes. On the other hand, the devices fabricated with electron beam lithography (EBL) have been processed at the Lund University (LUND).

3.1.1 CMOS INTEGRATION

The CMOS technology at CNM is a standard 2.5μm, twin well, 2-poly, 2-metal technology named CNM25. The MEMS is mechanized after the standard CMOS process into a specific area

called “nanoarea” using the first polysilicon layer available in the technology (Poly0). This layer is used in the CNM standard CMOS process as the bottom plate for integrate analog capacitors, and consequently, it is possible to slightly modify it without changing the transistor characteristics. In our case, the Poly0 layer thickness is increased from 350 to 600 nm to improve mechanical and electrical properties of the cantilever (higher cantilever thickness); the deposition temperature was reduced to 580 ºC and doped at 950 ºC with $POCl_3$. The final layer has a sheet resistance of 13.8 Ω/sq and the surface roughness have been reduced from 15 to 7 nm [Fig01]. This layer is oxidized during the growth of the gate oxide and covered by the second polysilicon layer (Poly1) to protect it.

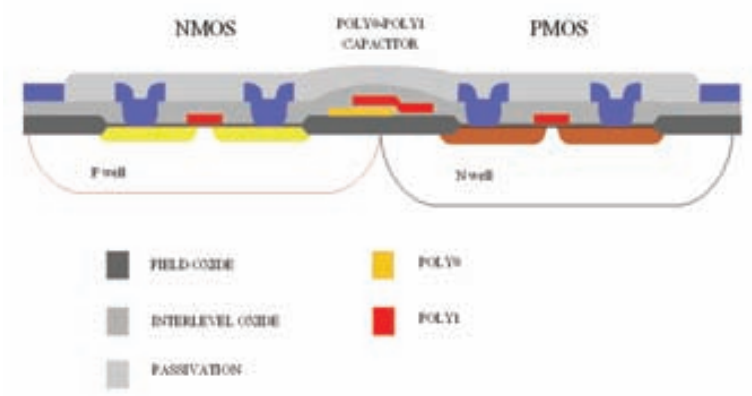

Figure 3.1.1 CMOS standard technology (CNM25) available at IMB-CNM-CSIC.

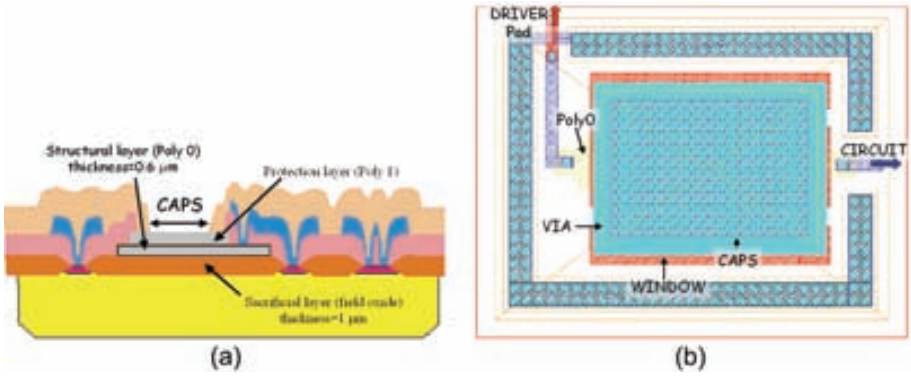

Figure 3.1.2 Cross-sectional view (a) and layout (b) of the area (*nanoarea*) where is fabricated the mechanical structures as a post-CMOS process.

Figure 3.1.2a shows a cross-sectional view of the nanoarea after the standard CMOS process. The layers are designed to remove oxide and metal layers on top of the “nanoarea”. The layers used (illustrated in Fig 3.1.2b) are:

Poly0: It is the structural layer and in consequence defines the area available to mechanize the structure.

Poly1: It is used to protect Poly0 during the rest of CMOS processes (metal depositions, contacts opening, etc.).

CAPS: It is used to remove the inter-level oxide deposited between Poly and Metal1 layers.

VIA: It is used to remove the inter-level oxide deposited between Metal1 and Metal2 layers.

WINDOW: It is used to remove the passivation oxide deposited on the chip.

Last three layers will define the final dimensions of the hole opened to access to the structural layer and allow the post-CMOS fabrication.

Electrical connections between the MEMS and the circuit and/or output pads are performed by defining contacts between Poly1 and Metal layers. The interconnection metal tracks and the rest of the chip are protected after the standard CMOS process due to the passivation layer.

On the other hand, an N-well under the "nanoarea" is also defined to prevent unfortunate short-circuits between an electrode and the chip substrate.

3.1.2 POST-CMOS FABRICATION

For prototyping purposes, the post-CMOS fabrication step is performed on a chip basis. The fabrication of the mechanical structures has been performed using direct laser lithography (DWL) at MIC[1].

The first step of the post-CMOS process is dry etching through the top Poly1 layer (Fig. 3.1.3a) to open the access to the structural layer (Poly0). This step is still performed at CNM. Then, the mechanical structures mask definition step is performed (Fig. 3.1.3b). A thin aluminum layer is deposited on the entire chip and it is selectively annealed using laser lithography, which presents a line-width resolution of around 700 nm. Next, the non-annealed Al is chemically etched leaving the annealed-Al mask [Dav00]. After the mask definition, the pattern is transferred to the Poly0 layer by dry etching (Fig. 3.1.3c) where the thick CMOS passivation layer is enough to protect the CMOS circuitry. Finally, the structures are released in BHF, which etches the underlying 1-μm-thick SiO2 layer (Fig. 3.1.3d). In this case the CMOS is protected by the deposition of a 3 μm thick resist layer and hole is opened over the MEMS area. To enable this post-CMOS process an additional contact mask (dark field) has been designed with some marks to allow a good alignment with the CMOS chip.

This fabrication technique was demonstrated in the NANOMASS project to be compatible with CNM25 CMOS technology [Dav03]. In this sense no significant difference on the electrical characteristics of CMOS circuitry were observed before and after the DWL processing.

In order to reduce the width of the cantilever, a similar process was developed employing e-beam lithography (EBL) instead of DWL. Since EBL at high energies was demonstrated to damage CMOS, a novel technique that combines DWL and low-energy EBL was developed at MIC and LUND. With this technique the cantilever width can be reduced below 500 nm and it is compatible with CNM25 CMOS technology [Gha05].

[1] This technique, developed at MIC, is reported in the thesis works of Z.J. Davis and E. Forsen [Dav03, For05].

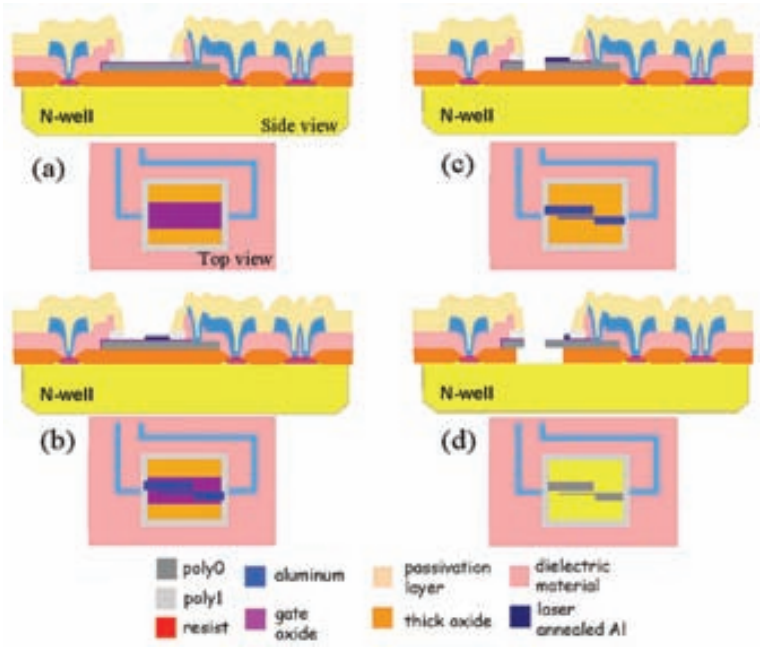

Figure 3.1.3 Diagram of the simplified post-CMOS process to fabricate resonant cantilevers using direct laser lithography compatible with CMOS.

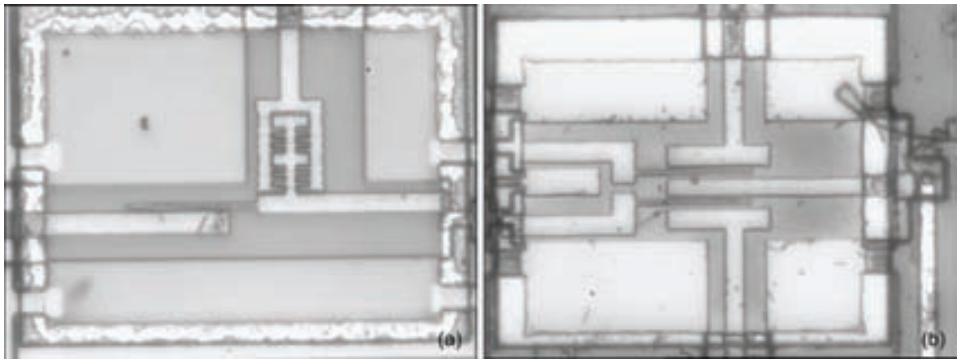

Figure 3.1.4 Optical images of cantilever resonators fabricated by DWL as a post-process on CNM25 CMOS chips. (a) Cantilever with 1 driver and comb-capacitor for circuit biasing. (b) 2-cantilever array where the top cantilever is resonating. Cantilever dimensions are: l = 40 μm, w = 840 nm, t = 600 nm and s = 1.3 μm.

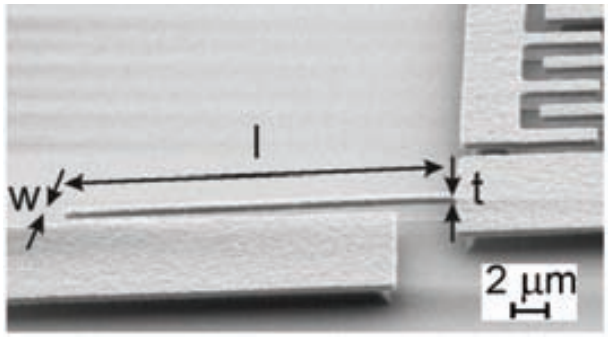

Figure 3.1.5 SEM image of a cantilever resonator fabricated by EBL+DWL as a post-process on CNM25 CMOS chips. Cantilever dimensions are: l = 20 µm, w = 425 nm, t = 600 nm and s = 1.3 µm.

3.1.3 RESULTS

Figure 3.1.4 shows polysilicon cantilevers fabricated using laser lithography on CNM25 chips. These cantilevers have a width of around 840 nm, a length of 40 µm and a gap to the electrodes of 1.3 µm. With these dimensions and the typical values of the Young's modulus and mass density for polysilicon (160 GPa and 2330 kg/m^3), the theoretical resonance frequency and the mass sensitivity of these resonators is 703 kHz and 32.5 ag/Hz (397 pg/Hz·cm^2) respectively.

On the other hand, Fig. 3.1.5 shows a polysilicon cantilever fabricated using electron beam lithography combined with laser lithography [Gha05]. In this case, the cantilever is 420 nm wide, 20 µm long and with a gap of 1.3 µm. The theoretical resonance frequency and mass sensitivity is 1.42 MHz and 4.1 ag/Hz (196 pg/Hz·cm^2) according to Equations 2.1.14 and 2.1.26.

3.2 NANOSYS APPROACH

The integration of CMOS circuitry with the electromechanical transducer in the NANOSYS approach is performed using a commercial CMOS technology from *austriamicrosystems* foundry [AMS]. This technology is accessed via Europractice [EurIC] using the Multi-Project Wafer (MPW) service that reduces the cost of ASIC prototyping by sharing the costs among a number of customers.

In opposite to the NANOMASS approach, the mechanical resonators are completely mechanized after the standard CMOS process (intra-CMOS) without any additional micro/nano-machined techniques. A standard CMOS layer is used as the structural layer and different silicon oxide underlying layers are used as the sacrificial layer. The resonators are released with a single mask-less wet etching post-CMOS process. The fabrication area for the resonators is designed specifically allowing a very fast etching of the sacrificial layers, which does not cause any damage to the CMOS and does not need any additional protection mask. This simple wet etching process has been carried out at the facilities of the *Institut de Microelectronica de Barcelona* (IMB) of the *Centro Nacional de Microelectrónica* (CNM-CSIC).

A similar strategy of CMOS-MEMS fabrication has been developed at the Carnegie Mellon University (USA) by the group of G. K. Fedder [Fed96, Luo02]. In this case, the resonator is constituted by a stack of the CMOS metal and oxide layers (three or four metal levels depending on the technology used). The top metal layer is used as the etch-resistant mask during the post-CMOS process that consists on one or two RIE etching steps (depending on the application) to define the mechanical structures and an additional isotropic silicon dry etching to release the free-standing structures. Recently, Fedder's group has been reported CMOS-MEMS fabricated using this technique for RF applications (i.e. Mixlers) [Che05].

3.2.1 CMOS INTEGRATION AND POST-CMOS FABRICATION

The commercial CMOS technology used is the C35 process family from *autriamicrosystems* (AMS-C35). This is a 3.3V 0.35μm CMOS technology with three of four metal levels (MET1-4) and a polysilicon capacitor module (POLY1-POLY2) to integrate capacitors. Figure 3.2.1 shows a cross-section schematic of this technology.

In this thesis work, metal and polysilicon resonators for mass sensing applications have been designed and fabricated. In next sections, the two techniques used to fabricate the resonators are described.

From the point of view of the CMOS layout designer is important to take into account two main design considerations:

- For this technology only N-Well regions can be defined in the layout edition. In this sense, all the N-MOS transistors share the same bulk polarization and only the P-MOS transistors can be fabricated in different and isolated N-Well regions.
- The MEMS layout design fails to fulfill some design rules of the technology that are found and assumed during the design rule checking stage.

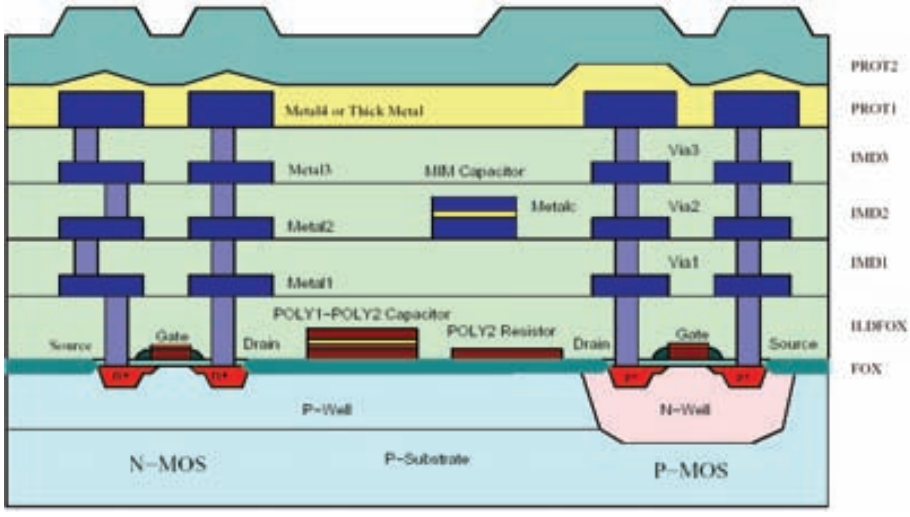

Figure 3.2.1 Commercial CMOS technology (AMS-C35) from *austriamicrosystems* foundry.

- **METAL RESONATORS**

In this approach the mechanical structures are fabricated using the top metal level provided by the AMS-C35 CMOS technology as the structural layer. The resonator along with the electrodes are defined using the top metal layer MET4 layer that is the thicker metal layer (t ~ 850 nm) of the technology, whereas the sacrificial layer is the underlying stack of silicon dioxide layers with a total thickness of ~ 4 μm corresponding to the different inter-metal oxides (i.e., IMD3, IMD2, and IMD1), metal1-poly oxide (ILDFOX), and field oxide (FOX). As it is depicted in Fig. 3.2.2a, the resonator along with the electrodes is completely defined in the conventional CMOS layout edition.

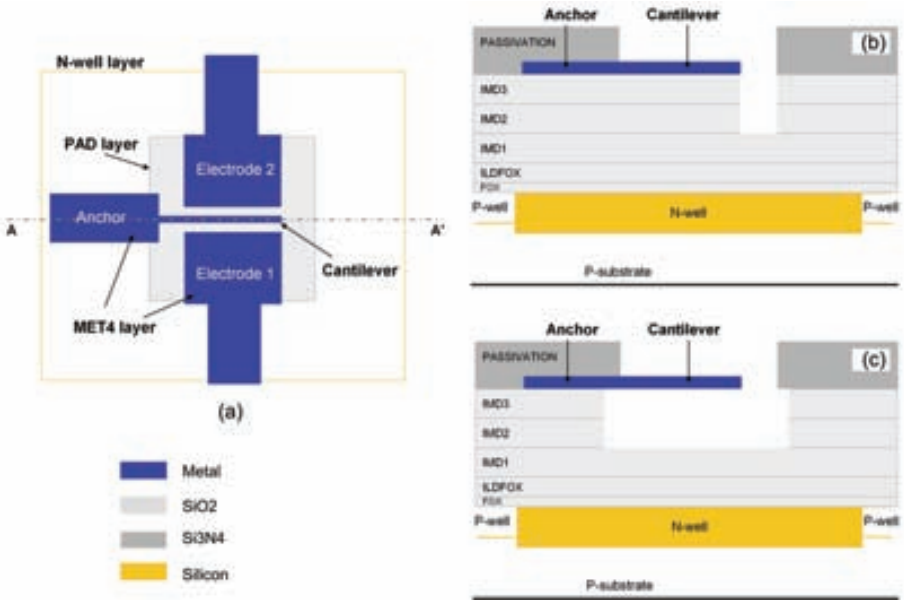

Figure 3.2.2 Schematic top-view showing the CMOS technology layers used to fabricate metal resonators in AMS-C35 technology (a), schematic cross-section view after standard CMOS process (b), and after the post-CMOS process (sacrificial layer etching). The profiles are made following the dotted line A-A' in (a).

To allow a direct post-processing of the MEMS, a pad cut (PAD layer) is defined over the resonator area. In this way, the resonator structure is kept free of the addition of any other layer over it. The PAD cut measures 15 × 15 μm^2 that is the minimum allowed by the technology. The rest of the chip area (except electrical contact pads) is covered by the passivation layer, which is a silicon nitride film (Si_3N_4) deposited by plasma-enhanced chemical vapor deposition (PECVD), which protects the circuitry during the post-CMOS process.

Fig. 3.2.2b shows a cross-section view, along the resonator, of the device after the standard CMOS process. On the other hand, in Fig. 3.2.3 SEM images of devices not post-processed are presented. We can observe that the structures are completely mechanized during the standard CMOS process and the sacrificial layer is only present underneath the resonator enabling a simple

etching of the silicon dioxide. With this approach, the minimum width of the resonator as well as the gap spacing to the electrodes is limited by the design rules of the technology. In this case, the AMS-C35 technology MET4 design rules limit the resonator width and the gap both to 600 nm.

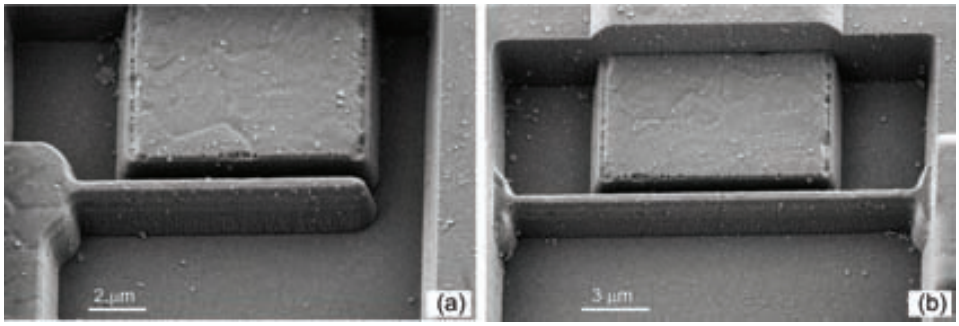

Figure 3.2.3 SEM images of metal resonators after the standard CMOS process. (a) Cantilever with 1 driver. (b) C-C beam with 1-driver.

After the standard CMOS process, a post-CMOS process based on a mask-less wet etching of the silicon dioxide is performed to release the resonator [Ver06, Ver06b]. In this sense, any additional photolithography step is needed after the standard CMOS process to fabricate the MEMS devices. The wet etching is performed using a solution based on hydrofluoric acid (HF) with pH control to be selective with the aluminum structures. The etch rate of a fresh solution is around 200 nm/min decreasing this rate with the time. In this sense, an etching process of 2 minutes is enough to release the 600-nm width metal MEMS.

- **POLYSILICON RESONATORS**

In this approach the mechanical structures are fabricated by using the polysilicon capacitor module available in the AMS-C35 technology. This module is constituted by two polysilicon layers: Poly1 is the bottom layer and it is 282 nm thick, and Poly2 is the top layer and it is 200 nm thick. This two polysilicon layers are separated by a 41 nm thick silicon oxide layer.

A first option adopted, depicted in Fig. 3.2.4, consists in the use of the Poly1 layer as the structural layer to fabricate both the resonator and the electrodes. In this case, the sacrificial layer is the underlying field oxide layer (FOX) that is 290 nm thick.

In this approach to allow the direct post-processing without any additional mask, a hole through the silicon dioxide is also opened over the resonator area in order to fasten the releasing process. This hole is defined in the AMS-C35 technology by using a stack of three layers: PAD layer, VIA3 layer and VIA2 layer. In this way, in opposite to the metal approach, the resonator structure remain still protected by the IMD1 and ILDFOX layers (neither CONTACT nor VIA1 are defined) to avoid any damage during the rest of the CMOS process (metal depositions and etchings). The rest of the chip area is covered by the passivation layer in the same way that in the metal approach.

Fig. 3.2.4b shows a cross-section view of the device after the standard CMOS process for this approach. In this case, the minimum width of the resonator and the gap to the electrodes is limited to 350 nm and 450 nm respectively.

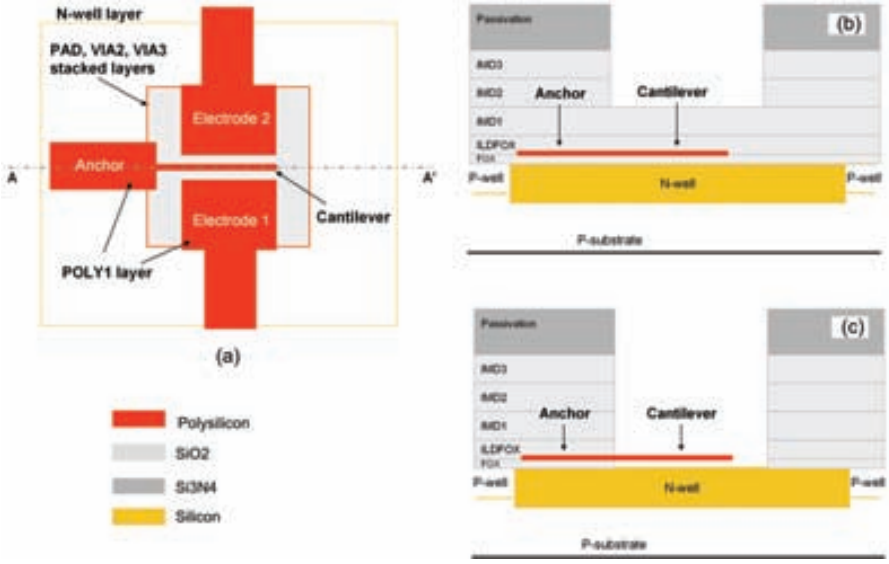

Figure 3.2.4 Schematic top-view showing the CMOS technology layers used to fabricate polysilicon resonators in AMS-C35 technology (a), schematic cross-section view after standard CMOS process (b), and after the post-CMOS process (sacrificial layer etching). The profiles are made following the dotted line A-A' in (a).

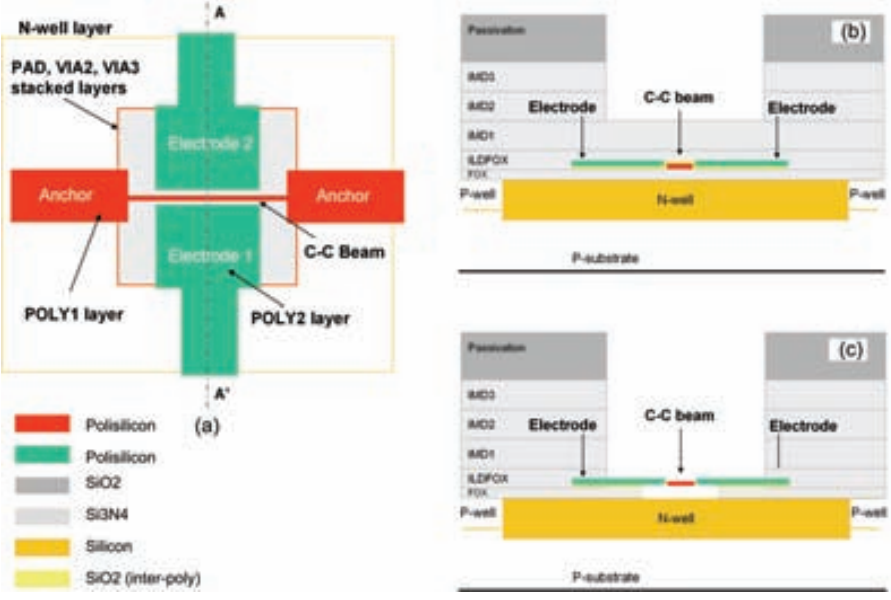

Figure 3.2.5 Schematic top-view showing the CMOS technology layers used to fabricate polysilicon resonators with small lateral gaps in AMS-C35 technology (a), schematic cross-section view after standard CMOS process (b), and after the post-CMOS process (sacrificial layer etching). The profiles are made following the dotted line A-A' in (a).

In order to release the resonator, the same post-CMOS process that in the metal approach is performed. In this case, since several oxide layers above the resonator have also to be removed, the post-process time is increased above 10 minutes.

A second option, depicted in Fig. 3.2.5, has been also considered in order to reduce the gap between the resonator and the electrodes. In this approach, the resonator is fabricated using the Poly1 layer and the electrodes are defined with the Poly2 layer. Since these two polysilicon layers are conformal layers, the minimum gap dimension is limited only by the thickness of the inter-poly oxide (~ 40 nm) that is used as spacer (Fig. 3.2.5b).

In this thesis, a gap dimension of 150 nm has been defined to fabricate a C-C beam polysilicon resonator for mass sensing applications. In any case, using the Poly1/Poly2 fabrication technique, resonators with lateral gaps of around 40 nm have been fabricated in the group for RF applications in the VHF band [Tev07, Tev07b].

3.2.2 RESULTS

In this section, examples of fabricated metal and polysilicon resonators are presented. All the resonators have been defined with the minimum width allowed by the AMS-C35 technology in order to maximize their mass sensitivity.

Figure 3.2.6 shows two metal resonators with two-driver configuration. The cantilever has been defined to be 10 μm long and 600 nm wide, while the C-C beam has been defined to be 18 μm long and 600 nm wide. The gap to the electrodes is 600 nm in all cases since it is the minimum that allows the top-metal design rules. On the other hand, in order to reduce the parasitic coupling between the excitation and the readout electrodes, their length is reduced some microns near the anchors. The cantilever electrodes are 8 μm and 10 μm long for the C-C beam.

The metal layer provided by the AMS-C35 technology is not constituted by a single metal layer but it is implemented with a double layer of Al and TiN with theoretical thickness of 750nm and 100 nm respectively. In this sense, the Young's modulus and the mass density of the metal structures have to be calculated taking into account these two materials. As a first approximation, these two physical parameters can be estimated as a weighted average [Sad95]. With typical values of the Young's modulus and mass density for Al (68 GPa and 2700 kg/m^3) and for TiN (600 GPa and 5220 kg/m^3), a weighted average values of 131 GPa and 3000 kg/m^3 are obtained for the Young's modulus and the mass density respectively.

With these material parameters, these metal resonators present a theoretical resonance frequency of 6.4 MHz and 12.6 MHz for the cantilever and the C-C beam respectively. On the other hand, the mass sensitivity is ~ 1.2 ag/Hz (80 pg/Hz·cm^2) and ~ 1.7 ag/Hz (41 pg/Hz·cm^2) for the cantilever and the C-C beam respectively according to Equations 2.1.14 and 2.1.26.

Figure 3.2.7 shows two polysilicon resonators with two-driver configuration fabricated with the polysilicon capacitor module of the AMS-C35 technology. The cantilever has been defined to be 6.5 μm long and 350 nm wide, while the C-C beam has been defined to be 13 μm long and 350 nm wide. In the case of the cantilever, the electrodes have been also fabricated with the Poly1 layer with a gap of 450 nm and a length of 4.5 μm. As in the metal resonators, the length of the electrodes is reduced some microns near the resonator anchors to reduce parasitic coupling. The electrodes of the C-C beam resonator have been implemented with the Poly2 layer defining a gap of 150 nm and a length of 9 μm.

Assuming the typical values of the Young's modulus and mass density for polysilicon (160 GPa and 2330 kg/m^3), the theoretical resonance frequency of these polysilicon resonators is 11.1 MHz and 17.6 MHz for the cantilever and the C-C beam respectively. On the other hand, the theoretical mass sensitivity is 65.5 zg/Hz (11.8 pg/Hz·cm^2) and 130 zg/Hz (7.44 pg/Hz·cm^2) respectively.

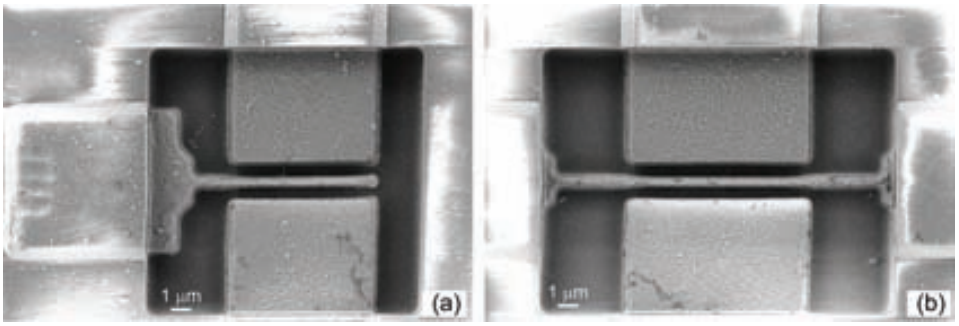

Figure 3.2.6 SEM images of two metal resonators with two-driver configuration fabricated using the top metal layer of the AMS-C35 technology. (a) Cantilever dimensions are l = 10 μm, w = 600 nm and s = 600 nm approximately. (b) C-C beam dimensions are l = 18 μm, w = 600 nm and s = 600 nm approximately.

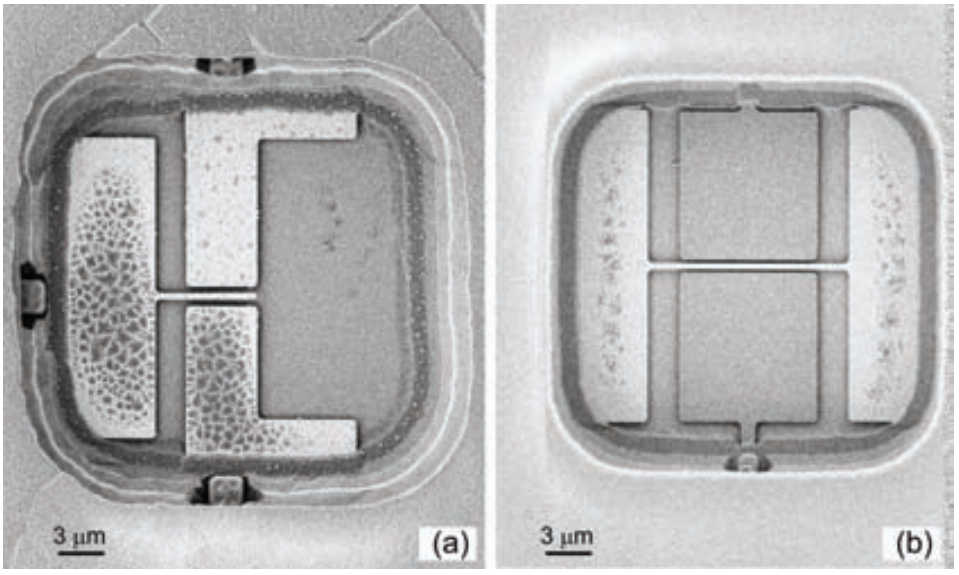

Figure 3.2.7 SEM images of two polysilicon resonators with two-driver configuration fabricated using the polysilicon capacitor module of the AMS-C35 technology. (a) The cantilever dimensions are l = 6.5 μm, w = 350 nm and s = 450 nm approximately. (b) The C-C beam dimensions are l= 13 μm, w = 350 nm and s = 150 nm approximately.

3.3 DISCUSSION AND SUMMARY

In this chapter, it has been described the different techniques used during this thesis work to fabricate monolithic CMOS-MEMS resonators for ultra-sensitive mass detection. Two main post-CMOS strategies have been carried out: a) Nanomass approach and b) Nanosys approach.

In the Nanomass approach the MEMS are mechanized on pre-processed CMOS chips, designed with a specific "nanoarea" for the post-CMOS fabrication, using different nanofabrication techniques developed at MIC and LUND [For05, Gha05]. This fabrication approach allows the monolithic integration of CMOS with nanoresonators but it is relatively complex since the need of additional post-CMOS lithography steps including reactive ion etching and wet etching that limits the throughput and the reproducibility of the devices. In addition, the time spent to pattern the MEMS structures is high (~1 hour) since the nanolithography techniques used are serial processes. Despite this limitation, polysilicon resonators with a width down to 500 nm have been successfully fabricated.

In the Nanosys approach the MEMS are completely mechanized during the standard CMOS process and only a mask-less wet etching post-CMOS process is needed to release the resonant structures. In this sense, the complexity and cost of the fabrication process is reduced drastically compared with the Nanomass approach increasing also the throughput. With this fabrication approach, submicrometer-scale metal and polysilicon beam resonators (cantilevers and CC-beams) have been fabricated with success.

Table 3.1 Summary of the theoretical parameters of the resonators fabricated for mass sensing applications.

Device	CMOS Tech. / Lithography	Dimensions $l \times w \times t$, s (in μm)	E / ρ	f_o	Mass Sensitivity	V_{SL}* V_{SV} (in V)
Nanomass Poly-Cantilever	CNM25 DWL	40×0.84×0.6, 1.3	160 GPa / 2330 kg/m^3	703 kHz	32.5 ag/Hz 397 pg/Hz·cm^2	90 37
Nanomass Poly-Cantilever	CNM25 DWL + EBL	20×0.42×0.6, 1.3	160 GPa / 2330 kg/m^3	1.42 MHz	4.1 ag/Hz 196 pg/Hz·cm^2	127 147
Nanosys Metal-Cantilever	AMS-C35 UVL	10×0.6×0.85, 0.6	131 GPa / 3000 kg/m^3	6.40 MHz	1.16 ag/Hz 79.5 pg/Hz·cm^2	246 7140
Nanosys Metal-Bridge	AMS-C35 UVL	18×0.6.0.85, 0.6	131 GPa / 3000 kg/m^3	12.6 MHz	1.70 ag/Hz 40.5 pg/Hz·cm^2	176 5120
Nanosys Poly-Cantilever	AMS-C35 UVL	6.5×0.35×0.28, 0.45	160 GPa / 2330 kg/m^3	11.1 MHz	65.5 zg/Hz 11.8 pg/Hz·cm^2	187 70
Nanosys Poly-Bridge	AMS-C35 UVL	13×0.35×0.28, 0.15	160 GPa / 2330 kg/m^3	17.6 MHz	130 zg/Hz 7.44 pg/Hz·cm^2	25 40.5

* Assuming the electrode length indicated in the text (sections 3.1 and 3.2).

Table 3.1 summarizes the theoretical main physical parameters of the resonators fabricated in this thesis for mass sensing applications. Although the width of the AMS-C35 metal resonators is similar than the obtained for the CNM25 polysilicon resonators, the first ones are superior in terms of mass sensitivity since they operate at a higher resonance frequency achieving expected mass

sensitivities of around 1 ag/Hz. In addition, the fabricated AMS-C35 polysilicon resonators are only 350 nm wide and their theoretical mass sensitivity is in the zeptogram range.

A way to reduce the motional resistance of the resonator is using high bias voltages (V_{DC}). The maximum bias voltage is ultimate limited by the snap-in voltage that produces the collapse towards the driver electrode (lateral snap-in voltage, V_{SL}). When applying the bias voltage to the free-standing structure (e.g. when using 2-drivers configuration), the substrate is also acting as an electrode and the maximum bias voltage that can be applied to avoid the collapse towards the substrate has to be considered (vertical snap-in voltage, V_{SV}). In this sense, the theoretical lateral and vertical snap-in voltages are also indicated in Table 3.1 which values have been obtained using Equation 2.1.39.

REFERENCES

[AMS] Austriamicrosystems AG, Austria, [Online]. Available: http://www.austriamicrosystems.com.

[Che05] Fang Chen; Brotz, J.; Arslan, U.; Chiung-Cheng Lo; Mukherjee, T.; Fedder, G.K., "CMOS-MEMS resonant RF mixer-filters," *Micro Electro Mechanical Systems, 2005, 18th IEEE International Conference on* , pp. 24-27, 30 Jan.-3 Feb. 2005

[Dav00] Z.J. Davis, G. Abadal, O. Kuhn, O. Hansen, F. Grey, and A. Boisen., "Fabrication and characterization of nanoresonating devices for mass detection" *J. Vac. Sci. Technol. B*, vol. 18, pp. 612-616, 2000.

[Dav03] Z.J. Davis, "Nano-resonators for high resolution mass detection", *PhD thesis,* Technical University of Denmark (MIC-DTU), Mar. 2003.

[EurIC] [Online]. Available: http://www.europractice-ic.com/prototyping.php

[For05] E. Forsen, "Nano-cantilevers fully integrated with CMOS for ultrasensitive mass detection", *PhD thesis,* Technical University of Denmark (MIC-DTU), Sep. 2005.

[Fed96] G.K. Fedder, S. Santhanam, M.L. Reed, S.C. Eagle, D.F. Guillou, M.S.-C. Lu, L.R. Carley, "Laminated high-aspect-ratio microstructures in a conventional CMOS process", *Sensors and Actuators A*, vol. 57, pp. 103-110, 1996.

[Fig01] E. Figueras, F. Campabadal, F. Pérez-Murano, J. Esteve, Z.J. Davis, G. Abadal, B. Helbo, O. Hansen, N. Barniol and A. Boisen, "Polysilicon layer for CMOS-compatible nanoresonators", in *Proc. of Microscopy,* pp. 551-552, Sep. 2001.

[Gha05] S.G.-Nilsson, E. Forsen, G. Abadal, J. Verd, F. Campabadal, F. Perez-Murano, J. Esteve, N. Barniol, A. Boisen and L. Montelius, "Resonators with integrated CMOS circuitry for mass sensing applications, fabricated by electron beam lithography", *Nanotechnology*, vol. 16, pp. 98-102, 2005.

[Luo02] H. Luo, G. Zhang, L.R. Carley, and G.K. Fedder, "A Post-CMOS Micromachined Lateral Accelerometer", Journal of Microelectromechanical Systems, vol. 11(3), pp. 188-195, 2002.

[Sad95] J.E. Sader, I. Larson, P. Mulvaney, and L.R. White. "Method for the calibration of atomic force microscope cantilevers", *Review of Scientific Instruments*, vol. 66 (7), pp. 3789–98, 1995.

[Tev07] J. Teva, G. Abadal, A. Uranga, J. Verd, F. Torres, J.L. Lopez, J. Esteve, F. Perez-Murano, N. Barniol, "VHF CMOS-MEMS resonator monolithically integrated in a standard 0.35um CMOS technology", in *Tec. Digest of the 20th International Conference on MicroElectroMechanical Systems (MEMS 2007),* pp. 789-792, Jan. 2007.

[Tev07b] J. Teva, "Integration of CMOS-MEMS resonators for radiofrequency applications in the VHF and UHF bands", *PhD thesis,* Universitat Autonoma de Barcelona , Jul. 2007.

[Ura07] A. Uranga, J. Verd, J.L. López, J. Teva, G. Abadal, F. Torres, J. Esteve, F. Pérez-Murano and N. Barniol, "Fully integrated MIXLER based on a VHF CMOS-MEMS clamped-clamped beam resonator", *Electronics Letters*, vol. 43 (8), pp. 452-454, 2007.

[Ver06] J. Verd, G. Abadal, J. Teva, A. Uranga, F. Pérez-Murano, J. Esteve, N. Barniol, "Resonant Metal Cantilever with Attogram/Hz Mass Sensitivity Fully Integrated in a Standard 0.35-um CMOS Process", *in Proc. of 19th International Conference on MicroElectroMechanical Systems (MEMS 2006)*, pp. 638-641, Jan. 2006.

[Ver06b] J. Verd, J. Teva, J. Teva, J. L. Lopez, F. Torres, J. Esteve, G. Abadal, F. Perez-Murano, N. Barniol, "Integrated CMOS-MEMS with On-Chip Readout Electronics for High-Frequency Applications", *IEEE Electron Device Letters*, vol. 27 (6), pp. 495-497, 2006.

CHAPTER 4

CMOS DESIGN

The tendency to decrease the size of the mechanical transducer into the new generation of micro-/nanoelectromechanical systems (M/NEMS) makes the readout method used for converting M/NEMS displacement into electrical signal to be a crucial topic. In this chapter different aspects related with the CMOS circuits designed in this thesis work to perform the capacitive readout of the beam resonators, presented in Chapter 3, are reported. Finally, a comparative study of the capacitive readout system resolution with the state-of-the-art of other readout systems is given.

4.1 ON-CHIP CAPACITIVE SENSING

In this work the motion of the resonator, in particular its frequency response is detected or sensed by means of the generated capacitive current (I_C) that is converted to a voltage. At resonance, the MEMS resonator with electrostatic excitation and capacitive readout can be modeled by the electrical scheme presented in Fig. 4.1.1 where the capacitive current can be expressed as the sum of the motional current (I_m) and the parasitic current (I_p).

From the point of view of the readout system design, two main intrinsic electrical characteristics of the MEMS resonator have to be taken into account: (i) the resonance frequency and (ii) the value of the motional resistance (R_m). From Eq. 2.1.47 and 2.2.1, the motional current at resonance can be expressed as a function of the motional resistance (Eq. 4.1.1). In these sense can be observed that as lower is the motional resistance as higher is the motional current generated at resonance ($I_{M,r}$) for the same excitation voltage (V_{AC}).

$$I_{M,r} = Q\frac{\eta^2 V_{AC}\omega}{k} = \frac{V_{AC}}{R_m}. \tag{4.1.1}$$

The beam resonators have been designed to present sensitivities in the attogram range. Due to the tradeoff between the mass sensitivity and the readout capability, these resonators present both a

relative high resonance frequency and high motional resistance making the readout system to be a crucial topic. From Table 4.1, it is appreciated that the typical motional resistances are higher than the MΩ resulting on motional currents in the order of tens of nA. On the other hand, the resonant frequency of the resonators is in the MHz range.

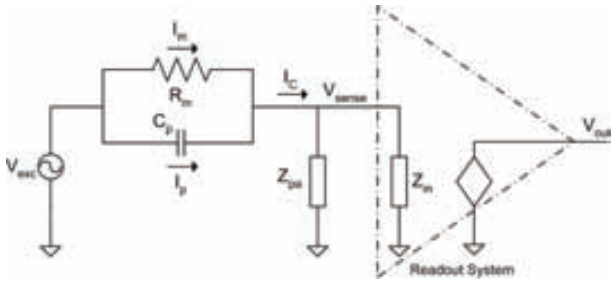

Figure 4.1.1 Conceptual schematic that models the MEMS performance at resonance together with the capacitive readout system.

Table 4.1 Summary of different mechanical and electrical parameters of the resonators designed in this thesis. A quality factor of 100 has been assumed to calculate the motional resistance.

Resonator	**Dimensions** $l \times w \times t$ **, s** (in μm)	E **/** ρ	k (N/m)	f_o (MHz)	V_{DC}	R_m (MΩ)	V_{SL} V_{SV} (in V)
Nanomass Poly-Cantilever	40×1×0.6, 1	160 GPa / 2330 kg/m^3	0.38	0.84	20	67.2	140 37
Nanosys Metal-Cantilever	10×0.6×0.85, 0.6	131 GPa / 3000 kg/m^3	6.0	6.4	60	14.2	246 7140
Nanosys Metal-Bridge	18×0.6.0.85, 0.6	131 GPa / 3000 kg/m^3	65.8	12.6	80	29.6	176 5120
Nanosys Poly-Cantilever	6.5×0.35×0.28, 0.45	160 GPa / 2330 kg/m^3	1.8	11.1	40	49.9	187 70
Nanosys Poly-Bridge	13×0.35×0.28, 0.15	160 GPa / 2330 kg/m^3	14.1	17.6	10	12.6	25 40.5

In order to sense the capacitive current, a good matching between the MEMS impedance and the impedance at the sense node (V_{sense}) is necessary in order to achieve low insertion losses in the frequency response of the mixed electromechanical system. In CMOS, the impedance at the sense node is basically capacitive (C_{pa}).

In the case of discrete resonators (not integrated), the impedance at the sense node is dominated by the output pads, wire bonding, coaxial cable and the input impedance of the measurement circuit/instrument. In this case, the capacitance may be in the order of tens of pF, resulting in an effective impedance of a few kΩ at the resonance frequency (MHz), which is much lower than the MEMS impedance.

On the other hand, a monolithic integration of the MEMS with the readout or front-end circuit allows the reduction of the parasitics capacitances at the sense node to tens of fF. In this case, C_{pa}

is dominated by the input capacitance of the circuit, the on-chip electrical interconnections and the structural layer to substrate capacitance. With monolithic integration the impedance matching can be improved several orders of magnitude resulting in a much better signal-to-noise ratio at the sense node.

Finally, the motional resistance can be reduced by increasing the bias voltage (V_{DC}) as explained in Chapter 2. In any case, the maximum value of this voltage is limited by the snap-in voltage or in last term by the breakdown voltage of the CMOS oxide layers. In Table 4.1 the theoretical lateral and vertical snap-in voltages are indicated. These values are really higher than the bias voltages used to calculate the motional resistance as well as in the experimental measurements as it is detailed in Chapter 5.

4.1.1 CMOS TOPOLOGIES

The use of readout circuits based on sampling techniques are widely common in capacitive sensors (like accelerometers [Bos96, Lu95]) since they are more insensitive to the parasitic capacitances [Yaz00], besides synchronous modulation/demodulation techniques improve the signal-to-noise ratio by means of flicker noise suppression [Ame01]. In our case an analog current-sensing method is necessary since the high resonance frequency to detect enabling the possibility to build a stand alone oscillator (see Chapter 6). In CMOS technology, there are only a few ways of detecting current using non-sampled techniques. Three of these methods are: common base detection, resistive detection and capacitive detection (Fig. 4.1.2.).

An important parameter of the readout circuit is the current noise introduced at the sense node (input refereed noise). In this sense, the capacitive method is intrinsically the best method for low-noise applications [Roe98].

In the common base detection the sense electrode is directly connected to the source or drain of a CMOS transistor. In this case the input current noise is proportional to the transconductance of the transistor (g_m). Without including the effects of the bias and load current sources, the input refereed noise (i_n) is

$$i_n = \sqrt{4K_B TBW\left(\frac{2}{3}g_m\right)}, \tag{4.1.1}$$

where K_B and T are the Boltzmann constant and the temperature respectively and BW is the readout bandwidth.

In the resistive method, a resistor in series with the resonator is used to create a voltage proportional to the capacitive current. This voltage can be measured with a CMOS gate without directly adding to the current noise on the sense node. In this case, the input current noise (ignoring the equivalent input noise of the amplifier) is:

$$i_n = \sqrt{\frac{4K_B TBW}{R_f}}. \tag{4.1.2}$$

Finally, the capacitive method uses a series capacitor to integrate the capacitive current and measure the resulting voltage. In this case the resistor is used for biasing purposes, but is large enough that the impedance at the sense node is dominated by the capacitor. The input current noise associated with this method (ignoring the equivalent input noise of the amplifier) is:

$$i_n = \sqrt{\frac{4K_B TBW}{R_{bias}}} \,. \tag{4.1.3}$$

From last equations can be appreciated that the capacitive method is intrinsically the lowest noise method. In addition, since it deliberately operates past the $R_{bias}C_I$ constant (acting as an integrator), the impedance at the input node is primarily reactive implying that the input not loads the Q of the resonator.

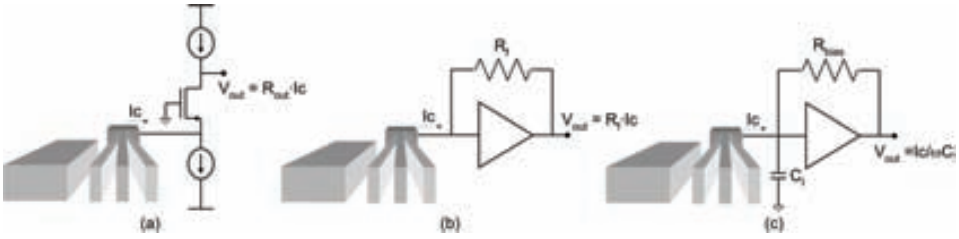

Figure 4.1.2 CMOS front-end preamplifiers used for sensing capacitive current in CMOS. (a) Common base detection, (b) resistive detection and (c) capacitive detection.

4.2 CNM25 CIRCUITS

In the context of the NANOMASS project, two main topologies of front-end preamplifiers have been proposed and fabricated with the CNM25 technology. These topologies are based on resistive detection and capacitive detection. In particular a buffer amplifier with low input capacitance and a transimpedance amplifier have been designed.

Both preamplifiers use an operational amplifier as the basic block in the case of the transimpedance amplifier or as a voltage follower for buffering purposes in the case of the buffer amplifier. A specific operational amplifier has been designed in the CNM25 technology. It is based on the OTA Miller topology, achieving a gain bandwidth product (GBW) as high as 5.6 MHz that is really high taking into account the limits of the technology used (2.5 μm CMOS technology).

4.2.1 RESISTIVE METHOD

The circuit designed with the resistive method is a transimpedance amplifier based on an OTA with resistive feedback, commonly called feedback ammeter. The main advantage of this kind of circuits is the fact that the effect of the parasitic capacitance (C_{pa}) is negligible by virtually grounding it through the operational amplifier.

Since the large motional resistance of the cantilever resonator, a large feedback resistance is necessary to amplify the low current at the resonance frequency. There are two problems to integrate this large resistance: i) the area and ii) the fact that large values of C_{pa} along with a high value of feedback resistance causes instabilities on the circuit. In addition any external resistance must be avoided, in order not to increase the overall stray capacitance.

Fig. 4.2.1 shows the electrical scheme of the TIA designed. It is based on a T-configuration feedback (R_3 and R_4) in order to increase the transimpedance gain minimizing the value of the feedback resistances. A shunt capacitance, C_f, is also used to compensate the effect of the parasitic capacitance C_{pa}, on the circuit stability.

The transfer function between the output voltage, V_{out}, and the capacitive current, I_C, at the transimpedance amplifier input, in Laplace domain, is:

$$\frac{V_{out}(s)}{I_C(s)} = \left(R_1 + \frac{R_2}{1+R_2C_F s}\right)\left(1+\frac{R_3}{R_4}\right). \tag{4.2.1}$$

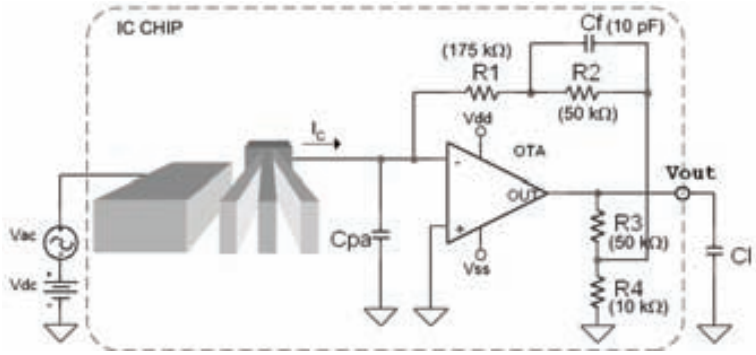

Figure 4.2.1 Circuit schematic of the transimpedance amplifier (TIA).

With this configuration and the parameters indicated in Table 4.1, an acceptable gain of 1.35 MΩ is obtained being the higher integrated resistance of 175 kΩ.

The parasitic capacitance at the sense node, C_{pa}, limits the bandwidth of the readout circuit. Figure 4.2.2 shows the frequency response of the transimpedance gain for different values of C_{pa}, assuming a capacitive load (C_l) of 30 pF. We can observe that the bandwidth is insensitive to variations of the parasitic capacitance for values of C_{pa} up to 100 fF being about 1.2 MHz. When C_{pa} increases too much, (i.e. 1 pF), a notable decrease of the bandwidth is observed as well as an increase of the overshoot with the consequent degradation of the circuit stability. In this sense, output connections at the sense node (i.e. output PAD) have to be avoided.

Table 4.2 summarize the main parameters of the TIA that presents a gain of 123 dBΩ in a bandwidth of 1.2 MHz with a input refereed noise of 280 fA/√Hz.

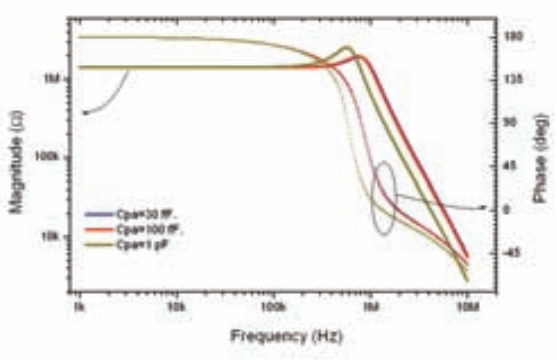

Figure 4.2.2 Simulated frequency response of the transimpedance gain of the TIA (CNM25).

Table 4.2 Specifications of the TIA (CNM25).

Parameter	Value	Condition
Supply voltage	± 2.5 V	
Transimpedance	1.35 MΩ (122.6 dBΩ)	@ DC
Bandwidth	1.2 MHz	Cl = 30 pF
Input current noise	2.8×10^{-13} A/√Hz	
Load capacitance	30 pF	at V_{out}
Output voltage swing	3.6 V	peak-to-peak

4.2.2 CAPACITIVE METHOD

The readout circuit has been designed in order to minimize the parasitic capacitance at the sense node in order to maximize the sensitivity. It is constituted (Fig. 4.2.3) by a CMOS voltage amplifier (BA) biased as source-follower (common drain configuration). The voltage at the gate or sense node (V_g) controls the current of M1, this current is mirrored and amplified through M3 and M4 and finally the voltage drop on M2 (configured as a load) is measured. This type of circuit is usually used for level shifting and buffering purposes. This scheme minimizes the input capacitance of the circuit since the dominant capacitance is C_{gd} (M1) which in the saturation region is smaller than C_{gs} (M1). A voltage follower has been also included for driving the load capacitance C_l.

In this configuration V_g is a floating node (no DC path to any fixed voltage) that has to be polarized properly at the linear region. In first prototypes, and with the aim to minimize the connections at the sense node and minimizing the parasitic capacitance, the amplifier was polarized by means of an extra capacitance (C_{pol} in Fig. 4.2.3) controlled by an external polarization voltage (V_{pol}). Values of C_{pol} around 1 fF allow the correct polarization without an appreciable increase of the total parasitic capacitance. Since this small capacitance cannot be fabricated with the CNM25 technology, it was fabricated in the "nanoarea" using the same nano-fabrication process that for the MEMS fabrication (Fig. 4.2.4).

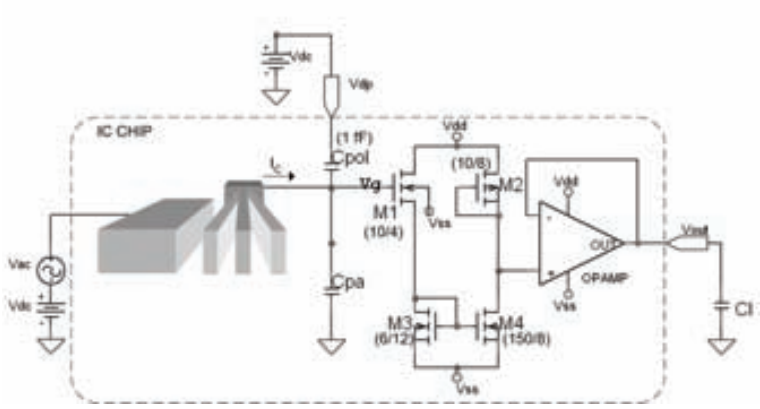

Figure 4.2.3 Circuit schematic of the voltage amplifier (BA) with an output voltage follower.

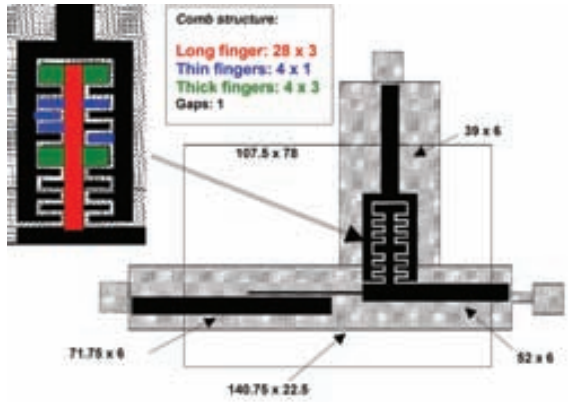

Figure 4.2.4 Layout of the mechanical structure to be fabricated into the nanoarea. Cantilever, driver and comb-capacitor for biasing the amplifier are shown. All dimensions are in microns.

The extremely high impedance at the sense node and the small leakage current through the CMOS devices produce that the time constant of the variation of the polarization voltage (DC voltage at the sense node) is high enough to allow electrical measurements during some minutes [Ver05]. Moreover a control of the polarization voltage may be performed on-line by means of V_{pol}.

The frequency response of the circuit is presented in Fig. 4.2.4 showing that the equivalent transimpedance gain depends on the frequency since the integration effect. A value of the transimpedance gain as high as 146.3 dBΩ and a low input refereed noise of 13 fA/√Hz is obtained at 1 MHz. The specifications of this front-end preamplifier are summarized in Table 4.3.

In order to improve the stability of the polarization of the circuit, a diode placed between the sense node (V_g) and the output node (V_o) of the voltage amplifier (Fig. 4.2.5) has been used to act like a very large resistance in order to keep a low noise configuration. The use of internal nodes to place the diode avoids the need of using additional pads and external DC supplies. Since there is

no DC current trough the diode the voltage drop on the diode is near zero, so the V_g(DC)=V_o(DC). The CMOS transistors of the buffer amplifier have been re-dimensioned in order to allow the correct polarization. Obviously in this case, C_{pol} is no longer necessary, making the post-processing easier.

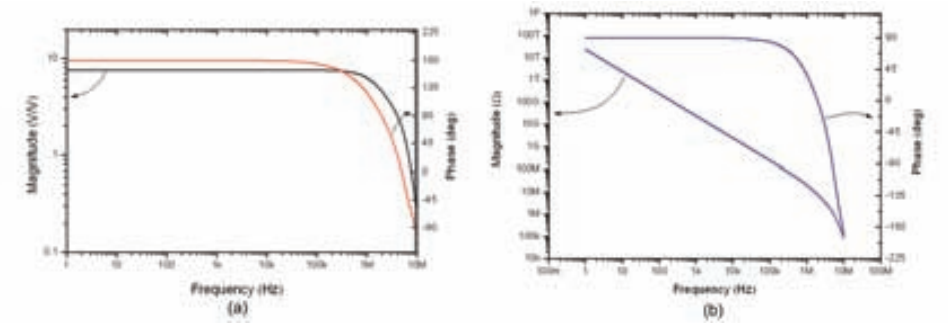

Figure 4.2.4 Simulated frequency response of the voltage gain (a) and the equivalent transimpedance gain (b) of the BA.

Table 4.3 Specifications of the front-end preamplifier assuming $C_{SB}+C_{CB} \approx 4$ fF.

Parameter	Value	Condition
Supply voltage	± 2.5 V	
Transimpedance	19.95 MΩ (146.3 dBΩ)	@ 1 MHz
Bandwidth	1.5 MHz	*Cpa* = 50 fF
Input current noise	1.3×10^{-14} A/√Hz	@ 1 MHz
Load capacitance	30 pF	at V_{out}
Output voltage swing	2.2 V	peak-to-peak

The layout of the diode is very critical since the existence of the parasitic well-substrate diode (Fig. 4.2.5c). With the configuration used, where the parasitic capacitance is located at the output, we prevent the increase of C_{pa} due to the reverse capacitance of the parasitic diode. A guard ring has been also added between the diode and the input transistor (M1) in order to prevent the *latch-up* effect.

In this case the transimpedance gain of the circuit becomes a slightly lower and the input refereed noise higher (Table 4.4) but with the benefit of a stable polarization of the CMOS circuitry.

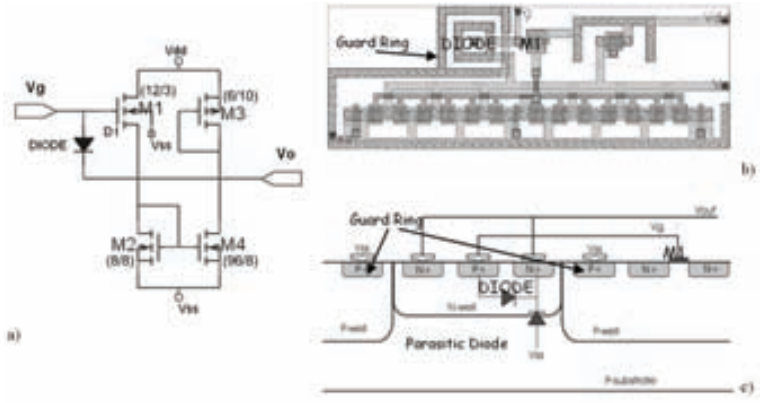

Figure 4.2.5 Circuit schematic (a) and layout (b) of the voltage amplifier with diode biasing (BA_D). c) Cross-section view illustrating the parasitic diode as well as the guard ring.

Table 4.4 Specifications of the CNM25 front-end preamplifier.

Parameter	Value	Condition
Supply voltage	± 2.5 V	
Transimpedance	3.93 MΩ (131.9 dBΩ)	@ 1 MHz
Bandwidth	1.6 MHz	Cpa = 50 fF
Input current noise	2.6×10^{-14} A/√Hz	@ 1 MHz
Load capacitance	30 pF	at V_{out}
Output voltage swing	0.9 V	peak-to-peak

4.3 AMS-C35 CIRCUITS

In this section are presented the different CMOS analog circuits designed during this thesis in the NANOSYS context. The front-end preamplifiers designed in the NANOSYS context are based on the capacitive detection topology since their intrinsic low-noise performance. As it has been explained in previous sections, the parasitic capacitance at the sense node limits the sensitivity of the current detection. Due to the MEMS and the CMOS are designed at the same time using the same IC CAD tools (see fabrication process in Chapter 3), the parasitics introduced by the MEMS can be extracted with relative accuracy.

4.3.1 FRONT-END PREAMPLIFIER

The front-end preamplifier designed to sense the MEMS capacitive current of the NANOSYS resonators is based on the capacitive method in a similar way that the circuits explained in section 4.2. In any case, this preamplifier has been improved in terms of sensitivity, noise and bandwidth.

Fig. 4.3.1 shows the conceptual circuit schematic of the front-end preamplifier. The capacitive current I_C is integrated through a capacitor C_I and the resulting voltage V_{in} is detected by means of the readout preamplifier, an unity-gain buffer in this case. The capacitor C_I is the parasitic capacitance at the sense node constituted by the input capacitance of the circuit (C_G), the cantilever-substrate capacitance (C_{SB}), the connection to the circuit (C_{CB}) and the capacitance of the bias element (C_{bias}): $C_I = C_G + C_{SB} + C_{CB} + C_{bias}$. All these parasitic capacitances are minimized in order to maximize the sensitivity of the readout. In this sense, a co-design of the CMOS and MEMS is necessary to maximize the readout sensitivity.

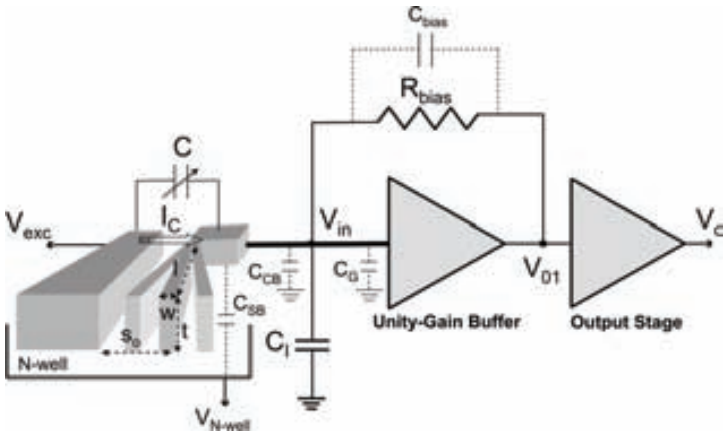

Figure 4.3.1 System block diagram of the front-end preamplifier for capacitive current sensing.

C_{CB} can be minimized, like in section 4.2, by reducing as much as possible the distance between the resonator and the circuit input and using the top metal layer for making the electrical connection.

The readout circuit used as preamplifier (Fig. 4.3.2a) has a very-low input capacitance (C_G = 7.4 fF) achieved by using a source-follower input stage based on a threshold independent level-shifter topology (M1...M5) [Fed96]. An additional source-follower output stage (M8, M9) has been added for testing purposes on capacitive loads (C_l). The unity-gain buffer stage has a gain of 0.974 and a bandwidth higher than 400 MHz when loaded with the output buffer stage. The output buffer has a gain of 0.782 and is capable of loading high capacitances ($C_l \approx 30$ pF) with a relative high bandwidth (~ 47 MHz) that allows the circuit test measurements.

In order to keep the large impedance at the sense node and consequently a low input-referred noise, a MOS-bipolar device acting as a pseudo-resistor (R_{bias}) is used as the bias. This element consists of a PMOS transistor (*MB*) with its body terminal connected to its source and its gate terminal connected to the drain (Fig. 4.3.2b) [Del94]. This adaptive element exhibits an extremely high resistance of around 10^{12} Ω in nominal conditions, not DC current (Fig. 4.3.2c). The parasitic capacitance associated to the bias element C_{bias}, sometimes on the same order of magnitude than C_I, may decrease the sensitivity of the readout system by increasing C_I directly (e.g. in [Fed96, Tav03]) or by Miller effect (e.g. in [Roe98]). A novel biasing scheme that strongly minimizes the contribution of C_{bias} on the sense node has been implemented. The bias element R_{bias} is connected

between V_{o1} and V_{in} circuit nodes. Since the readout circuit has been designed to have unity gain ($G_{UGB}=V_{in}/V_{o1}\approx 1$), the increment of C_I by Miller effect is extremely small, $C_{bias(in)} = C_{bias}\,(1-G_{UGB}) \approx 0$. In addition, the PMOS transistor is laid out so that the parasitic well-substrate capacitance does not shunt C_I (body terminal connected to V_{o1}).

With this bias scheme, the circuit is self-polarized at $V_{in}=V_{o1}\approx 2$ V (Fig. 4.3.3) without the need of any additional bias terminal. Monte Carlo analysis of the bias point corroborates the stability and viability of this approach.

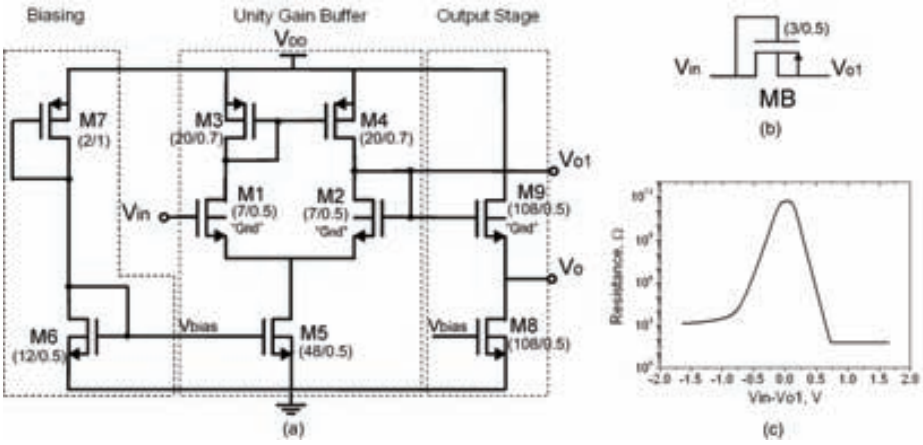

Figure 4.3.2 (a) Transistor-level circuit schematic diagram of the capacitive current preamplifier. (b) pMOS transistor configured as pseudo-resistor. (c) Resistance of the pseudo-resistor versus voltage applied in its terminals. Transistor dimensions (W/L) in microns.

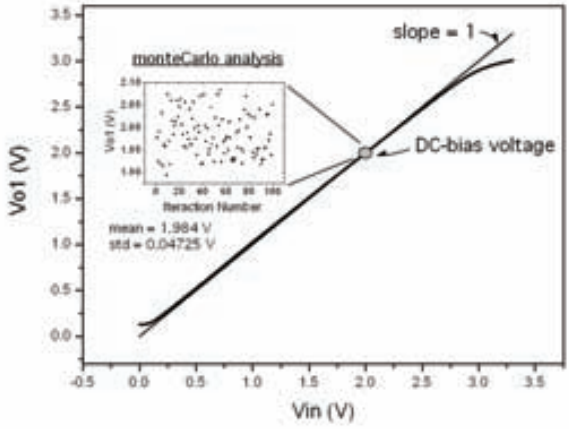

Figure 4.3.3 Static transfer function of the unity-gain buffer stage indicating the bias point. Inset: Monte Carlo analysis results of the bias point.

With this pre-amplifier, a very high transimpedance gain is obtained with a single CMOS amplifier stage. For example, for a metal cantilever in a 1-electrode configuration where $C_{SB}+C_{CB} \approx 4$ fF, an equivalent transimpedance gain of 10 MΩ or 140 dBΩ is obtained at 1MHz. Fig. 4.3.4 shows the frequency response of the circuit at nodes V_o and V_{o1}.

In addition, the parasitic capacitance of the mechanical structure C_{sb} can also be strongly reduced with this scheme if the unity-gain buffer output terminal (V_{o1}) is connected to the polarization of the N-well defined under the MEMS ($V_{n\text{-}well}$). With this bootstrapping, the gain of the readout system can be further increased.

Figure 4.3.5 shows voltage and current noise refereed to the sense node versus frequency. It is appreciated that although the voltage noise decreases with the frequency, the current noise increases with it since the transimpedance gain of the circuit also decreases with the frequency. The input refereed current noise at 1 MHz and 10 MHz is as low as 2.7 fA/√Hz and 18 fA/√Hz respectively. Other specifications of the front-end preamplifier are indicated in Table 4.5.

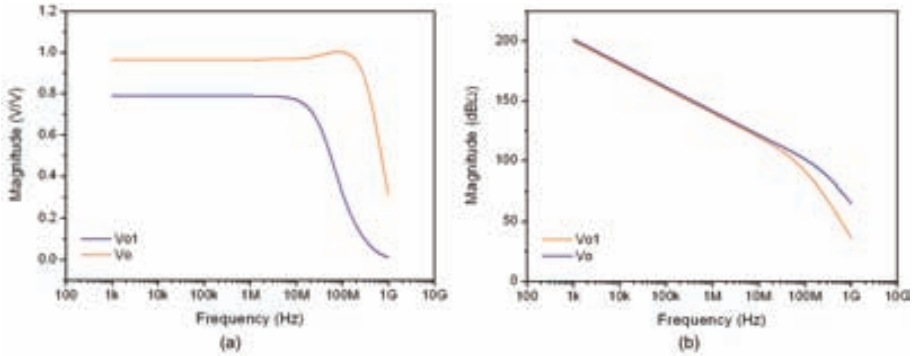

Figure 4.3.4 Voltage (a) and transimpedance (b) gain versus frequency of the front-end preamplifier at nodes V_o and V_{o1} assuming $C_{SB}+C_{CB} \approx 4$ fF.

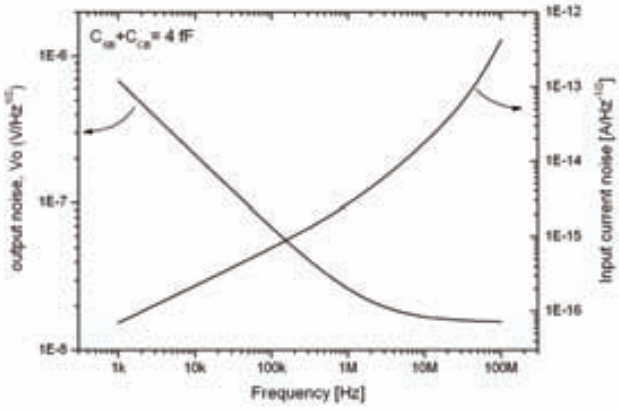

Figure 4.3.5 Input-referred voltage and current noise versus frequency assuming $C_{SB}+C_{CB} \approx 4$ fF.

Table 4.5 Specifications of the front-end preamplifier assuming $C_{SB}+C_{CB} \approx 4$ fF.

Parameter	Value	Condition
Supply voltage	3.3 V	
Consumption	4.6 mW	
Transimpedance	9.7 MΩ 947 kΩ	@ 1MHz @ 10 MHz
Bandwidth	47 MHz	V_o
Input current noise	2.7 fA/√Hz 18 fA/√Hz	@ 1MHz @ 10 MHz
Load capacitance	30 pF	at V_o
Output voltage swing	2 V	symmetric

4.3.2 VOLTAGE AMPLIFIER

A high-gain voltage amplifier has also been designed to give an additional gain to the capacitive readout circuit in order to allow the operation of the MEMS in closed loop as a stand-alone oscillator. Since many of the MEMS devices characterized in this thesis work uses this amplifier, the main characteristics of this circuit is presented in this section. A further discussion of the oscillator performance is presented in Chapter 6.

The amplifier is based on a cascode with cascode-load configuration (see Fig. 4.3.6). Since the high-gain of this amplifier, the stage is also self-polarized by means of a PMOS pseudo-resistor (M_B) and AC-coupled with the front-end preamplifier in order to assure a correct biasing at the input node. The capacitor is implemented using the poly1-poly2 module of the technology that offers high linearity with respect to the applied voltage (85 ppm/V).

The intrinsic voltage gain of the amplifier (without the AC coupling) is around 60 dB but this value is reduced when using the AC coupling since the capacitive divider produced between the C_{ac} and input capacitance of the cascode amplifier. The parasitic capacitance of the PMOS pseudo-resistor also increases the input capacitance by Miller effect. Fig. 4.3.7a shows the static characteristic of the amplifier indicating the bias voltage and Fig. 4.3.7b shows the frequency response of the amplifier with the AC-coupling. Finally, Table 4.6 presents the specifications of this voltage amplifier.

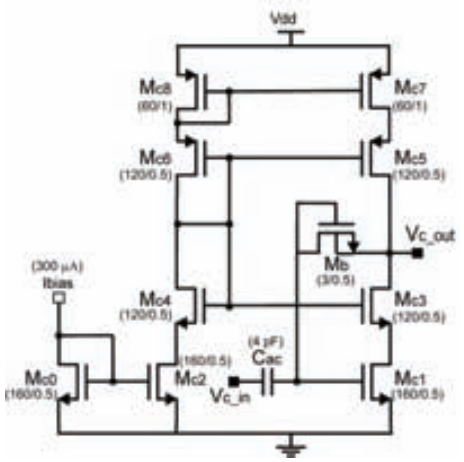

Figure 4.3.6 Transistor-level circuit schematic of the cascode with cascode-load amplifier with AC-coupling. Transistor dimensions (W/L) in microns.

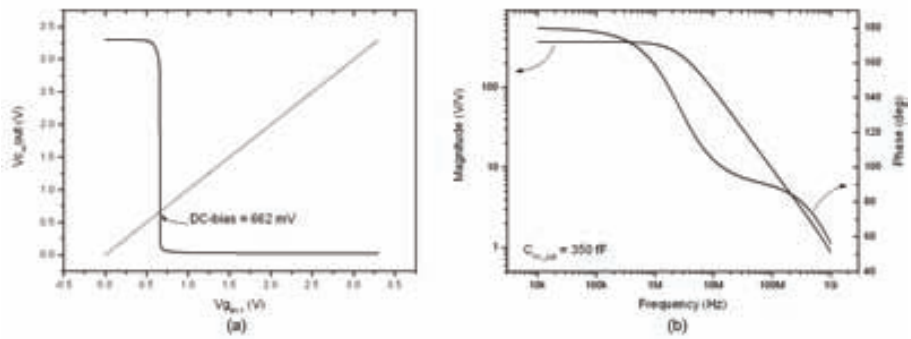

Figure 4.3.7 Static characteristic indicating the DC-bias voltage (a) and frequency response of the cascode with cascode-load amplifier with AC-coupling.

Table 4.6 Specifications of the cascode amplifier (CA) implemented in the AMS-C35 technology.

Parameter	Value	Condition
Supply voltage	3.3 V	
Consumption	2.8 mW	
Voltage Gain	51.3 dB	V_{c_out} / V_{c_in}
Bandwidth	25 MHz	350 fF
Load capacitance	350 fF	at V_{c_out}
Output voltage swing	1.3 V	symmetric

4.3.3 OTHER ANALOG BLOCKS

Additional analog blocks implemented in AMS-C35 technology have been also designed in this thesis. The blocks presented in this section have been designed in collaboration with Dra. Arantxa Uranga from the UAB and have been used in different developed devices in the NANOSYS project for mass sensing and RF applications.

- **50-Ω OUTPUT BUFFER**

An output buffer stage (see Fig. 4.3.8) has been designed to drive the 50-Ω input impedance of the RF measurement instruments (i.e. network analyzer, spectrum analyzer, etc.). It is based on a two source follower stages. In order to reduce the power consumption of this stage, the output is AC-coupled to the external instrument by means of an external capacitor (i.e. bias-T) (Fig. 4.3.9).

Fig. 4.3.10 shows the static characteristic and frequency response of the designed output buffer. At the frequencies range of interest (1-20 MHz), the phase shift introduced by this stage is almost negligible. On the other hand, the input signal is attenuated 8.8 dB since the use of source follower stages and the AC-coupling on the 50-Ω load (Table 4.7).

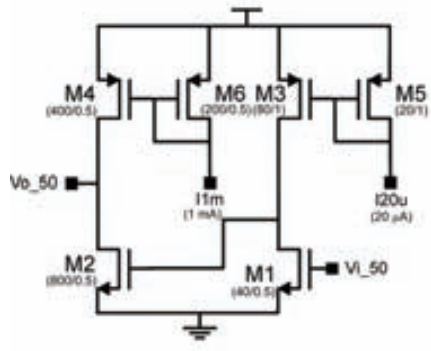

Figure 4.3.8 Transistor-level circuit schematic (a) and layout (b) of the 50-Ω output buffer. Transistor dimensions (W/L) in microns.

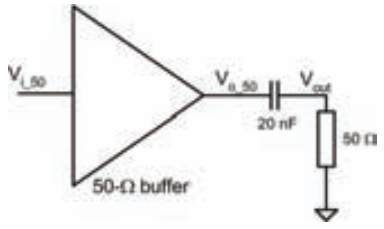

Figure 4.3.9 Schematic indicating how the output buffer is coupled to load 50Ω.

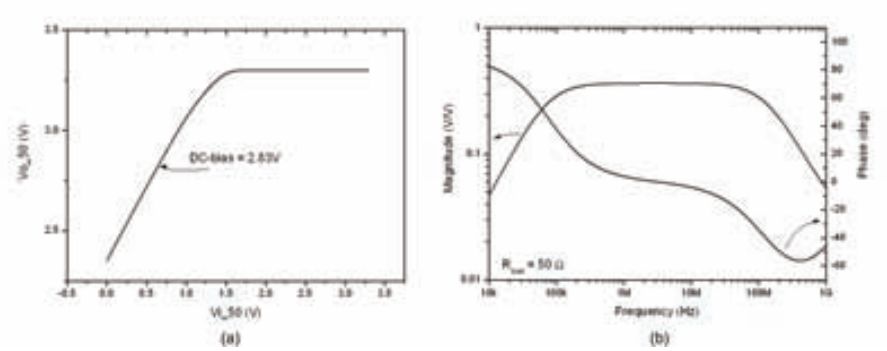

Figure 4.3.10 Static characteristic indicating the DC-bias voltage (a) and frequency response of the 50-Ω output buffer.

Table 4.7 Specifications of the 50-Ω output buffer implemented in the AMS-C35 technology.

Parameter	Value	Condition
Supply voltage	3.3 V	
Consumption	10.5 mW	
Voltage Gain	-2.5 dB	V_{o_50} / V_{i_50}
	-8.8 dB	V_{out} / V_{i_50}
Bandwidth	125 MHz	
Load	50 Ω	at V_{out}
Output voltage swing	0.95 V	symmetric

- **CMOS BIASING**

An analog standard cell (BBIAS module) has been designed as a highly stable bias current of 10 μA (Figure 4.3.11). This module is used to generate the bias currents for the different stages of the readout circuit (i.e. cascode amplifier, 50-Ω output buffer).

Different current mirrors stages have been designed (Fig. 4.3.12 and 4.3.13) from this BBIAS module in order to generate the currents that need the different amplifier blocks. The layout of the BBIAS module and the current mirrors is depicted in Fig, 4.3.14). The resistance of 4 kΩ has been implemented using the high resistive polysilicon layer available in the technology.

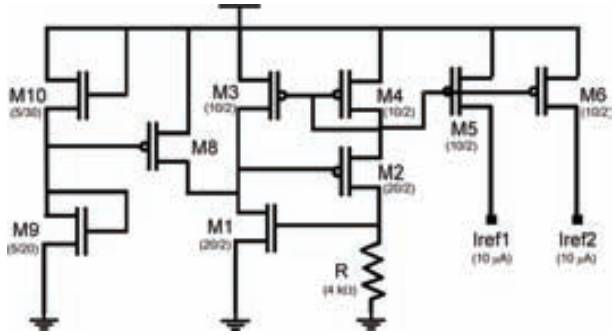

Figure 4.3.11 Transistor-level circuit schematic of the BBIAS module designed to generate stable 10 μA currents. Transistor dimensions in microns.

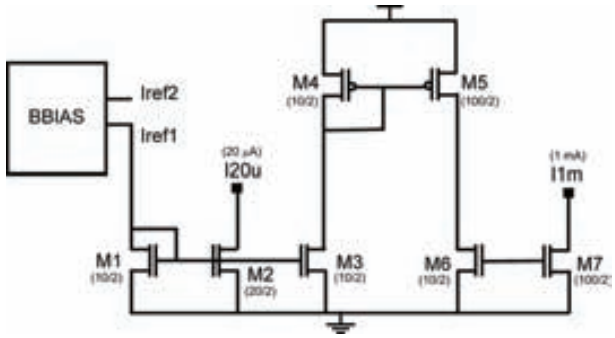

Figure 4.3.12 Transistor-level circuit schematic of current mirrors designed to generate 20 μA and 1 μA currents from the BBIAS module. Transistor dimensions in microns.

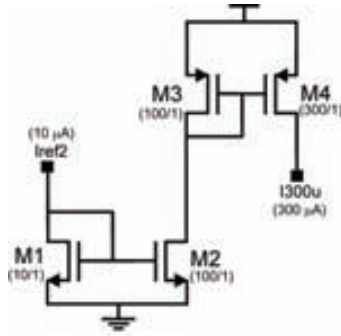

Figure 4.3.13 Transistor-level circuit schematic of the current mirror to generate 300 μA from the BBIAS module. Transistor dimensions (W/L) in microns.

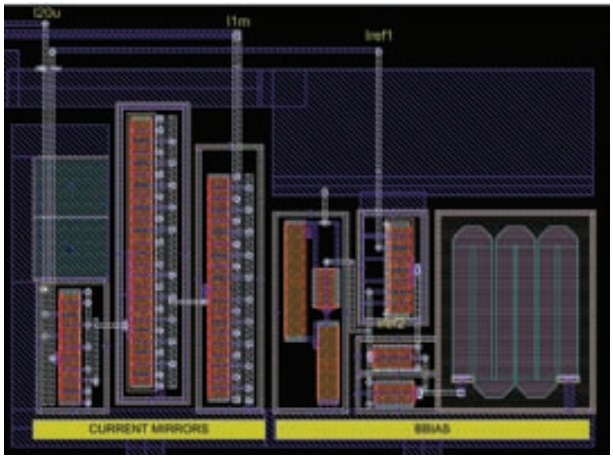

Figure 4.3.14 Layout of the BBIAS and the current mirrors implemented in the AMS-C35 technology.

4.4 MIXED CMOS-MEMS LAYOUT AND PERFORMANCE

The mass sensors designed are constituted by MEMS based on resonant beams connected to the CMOS readout circuit in a monolithic way. In this section, the layout and the theoretical electrical performance of the most significant devices developed in this thesis are presented.

The layout have been arranged in order to allow an easy electrical characterization of the devices. In the Appendix B are presented the entire chips layouts that have been designed in the framework of this thesis.

4.4.1 NANOMASS DEVICES

The mixed CMOS-MEMS based on the TIA and BS circuit are arranged in rows with 16 connection pads (Fig. 4.4.1). The TIA based devices need five output pads to perform the electrical characterization as depicted in Fig. 4.4.2a. In the other hand, the BS circuit based devices need an additional pad to able the polarization of the sense node (Fig. 4.4.2b). In the case of the BS circuits with polarization diode, this additional pad is not necessary.

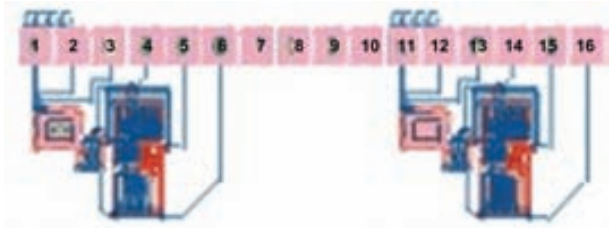

Figure 4.4.1 Layout showing how the PADs are arranged to enable the electrical test with a 16-contacts probe card.

In order to perform a system level electrical simulation of the mixed CMOS-MEMS devices, the RLC electrical model introduced in Chapter 2 has been used. The parameters of the electrical model are indicated in Table 4.8 for a polysilicon cantilever with a 1-driver configuration and the characteristics already introduced in Table 4.1. The frequency response of the mixed CMOS-MEMS is shown in Fig. 4.4.3 for the TIA and the BS circuit. It is appreciated in both graphs the peak in the magnitude plot that are corresponding with the mechanical resonance frequency of the cantilever. On the other hand, this resonance frequency produces an electrical phase shift between the excitation and the readout electrical signals. Finally, it is appreciated that the insertion losses introduced by the CMOS-MEMS are lower in the case of the BS circuit.

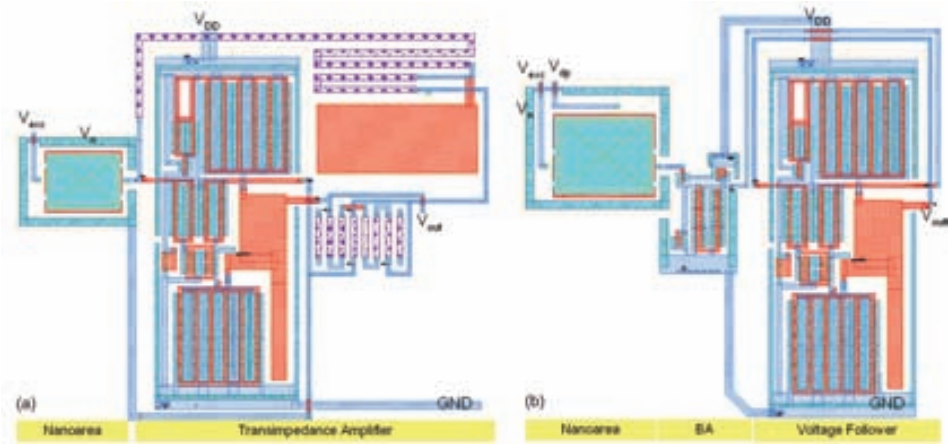

Figure 4.4.2 Layout of the mixed CMOS-MEMS implemented in the CNM25 technology showing the nanoarea connected to the corresponding pre-amplifier: (a) TIA and (b) BA.

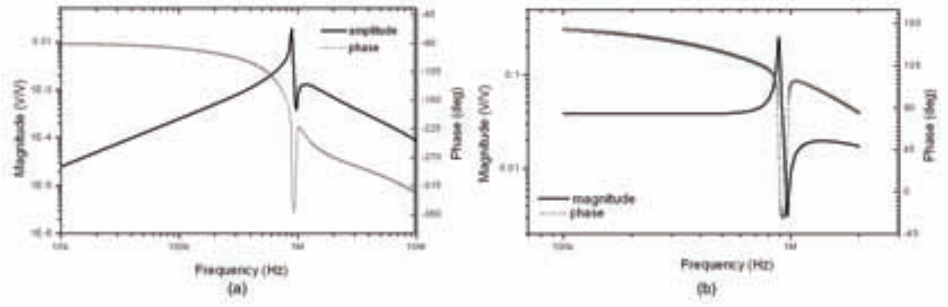

Figure 4.4.3 Simulated frequency response of the mixed CMOS-MEMS obtained for the TIA preamplifier (b) and the BA circuits.

Table 4.8 Theoretical small-signal electromechanical model parameters for a polysilicon cantilever with l=40 μm, w=s=1 μm and t=600 nm (V_{DC} = 22 V and Q = 50).

Parameter	Value
R_S	82.5 MΩ
L_S	740 H
C_S	44 aF
C_P	237 aF

4.4.2 NANOSYS DEVICES

The experimental measurements on the mixed CMOS-MEMS in the AMS-C35 technology reported in next chapter have been performed using the circuit depicted in Fig. 4.4.4. The readout circuit is constituted by three main modules; the front-end preamplifier (UGB module), the voltage amplifier (CA module), and the 50-Ω output buffer (B50). The overall circuit is addressed in this work as UGBCA50. The layout has been arranged to be used with two modules of the 5-tips RF probes presented in next chapter (see Fig. 4.4.5). For the electrical characterization of the devices with MEMS based on 2-driver configuration, five output pads are needed (V_{DD}, V_{DC}, V_{AC}, GND, and V_{o_50}). An additional pad has been also included to allow access at the output node of the cascode amplifier (V_{c_out}).

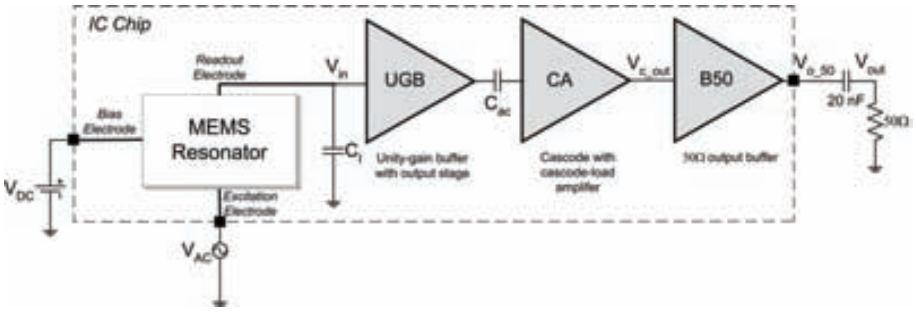

Figure 4.4.4 Electrical scheme of the mixed CMOS-MEMS with the MEMS area connected to the readout circuitry (UGBCA50).

The simulation results presented in this section have been obtained from the layout in order to take into account all the parasitics introduced by the connections tracks, the mechanical structures and the pads (extracted view). On the other hand, the MEMS performances have been modeled using in this case the nonlinear electromechanical model implemented in the Verilog-A language (see Appendix A). The values related with the physical and geometrical parameters that have been introduced in the model are the indicated in Table 4.1.

The parasitic capacitance at the sense node (V_{in}) is one of the main factors in setting the transimpedance gain of the readout circuit. The total value of this capacitance, which has been extracted from the layout, depends on the type of beam resonator used since the value of C_{SB} plus C_{CB} is different depending if using metal structures (~ 8.5 fF) or polysilicon structures (~ 20.5 fF).

C_G is obviously the same in both cases (~ 7 fF). Figure 4.4.6 plots the frequency response of the UGBCA50 equivalent transimpedance gain in the case of metal structures.

On the other hand, the value of the parasitic coupling between the excitation and the readout nodes (C_p) have to be obtained empirically since it is not extracted from the layout. In this sense, the electrical simulations have been performed for different values in order to illustrate the effect on the frequency response.

Figure 4.4.7 shows the simulation results for the metal cantilever resonator where it is appreciated that large values of the parasitic coupling reduce the height of the resonance peak in the magnitude plot and the phase shift in the phase plot. The same effects can be appreciated for the metal CC-beam resonator (Fig. 4.4.8), the polysilicon cantilever resonator (Fig. 4.4.9), and the polysilicon CC-beam resonator (Fig. 4.4.10).

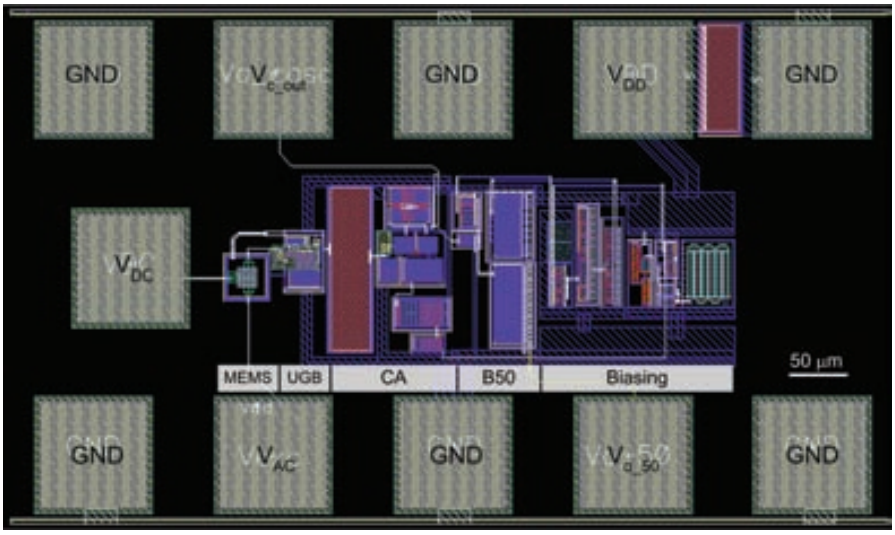

Figure 4.4.5 Layout of the mixed CMOS-MEMS with the MEMS area connected to the readout circuitry (UGBCA50) implemented in the AMS-C35 technology.

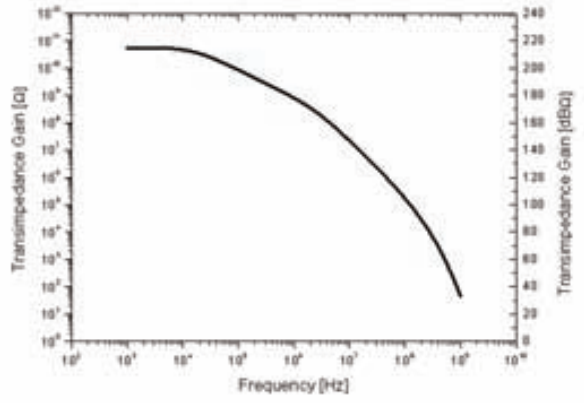

Figure 4.4.6 Transimpedance gain of the UGB50CA circuit.

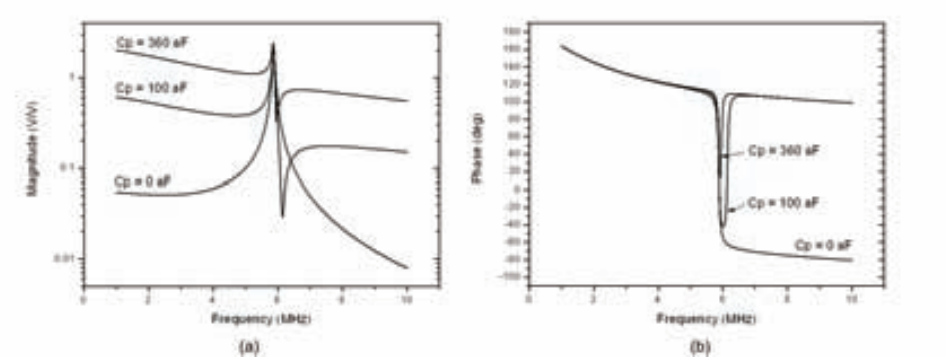

Figure 4.4.7 Simulated frequency response (magnitude (a) and phase (b)) of the mixed AMS-C35 CMOS-MEMS obtained for the metal cantilever.

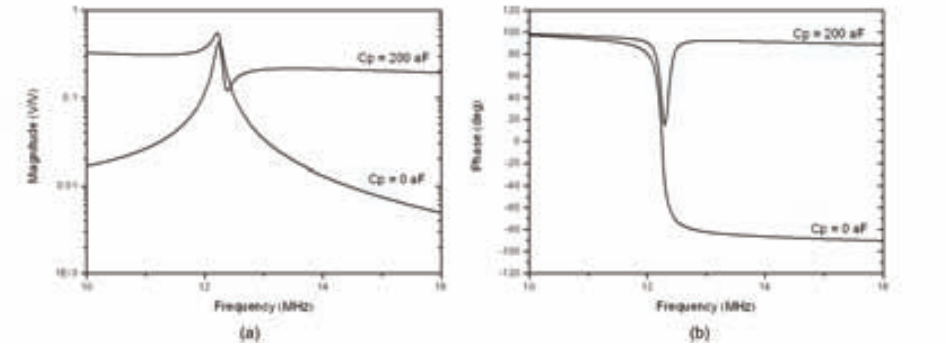

Figure 4.4.8 Simulated frequency response (magnitude (a) and phase (b)) of the mixed AMS-C35 CMOS-MEMS obtained for the metal CC-beam.

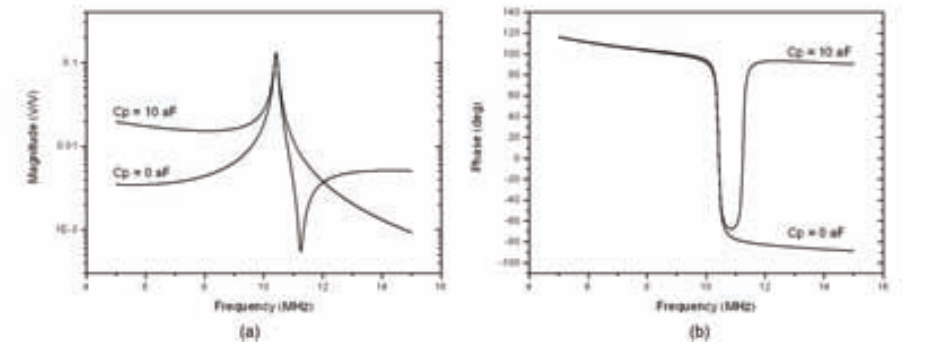

Figure 4.4.9 Simulated frequency response (magnitude (a) and phase (b)) of the mixed AMS-C35 CMOS-MEMS obtained for the polysilicon cantilever.

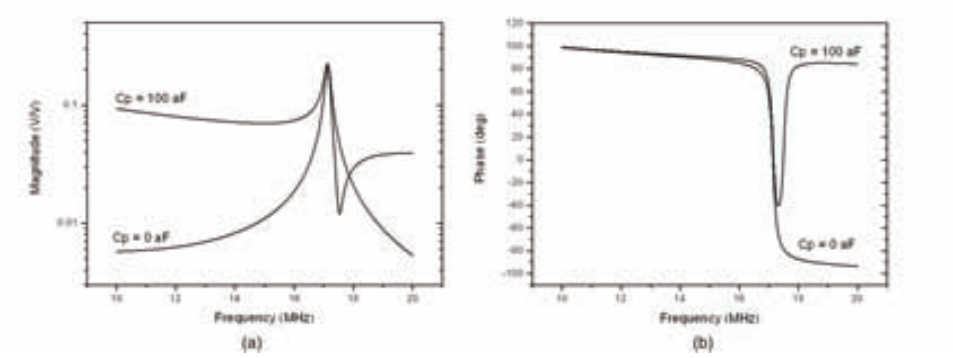

Figure 4.4.10 Simulated frequency response (magnitude (a) and phase (b)) of the mixed AMS-C35 CMOS-MEMS obtained for the polysilicon CC-beam.

4.5 DISPLACEMENT RESOLUTION: A COMPARATIVE STUDY

We previously commented that the readout system or displacement transducer used to sense the resonator movement can set the limit on the final resolution of the overall mass sensor system since it sets the minimum detectable displacement (MDD).

The MDD is a figure of merit that allows an objective comparison between different readout or transduction methods. The MDD depends not only on the displacement sensitivity but is limited by the noise level of the readout system. In this sense, the MDD or displacement resolution is defined as the equivalent displacement of the resonator that produces a voltage signal equal to the total noise of the readout system, that is, the noise-equivalent resonator displacement for a SNR=1:

$$MDD = \frac{S_V^{1/2}}{D_S}, \tag{4.5.1}$$

where S_V is the output voltage noise power and D_S is the displacement sensitivity of the readout system.

In this section, the MDD for the different capacitive readout circuits designed in this thesis is evaluated and compared with the state-of-the-art of other readout methods commonly used in MEMS (i.e. capacitive, piezoresistive and optical).

For the capacitive readout method, the displacement sensitivity can be calculated from the motional current, that it is proportional to the resonator displacement, and the transimpedance gain of the readout circuit. Using Eq. 2.1.44 to find the relation between the motional current and the resonator displacement x, we obtain next expression for the displacement sensitivity parameter: In the case of a beam resonator, according with next expression:

$$D_S = \left|\frac{\partial I_M}{\partial x}\right| G_T \approx V_{DC}\frac{C_o \omega}{s_o} G_T \times 0.4, \tag{4.5.2}$$

where G_T is the transimpedance gain of the readout circuit and the factor 0.4 is approximately the relation between the displacement of the equivalent parallel plate capacitor and the effective

displacement at the cantilever free-end or at the middle point in the case of a CC-beam. This factor can be obtained from Eq. A.2.5 or A.2.6 (see Appendix A) by performing the integral of the displacement along the beam divided by the beam length.

Table 4.9 summarizes the theoretical values of the noise and displacement sensitivity for every capacitive readout circuit presented in section 4.2 and 4.3, as well as the displacement resolution (MDD) obtained from these values. A theoretical MDD value of around 10 fm/√Hz is obtained with the devices developed in the AMS-C35 technology. We can appreciate that the Nanosys circuits presents a better MDD parameter of around two orders of magnitude with respect to the Nanomass circuits.

Table 4.9 Summary of different parameters of the resonators fabricated for mass sensing applications.

MEMS	**CMOS Circuit**	C_o $l_{eff} \times t$ **, s** (in μm)	f_o	$S_V^{1/2}$ (V/Hz$^{1/2}$)	D_S^* (V/m)	***MDD*** (m/Hz$^{1/2}$)
Nanomass Poly-Cantilever	TIA	159 aF 30×0.6, 1	837 kHz	3.8×10^{-7}	1.4×10^{4}	2.7×10^{-11}
Nanomass Poly-Cantilever	BA	159 aF 30×0.6, 1	837 kHz	2.5×10^{-7}	3.0×10^{5}	8.5×10^{-13}
Nanomass Poly-Cantilever	BAD	159 aF 30×0.6, 1	837 kHz	1.0×10^{-7}	8.8×10^{4}	1.2×10^{-12}
Nanosys Metal-Cantilever	UGB	88.5 aF 8×0.75, 0.6	6.40 MHz	2.3×10^{-8}	2.3×10^{6}	1.0×10^{-14}
Nanosys Metal-Bridge	UGB	111 aF 10×0.75, 0.6	12.6 MHz	2.2×10^{-8}	3.0×10^{6}	7.3×10^{-15}
Nanosys Poly-Cantilever	UGB	25 aF 4.5×0.28, 0.45	11.1 MHz	2.3×10^{-8}	3.2×10^{4}	7.2×10^{-13}
Nanosys Poly-Bridge	UGB	149 aF 9×0.28, 0.15	17.6 MHz	2.2×10^{-8}	1.3×10^{6}	1.7×10^{-14}

* Assuming the resonator bias voltage (V_{DC}) indicated in Table 4.1.

Table 4.10 presents a comparative of the MDD of the capacitive readout system developed in this thesis work with the state-of-the-art, from our point of view, of the commonly used readout methods used in MEMS based sensors.

Traditionally, capacitive sensing schemes have been used in accelerometers applications where the MEMS are a membrane structure that work in static mode (non-resonant mode). Despite this readout circuits [Bos96, Tav03 and Wu04] are not valid for resonant structures like our beam resonators, an evaluation of the MDD have been performed indicating that are one order of magnitude worse than the circuit of this work. On the other hand, recently capacitive detection has been applied to sense cantilever resonators. S.-J. Kim and co-workers have reported a capacitive scheme based on FM modulation using external electronics allowing the detection of capacitances changes of 2.4 zF/√Hz (1 zepto = 10^{-21}) equivalent to a displacement resolution of 50 pm/√Hz [Kim07]. P.A. Truitt and co-workers have been reported a similar work where a cantilever resonator is embedded in a LC oscillator circuit using external components. In this case the minimum capacitance that is able to detect is 1.2 zF/√Hz equivalents to a MDD of 4 pm/√Hz

[Tru07]. J. Arcamone and co-workers have been implemented at the CNM, using a similar approach that presented in this thesis, a monolithic resonant cantilever-based mass sensor [Arc07]. The readout circuit used is based on a common base detection and the MDD obtained from their specifications is 15 pm/√Hz.

Table 4.10 Summary of different parameters of the resonators fabricated for mass sensing applications.

Reference	*Detection method*	*SoC*	f_o *or* $BW_{circuit}$	$S_V^{1/2}$ ($V/Hz^{1/2}$)	D_S (V/m)	*MDD* ($m/Hz^{1/2}$)	δC_o ($F/Hz^{1/2}$)
This work	Capacitive	Monolithic	12.6 MHz	2.2×10^{-8}	3.0×10^{6}	7.3×10^{-15}	1.4×10^{-24}
[Bos96]	Capacitive	Monolithic	10 MHz	---	---	1×10^{-13}	1×10^{-19}
[Tav03]	Capacitive	Hybrid	1 MHz	---	---	2.5×10^{-13}	3.8×10^{-20}
[Wu04]	Capacitive	Monolithic	3 MHz	---	---	5×10^{-13}	2×10^{-20}
[Kim07]	Capacitive	NOT	1 GHz	---	---	5×10^{-11}	2.4×10^{-21}
[Tru07]	Capacitive	NOT	11 MHz	---	---	4×10^{-12}	1.2×10^{-21}
[Arc07]	Capacitive	Monolithic	1.5 MHz	3.5×10^{-8}	---	1.5×10^{-11}	2.6×10^{-21}
[Chu98]	Piezoresistive	NOT	280 kHz	---	---	1.6×10^{-12}	---
[Yu02]	Piezoresistive	NOT	---	4.7×10^{-10}	2.5×10^{3}	1.9×10^{-12}	---
[Li07]	Piezoresistive	NOT	127 MHz	9.2×10^{-10}	4.0×10^{4}	3.9×10^{-14}	---
[Vil06]	Piezoresistive	Monolithic	310 kHz	1.4×10^{-5}	4.2×10^{4}	3.2×10^{-10}	----
[Rug89]	Optical	NOT	---	---	---	5.5×10^{-14}	---
[Gar98]	Optical	NOT	10 – 40 kHz	4.7×10^{-8}	1.9×10^{6}	1.3×10^{-14}	---
[Lee04]	Optical	Hybrid	2 MHz	4.1×10^{-8}	1×10^{5}	1.3×10^{-14}	---
[Bun07]	Optical	NOT	36 MHz	---	---	1.3×10^{-15}	

The best values of MDD obtained with piezoresistive detection in sensing cantilever structures are ~ 1 pm/√Hz [Chu98, Yu02]. Nevertheless, M. Li and co-workers have been recently reported a nano-cantilever with integrated piezoresistances reporting a MDD value as low as 39 fm/√Hz [Li07]. The success is in the fact that the value of the piezoresistances is very small and the noise associated to them is minimized. All these works use external readout circuitry to detect and amplify the signal provided by the piezoresistances. On the other hand, G. Villanueva and co-workers have been developed at the CNM a monolithic force sensor based on a cantilever with piezoresistive detection by means of an integrated circuit [Vil06]. The MDD value obtained is far from the state-of-the-art being of 320 pm/√Hz.

Optical detection has been widely used as a high-sensitivity method to sense cantilevers in AFM-based microscopy or for sensing applications. The best values of MDD obtained are around tens of fm/√Hz [Rug89, Gar98]. The main inconvenient of this technique is the bulky equipment required that prevents a monolithic approach. In any case, W. Lee and co-workers have reported a hybrid integration of optoelectronics with an acoustic sensor achieving a MDD of 13 fm/√Hz. The

acoustic sensor is a 200-μm-diameter aluminum membrane built on a quartz substrate. In this sense, this hybrid approach with small resonant structures like submicrometer-scale cantilever has not still demonstrated. Recently, the group of Prof. Craighead has reported a NEMS resonator based on a graphene sheet which is detected optically by interferometry with a resolution as low as 1.3 fm/√Hz [Bun07].

In summary, the capacitive readout circuits designed in this thesis work shows a theoretical MDD value better than other capacitive or piezoresistive methods and similar than the state-of-the-art of optical methods with the additional benefit of allowing its use in system-on-chip applications.

REFERENCES

[Ame01] G. Amendola et al., "Signal-Processing Electronics for a Capacitive Micro-Sensor", *Analog Integrated Circuits and Signal Processing*, vol. 29, pp. 105-113, 2001.

[Arc07] J. Arcamone, B. Misischi, F. Serra-Graells, M.A.F. van den Boogaart, J. Brugger, F. Torres, G. Abadal, N. Barniol, and F. Perez-Murano, "A Compact and Low-Power CMOS Circuit for Fully Integrated NEMS Resonators", *IEEE T. Circuits and Systems-II*, vol. 54 (5), pp. 377-381, 2007.

[Bos96] B.E. Boser and R.T. Howe, "Surface Micromachined Accelerometers", *IEEE J. Solid-State Circuit*, vol. 31 (3), pp. 366-375, 1996.

[Bun07] J.S. Bunch, A.M. van der Zande, S.S. Verbridge, I.W. Frank, D.M. Tanenbaum, J.M. Parpia, H.G. Craighead, P.L McEuen, "Electromechanical Resonators from Graphene Sheets", *Science*, vol. 315, (5811), pp. 490-493, 2007.

[Chu98] B.W. Chui, T.D. Stowe, Y.S. Ju, K.E. Goodson, T.W. Kenny, H.J. Mamin, B.D. Terris, R.P. Ried, and D. Rugar, "Low-Stiffness Silicon Cantilevers with Integrated Heaters and Piezoresistive Sensors for High-Density AFM Thermomechanical Data Storage", *Journal of Microelectromechanical Systems,* vol. 7 (1), pp. 100-112, 1998.

[Del94] T. Delbruck, D. Oberhof, "Self biased low power adaptive photoreceptor", in *Proc. of the International Symposium on Circuits and Systems (ISCAS 2004)*, pp. IV-844-847, 2004.

[Fed96] G. K. Fedder and R. T. Howe, "Multimode Digital Control of a Suspended Polysilicon Microstructure", *Journal of Microelectromechanical Systems*, vol. 5, no. 4, pp. 283-297, 1996.

[Gar98] A. Garcia-Valenzuela, J. Villatoro, "Noise in optical measurements of cantilever deflections", *Journal of Applied Physics*, vol. 84 (1), pp. 58-63, 1998.

[Kim07] S-J. Kim, T. Ono, and M. Esashi, "Mass detection using capacitive resonant silicon resonator employing LC resonant circuit technique", *Rev. Sci. Instrum.*, vol. 78, pp. 085103, 2007.

[Lee04] W. Lee, N.A. Hall, Z. Zhou, and F.L. Degertekin, "Fabrication and Characterization of a Micromachined Acoustic Sensor with Integrated Optical Readout", *IEEE J. of Selected Topics in Quantum Electronics*, vol. 10 (3), pp. 643-651, 2004.

[Li07] M. Li, H. X. Tang, and M. L. Roukes, "Ultra-sensitive NEMS-based cantilevers for sensing, scanned probe and very high-frequency applications", *Nature nanotechnology*, vol. 2, pp. 114-120, 2007.

[Lu95] C. Lu, M. Lemkin and B. E. Boser, "A Monolithic Surface Micromachined Accelerometer with Digital Output", *IEEE Journal of Solid-State Circuits*, vol. 30, no. 12, 1995.

[Roe98] T. A. Roessig, R. T. Howe, A. P. Pisano, and J. H. Smith, "Surface-micromachined 1MHz oscillator with low-noise pierce configuration", in *Proc. of Solid-State Sensor and Actuator Workshop*, pp. 859-862, 1998.

[Rug89] Rugar, D., Mamin, H.J., and Guethner, P., "Improved fiber-optic interferometer for atomic force microscopy", *Appl. Phys. Lett.*, vol. 55, pp. 2588–2590, 1989.

[Tav03] M. Tavakoli, and R. Sarpeshkar, "An Offset-Canceling Low-Noise Lock-In Architecture for Capacitive Sensing", *IEEE J. Solid-State Circuit*, vol. 38 (2), pp. 244-253, 2003.

[Tru07] P.A. Truitt, J.B. Hertzberg, C.C. Huang, K.L. Ekinci, and K.C. Schwab, "Efficient and Sensing Capacitive Readout of Nanomechanical Resonator Arrays", *Nanoletters*, vol. 7 (1), pp. 120-126, 2007.

[Ver05] J. Verd, G. Abadal, J. Teva, M. Villarroya, A. Uranga, X. Borrisé, F. Campabadal, J. Esteve, E. Figueras, F. Pérez-Murano, Z.J. Davis, E. Forsen, A. Boisen and N. Barniol, "Design, fabrication and characterization of a submicroelectromechanical resonator with monolithically integrated CMOS readout circuit", *Journal of Microelectromechanical Systems*, vol. 14 (3), pp. 508-519, 2005.

[Vil06] G. Villanueva, F. Perez-Murano, M. Zimmermann, J. Lichtenberg, J. Bausells, "Piezoresistive cantilevers in a commercial CMOS technology for intermolecular force detection", *Microelectronic Engineering*, vol. 83, pp. 1302-1305, 2006.

[Yaz00] N. Yazdi et al., "A generic interface chip for capacitive sensors in low-power multi-parameter Microsystems", *Sensors and Actuators*, vol. 84, pp. 351-361, 2000.

[Yu02] X. Yu, J. Thaysen, O. Hansen, and A. Boisen, "Optimization of sensitivity and noise in piezoresistive cantilevers", *Journal of Applied Physics,* vol. 92 (10), pp. 6296-6301, 2002.

[Wu04] J. Wu, G.K. Fedder, and L.R. Carley, "A Low-Noise Low-Offset Capacitive Sensing Amplifier for a 50-ug/√Hz Monolithic CMOS MEMS Accelerometer", *IEEE J. Solid-State Circuit*, vol. 39 (5), pp. 722-730, 2004.

CHAPTER 5

CMOS-MEMS CHARACTERIZATION

In this chapter the characterization of the different mass sensors based on CMOS-MEMS resonators fabricated in this thesis are presented. The devices are arranged in two groups corresponding with the Nanomass (CNM25 devices) and Nanosys (AMS-C35 devices) approaches. The experimental results presented are related with electrical, including nonlinearities and thermomechanical noise measurements, and functional characterization as well as an analysis of the mass resolution obtaining a complete datasheet of the CMOS-MEMS resonators.

5.1 ELECTRICAL MEASUREMENT SETUP

The electrical characterization of the different devices presented in this thesis work has consisted basically in the measurement of the frequency characteristics of the beam resonators integrated monolithically with the CMOS readout circuit (mixed CMOS-MEMS devices). In this sense, the frequency response of the transmission parameter (S_{21} parameter) of the mixed CMOS-MEMS and the frequency spectrum of the output signal have been performed using a Network Analyzer (Agilent E5100A) and a Spectrum Analyzer (Agilent E4404B) respectively.

Two main setups have been used to test the devices related with the use of a probe station or a PCB (printed circuit board) as electrical support.

- **MEASUREMENTS WITH THE PROBE STATION**

The use of a probe station allows the testing of the different circuits integrated in each chip in a low-cost and simple way. Fig. 5.1.1 shows the set-up comprising the probe station (Süss-Microtech PM-8) and the different instruments to perform the electrical characterization. The probe station incorporates an optical microscopy (Mitutoyo) with 5X, 10X, and 100X optical

zoom that jointly with the CCD color camera (Philips LTC 0450/51) allows the acquisition of photograph or video with an enough zoom to observe the MEMS structures.

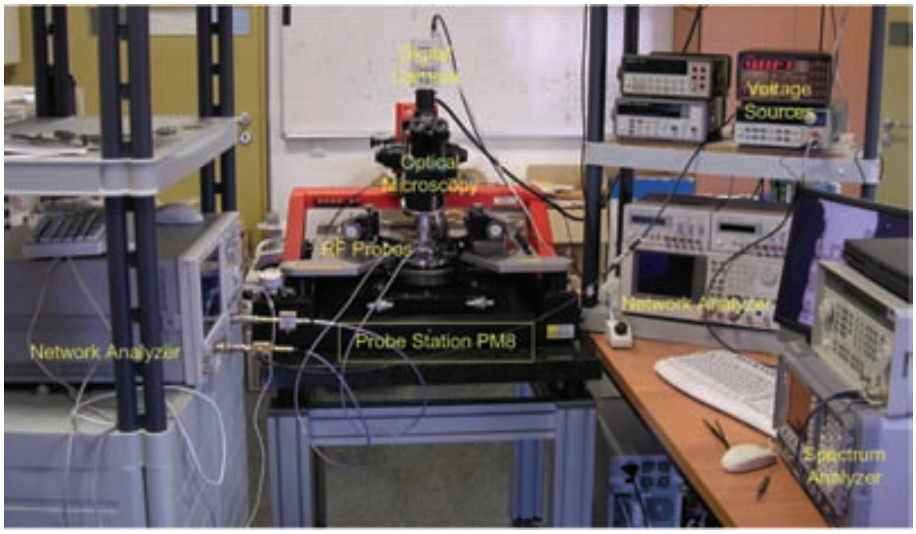

Figure 5.1.1 Photograph of the set-up used to measure the CMOS-MEMS devices with a Probe Station.

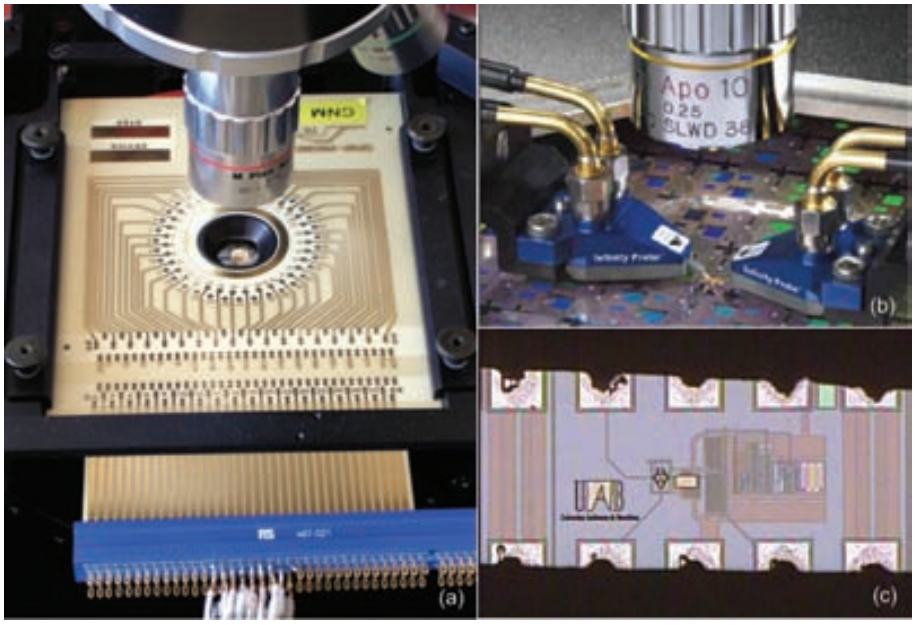

Figure 5.1.2 (a) Detail of the probe station with the 16-tips probe card used to test the Nanomass devices. (b) RF probes used to test the Nanosys devices. (c) Optical image captured with the digital camera of the probe station showing a Nanosys chip contacted with two RF probes (GSGSG type).

With the probe station, a specific 16-tips probe card have been used to test the circuits arranged in rows of 16-pads (Fig. 5.1.2a) and two RF probes (Cascade Infinity 126-102) to test the circuits arranged in two rows of 5-pads (Fig. 5.1.2b,c). The RF probes use a GSGSG configuration allowing the measurements of two signals that are shielded in order to operate up to 40 GHz. RF cables (Cascade 101-162-B) have been also used in most cases with SMA terminations.

- **MEASUREMENTS WITH A PCB (VACUUM CHAMBER)**

For a full functional characterization it is important to perform the test under different pressure conditions. To do that a specific home-made vacuum chamber[1] has been used (Fig. 5.1.3). In this case the chip is mounted on a PCB (printed circuit board) and the pads of the selected device of the chip are bounded directly onto the PCB. Fig. 5.1.3b shows a detail of the PCB that has been specifically designed to allow the direct bounding and address the signals with SMA connectors.

The vacuum chamber allows electrical measurements at different pressures by means of five RF electrical feedthroughs to external instrumentation (Fig. 5.1.3a). The chamber can operate at a vacuum level down to 10^{-3} mbar.

Fig. 5.1.4 shows a set-up for two-port measurement where the different instruments and connections are indicated. The frequency response (magnitude and phase) of the CMOS-MEMS is measured with the Network Analyzer. Before any electrical measurement of the S_{21} parameter, a through calibration is previously performed, in which the CMOS-MEMS device is replaced by a short and the Network Analyzer is baseline corrected against this measurement. The measurement data is acquired by a computer through GPIB.

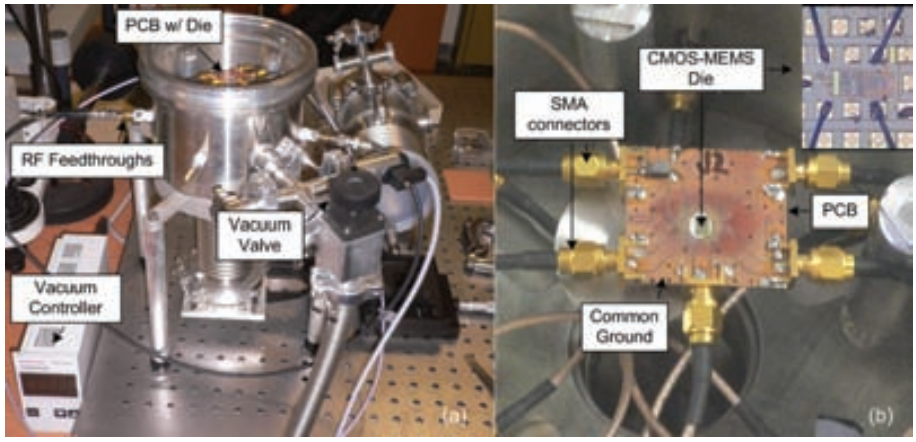

Figure 5.1.3 (a) Photograph of the custom-built vacuum chamber used to measure CMOS-MEMS devices under different pressures. (b) Photograph of the printed circuit board (PCB) used to electrically contact the die with wire-bonding.

[1] The vacuum chamber was custom built by Dr. F. Torres from ECAS group at UAB.

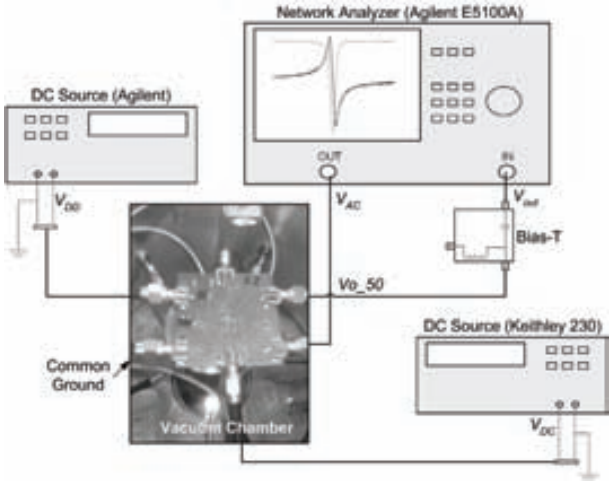

Figure 5.1.4 Test setup for two-port measurements using the vacuum chamber.

5.2 CNM25 DEVICES

The different CMOS readout circuits designed and fabricated with the CNM25 technology (Nanomass approach) in this thesis work and detailed in Chapter 3 have been monolithically integrated with different cantilever resonators fabricated during the Nanomass project. In addition, most of the results obtained (from electrical and functional characterization) with these monolithic CMOS-MEMS devices have been reported in three thesis works [Dav03, For05b, Vil05] as well as in several journals [Vil06, For05, Gha05, Ver05, For04, Dav03]. In this sense, in this section only a brief summary of the main results are presented allowing a comparison with the devices developed with the Nanosys approach (AMS-C35 devices).

5.2.1 CMOS CHARACTERISTICS

Some dispersion of the CMOS electrical parameters of the different devices fabricated using the CNM25 CMOS technology was appreciated. This dispersion was appreciated both between the chips of the same wafer as well as between the wafers fabricated in the different submitted runs. In this sense, several circuits were electrical characterized in order to obtain a minimum statistic of the CMOS performance.

Table 5.1 summarizes the results obtained from the measurements of the BS circuits performance. In particular the bandwidth and the DC-gain were measured for the different runs executed. The mean of the bandwidth value is more than 30% higher than the obtained from simulations and the mean of the DC-gain value is 17% lower than the obtained from simulations indicating the luck of accuracy in the model parameters of the CMOS elements. On the other hand, the standard deviation between the different runs is around 12% and 6% for the bandwidth and DC-gain parameters respectively.

In the case of the TIA circuits, the measured bandwidth is lower than the simulated. The standard deviation of the gain value for circuits on the same wafer was found to be around 10% of its nominal value (Table 5.2). On the other hand, this value was found to be still higher for circuits on different wafers (around 25 %).

Table 5.1 Summary of the mean values of the bandwidth and the gain of the BS circuit obtained in the different RUNs fabricated in the Nanomass project.

Parameter	Simulated	RUN 1995	RUN2000	RUN2380	Mean (μ)	Std. Dev. (σ)
Bandwidth (MHz)	1.51	1.75	1.9	2.2	1.95	0.23 (11.8%)
Gain (DC)	7.6	6.2	6.7	6	6.3	0.36 (5.7%)

Table 5.2 Summary of the mean values of the bandwidth and the gain of the TIA circuit obtained for different wafers of the RUN 2380 fabricated in the Nanomass project.

Parameter		Simulated	Wafer5	Wafer6	Wafer8
Bandwidth (kHz)	Mean (μ)	1180	986	925	941
	Std. Dev. (σ)	--	15 (1.5%)	79 (8.5%)	24 (2.6%)
Gain, (a.u.)	Mean (μ)	95	80.1	80	102
	Std. Dev. (σ)	--	8.1 (10%)	7.4 (9.3%)	12 (11.8%)

5.2.2 CMOS-MEMS PERFORMANCE

As reported in Chapter 3, the fabrication of the CMOS-MEMS with the Nanomass approach is complex resulting in a low yield (< 5%) of the devices. Despite of that, several devices have been characterized, both electrical and functional, with success.

An optical image of a monolithic CMOS-MEMS device fabricated with the CNM25 technology is presented in Figure 5.2.1. The cantilever resonator was fabricated using DWL on aluminum and the integrated readout circuit is the BS circuit.

Figure 5.2.2 shows the first electrical characterization results obtained from a monolithic CMOS-MEMS device in the Nanomass framework [Ver05]. A resonance frequency of 645 kHz and a quality factor of Q≈21 were measured for a DC-bias voltage of 20 V. In this case the magnitude of the frequency response was measured with an oscilloscope. The spring softening effect was also observed with this device deducing a natural resonance frequency of 703 kHz. The theoretical mass sensitivity of the cantilever was found to be 34 ag/Hz.

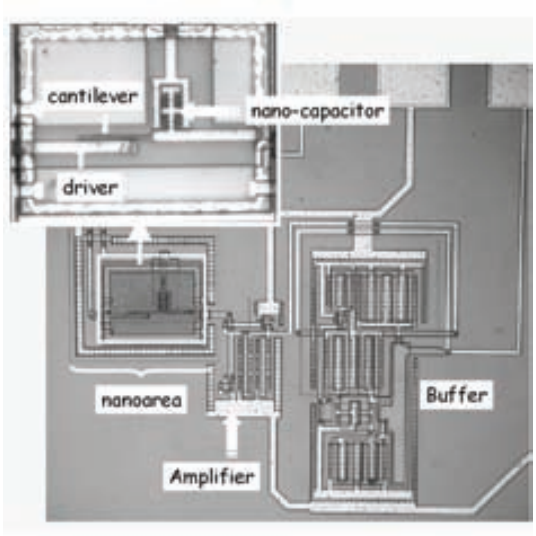

Figure 5.2.1 Optical image of the CNM25 polysilicon CMOS-MEMS device. Inset: zoom image of the "nanoarea" with the cantilever resonator fabricated using in this case DWL. Cantilever dimensions are: l=40 μm, w=840 nm and t=600 nm).

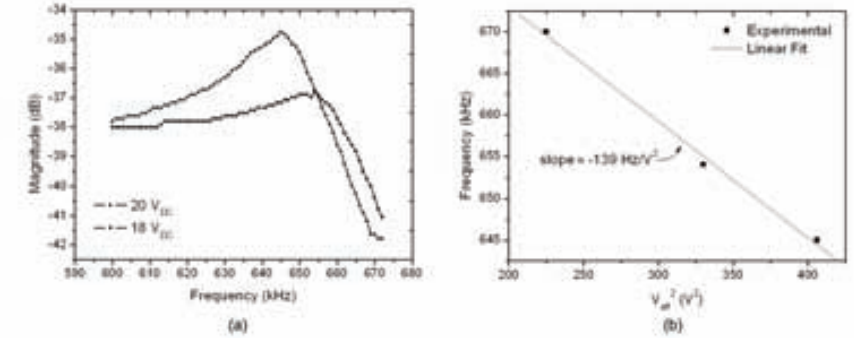

Figure 5.2.2 Electrical characterization of the CNM25 polysilicon CMOS-MEMS resonator: (a) frequency response and (b) dependence of the resonance frequency versus the applied bias voltage.

5.2.3 SUMMARY OF THE CNM25 DEVICES

In addition to the results presented in the previous section, different CMOS-MEMS cantilever resonators were fabricated using the Nanomass approach (see Chapter 3) with success. Table 5.3 summarizes the main parameters of these CMOS-MEMS devices indicating the nanofabrication technique used to fabricate the cantilever resonator as well as the reference.

In [For05] a 1.49-MHz polysilicon cantilever with dimensions of 20μm×0.42μm was fabricated using EBL combined with DWL. A mass sensitivity of 4 ag/Hz was determined in air by placing a single glycerine drop having a measured weight of 57 fg. The readout circuit used is the same that in Figure 5.2.1, a BS circuit with capacitive polarization. A quality factor of 70 and 5000 were measured in air and vacuum conditions respectively. Finally, the frequency noise of these devices was found to be 100 Hz/√Hz and 0.46 Hz/√Hz in air and vacuum respectively.

In [Vil06] different arrays of four and eight resonant polysilicon cantilevers, with and without multiplexing circuitry, were fabricated using UVL on pre-processed CNM25 CMOS devices. The electrical readout is performed by means of TIA circuits. In particular, a cantilever with dimensions of 50μm×1.1μm was electrically characterized presenting a resonance frequency of 520 kHz and a theoretical mass sensitivity of 36 ag/Hz. The measured quality factor in vacuum conditions was of 1380 and the frequency noise of 6.4Hz/√Hz.

Finally, in [Vil07] time-resolved evaporation rate of attoliter glycerine drops was reported on a 23μm×1.3μm cantilever with a 7.9 ag/Hz mass sensitivity. In this case the cantilever resonator was fabricated on crystalline silicon, using silicon-on-insulator (SOI) substrates for the integration of the CMOS-MEMS. The resonance frequency of 2.76 MHz was readout using a BS circuit with diode of polarization. The measurements were performed in air conditions and a frequency noise of 141 Hz/√Hz was estimated.

Table 5.3 Summary of the main parameters of the measured frequency response of the CNM25 devices.

	Parameter	**Cantilever**			
	Fabrication process [Reference]	Poly_DWL [Ver05]	Poly_DWL+EBL [For05]	Poly_UVL [Vil06]	SOI_UV [Vil07]
	Dimensions (l×w×t) μm	40×0.84×0.6	20×0.42×0.6	50×1.1×0.6	23×1.3×0.65
	Circuit	BS	BS	TIA	BS_D
	Resonance frequency	701 kHz	1.49 MHz	520 kHz	2.76 MHz
	Mass Sensitivity	34 ag/Hz	4 ag/Hz	36 ag/Hz	7.9 ag/Hz
Air	Quality factor, Q	21	70	---	---
Air	Frequency noise, δf	---	100 Hz/√Hz	---	141 Hz/√Hz
Air	Peak Height	~ 3 dB	~ 0 dB	~ 0.5 dB	~ 0.5 dB
Air	Phase Shift, $\Delta\phi$	---	~ 25º	~ 10º	~ 22º
Vacuum	Quality factor, Q	---	5000	1380	---
Vacuum	Frequency noise, δf		0.46 Hz/√Hz	6.4 Hz/√Hz	---
Vacuum	Peak Height	---	~ 10 dB	~ 0 dB	---
Vacuum	Phase Shift, $\Delta\phi$	---	~ 5º	~ 100º	---

In general the measured frequency characteristics of the CNM25 devices present a low resonance peak and phase shift as reported in Table 5.3. This result indicates that the electrostatic transduction is not quite optimal due to the magnitude of the parasitic current is relatively high.

Figure 5.2.3 plots the theoretical mass resolution of the most relevant CMOS-MEMS mass sensors fabricated in the Nanomass approach. The values have been obtained from the experimental measurements of the frequency noise and the mass sensitivities indicated in Table 5.3.

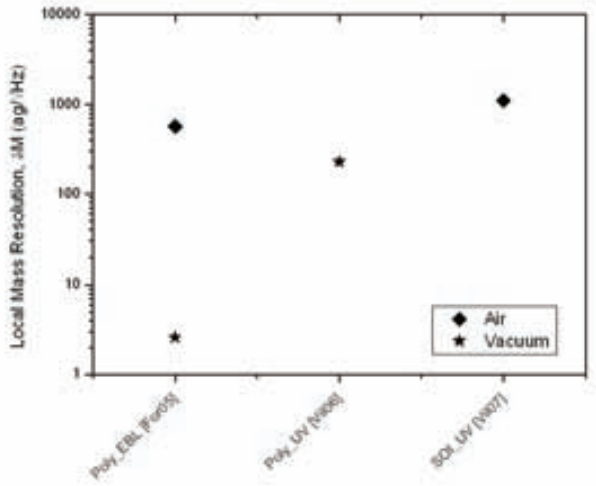

Figure 5.2.3 Local mass resolution of the CNM25 devices obtained in air and vacuum conditions.

5.3 AMS-C35 DEVICES

In this section, the characterization of the monolithic CMOS-MEMS devices designed with the AMS-C35 technology is presented. The fabricated devices have been post-processed following the technique presented in Chapter 3.

The devices are constituted by the MEMS resonator in a 2-port configuration monolithically integrated with the UGBCA50 readout circuit described in Chapter 4 (see Fig. 5.3.1.). Fig. 5.3.2 shows the photograph of a fabricated device, in this case a metal cantilever resonator, indicating the use of every pad. It is important to note that for this configuration, the effective DC-bias voltage applied to the resonator is not corresponding with the voltage V_{DC} since the DC component present at node V_{in} (~ 2V, see Chapter 4). In this case, the effective DC-bias voltage becomes $V_{eff}=V_{DC}-2$ V. In this section, V_{DC} indicates the voltage applied at the bias electrode while V_{eff} is the effective bias voltage of the resonator. On the other hand, the V_{AC} voltage does not contributes on the effective bias voltage since the use of a 2-port configuration.

The different resonators that have been characterized are depicted in Fig. 5.3.3. In particular, two metal resonators (cantilever and CC-beam) and two polysilicon resonators (cantilever and CC-

beam). As explained in Chapter 3, the metal structures have been fabricated using the top metal layer of the technology. On the other hand, the polysilicon structures have been fabricated using the Poly1 layer with the exception of the electrodes of the CC-beam resonator that have been implemented with the Poly2 layer. The designed parameters and theoretical characteristics of these four resonators were presented in Table 3.1.

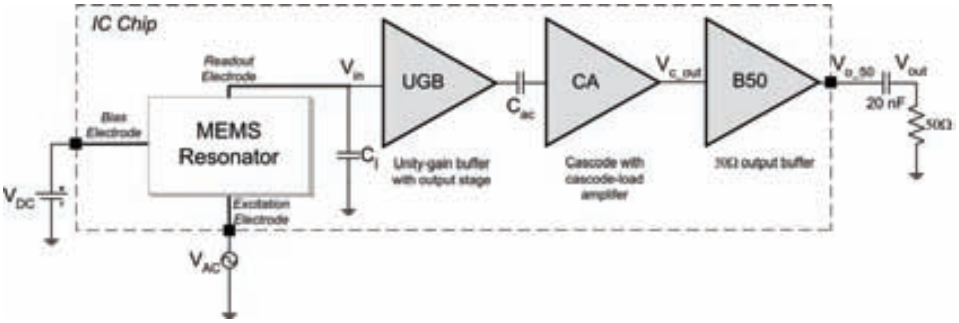

Figure 5.3.1 Electrical schem of the mixed CMOS-MEMS devices fabricated in AMS-C35 technology.

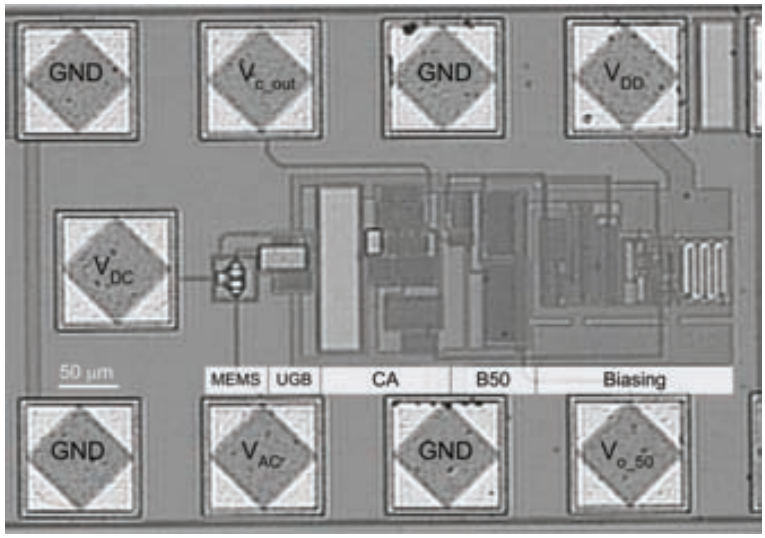

Figure 5.3.2 Photograph of a fabricated CMOS-MEMS in AMS-C35 technology.

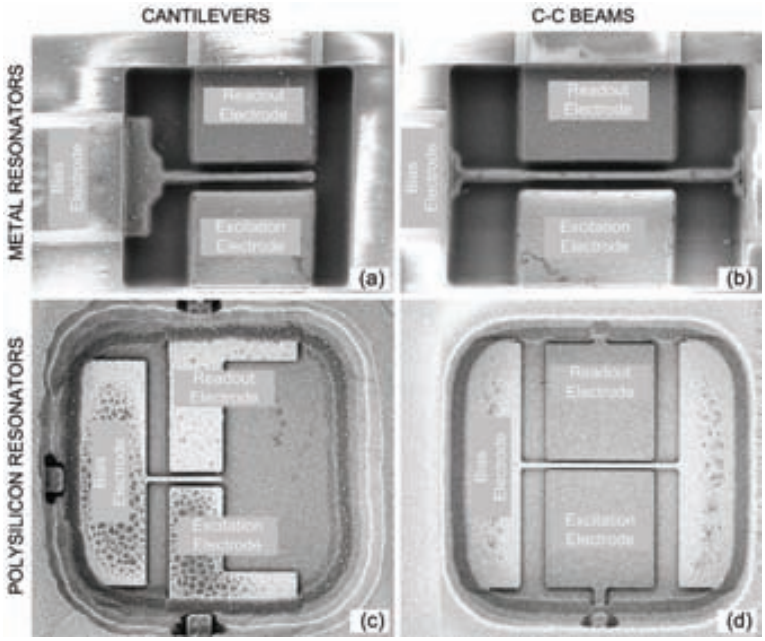

Figure 5.3.3 SEM images of the MEMS resonators fabricated in AMS-C35 technology.

5.3.1 ELECTRICAL CHARACTERIZATION

In this section, the experimental results related with the electrical characterization of the different CMOS-MEMS devices are presented. The fabricated devices were first tested using the probe station to corroborate the correct performance. All the experimental results reported in this section have been obtained inside the vacuum chamber with PCB support and under vacuum conditions or not as it will be indicated.

First, the measured output noise of the readout circuit (V_{o_50} node) is presented in Fig. 5.3.3 and compared with the simulation results. This measurement has been performed using the spectrum analyzer with V_{AC} = "gnd". The measured noise spectrum is in good agreement with the simulations and presents a power of around -108 dBm/Hz (@ 6 MHz) that it is equivalent to 0.9 $\mu V/Hz^{1/2}$ (Fig. 5.3.3). It is appreciated that the voltage noise decreases with the frequency since the circuit is operating past its bandwidth.

Each of the other electrical measurements presented in this section have been performed with the Network Analyzer using the setup of 5.1.4 with the aim of obtaining the frequency characteristic of the different CMOS-MEMS devices.

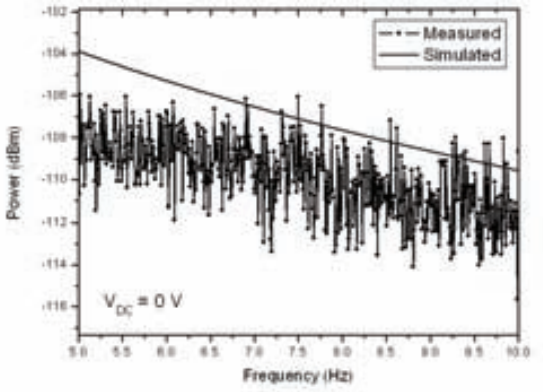

Figure 5.3.3 Comparative of the measured and simulated noise spectrum of the UGBCA50 readout circuit.

5.3.1.1 METAL CMOS-MEMS RESONATORS

- **METAL CANTILEVER**

Fig. 5.3.4 presents the measured frequency response, in magnitude and phase, for the metal cantilever resonator. The measurements have been performed in ambient conditions (room temperature and atmospheric pressure) using an excitation voltage of V_{AC} = -30 dBm (50Ω), and different resonator bias voltages (V_{DC}). It can be appreciated that the resonance peak is at a frequency of around 6 MHz and shift down when the bias voltage increases due to the spring-softening effect. Bias voltages up to 80V have been applied to the cantilever without the notice of any negative effect indicating the robustness of these devices. In any case, the anti-resonance (or parallel resonance) peak is also presents in the spectrum which indicates that, despite the use of a 2-port configuration, a parasitic coupling between the excitation and the readout nodes is still present (see Chapter 2).

The value of this parasitic coupling capacitance can be obtained from the background level (B_L) of the magnitude plot. When the resonator is not vibrating (V_{DC}=0), the magnitude value of the frequency response is due to the parasitic feedthrough current (I_p) associated with the parasitic capacitance C_p. In this sense, the value of C_p can be obtained as

$$C_p = \frac{10^{B_L/20}}{2\pi f G_T}, \tag{5.3.1}$$

where f is the frequency of measurement, and G_T is the equivalent transimpedance gain of the readout circuit (@ f) which value can be obtained from simulations.

The measured value of B_L from Fig. 5.3.4a is -11 dB at 6 MHz where the readout circuit presents an equivalent transimpedance gain of 58.7 MΩ (see Fig. 4.4.6). With these values, the parasitic capacitance is found to be C_p = 0.13 fF.

When using 1-port configuration, the background level of the transmission is determined by the direct coupling between the cantilever and the corresponding electrode (C_o, see Chapter 2). This coupling capacitance can be extracted from the layout using the CAD tools for design the integrated circuit. The extraction tool of the parasitic capacitances takes into account the dielectric (i.e. SiO_2) and the fringing field effects between two adjacent lines. In this sense, the value obtained, 1.4 fF, have to be divided by the SiO_2 relative dielectric constant (~ 3.9) in order to find a more realistic value for the released resonators. The value obtained is C_o = 0.36 fF which indicates that the use of a 2-port configuration in front of a 1-port configuration reduces, in this case, around three times the parasitic capacitance value (C_p/C_o = 2.8).

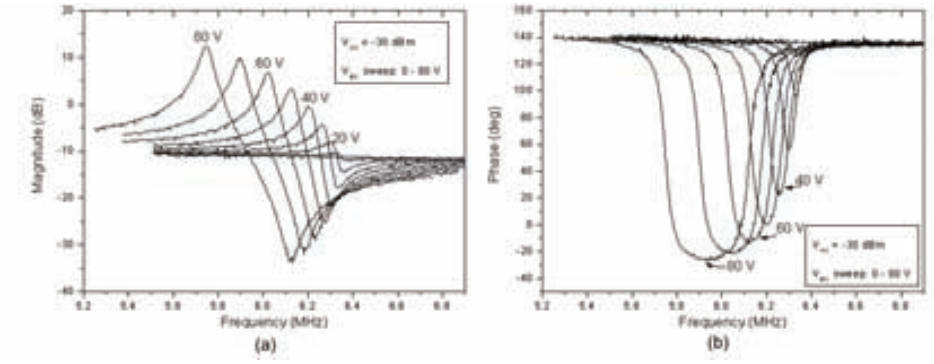

Figure 5.3.4 Frequency response (V_{out}/V_{AC}), magnitude (a) and phase (b), of the metal cantilever CMOS-MEMS resonator for different DC-bias voltages of the resonator measured in air conditions (room temperature and atmospheric pressure).

From the plots of Fig. 5.3.4 it can be also seen that the use of higher bias voltages results in a higher resonance peak coherent with the theory since the motional resistance decreases (Eq. 2.2.1). The high peaks together (up to 20dB) with the large phase shifts (up to 160º) measured indicate the optimal electrostatic transduction achieved with this metal cantilever resonator due to the motional current is much higher than the parasitic current.

For a specific bias voltage, the experimental value of the motional resistance (R_m) can be obtained from the measured frequency response using next relation (based on Eq. 2.2.4),

$$R_m = \frac{|G_T|}{\left|10^{I_L/20} - j10^{B_L/20}\right|}, \tag{5.3.2}$$

where I_L are the insertion loss of the system, that is, the magnitude of the transmission parameter at the resonance frequency. Using Eq. 5.3.2, an experimental value of R_m = 29.3 MΩ is obtained for a bias voltage of 60 V.

From the plots obtained at higher bias voltages, which presents a large phase shift, the Q-factor can be measured from the phase data or the magnitude data (Eq. 2.2.3) obtaining similar results. The Q-factor obtained for these metal cantilever measured in air conditions is around 108.

The dependence of resonance frequency on the DC bias V_{DC} has been systematically observed for the resonators tested in this thesis. Fig. 5.3.5 shows the linear dependence between the resonance frequency and the square of the effective driving voltage due to the spring-softening effect. The measured slope is -95 Hz/V^2 which is more than twice the theoretical value. Different factors may determine this fact (i.e. uncertainties regarding the resonator parameter), but the main one is the effect of the fringing fields that effectively increase the coupling capacitance value and consequently the effects of the driving voltage on the electrical spring constant are more remarkable.

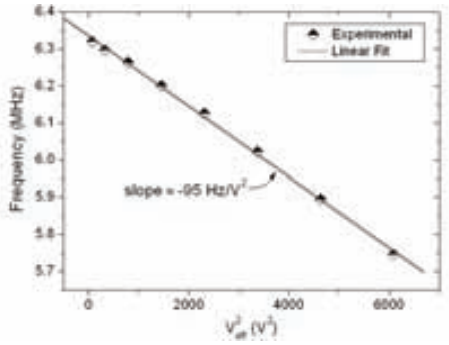

Figure 5.3.5 Plot of resonance frequency versus squared effective DC-bias voltage for the metal cantilever CMOS-MEMS resonator.

Figure 5.3.6a plots the frequency response of the device obtained at different pressures maintaining constant all the other parameters. It is appreciated that the peak height increases when reducing the pressure level due to the reduction of the air squeezing effect (higher Q-factor) and consequently the motional resistance decreases.

As explained in Chapter 2, for low bias voltages the frequency response is degraded and the measured quality factor (electrical quality factor) is lower than the intrinsic mechanical quality factor of the structure. This fact is observed in Figure 5.3.4 since with the same resonator the electrical performance is degraded (wider resonant peak and lower phase slope) at low bias voltages (i.e. less than 20V). In this sense, in order to analyze the performance of the intrinsic Q-factor at different pressures, the measurements have been performed using optimal biasing voltages for each pressure level so the phase shift was at least 140º. The dependence of the Q-factor versus the pressure is presented in Fig. 5.3.6b. It is appreciated that the Q-factor is enhanced by around one order of magnitude when operating in vacuum. In any case, it is observed that below 1 mbar the plot saturates (Q_{max} ~ 880) indicating that at lower pressures the quality factor is not longer dominated by viscous damping but by intrinsic mechanisms due to the material or device (i.e. anchors losses, roughness, defects, etc.).

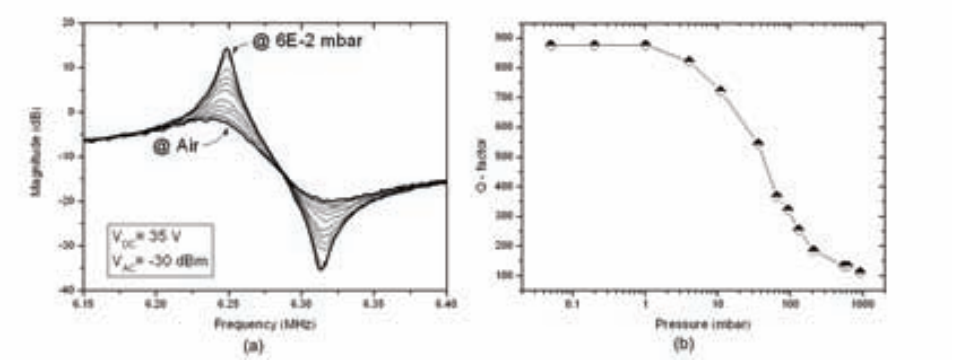

Figure 5.3.6 (a) Measured frequency response (V_{out}/V_{AC}) of the metal cantilever CMOS-MEMS resonator at different pressure conditions. (b) Plot of the Q-factor versus pressure measured at room temperature.

Accurate electrical characterizations in air and vacuum conditions have been performed in order to experimentally determine the minimum detectable shift of the resonance frequency.

Figure 5.3.7 shows the magnitude and phase of the frequency response obtained in air conditions with V_{DC}=60 V and V_{AC} = −20 dBm. A zero-span acquisition at the resonance frequency of the phase measurements has been performed. The root mean squared value of the phase data gives an equivalent phase noise of $\delta\phi$=0.05° in a readout bandwidth of 50 Hz (inset of Fig. 5.3.7).

From the slope of the phase at the resonance frequency, we obtain the minimal frequency shift we can measure, assuming a unity signal-to-noise ratio of δf=33 Hz (in a readout bandwidth of 50 Hz) corresponding with a frequency noise spectral density in this conditions of δf=4.7 Hz/√Hz.

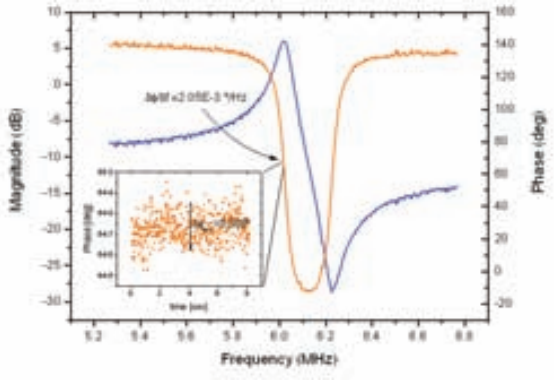

Figure 5.3.7 Frequency response (V_{out}/V_{AC}) of the cantilever CMOS-MEMS resonator measured in air conditions with V_{DC} = 60 V and V_{AC} = -20 dBm. Inset: signal phase fluctuations measured in a 50 Hz bandwidth.

The same measurement and analysis have been performed at vacuum conditions (0.1 mbar) with V_{DC}=20 V and V_{AC} = −20 dBm. In this case the phase noise is found to be $\delta\phi$=0.18° which is

higher than in air conditions (higher Q). In any case, due to the phase slope is higher in these conditions, the final frequency noise spectral density obtained in this case is lower than in air (δf=1.6 Hz/√Hz).

In vacuum conditions, an experimental value of R_m = 34.9 MΩ is obtained, using Eq. 5.3.2, for a bias voltage of 20 V. This value is similar than the obtained in air conditions but using in this case a three times lower bias voltage.

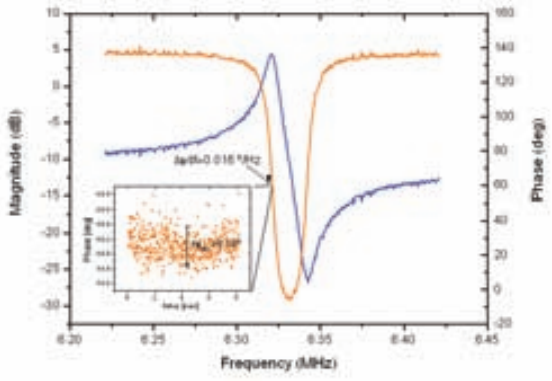

Figure 5.3.8 Frequency response (V_{out}/V_{AC}) of the metal cantilever CMOS-MEMS resonator measured at 0.1 mbar vacuum pressure with V_{DC} = 20 V and V_{AC} = -20 dBm. Inset: signal phase fluctuations measured in a 50 Hz bandwidth.

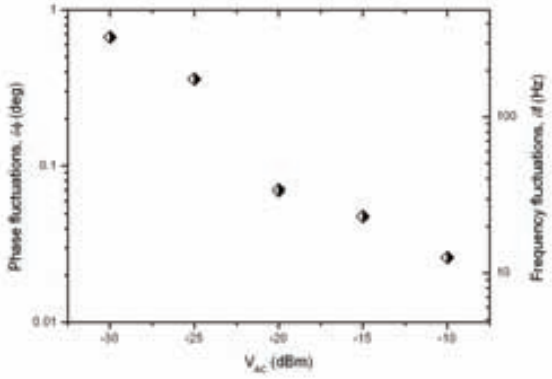

Figure 5.3.9 Measured short-term phase and frequency fluctuations of the metal cantilever CMOS-MEMS resonator for different excitation-voltage amplitudes (V_{AC}) in a 50 Hz bandwidth.

As indicates Eq. 2.3.7, the frequency noise depends inversely on the signal-to-noise ratio of the measurement. The use of higher excitation voltages V_{AC} produces the resonator to oscillate at higher amplitudes (see Eq. 2.1.46) and consequently the CMOS-MEMS generates a higher output signal. In this sense, it is expected that the use of a higher excitation voltage V_{AC} reduces the frequency noise. In order to corroborate this assumption, different measurements of the frequency noise have been performed at different excitation voltages. The results are presented in Fig. 5.3.9 corroborating this hypothesis and giving more information on how the performance of these devices can be improved. In any case, this analysis is limited to cantilever oscillation amplitudes not exceeding the linear regime.

- **METAL CC-BEAM**

Figure 5.3.10 presents the measured frequency response, in magnitude and phase, for the metal CC-beam resonator. The measurements have been performed in ambient conditions using an excitation voltage of V_{AC} = -30 dBm (50Ω), and different resonator bias voltages (V_{DC}). In this case the V_{DC} sweep has been performed from 10 to 100 V. In this case the resonance peak is located between 13.6 – 13.9 MHz depending on the bias voltage.

In addition, it is appreciated a small peak both in the magnitude and phase plots located at around 14.7 MHz. The lateral electrostatic force applied to the resonator, which is an asymmetric structure (i.e. two layers), causes in addition to the logical lateral force component, a vertical force component that excites the vertical mode of vibration of the resonator. A vertical oscillation of the resonator is also translated into a variation on the coupling capacitance C_o that is detected by the readout circuit. In any case, this capacitance variation is much smaller than for the lateral mode resulting in a small resonance peak in the system frequency response. This effect have been also observed and reported [Ura07] for 1-driver metal cantilever resonators fabricated during this thesis.

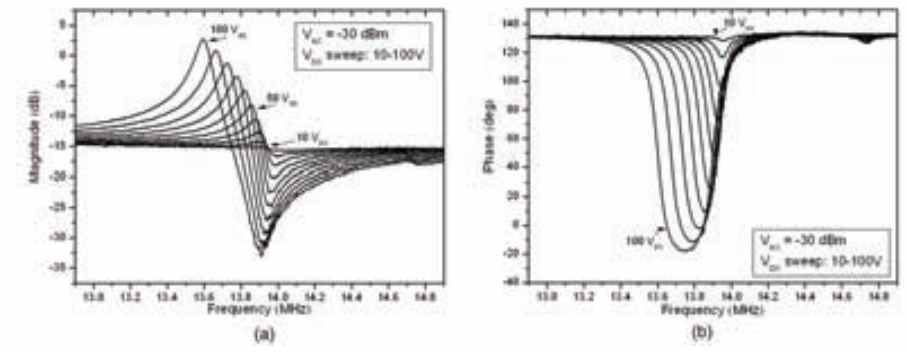

Figure 5.3.10 Frequency response (V_{out}/V_{AC}), magnitude (a) and phase (b), of the metal CC-beam CMOS-MEMS resonator for different DC-bias voltages of the resonator measured in air conditions (room temperature and atmospheric pressure).

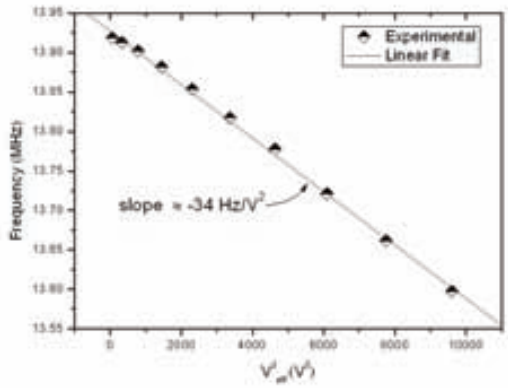

Figure 5.3.11 Plot of resonance frequency versus squared effective DC-bias voltage for the metal CC-beam CMOS-MEMS resonator.

From the measurements we obtain a dependence of the resonant frequency with the effective bias voltage of -34 Hz/V^2 (Fig. 5.3.11) which is lower than in the metal cantilever resonator. Despite the coupling capacitance of this CC-beam resonator is similar or even higher than the cantilever resonator; the spring constant is also higher resulting in a lower spring-softening effect (see Table 5.4).

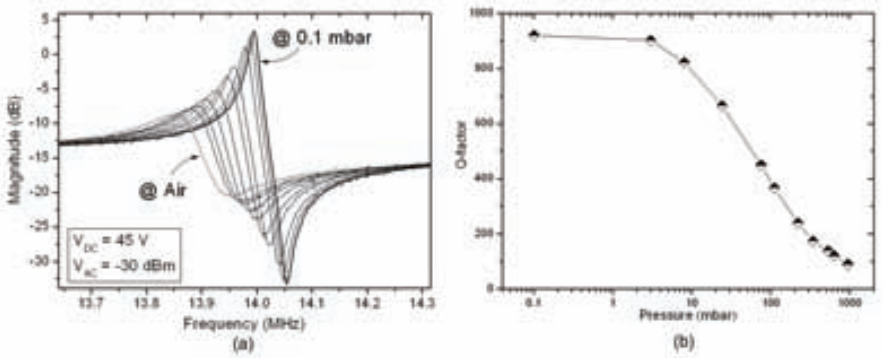

Figure 5.3.12 (a) Measured frequency response (V_{out}/V_{AC}) of metal CC-beam CMOS-MEMS resonator at different pressure conditions. (b) Plot of the Q-factor versus pressure measured at room temperature.

Figure 5.3.12a plots the frequency response of the device obtained at different pressures for the same biasing conditions. As the Q-factor decreases, since the operation at a higher pressure, the resonance frequency shifts to smaller values coherent with Eq. 2.1.24.

The quality factors measured with optimal biasing are similar than for the cantilever resonator. In particular a Q = 156 in ambient pressure and Q = 918 in vacuum have been measured. The saturation pressure is also produced at around 1 mbar (Fig. 5.3.12b).

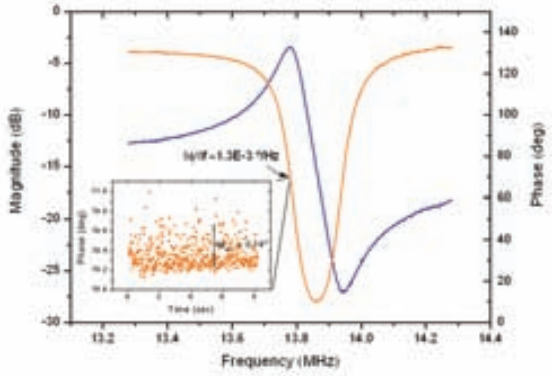

Figure 5.3.13 Frequency response (V_{out}/V_{AC}) of the metal CC-beam CMOS-MEMS resonator measured in air conditions with V_{DC} = 70 V and V_{AC} = -20 dBm. Inset: signal phase fluctuations measured in a 50 Hz bandwidth.

The frequency noise of this device has been also measured following the same analysis than for the metal cantilever. The results obtained, both in air and vacuum conditions, are around three times worse than for the metal cantilever. Figure 5.3.13 shows the measurements performed in air conditions with V_{DC}=70 V and V_{AC} = −20 dBm. In this case the phase noise is found to be $\delta\phi$=0.14° in a 50 Hz bandwidth that is corresponding with a frequency noise spectral density of δf=15.3 Hz/√Hz.

Although the insertion loss of the metal CC-beam is higher (I_L = 3.47 dB, Fig. 5.3.13) than the obtained for the cantilever (I_L = -4.39dB, Fig. 5.3.7), the motional resistance is found to be lower R_m = 15.4 MΩ. This results is due to the resonator is working at a higher frequency and the readout circuit exhibits a lower transimpedance gain (see Eq. 5.3.2). For more details on the other experimental and design values of this resonator see Table 5.4.

5.3.1.2 POLYSILICON CMOS-MEMS RESONATORS

As indicated in Table 3.1, the polysilicon resonators fabricated in the AMS-C35 technology are at least one order of magnitude superior to the metal resonators from the point of view of mass sensitivity. These resonators have been also characterized in order to compare their electrical performance in front of the metal resonators and the results are reported in this section.

- **POLYSILICON CANTILEVER**

Figure 5.3.14 presents the measured frequency response in ambient conditions, magnitude and phase, near the resonance for different DC-bias voltages applied to the polysilicon cantilever resonator which resonance frequency is ~ 11 MHz. The frequency response presents a large peak height (~20 dB) as well as a large phase shift (~160º) for the maximum applied bias voltage (V_{DC}=45 V). These results indicate, as in the case of the metal resonators, the optimal electrostatic transduction achieved with this polysilicon cantilever resonator.

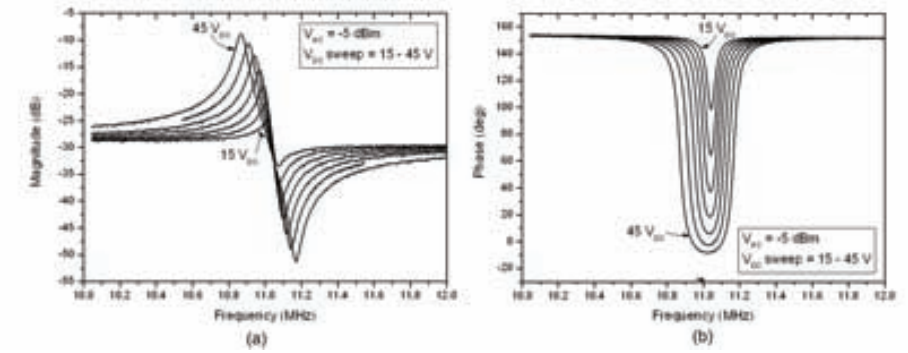

Figure 5.3.14 Frequency response (V_{out}/V_{AC}), magnitude (a) and phase (b), of the polysilicon cantilever CMOS-MEMS resonator for different DC-bias voltages of the resonator measured in air conditions (room temperature and atmospheric pressure).

The measured dependence of the resonant frequency with the effective bias voltage is shown in Figure 5.3.15. The slope found in this case is -88 Hz/V^2 which is similar than the obtained for the metal cantilever resonator. In this case, the experimental value is also similar to the theoretical one (-78 Hz/V^2) unlike in the metal cantilever. This is, as a first approximation, due to the ratio between the gap and the thickness of the structure (s/t) is higher for the polysilicon cantilever causing the fringing field effect to be lower.

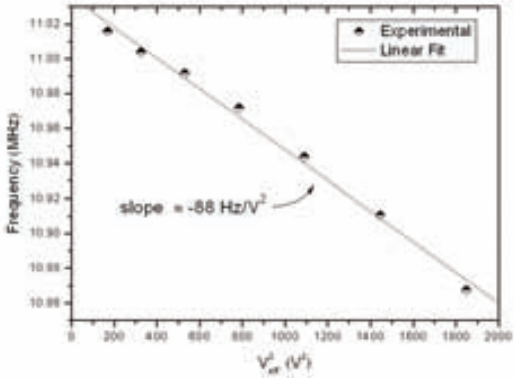

Figure 5.3.15 Plot of resonance frequency versus squared effective DC-bias voltage for the polysilicon cantilever CMOS-MEMS resonator.

Figure 5.3.16 plots the frequency response (magnitude and phase) of the device obtained at different pressures for the same biasing voltages (V_{DC} = 12V). The effect of the pressure level on the change of the resonance frequency, related with the change of the Q-factor, can be observed.

In ambient conditions, with V_{DC}=70 V and V_{AC} = −10 dBm (Fig. 5.3.17), the quality factor measured is Q = 205 which value is twice than the obtained for the metal cantilever. The motional resistance measured with that conditions is R_m = 33.7 MΩ and the phase noise is found to be

$\delta\phi$=0.053° in a 50 Hz bandwidth that is corresponding with a frequency noise spectral density of δf=3.5 Hz/√Hz.

On the other hand, in vacuum conditions with V_{DC}=12 V and V_{AC} = −10 dBm (Fig. 5.3.18), the quality factor measured is Q = 3536 which value is in this case four times higher than the obtained for the metal cantilever. The motional resistance measured with that conditions is R_m = 29 MΩ and the phase noise is found to be $\delta\phi$=0.1261 in a 50 Hz bandwidth that is corresponding with a frequency noise spectral density of δf=0.5 Hz/√Hz.

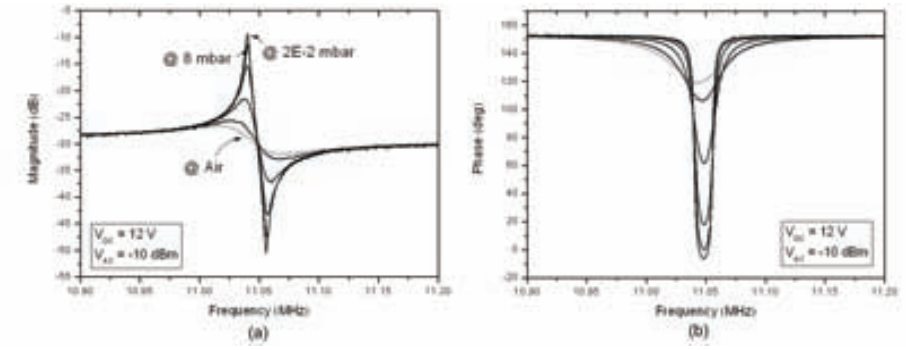

Figure 5.3.16 Measured frequency response (V_{out}/V_{AC}) of the polysilicon cantilever CMOS-MEMS resonator at different pressure conditions.

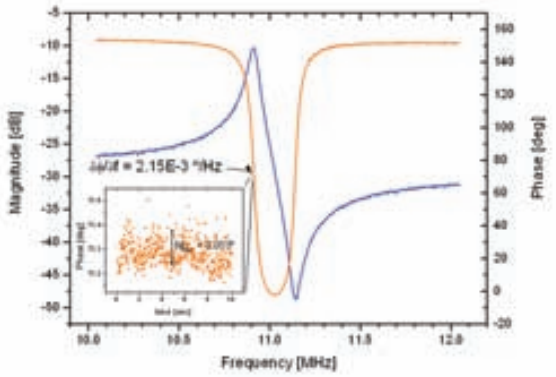

Figure 5.3.17 Frequency response (V_{out}/V_{AC}) of the polysilicon cantilever CMOS-MEMS measured in air conditions with V_{DC} = 40 V and V_{AC} = -10 dBm. Inset: signal phase fluctuations measured in a 50 Hz bandwidth.

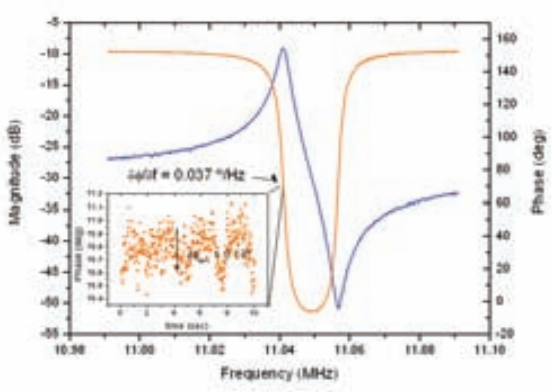

Figure 5.3.18 Frequency response (V_{out}/V_{AC}) of the polysilicon cantilever CMOS-MEMS measured at 0.1 mbar vacuum pressure with V_{DC} = 12 V and V_{AC} = -10 dBm. Inset: signal phase fluctuations measured in a 50 Hz bandwidth.

- **POLYSILICON CC-BEAM**

The resonance frequency of this device is the highest of the four AMS-C35 resonators and it has been measured to be 22 MHz with V_{DC}=12 V in air conditions. This value is 20% higher than the theoretic value. In addition to the already commented uncertainties in the resonator parameters, a reasonable cause of this fact is the residual fabrication stress that may experiment doubly clamped devices and that has not been considered in the theoretic analysis. In fact, this effect is not appreciated in the case of CC-beam metal resonators where the bi-layer structural characteristics of the device may reduce the stress effects.

Figure 5.3.19 presents the measured frequency response in air conditions, magnitude and phase, near the resonance for different DC-bias voltages. In this case an optimal electrostatic transduction is achieved at much lower bias voltages. With only V_{DC}=14 V a large peak height of ~ 20 dB as well as a large phase shift of ~ 160º is achieved.

The measured dependence of the resonant frequency with the effective bias voltage is shown in Figure 5.3.15. The slope found in this case is much higher than in the previous resonators (-3600 Hz/V^2). The much smaller gap between the resonator and the electrodes that present this device (s=150 nm) since the use of the Poly1-Poly2 fabrication approach (see Chapter 3) is translated into a high spring softening effect. In this case, the experimental value obtained is again much higher than theoretical one (-1570 Hz/V^2). This is due to the ratio between the gap and the thickness of the structure (s/t) is smaller than for the polysilicon cantilever causing the fringing field effect to be higher.

Figure 5.3.21 plots the frequency response (magnitude and phase) of the device obtained at different pressures for the same biasing voltages (V_{DC} = 5V).

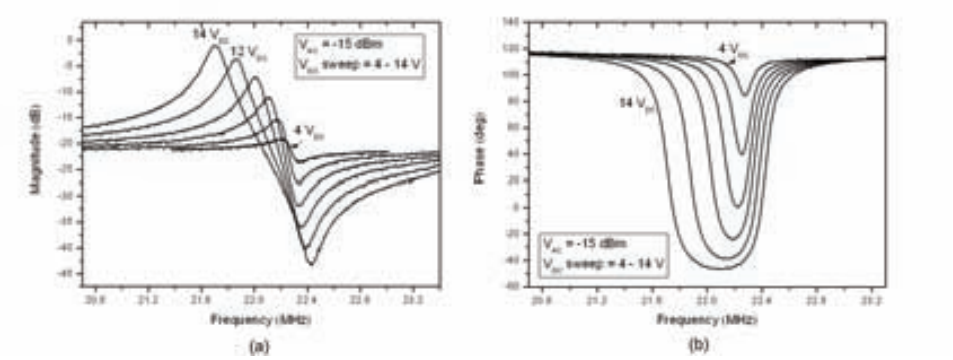

Figure 5.3.19 Frequency response (V_{out}/V_{AC}), magnitude (a) and phase (b), of the polysilicon cantilever CMOS-MEMS resonator for different DC-bias voltages of the resonator measured in air conditions (room temperature and atmospheric pressure).

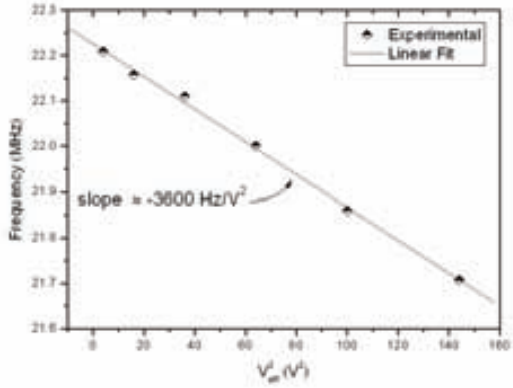

Figure 5.3.20 Plot of resonance frequency versus squared effective DC-bias voltage for the polysilicon CC-beam CMOS-MEMS resonator.

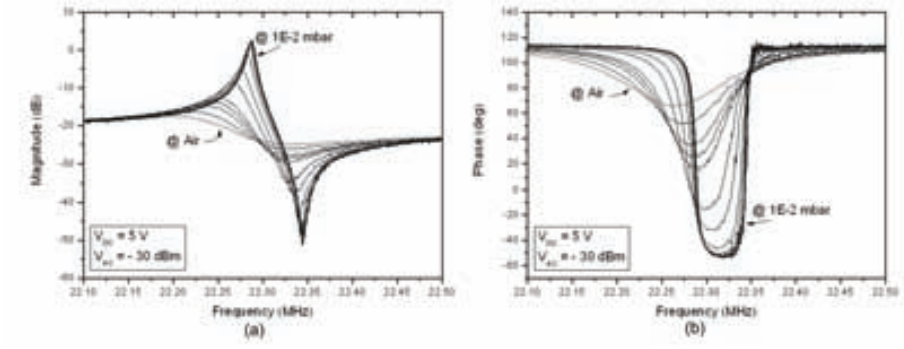

Figure 5.3.21 Measured frequency response (V_{out}/V_{AC}) of the polysilicon CC-beam CMOS-MEMS resonator at different pressure conditions.

In vacuum conditions, the bias voltage needed for a good electrostatic transduction is still lower than for the polysilicon resonator. In particular, Figure 5.3.22 shows the frequency response at vacuum that presents a large peak height (<10 dB) as well as a large phase shift (~ 120º) for a DC-bias voltage as low as V_{DC} = 3V. This result indicates that is fully feasible the operation of this resonator with a single voltage source for biasing both the resonator and the CMOS (V_{DD}=3.3V). It is important to remark that the available source power is not any impediment since there is not DC power consumption from capacitive MEMS resonators.

In ambient conditions, with V_{DC}=12 V and V_{AC} = −15 dBm (Fig. 5.3.23), the quality factor measured is Q = 165 which is slightly lower than the obtained for the polysilicon cantilever. The motional resistance measured with that conditions is as low as R_m = 3.6 MΩ and the frequency noise spectral density is δf=29.5 Hz/√Hz.

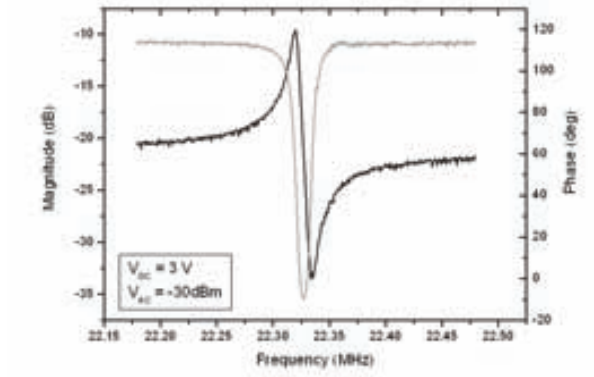

Figure 5.3.22 Frequency response (V_{out}/V_{AC}) of the polysilicon CC-beam CMOS-MEMS resonator measured at 0.1 mbar vacuum pressure with V_{DC} = 3 V and V_{AC} = -30 dBm.

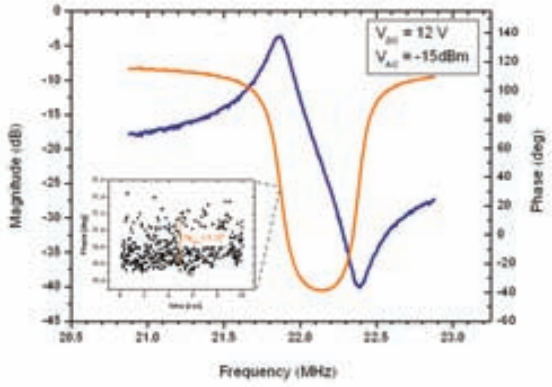

Figure 5.3.23 Frequency response (V_{out}/V_{AC}) of the polysilicon CC-beam CMOS-MEMS resonator measured in air conditions with V_{DC} = 12 V and V_{AC} = -15 dBm. Inset: signal phase fluctuations measured in a 50 Hz bandwidth.

In vacuum conditions with V_{DC}=4 V and V_{AC} = −30 dBm (Fig. 5.3.24), the quality factor measured is Q = 2600 which value is also slightly lower than the obtained for the polysilicon cantilever. Finally, the motional resistance measured with that conditions is R_m = 3.3 MΩ and the frequency noise spectral density is δf=2.8 Hz/√Hz.

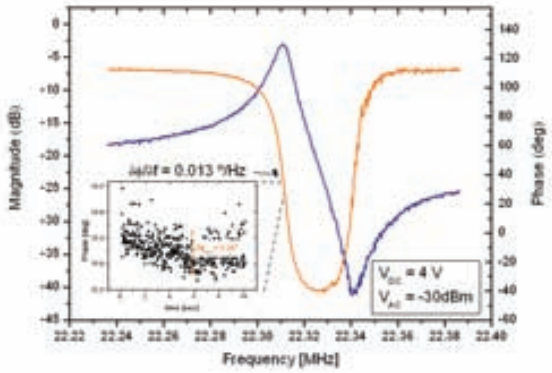

Figure 5.3.24 Frequency response (V_{out}/V_{AC}) of the polysilicon CC-beam CMOS-MEMS resonator measured at 0.1 mbar with V_{DC} = 4 V and V_{AC} = -30 dBm. Inset: signal phase fluctuations measured in a 50 Hz bandwidth.

5.3.2 NONLINEARITIES

As commented in Chapter 2, micromechanical resonators may present nonlinear performance for example the Duffing effect characterized by the frequency shift in the resonance peak from the linear resonance frequency when the vibration amplitude is too high [Lan99, Ran04]. In this section, Duffing effects on both the metal cantilever resonator and the polysilicon CC-beam resonator are reported.

- **CANTILEVER RESONATOR**

The nonlinear performance of the cantilever resonator has been observed at high excitation voltage amplitudes. In order to non saturate the CMOS readout circuit, the accessible node V_{c_out} was load with an external capacitor in order to reduce the bandwidth of the circuit and consequently the voltage gain at the operating frequencies.

Figure 5.3.25 shows the frequency response of the device measured in air condition for different excitation voltages with V_{DC}=50 V. It is appreciated that for relative high excitation voltages (V_{AC} > 0 dBm), the resonance curves bend towards lower frequencies. This spring-softening effect is due to the nonlinearity in the capacitive transducer.

At large oscillation amplitude levels of the cantilever, the frequency characteristics become hysteretic. In Figure 5.3.26 the frequency response of the device is presented for a V_{AC}=16 dBm by sweeping the frequency up and down.

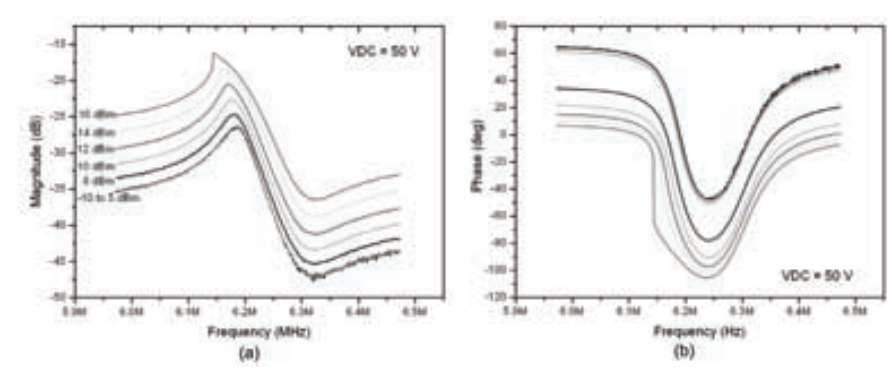

Figure 5.3.25 Frequency response (magnitude (a) and phase (b)) of the metal cantilever CMOS-MEMS resonator measured for different excitation-voltage amplitudes in air conditions with frequency swept upward.

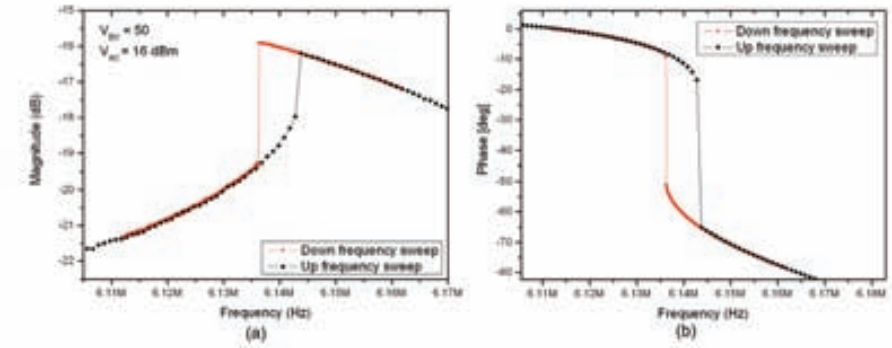

Figure 5.3.26 Hysteresis caused by the nonlinear bistable response of the cantilever resonator under strong driving (V_{AC}=16 dBm).

- **CC-BEAM RESONATOR**

For the polysilicon CC-beam resonator, the nonlinear performance has been observed at low excitation voltage amplitudes. The reason is due to the small gap between the resonator and the driver electrode that allows inducing high oscillation amplitudes with low excitation signals. In this sense, a reduction of the CMOS circuit bandwidth has not been necessary.

Figure 5.3.27 shows the frequency response of the device measured in air condition for different excitation voltages with V_{DC}=5 V. It is appreciated that for excitation voltages higher than -30 dBm, the resonance curves bend towards higher frequencies. In this case, the observed spring-hardening effect is due to the cubic nonlinearity of the spring coefficient of the CC-beam resonator.

The frequency hysteretic characteristic has been also observed. In Figure 5.3.28 the frequency response of the device is presented by sweeping the frequency up and down.

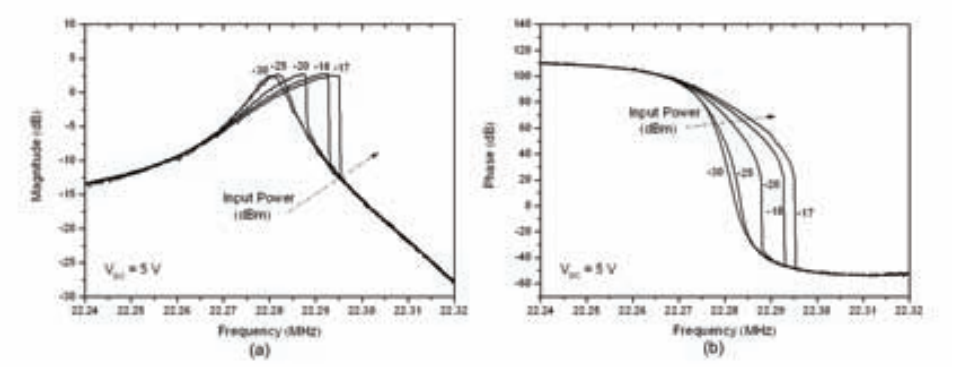

Figure 5.3.27 Frequency response (magnitude (a) and phase (b)) of the polysilicon CC-beam CMOS-MEMS resonator measured in air conditions with frequency swept upward.

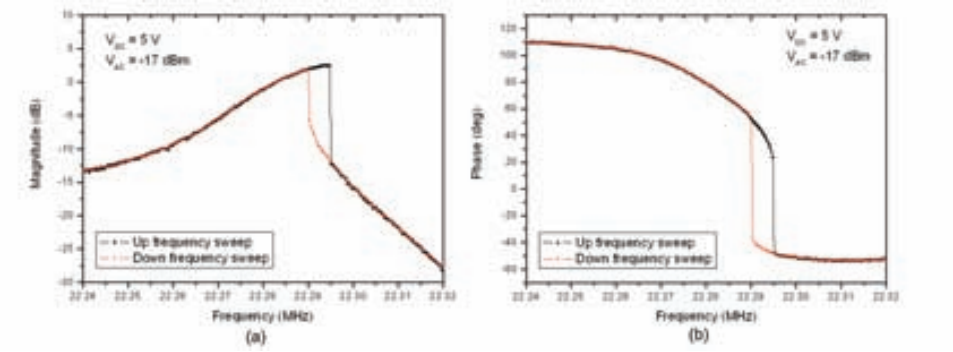

Figure 5.3.28 Hysteresis caused by the nonlinear bistable response of the polysilicon CC-beam resonator under V_{AC}=-17 dBm.

These results demonstrate the ability of the electrostatic transduction scheme used in this thesis to operate with sub-micrometer scale beams into the non-linear regime. Some works have demonstrated that the operation in this non-linear regime can further enhance the performance of MEMS systems. In particular, the presence of cubic mechanical and electrostatic nonlinearity in addition with the use of parametric amplification can be used to improve the mass change detection [Zha02]. Buks and Yurke [Buk06] have recently demonstrated that in the nonlinear region the system acts as a phase-sensitive mechanical amplifier and the mass resolution of the resonator may exceed the upper bound imposed by thermomechanical noise.

5.3.3 THERMOMECHANICAL NOISE

As we pointed out in Chapter 2, the mechanical resonator has associated a thermomechanical noise (for T>0 K) corresponding with an intrinsic motion of the resonator without any external excitation (e.g. electrostatic excitation). This noise is related with the resonator mechanical

dissipation that is conveniently described by its equivalent motional resistance R_m. In this sense, the thermomechanical noise voltage of the resonator is $Vn_{Rm}=(4K_BTR_m)^{1/2}$ V/Hz$^{1/2}$.

Figure 5.3.28 shows the equivalent electrical circuit of our CMOS-MEMS in order to evaluate the thermomechanical noise performance. At resonance the resonator can be replaced by the equivalent motional resistance. On the other hand, since any external electrical excitation (V_{AC}) is present the parasitic capacitance C_p can be omitted in the analysis. The voltage source $Vn_{circuit}$ represents the input-refereed noise of the readout circuit.

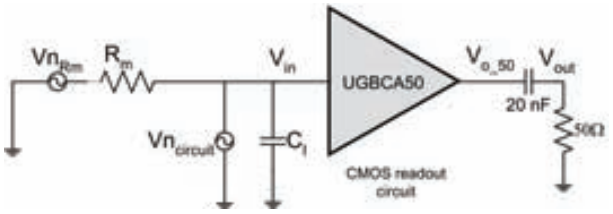

Figure 5.3.29 Schematic circuit used to calculate the thermomechanical noise in the capacitive readout circuit.

A noise-matching between the MEMS resonator and the readout circuit means that the resonator oscillation, being at T = 300º K, can be detected with a negligible contribution of the readout circuit noise [Mat02]. In our approach, this means that the input-refereed noise of the readout circuit is lower than the resonator noise contribution at the sense node according with next expression:

$$V_{n,circuit} < \sqrt{4K_BTR_m}\,\frac{Z_{C_I}}{Z_{C_I}+R_m}, \tag{5.3.3}$$

where $Z_{CI} = 1/(2\pi f_o C_I)$ and represents the equivalent impedance at the sense node which value depends on the input capacitance and the frequency of operation.

In the case of the metal cantilever CMOS-MEMS, the input capacitance is ~15 fF that is corresponding with an equivalent input impedance of ~ 1.7 MΩ at the resonance frequency ($f_o \approx 6$ MHz). On the other hand, the measured output noise of the circuit is ~1.25 μV/Hz$^{1/2}$ corresponding with $Vn_{circuit} \approx 32$ nV/Hz$^{1/2}$. From Eq. 5.3.3 one can find the maximum value of R_m that causes the noise at the sense node dominated by the thermomechanical noise. The value find is ~44 MΩ which indicates that the readout circuit implemented is able to detect the thermomechanical noise of the metal cantilever resonator since the R_m experimental values are lower with feasible bias voltages.

In order to corroborate this assumption experimental electrical measurements of the thermomechanical noise have been performed with a metal cantilever CMOS-MEMS resonator. In this case, the network analyzer has been replaced by the spectrum analyzer in the setup of Fig. 5.1.4 and the V_{AC} terminal has been grounded. In any case, a DC-bias voltage is still necessary in order to generate a capacitive current due to the Brownian motion of the cantilever.

In Figure 5.3.30 is appreciated the absence of any peak (flat spectrum) when any DC-bias voltage is applied. In this case the signal is corresponding with the circuit noise. On the other hand, for a V_{DC} = 100 V, a resonance peak at ~5.6 MHz can be fully noticed both in air and vacuum conditions. It is also appreciated that the peak height is higher in vacuum conditions since the

motional resistance is lower (Q-factor higher) as well as the effect of the Q-factor on the resonance frequency according with Eq. 2.1.24. These results corroborates that the peaks measured are corresponding with the cantilever resonance.

Measurements for different bias voltages have been also performed in vacuum conditions. The results, depicted in Figure 5.3.31, show the spring-softening effect of the resonator. As high is the bias voltage as high is the resonant peak that is still observe for a V_{DC} =50 V. With that progression in the magnitude decreasing it is expected the detection of the resonance peak to be achieved for V_{DC} =20 V that is in good agreement with the experimental motional resistance measured in these conditions (R_m = 35 MΩ).

The results presented in this section indicates the high performance of the monolithic capacitive readout circuit designed in this thesis making possible the detection of the resonance frequency of a sub-micrometer scale MEMS resonator by reading its thermomechanical noise.

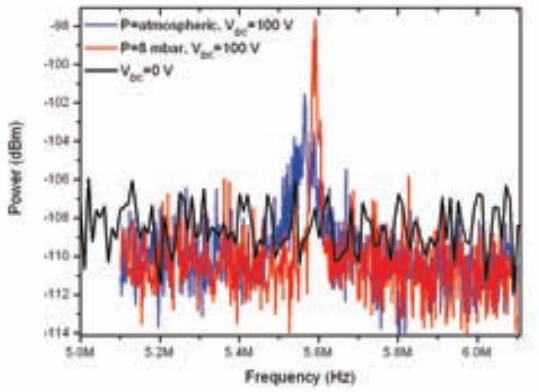

Figure 5.3.30 Measured power spectrum of the metal cantilever CMOS-MEMS resonator output signal in air and in vacuum conditions (8 mbar).

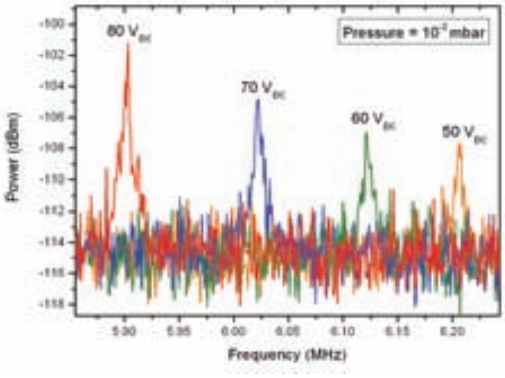

Figure 5.3.31 Measured power spectrum of the metal cantilever CMOS-MEMS resonator output signal in vacuum conditions (10^{-2} mbar) for different DC-bias voltages.

5.3.4 FUNCTIONAL CHARACTERIZATION

This section is focused on the functional characterization of the AMS-C35 resonators as mass sensors. Preliminary calibration results performed on metal resonators as well as on-line measurements are reported. Finally an analysis of the mass resolution of the CMOS-MEMS resonators is performed.

5.3.4.1 CALIBRATION

The calibration process sequence follows an iterative methodology. First the selected devices are on-chip electrically characterized using the probe station at the laboratory of the group. Then, the chip is taken to another laboratory (at UAB) for a uniform mass deposition using an electron beam chamber. Once the deposition has been performed, the chip is again electrically characterized at the lab group. If new depositions are needed, the chip is taken again to the electron beam lab. This tedious process makes that some devices fail and only few depositions were performed.

The calibration of the metal cantilever-based sensors have been performed on two devices by two successive depositions of magnesium fluoride (MgF_2[†]) thin layers of 20 and 10 nm thick over the devices by means of electron beam deposition Figure 5.3.32 shows the frequency shifts, measured in air conditions, induced by these depositions obtaining an experimental average distributed mass sensitivity, assuming the nominal cantilever dimensions (see Chapter 2 and Table 5.4), of around 6.3×10^{-11} g/cm^{2}Hz equivalent to a local or punctual mass sensitivity of 9.2×10^{-19} g/Hz that is in agreement with theoretical values.

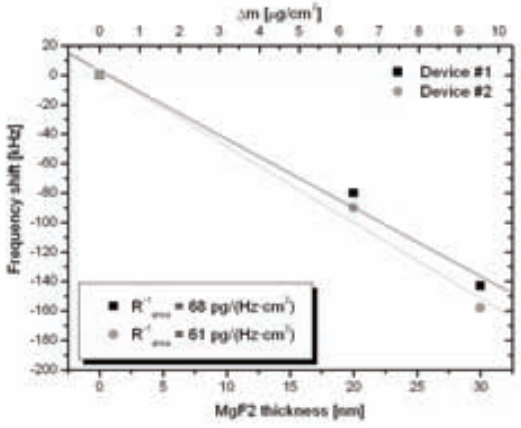

Figure 5.3.32 Plot of the resonance frequency shifts induced by sequential depositions of MgF_2 layers of 20 and 10 nm thick, respectively. The equivalent accreted mass (Δm) for a 10×0.6 μm^2 cantilever is indicated in the top x-axis.

[†] The density of MgF_2 is 3.2×10^3 kg/m^3.

In the case of the CC-beam, only one deposition of an MgF_2 layer of 20 nm thick was successful performed and measured. The frequency shift was 190 kHz corresponding with a distributed mass sensitivity of around 3.4×10^{-11} g/cm^{2}Hz equivalent to a local or punctual mass sensitivity of 1.4×10^{-18} g/Hz that is also in agreement with theoretical values.

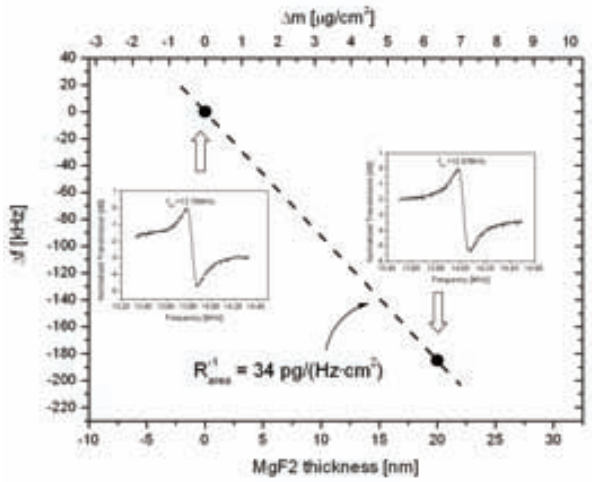

Figure 5.3.33 Plot of the resonance frequency shift induced by the deposition of a MgF_2 layer of 20 nm thick. The equivalent accreted mass (Δm) for a 18×0.6 μm^2 CC-beam is indicated in the top x-axis.

5.3.4.2 ON-LINE MEASUREMENTS

Time-resolved mass measurement experiments have been performed by monitoring the deposition of ultra-thin gold layers. This experiment has been carried out using a deposition chamber designed and assembled by Dr. Jordi Fraxedas from ICMAB-CSIC (Bellaterra). The experimental set-up was performed in collaboration with Julien Arcamone from CNM-CSIC (Bellaterra).

The monolithic device is exposed to a gold atom flux, controlled by a shutter, and monitoring the changes of the frequency response of the transmission parameter (S_{21}) using the network analyzer. The experiment was performed under base pressure of $\sim10^{-7}$ mbar.

Figure 5.3.34 shows the different measurements of the frequency response of the monolithic mass sensor when the device was exposed to a gold atom flux. When the shutter is closed, for example before any deposition (black lines), the different curves are superposed indicating that the resonator does not experiment any change in the frequency characteristic. On the other hand, when the shutter is open, the curves are continuously shifting to lower frequencies due to the increment of the resonator mass. The blue lines are corresponding with the curves obtained with the shutter closed after the deposition.

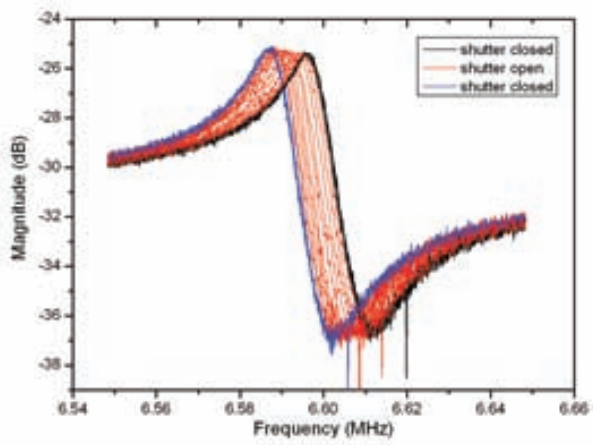

Figure 5.3.34 Plot of different curves of the frequency response of the monolithic mass sensor during the exposition to a gold atom flux. V_{DC} = 20 V and V_{AC} = -30 dBm.

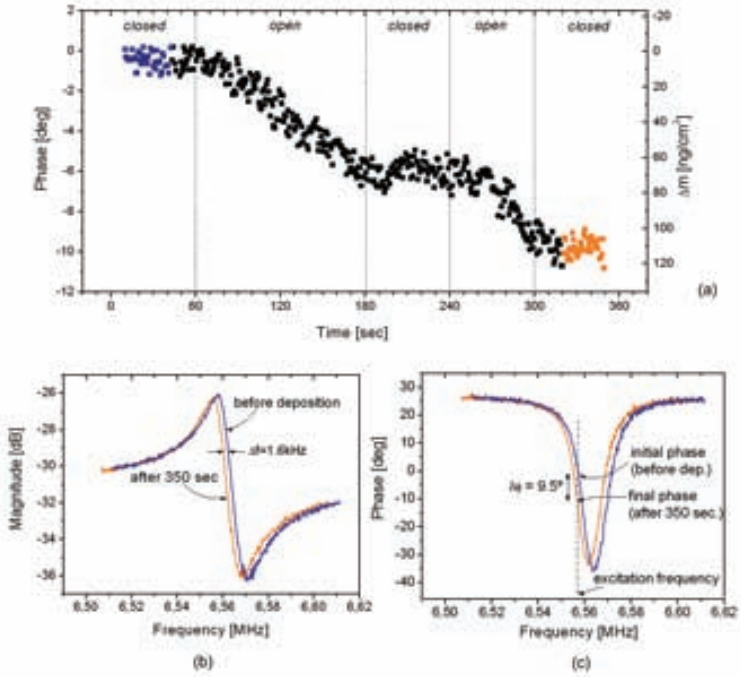

Figure 5.3.35 Real time attogram-scale mass sensing experiment with the monolithic metal cantilever CMOS-MEMS resonator. The device is biased with V_{DC} = 20 V and excited (V_{AC}) with -30 dBm. (a) Zero-span plot of the S_{21} parameter phase showing the changes induced by successive expositions to a gold atom flux. Frequency response, magnitude (b), and phase (c), before the deposition (time = 0 s) and after successive depositions (time = 360 s).

Fig. 5.3.35(a) plots the phase of the frequency response for zero-span measurements at the resonance frequency when the atom flux is open and closed successively. The phase remains constant when the shutter is closed and decreases when it is open. An on-line tracking of the frequency shift is performed indirectly by monitoring the phase during the experiment. Since the phase slope of the frequency response is negative around the resonance frequency, a phase decrease means a downshift of the resonance frequency that represents and increase of the cantilever mass. A total phase shift of around 9.5º is observed after the experiment, equivalent to a change of the resonance frequency of around 1.6 kHz (Figs. 5.3.34(b) and 5.3.34(c)) that corresponds to a total added mass of around 100 ng/cm^2 (distributed mass) or 1.4 fg (punctual mass).

These results show the stability and repeatability of the device on detecting on-line small mass depositions.

5.3.4.3 MASS RESOLUTION ANALYSIS

The mass resolution of the devices can be obtained from the experimental measurements of the frequency noise presented in section 5.3.1 and the mass sensitivity that presents these resonators. The experimental sensitivities obtained in the previous section indicate a good agreement with the theoretical values. In this sense, the theoretical values of the mass sensitivity have been used together with the experimental frequency noise values to estimate the mass resolution of these devices.

Figure 5.3.36 plots the local mass resolution of the four fabricated AMS-C35 devices measure in air and vacuum conditions. On the other hand, the distributed mass resolution is also plotted in Figure 5.3.37. We can observe that the polysilicon resonator presents better mass resolutions than the metal resonators being also superior the cantilever structure in front of the CC-beam structure.

For the polysilicon cantilever device a frequency noise of δf=0.5 Hz/√Hz in vacuum conditions was obtained in section 5.3.1.2. This low value together with the expected mass sensitivity of 65.5 zg/Hz leads to a final mass resolution as high as 30 zg/√Hz (equivalent to ~6 pg/cm^2√Hz) resulting the best AMS-C35 device both for local and distributed mass sensing.

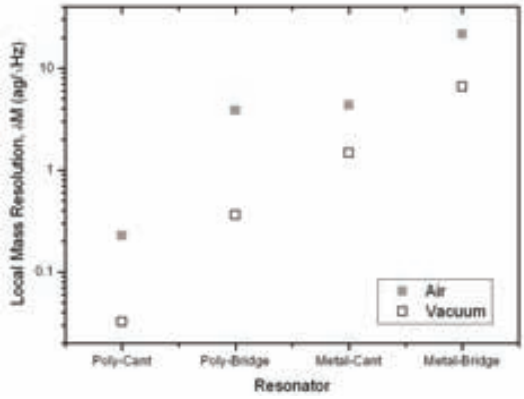

Figure 5.3.36 Local mass resolution of the AMS-C35 devices in air and vacuum conditions.

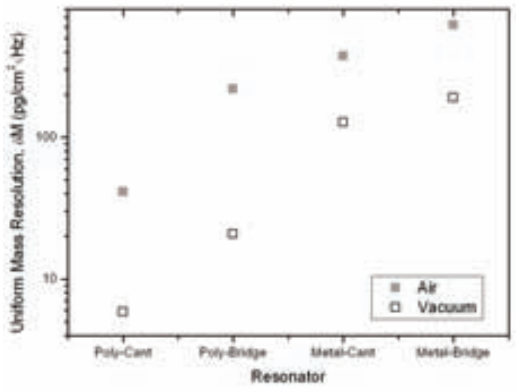

Figure 5.3.37 Distributed mass resolution of the AMS-C35 devices in air and vacuum conditions.

5.3.5 SUMMARY OF THE AMS-C35 DEVICES

In this section a summary of the design parameters and performance of the AMS-C35 resonators designed and fabricated in this thesis work are reported. Table 5.4 reports the parameters corresponding with the metal resonators while Table 5.5 reports the parameters of the polysilicon resonators.

Table 5.4 Metal resonators design and performance summary.

	Parameter	Source	Cantilever	CC-Beam	Units
	Fabrication Process	––	Met4 AMS-C35 Technology		––
Designed/Given	Young's Modulus, E	typical	131		GPa
	Density, ρ	typical	3000		kg/m^3
	Length, l	layout	10	18	μm
	Coupling length, l_c	layout	8	10	μm
	Width, w	layout	600		nm
	Thickness, t	technology	850		nm
	Gap, s	layout	600		nm
Measured	Nominal Resonance frequency, f_o	measured	6.33	13.9	MHz
	DC-Bias Voltage used, V_{DC} (Air / Vacuum)	measured	60 / 20	70 /35	V
	AC Voltage used, V_{AC}	measured	- 20		dBm
	Quality factor, Q (Air / Vacuum)	measured	108 / 880	156 / 918	––
	Resonance frequency, f_{res} (Air / Vacuum)	measured	6.02 / 6.32	13.78 / 14.03	MHz
	Spring softening	measured	95	34	Hz/V^2
	Motional Resistance, R_m (Air / Vacuum)	meas./ Eq. 5.3.2	29.3 / 34.9	15.4 / 11.9	MΩ
	Parasitic capacitance, C_p	meas./ Eq. 5.3.1	128	174	aF
	Frequency noise, δf (Air / Vacuum)	measured	4.7 / 1.6	15.3 / 4.7	Hz/√Hz
	Mass Sensitivity, $\Re^1$/ $\Re^1_{area}$	measured	0.9 / 63	1.4 / 34	ag/Hz pg/cm^{2}Hz
	Mass resolution, δM (Air / Vacuum)	measured	4.3 / 1.5	21.4 / 6.6	ag/√Hz
Analytically Determined	Nominal Resonance frequency, f_o	Eq. 2.1.14	6.40	12.6	MHz
	Resonance frequency, f_{res} (Air / Vacuum)	Eq. 2.1.38	5.85 / 6.34	12.4 / 12.5	MHz
	Spring constant, k	Eq. 2.1.5,6	6.0	65.8	N/m
	Spring softening	Eq. 2.1.38	38.6	4.4	Hz/V^2
	Effective Mass, M_{eff}	Eq. 2.1.17,18	3.7×10^{-15}	1.05×10^{-14}	kg
	Motional Resistance, R_m (Air / Vacuum)	Eq. 2.2.1	12.6 / 15.1	24.7 / 16.9	MΩ
	Mass Sensitivity, $\Re^1$/ $\Re^1_{area}$	Eq. 2.1.26	1.16 / 79.5	1.7 / 40.5	ag/Hz pg/cm^{2}Hz
	Vibration amplitude, x_r (Air / Vacuum)	Eq. 2.3.44	5 / 13.7	1.4 / 4.1	nm
	Intrinsic Frequency noise, δf (Air / Vacuum)	Eq. 2.3.5	0.5 / 0.06	0.6 / 0.1	Hz/√Hz
	Intrinsic Mass resolution, δM (Air / Vacuum)	Eq. 2.3.6	0.6 / 0.08	1.1 / 0.15	ag/√Hz

Table 5.5 Polysilicon resonators design and performance summary.

	Parameter	Source	Cantilever	CC-Beam	Units
	Fabrication Process	––	Poly AMS-C35 Technology		––
Designed/Given	Young's Modulus, E	typical	160		GPa
	Density, ρ	typical	2330		kg/m^3
	Length, l	layout	6.5	13	μm
	Coupling length, l_c	layout	4.5	9	μm
	Width, w	layout	350		nm
	Thickness, t	technology	282		nm
	Gap, s	layout	450	150	nm
Measured	Nominal Resonance frequency, f_o	measured	11.03	22.26	MHz
	DC-Bias Voltage used, V_{DC} (Air / Vacuum)	measured	40 / 12	12 / 4	V
	AC Voltage used, V_{AC}	measured	- 10	-15 / -30	dBm
	Quality factor, Q (Air / Vacuum)	measured	205 / 3536	165 / 2600	––
	Resonance frequency, f_{res} (Air / Vacuum)	measured	10.91/ 11.04	21.87 / 22.31	MHz
	Spring softening	measured	88	3600	Hz/V^2
	Motional Resistance, R_m (Air / Vacuum)	meas./ Eq. 5.3.2	33.7 / 29	3.58 / 3.33	MΩ
	Parasitic capacitance, C_p	meas./ Eq. 5.3.1	48	252	aF
	Frequency noise, δf (Air / Vacuum)	measured	3.5 / 0.5	29.5 / 2.8	Hz/√Hz
Analytically Determined	Nominal Resonance frequency, f_o	Eq. 2.1.14	11.1	17.64	MHz
	Resonance frequency, f_{res} (Air / Vacuum)	Eq. 2.1.38	10.45 / 11.03	17.0 / 17.6	MHz
	Spring constant, k	Eq. 2.1.5,6	1.8	14.1	N/m
	Spring softening	Eq. 2.1.38	77.8	1570	Hz/V^2
	Effective Mass, M_{eff}	Eq. 2.1.17,18	3.6×10^{-16}	1.1×10^{-15}	kg
	Motional Resistance, R_m (Air / Vacuum)	Eq. 2.2.1	23.6 / 16.1	5.18 / 3.05	MΩ
	Mass Sensitivity, $\mathcal{R}^1$/ $\mathcal{R}^1_{area}$	Eq. 2.1.26	65.5 / 11.8	130 / 7.44	zg/Hz pg/cm^{2}Hz
	Vibration amplitude, x_r (Air / Vacuum)	Eq. 2.3.44	26.4 / 136	8.1 / 7.5	nm
	Intrinsic Frequency noise, δf (Air / Vacuum)	Eq. 2.3.5	0.17 / 0.008	0.27 / 0.074	Hz/√Hz
	Intrinsic Mass resolution, δM (Air / Vacuum)	Eq. 2.3.6	11.2 / 0.5	36.1 / 9.7	zg/√Hz

5.4 COMPARATIVE

Figure 5.4.1 shows a comparative between the CNM25 and the AMS-C35 devices in terms of its local mass resolution obtained in air and vacuum conditions. We can appreciate than in general the AMS-C35 devices are around two orders of magnitude superior to the CNM25 devices. Only the CNM25 cantilever fabricated with EBL is comparable in vacuum conditions, due to its high quality factor, with the AMS-C35 metal resonators. In any case, in air conditions the AMS-C35 metal resonators become more than two orders of magnitude superior. On the other hand, the AMS-C35 polysilicon cantilever is also two orders of magnitude superior to the best CNM25 device in vacuum conditions and more than three orders of magnitude in air conditions.

In addition, as reported in this chapter, the AMS-C35 devices present better electrical characteristics, that is, higher resonance peak and phase shift as well as lower insertion losses enabling its operation as self-sustaining oscillator as will be reported in Chapter 6.

By comparing the excellent results presented in this chapter, mass resolutions down to tens of zeptogram, with the state-of-the-art of the mass sensors presented in Table 1.2, we can state that the mass resolution showed by the AMS-C35 polysilicon cantilever device is similar than the best value previously reported with not integrated sensors (i.e. [Yan06] and [Ili05]).

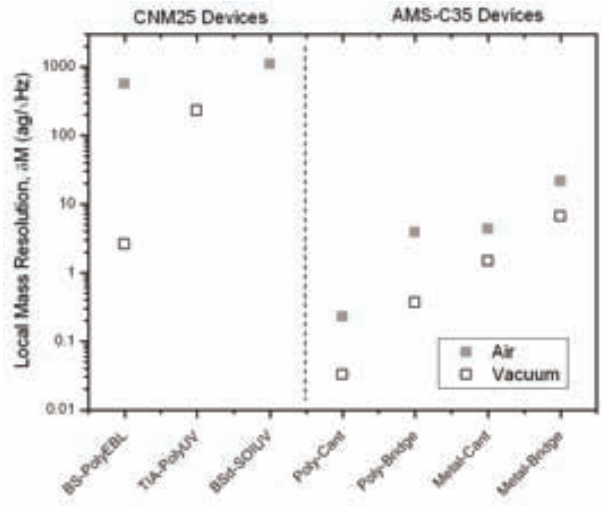

Figure 5.4.1 Comparative between CNM25 and AMS-C35 devices in terms of local mass resolution.

REFERENCES

[Buk06] E. Buks, B. Yurke, "Mass detection with a nonlinear nanomechanical resonator", *Physical Review E*, vol. 74, pp. 046619, 2006

[Dav03] Z.J. Davis, "Nano-resonators for high resolution mass detection", *PhD thesis,* Mikroelektronik Centret, Technical University of Denmark, Denmark, March 2003.

[For04] E. Forsén, SG. Nilsson, P. Carlberg, G. Abadal, F. Pérez-Murano, J. Esteve, J. Montserrat, E. Figueras, F. Campabadal, J. Verd, L. Montelius, N. Barniol and A. Boisen, "Fabrication of cantilever based mass sensors integrated with CMOS using direct wrtite laser lithography on resist", *Nanotechnology*, vol. 15 (10), pp. S628-S633, 2004.

[For05] E. Forsen, G. Abadal, S Ghatnekar-Nilsson, J. Teva, J. Verd, R. Sandberg, W. Svendsen, F. Perez-Murano, J. Esteve, E. Figueras, F. Campabadal, L. Montelius, N. Barniol, A. Boisen, "Ultrasensitive mass sensor fully integrated with complementary metal-oxide-semiconductor circuitry", *Applied Phsyics Letters*, vol. 87 (4), pp. 04357, 2005.

[For05b] E. Forsen, "Nano-cantilevers fully integrated with CMOS for ultrasensitive mass detection", *PhD thesis,* Mikroelektronik Centret, Technical University of Denmark, Denmark, Sep. 2005.

[Gha05] S Ghatnekar-Nilsson, E Forsen, G Abadal, **J Verd**, F Campabadal, F Perez-Murano, J Esteve, N Barniol, A Boisen and L Montelius, "Resonators with integrated CMOS circuitry for mass sensing applications fabricated by electron beam lithography", *Nanotechnology*, vol. 16 (1), pp. 98-102, 2005.

[Ili05] B. Illic, Y. Yang, K. Aubin, R. Reichenbach, S. Krylov, and H. C. Craighead, "Enumeration of DNA Molecules Bound to a Nanomechanical Oscillator", *Nanoletters*, vol. 5 (5), pp. 925-929, 2005.

[Lan99] Landau L D and Lifshitz E M 1999 *Mechanics* 3rd edn, (Oxford, UK: Butterworth-Heinemann)

[Mat02] T. Mattila, O. Jaakkola, J. Kiihamäki, J. Karttunen, T. Lamminmäki, P. Rantakari, A. Oja, H. Seppä, H. Kattelus, I. Tittonen, "14 MHz micromechanical oscillator", *Sensors and Actuators A*, vol. 97-98, pp. 497-502, 2002.

[Ran04] R. H. Rand. (2004) *Lecture Notes on Nonlinear Vibrations* [Online]. Available: http://dspace.library.cornell.edu/handle/1813/79

[Ura07] A. Uranga, J. Verd, F. Torres, J. Teva, J.L. López, G. Abadal, J. Esteve, F. Pérez-Murano and N. Barniol, "Electrical detection of multiple resonant modes in a CMOS-MEMS cantilever", *Microelectronic Engineering*, vol. 84 (5-8), pp. 1374-1378, 2007.

[Ver05] J. Verd, G. Abadal, J. Teva, M. Villarroya, A. Uranga, X. Borrisé, F. Campabadal, J. Esteve, E. Figueras, F. Pérez-Murano, Z.J. Davis, E. Forsen, A. Boisen and N. Barniol, "Design, fabrication and characterization of a submicroelectromechanical resonator with monolithically integrated CMOS readout circuit", *Journal of Microelectromechanical Systems*, vol. 14 (3), pp. 508-519, 2005.

[Vil05] M. Villarroya, "Diseño y fabriación de sistemas micro / nano electromecánicos integrados monolíticamente para aplicaciones de sensors de masa y sensors biológicos con palancas como elementos transductores", *PhD thesis,* Universitat Autonoma de Barcelona, Spain, June 2005.

[Vil06] M. Villarroya, J. Verd, J. Teva, G. Abadal, E. Forsen, F. Pérez-Murano, A. Uranga, E. Figueras, J. Montserrat, J. Esteve, A. Boisen, N. Barniol, "System on chip mass sensor based on polysilicon cantilevers arrays for multiple detection", *Sensors and Actuators A-Physical*, vol. 132, pp. 154-164, 2006.

[Vil07] M. Villarroya, G. Abadal, J. Verd, J. Teva, F. Pérez-Murano, E. Figueras, J. Montserrat, A. Uranga, J. Esteve, N. Barniol, "Time resolved evaporation rate of attoliter glycerine drops using on-chip CMOS mass sensors based on resonant silicon micro cantilevers", *IEEE Transactions on Nanotechnology*, vol. 6 (5), pp. 509-512, 2007.

[Yan06] Y. T. Yang, C. Callegari, X. L. Feng, K. L. Ekinci, and M. L. Roukes, "Zeptogram-Scale Nanomechanical Mass Sensing", *Nanoletters*, vol. 6 (4), pp. 583-586, 2006.

[Zha02] W. Zhang, R. Baskaran K.L. Turner, "Effect of cubic nonlinearity on auto-parametrically amplified resonant MEMS mass sensor", *Sensors and Actuators A*, vol. 102, pp. 139-150, 2002

CHAPTER 6

CMOS-MEMS OSCILLATOR CIRCUIT

This chapter presents the design and characterization of a Pierce oscillator circuit adapted to work with the metal beam resonators described in Chapter 5. The mechanical resonator is the frequency-determining element of the oscillator circuit that is monolithically integrated in the AMS C35 process. This approach allows the use of the mass sensor in system-on-chip applications (SoC). The electrical characterization of the oscillator circuit running with the cantilever and CC-beam resonator are presented and compared.

6.1 INTRODUCTION AND MOTIVATION

The mass sensing principle of the devices described in this work is based on measuring the resonance frequency shift of the MEMS device due to the accreted mass. System-on-chip applications demand the integration not only of the signal conditioning circuitry (pre-amplifiers) but also of the electronics for driving the resonator at resonance and continuously tracking its resonance frequency (self-tracking circuit) [Bra06]. An advantage of the self-tracking oscillator is the inherent nature of the output being frequency rather than analog voltage.

Two basic techniques are used to sustain vibratory resonant motion in mechanical structures. The first technique uses an oscillator circuit where the resonator (including transduction elements) is placed in the feedback loop of an electronic amplifier, where the MEMS resonator is the frequency-determining element in a similar way to quartz crystal based oscillators [Vit98]]. The second technique, commonly used in AFM microscopy [Dür97], uses an electronic oscillator to excite the mechanical resonator using a phase locked loop (PLL) [Bat01].

The advantage of the oscillator approach is the lower complexity of the hardware with respect to the PLL approach. In these sense, the oscillator circuit base topology do not need any additional oscillator and the frequency output is easily converted to a digital format for low bandwidth applications by measuring the period of oscillation without the need of any A/D converter.

The main challenge of the oscillator technique is the large motional resistance of the MEMS resonator (R_m) mainly in CMOS high-sensitivity resonators, especially in view of the small dimensions (low capacitive coupling), relative high-frequency, and low quality factor (see chapter 5).

- **OSCILLATOR TOPOLOGIES**

The two main types of CMOS oscillator topologies that have found applicability to MEMS resonators are: a transresistance amplifier based oscillator and a Pierce oscillator circuit.

A transresistance amplifier uses a resistor as the primary gain element (Fig. 6.1.1b). Gain stages may be added to the initial transresistance stage to provide for the necessary loop gain. Since a resistor is used as the primary gain element implies that the noise performance of the oscillator is usually quite poor and is dominated by the input resistor (R). Nguyen et al. demonstrated in 1999 a monolithic 16.5 kHz transresistance amplifier based micromechanical resonator oscillator [Ngu99].

The Pierce oscillator topology uses a capacitive input to integrate the motional current from the resonator. The Pierce circuit operates at a frequency slightly higher than the actual series resonant where the mechanical resonator acquires an inductive behavior. In general, the Pierce circuit topology is superior to the transresistance amplifier approach in terms of the noise figure of the oscillator. The reason, already commented in Chapter 4, is due to the fact that most of the gain is provided by a (ideally) noiseless capacitive input element rather than a loss resistive element. Roessig et al. reported in 1998 a 1MHz oscillator with a low-noise pierce configuration stating that offers superior noise performance over previous resistive methods [Roe98]. Different examples of MEMS oscillator circuits using a Pierce topology can be found in the literature [Lee01, Roe98, Ran05, Ses02].

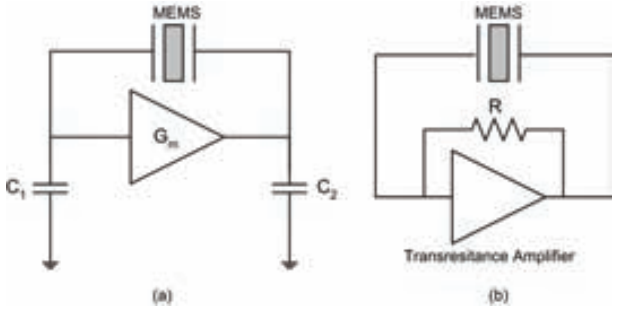

Figure 6.1.1 Conceptual schematic of MEMS oscillator circuits: (a) Pierce circuit oscillator and (b) transresistance amplifier based oscillator.

6.2 OSCILLATOR DESIGN

The sustaining circuit of the oscillator has to present an equivalent transimpedance gain higher than MΩ at a frequency of around 10 MHz in order to overcome the losses exhibit for the metal MEMS resonators measured in the previous chapter.

A Pierce oscillator topology has been chosen to implement the oscillator. Fig. 6.2.1 presents the block diagram of the oscillator where the MEMS resonator (cantilever in this case) is electrostatically self-excited setting the oscillation frequency of the circuit. Referring to this scheme, the loop gain expression for the Pierce configuration can be written as

$$G(j\omega_o)=\frac{A_V Z_1}{Z_1+Z_2+Z_m}=\frac{A_V}{1+\dfrac{Z_2+Z_m}{Z_1}}, \text{ where} \tag{6.2.1}$$

$$Z_1(j\omega_o)=\frac{1}{j\omega_o C_1}, Z_2(j\omega_o)=\frac{1}{j\omega_o C_2}, Z_M(j\omega_o)=j\omega_o L_{eff}+R_r. \tag{6.2.2}$$

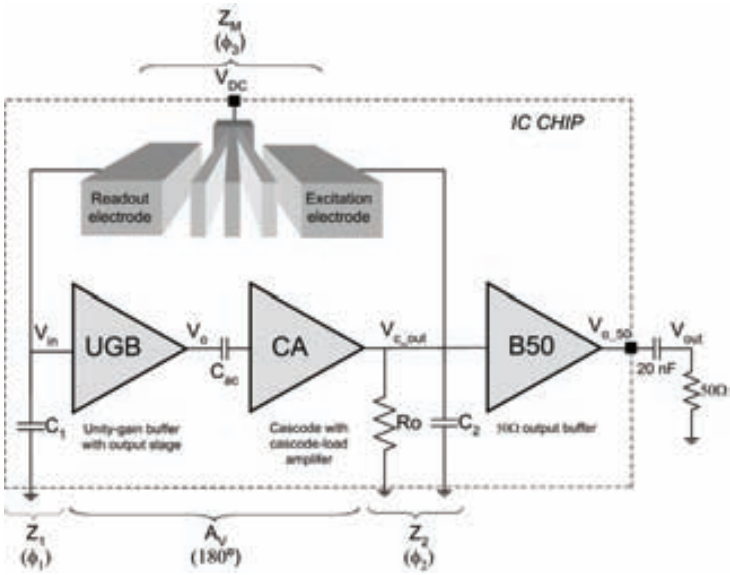

Figure 6.2.1 Conceptual circuit schematic for an electrostatically self-excited cantilever resonator based on a modified Pierce oscillator topology.

A_V is the steady-state voltage gain of the sustaining amplifier (*UGB+CA*), Z_1 and Z_2 are the impedances indicated in Fig. 6.2.1, Z_M is the impedance of the MEMS resonator, and R_o is output impedance of the sustaining amplifier (*CA* in this case). It has been assumed that the resonator looks inductive at the frequency of oscillation ω_o. In this sense, the oscillation frequency is slightly higher than the series resonance peak of the MEMS ($\omega_o > 2\pi f_{res}$). On the other hand, the equivalent resistance of the resonator at the circuit oscillation frequency (R_r) becomes slightly higher than the MEMS motional resistance (R_m).

For a proper oscillation at frequency ω_o, the loop gain magnitude and phase should satisfy the Barkhausen criteria:

$$|G(j\omega_o)|\geq 1 \tag{6.2.3}$$

$$\angle G(j\omega_o)=180^\circ+\phi_1+\phi_2+\phi_3=0^\circ. \tag{6.2.4}$$

ϕ_1 and ϕ_2 are the phase of the input and output impedances of the sustaining circuit respectively. On the other hand, ϕ_3 is the phase of the MEMS that ideally (without parasitic feedthrough capacitances) moves from +90º (at frequencies < ω_o) to -90º (at frequencies > ω_o).

Last equations indicate that when working with high motional resistances, the voltage gain of the sustaining amplifier (A_V) and the impedance at the sense node (Z_1) have to be maximized. The Pierce oscillator topology presented in Fig. 6.2.1 has been adapted to overcome the large motional resistance of the resonator as well as to ensure the overall loop phase criterion.

The sustaining circuit uses two CMOS amplifier stages presented in Chapter 4: the front-end buffer (*UGB*, Fig. 4.3.2) and the high-gain voltage amplifier (*CA*, Fig. 4.3.7). The additional buffer (*B50*, Fig. 4.3.9) has been also introduced for testing purposes on 50-Ω loads with some loss of amplitude and voltage swing as discussed in Chapter 4.

With the first-stage *UGB*, the input capacitance at the sense node (C_1) is minimized resulting in a very high transimpedance gain. As the input node (V_{in}) is polarized with an extremely high resistance element (see Chapter 4), the input impedance will be primarily reactive and, consequently, the phase shift at this node is maximized ($\phi_1 \approx$-90º).

The second-stage *CA* is a high-gain voltage amplifier used to provide the additional gain needed for oscillation. As is described in Chapter 4, a cascode with cascode-load configuration has been chosen and designed to present a very high output impedance (R_o), in order to operate past the bandwidth of the amplifier ($BW_{-3dB} \approx$ 230 kHz), resulting in a large phase shift ($\phi_3 \approx$-65º @ 6 MHz) at the oscillation frequency but having a high-gain enough. This stage is self-polarized by means of a PMOS pseudo-transistor and AC-coupled (C_{ac}) with the first stage in order to assure the correct biasing of this amplifier, as well as to actuate as a high-pass filter minimizing the flicker noise effects of the front-end buffer.

The interaction of the large R_m and the parasitic feedthrough current tend to constrain the phase shift of ϕ_3 to small values as we have discussed in Chapter 2. In this sense, the 2-port configuration used for the MEMS resonator minimizes this effect resulting in an increase in the phase shift ϕ_3. On the other hand, the use of the 2-port configuration allows to decoupling of the bias voltage (V_{DC}) and the excitation voltage (V_{AC}) and consequently to implement the oscillator circuit without the need of any bias-T element.

Fig. 6.2.2 shows the magnitude of the oscillator loop gain ($|G(j\omega_o)|$) as a function of the motional resistance for different oscillator output frequencies. The MEMS resonator has been replaced in the oscillator circuit by its equivalent motional resistance. The simulation results indicate that the designed oscillator circuit can be used to operate with mechanical resonators with motional resistances up to ~100 MΩ for an oscillation frequency of 10 MHz.

In Fig. 6.2.3 is plotted the open-loop frequency response of the oscillator. The magnitude plot (Fig. 6.2.3a) has been obtained replacing the resonator by an equivalent motional resistance of 50 MΩ. It is appreciated that for this resistance value the oscillator loop gain is higher than unity for a frequency up to 10 MHz or more. In the other hand, the phase plot has been obtained with the resonator acting as a static capacitor. The simulation results (Fig. 6.3.2b) indicate than only a phase of $\phi_3 \approx$105º (@ 10MHz) introduced by the resonance of the MEMS is needed to achieve the loop phase criterion.

Figure 6.2.4 shows the layout of the MEMS-based oscillator circuit using the AMS-C35 technology. The layout is similar that presented in Chapter 4 with the peculiarity that in this case the output of the sustaining amplifier is feedback to the excitation electrode of the MEMS resonator (V_{c_out}). Furthermore, in this case an additional connection pad to the pre-amplifier

output (V_o) has been also disposed to achieve an external control of the load impedance in order to enable a downshift of the loop phase if needed.

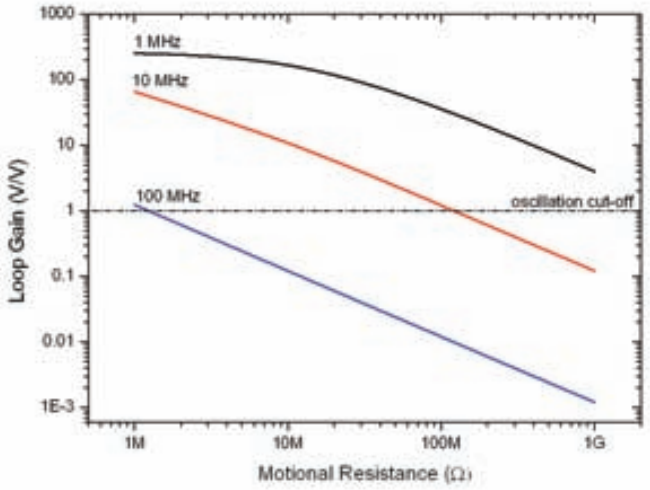

Figure 6.2.2 Magnitude of the loop gain as a function of motional resistance of the resonator for different oscillation frequencies.

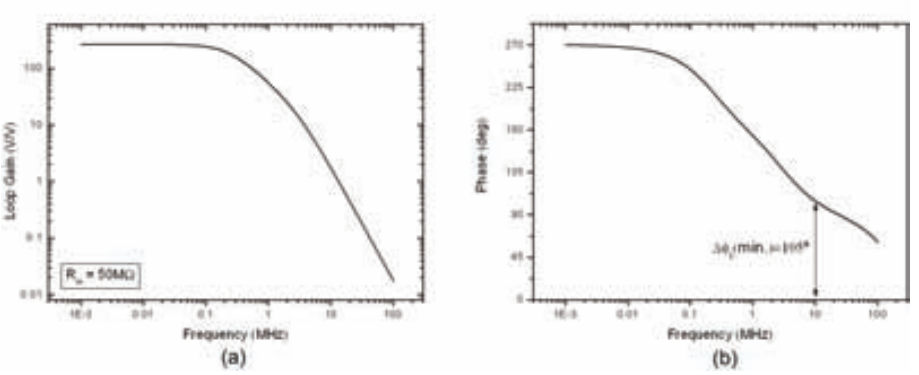

Figure 6.2.3 Open-loop frequency response. In the magnitude plot (a) the MEMS have been replaced for a resistance of 50 MΩ. In the phase plot (b) the MEMS is acting as a capacitor.

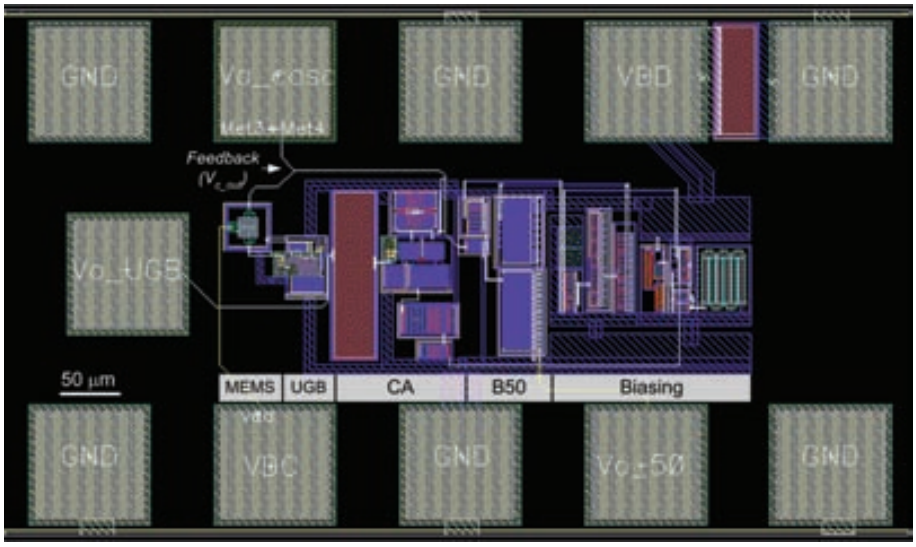

Figure 6.2.4 Layout of the MEMS-based oscillator circuit monolithically integrated in the AMS-C35 technology.

6.3 EXPERIMENTAL RESULTS

In this section the experimental results of cantilever and CC-beam based oscillators are presented and discussed. The results obtained indicate that these CMOS-MEMS oscillator circuits are able to operate both in air and in vacuum conditions resulting on the highest sensitivity on-chip fully integrated oscillators previously reported.

Fig. 6.3.1 shows the setup used to perform the oscillator measurements using a spectrum analyzer to obtain the power spectrum as well as the phase noise of the oscillator output. A DC-source is used to power supply the CMOS circuitry and another high-voltage DC-source is used to bias the MEMS resonator. This setup allows to perform measurements in air and in vacuum using the custom vacuum chamber. For time measurements, the spectrum analyzer can be replaced by an oscilloscope or a counter. The measurements performed by the spectrum analyzer and the oscilloscope are acquired by a computer through GPIB.

Both measurements with the spectrum analyzer and the digital oscilloscope are performed using a Bias-T element. The acquired data values with the oscilloscope, that presents high input impedance, are ~6 dBm higher than obtained with the spectrum analyzer which input impedance is 50Ω.

6.3.1 CANTILEVER BASED OSCILLATOR

The cantilever resonator used in the oscillator circuit is the same that presented in Chapter 5, a metal cantilever 10 μm long, 600 nm wide and 750 nm thick with a gap to the electrodes of 600 nm.

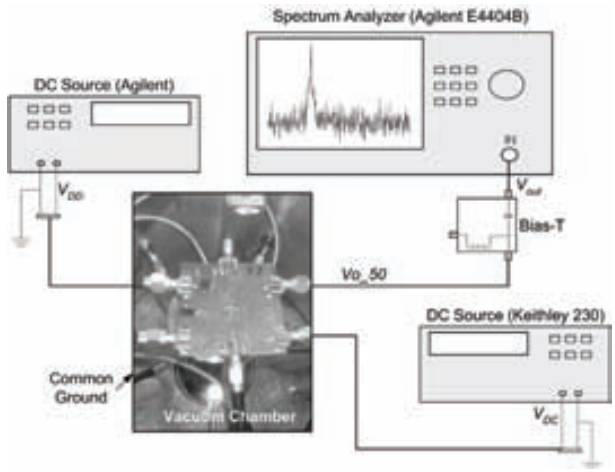

Figure 6.3.1 Test setup for oscillator measurements using the vacuum chamber.

Fig. 6.3.2a shows the power spectrum, measured with the spectrum analyzer, of the cantilever based oscillator output over 80 kHz range centered on the carrier frequency that is located at 6.32 MHz. On the other hand, Fig. 6.3.2b shows the time waveform obtained with the oscilloscope. The oscillator output signal amplitude measured with the oscilloscope is around 520 mV_{pp} that is limited by the sustaining amplifier and the output buffer. These results have been obtained in air conditions for a resonator bias voltage of V_{DC}=45 V. From experimental measurements, we found that the oscillator start-up is produced for bias voltages higher than 44 V in air conditions.

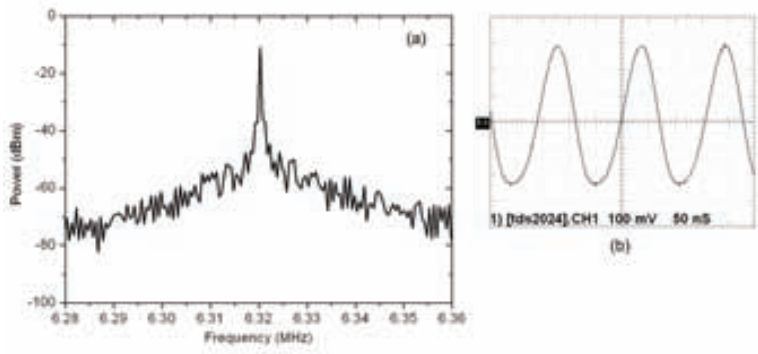

Figure 6.3.2 Power spectrum and oscilloscope waveform of the cantilever based oscillator measured in air conditions (V_{DC}=45V).

- **NOISE AND MASS RESOLUTION**

The short-term stability of the oscillator is characterized in terms of the frequency and phase instabilities in the time or in the frequency domain. In the frequency domain, the single side band phase noise-to-carrier ratio, $L(f_m)$, is the prevailing measure of phase noise among manufactures

and users (e.g. Spectrum Analyzer). This noise can be expressed, using the Leeson equation [Lee66], as:

$$L(f_m) \approx 10\log\left\{\frac{S_v^2}{2P_c}\left[1+\left(\frac{f_o}{2Qf_m}\right)^2\right]\right\}, \tag{6.3.1}$$

where f_m is the offset frequency where the phase noise is measured, S_v^2 is the noise power of the oscillator measured in open-loop, and P_c is the carrier output power of the carrier. Last equation assumes that the noise is white and that oscillator operation remains linear.

The close-to-carrier noise, which slope is proportional to $1/f^2$, is limited by the electrical quality factor of the resonator. On the other hand, the far-from-carrier noise floor is limited by the sustaining amplifier noise of the oscillator loop.

The experimental results presented in Fig. 6.3.3 show a noise floor of $L(f)$=-94.3 dBc/Hz from the carrier with a power of P_c=-10.7 dBm. Since the sustaining amplifier is designed with a very high transimpedance gain to overcome the high motional resistance of the resonator, it presents an output noise, which sets the noise floor, higher than other sustaining amplifiers that operate with low motional resistance resonators (~kΩ or less) [Lee01, Lin04, Lin05, Ran05]. The noise of the sustaining amplifier can be deduced from Eq. 6.3.1, as $S_v^2 = L(f) + P_c + 3$, giving an experimental value of -102 dBm/Hz that corresponds with an output voltage noise density of 1.77 μV/Hz$^{1/2}$. This value is in good agreement with the experimental results presented in Chapter 5.

At small frequency offsets the slope of the measured phase noise (Fig. 6.3.3) is in fact not the $1/f^2$ predicted by Eq. 6.3.1, but rather $1/f^3$. This close-to-carrier phase noise is generated mainly due to the nonlinear electrostatic transduction of the resonator that aliases the $1/f$ electronic noise (e.g. from the sustaining amplifier) onto the carrier frequency, generating a $1/f^3$ component [Kaa05].

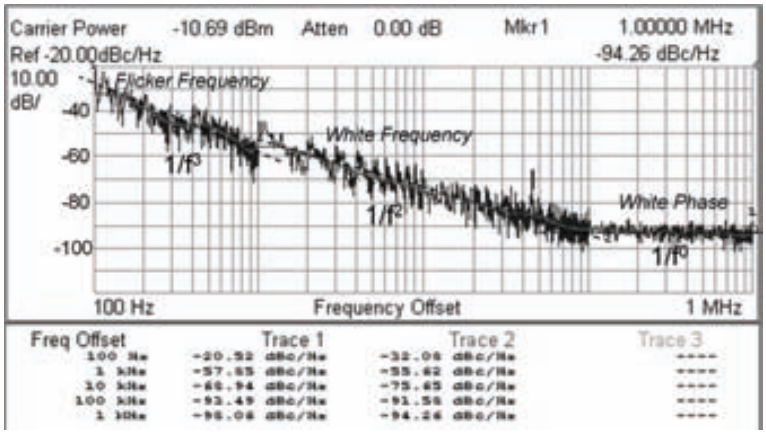

Figure 6.3.3 Measured phase noise versus frequency offset from the carrier (@ 6.32 MHz) of the cantilever based oscillator measured in air (V_{DC}=45V).

In the time domain, normalized frequency fluctuations are usually expressed in terms of the Allan variance, $\sigma_y^2(\tau)$, as a function of averaging time (τ) [All88]. Allan variance can be estimated

using the power-law model to represent the normalized frequency fluctuations spectrum ($Sy(f_m)$) that is related with the phase noise spectrum as $Sy(f_m)=2L(f_m)f^2/f_o^2$ [All88]. From the measured phase noise three different types of noise can be identified: flicker frequency modulation ($1/f^3$), white frequency modulation ($1/f^2$) and white phase modulation ($1/f^0$). Assuming that the random driving mechanism for each noise component is independent of the others, the Allan variance can be expressed using next Cutler's equation [All88]:

$$\sigma_y^2(\tau) = h_{-1} 2\log_e(2) + h_o \frac{1}{2\tau} + h_2 \frac{3 f_h}{(2\pi)^2 \tau^2}, \tag{6.3.2}$$

where the power-law model coefficients h_{-1}, h_0, and h_{-1} are corresponding with the flicker FM, white FM and white PM respectively, and f_H is the high frequency cut-off. Using regression techniques, the values of the coefficients obtained are: $h_{-1} = 5.3\times10^{-16}$, $h_0 = 1.3\times10^{-13}$, $h_2 = 1.5\times10^{-23}$, and $f_H = 80$ kHz.

For a typical averaging time of $\tau = 1$ s, the Allan deviation (root Allan variance) obtained is 2.5×10^{-7} corresponding with a frequency fluctuation of 1.59 Hz given by $\delta f_o=\sigma_y(\tau)f_o$. When this oscillator is used for resonant mass sensing, this frequency stability level, combined with the device mass sensitivity of 0.9 ag/Hz (see Chapter 5), leads to unprecedented mass resolution for a fully integrated MEMS oscillator of $\delta M = 1.4$ ag.

The intrinsic thermomechanical noise of the MEMS resonator also generates a frequency and phase noise that limits the resolution of the sensor. Assuming that the thermomechanical noise generates a white frequency noise, the Allan variance can be expressed as [Cle02]:

$$\sigma_y^2(\tau) = \frac{k_B T}{8\omega_o E_c Q \tau} = \frac{k_B T}{8 M_{eff} \omega_o^3 \langle x_c^2 \rangle Q \tau}. \tag{6.3.3}$$

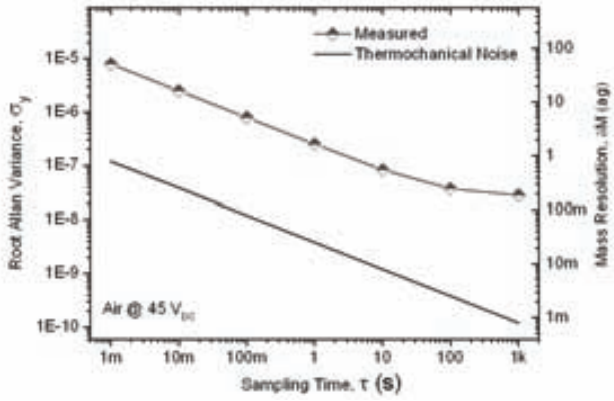

Figure 6.3.4 Allan deviation and mass resolution obtained in air conditions compared with that of thermomechanical noise limit.

Fig. 6.3.4 plots the Allan deviation and the corresponding mass resolution for different averaging times obtained from the experimental values of the phase noise obtained in air conditions for a resonator bias voltage of 45 V. These results are compared on the same graph with

the theoretical limit due to the thermomechanical noise calculated from Eq. 6.3.3. The Allan variance due to the thermomechanical noise has been calculated using a resonator vibration amplitude of 38 nm that has been obtained for an excitation voltage of V_{AC}= 0 dBm and assuming the parameters indicated in Table 6.1.

- **PERFORMANCE AT VACUUM**

This oscillator has been also measured in vacuum conditions (1×10^{-2} mbar). In this case, the peak of the measured output spectrum (Fig. 6.3.5a) is narrower than in air since the quality factor of the resonator is higher (air squeezing is minimized). On the other hand, the oscillator output signal amplitude measured with the oscilloscope is around 540 mV_{pp} quite similar to that obtained in air conditions. In these vacuum conditions, the oscillator start-up is produced for bias voltages higher than 16.5 V.

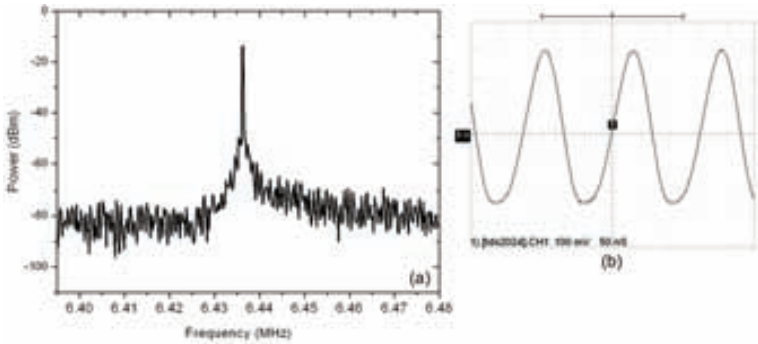

Figure 6.3.5 Power spectrum and oscilloscope waveform of the cantilever based oscillator measured in vacuum (V_{DC}=17V).

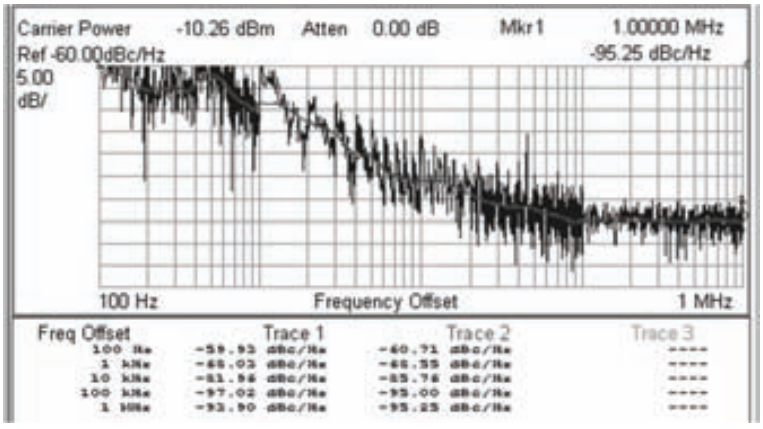

Figure 6.3.6 Measured phase noise versus frequency offset from the carrier of the cantilever based oscillator measured in vacuum (V_{DC}=17V).

The plot of the measured phase noise is presented in Fig. 6.3.6. In this case, the close-to-carrier noise is lower than the measured in air conditions mainly due to the higher quality factor. The use of a lower bias voltage reduces the effect of the nonlinear electrostatic transduction on the mixing mechanism that results also in a reduction of the $1/f^3$ noise component [Kaa05]. On the other hand, the noise floor measured is in this case $L(f)$=-95.3 dBc/Hz from the carrier (@ 6.44 MHz) with a power of P_c=-10.3 dBm, resulting a noise value of the sustaining amplifier of -105.5 dBm/Hz that is quite similar to the value obtained in air conditions since the far-from-carrier noise not depends on the quality factor of the resonator.

Fig. 6.3.7 shows the Allan deviation and the corresponding mass resolution for different averaging times for air and vacuum measurements. It is appreciated that the mass resolution obtained in vacuum is still better than in air since the higher quality factor.

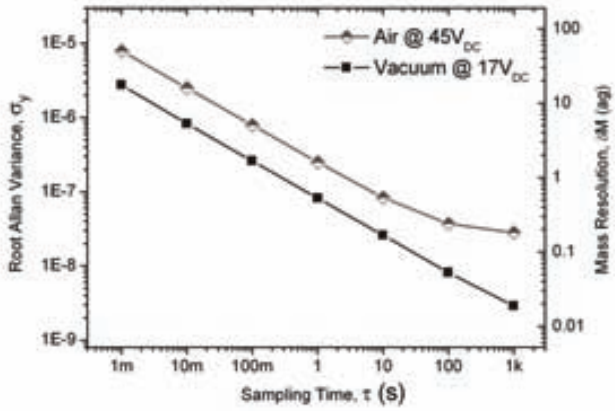

Figure 6.3.7 Allan deviation as a function of averaging time and the corresponding mass resolution in air and vacuum of the cantilever based oscillator.

- **PERFORMANCE AT HIGHER BIAS VOLTAGES**

We have observed that the use of higher resonator bias voltages (V_{DC}) reduces the measured phase noise of the resonator. In this case, it is appreciated that the output voltage waveform becomes asymmetric and distorted as the bias voltage is increased (Fig. 6.3.8).

As the bias voltage is increased the vibration amplitude of the resonator increases generating a higher AC voltage signal that is limited by the voltage swing of the sustaining amplifier that at the same time limits the AC signal that feedbacks to the resonator. Since the voltage swing is not symmetric, the oscillator output signal is only attenuated for negative values. On the other hand, the distortion of the signal is produced by the nonlinear performance of the electrostatic transduction which effects increase as the bias voltage is increased.

Despite of the distortion of the oscillator output signal, it presents a lower phase noise than for lower bias voltages. This fact would have to mean a reduction of the oscillator frequency fluctuations and consequently an improvement on the mass resolution of the sensor. With these conditions, it is very difficult to identify the types of noise sources presents on the phase noise

spectrum and consequently is not possible to evaluate the Allan variance from these measurements. In this sense, a direct measurement of the Allan variance using a counter would be necessary in order to corroborate this assumption.

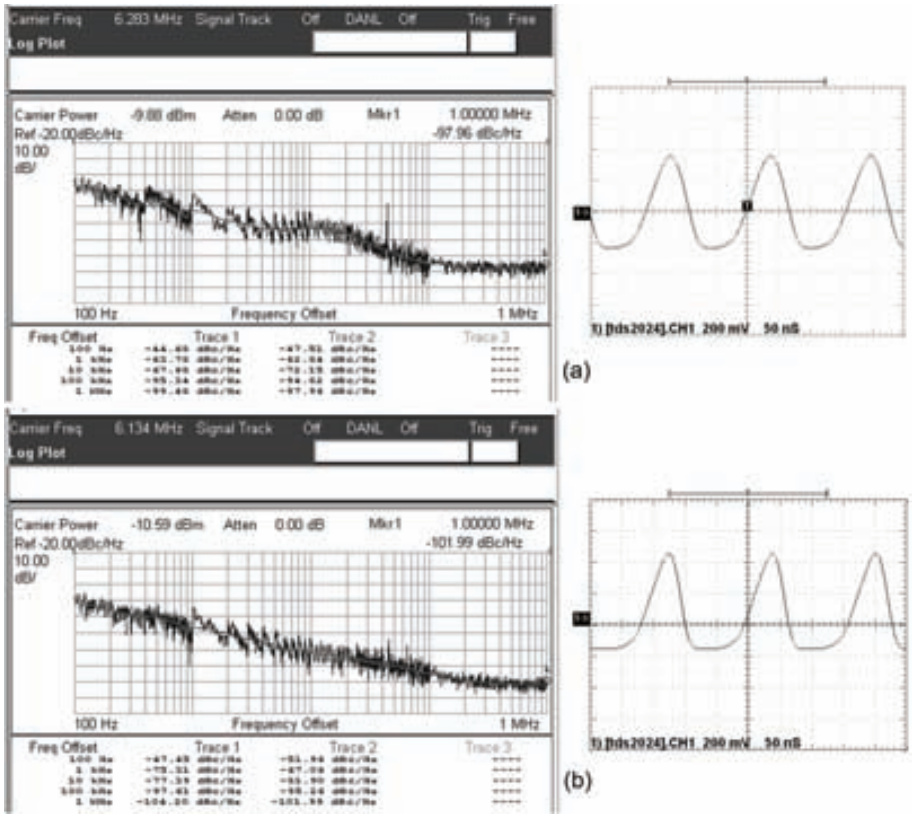

Figure 6.3.8 Plot of the phase noise and oscilloscope waveform of the cantilever based oscillator output for a bias voltage of 50 V (a) and 65 V (b).

6.3.2 CC-BEAM BASED OSCILLATOR

The CC-Beam resonator used in the oscillator circuit is also the same that presented in Chapter 5, a metal beam 18 μm long, 600 nm wide and 750 nm thick with a gap to the electrodes of 600 nm.

Fig. 6.3.9a shows the power spectrum, measured with the spectrum analyzer, of the CC-Beam based oscillator output over 600 kHz range centered on the carrier frequency that is located at 15.36 MHz. On the other hand, Fig. 6.3.9b shows the time waveform obtained with the oscilloscope. The oscillator output signal amplitude measured with the oscilloscope is around 420 mV_{pp}. In this case the amplitude is limited by the resonator nonlinearity that induces a variation of the resonator motional resistance that decrease as the excitation voltage increase. It is also

appreciated a higher signal distortion with respect to the cantilever-based oscillator. In this sense, an automatic level control (ALC) circuitry should be used for more precise control of oscillation amplitude [Lin04].

These results have been obtained in air conditions for a resonator bias voltage of V_{DC}=70 V. From experimental measurements, we found that the oscillator start-up is produced for bias voltages higher than 65 V.

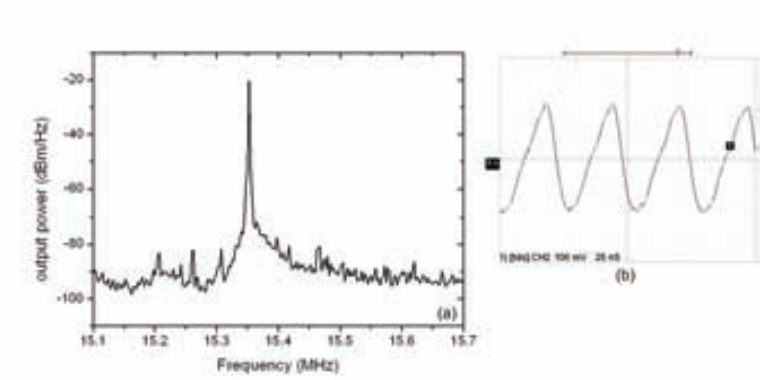

Figure 6.3.9 Power spectrum (a) and oscilloscope waveform (b) of the CC-Beam based oscillator measured in air conditions (V_{DC}=70V).

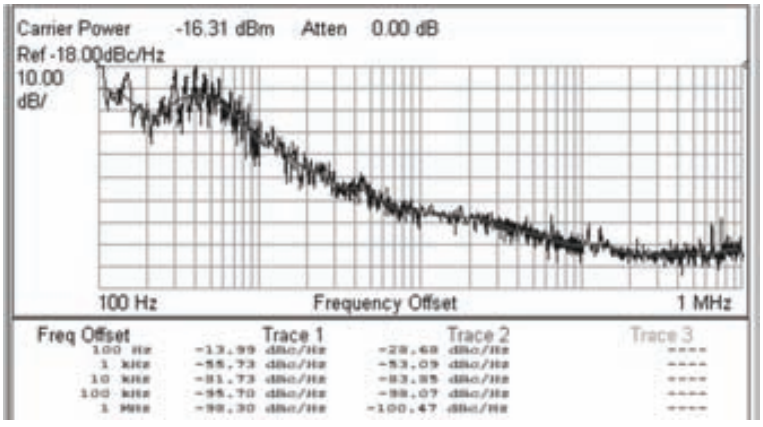

Figure 6.3.10 Measured phase noise versus frequency offset from the carrier (@ 15.36 MHz) of the CC-Beam based oscillator measured in air (V_{DC}=70V).

- **PHASE NOISE**

The experimental results presented in Fig. 6.3.10 show a noise floor of *L(f)*=-100.47 dBc/Hz from the carrier with a power of P_c=-16.3 dBm that is lower than for the cantilever-based oscillator. The noise of the sustaining amplifier results in this case -114 dBm/Hz that is

corresponding with an output voltage noise density of $0.45\mu V/Hz^{1/2}$. This value is lower than the obtained for the cantilever-based oscillator since in this case the sustaining circuit is operating at a higher frequency exhibiting a lower gain (see Chapter 4).

The measured close-to-carrier phase noise is higher than the measured for the cantilever-based oscillator. On the other hand, at offset frequencies higher than 10 kHz the noise becomes lower than for the cantilever since it is limited by the sustaining amplifier as we previously commented. With this phase noise performance it is expected that the frequency stability of the CC-Beam oscillator will be worse than for the cantilever oscillator.

- **PERFORMANCE AT VACUUM**

This oscillator has been also measured in vacuum conditions (1×10^{-2} mbar). In this case, the peak of the measured output spectrum (Fig. 6.3.11a) is also narrower than in air since the quality factor of the resonator is higher. On the other hand, the oscillator output signal amplitude measured with the oscilloscope is around 430 mV_{pp} quite similar to that obtained in air conditions. In these vacuum conditions, the oscillator start-up is produced for bias voltages higher than 29 V.

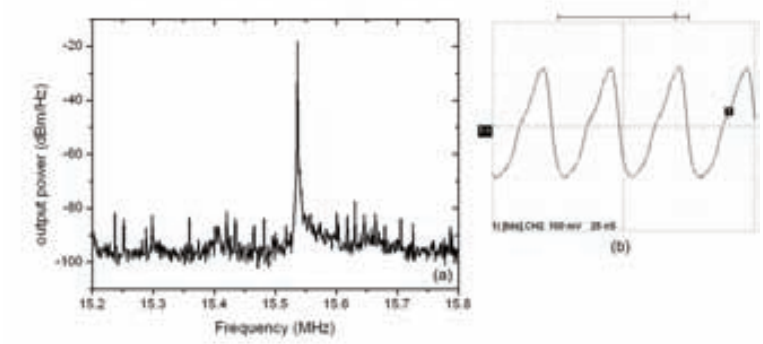

Figure 6.3.11 Power spectrum (a) and oscilloscope waveform (b) of the CC-Beam based oscillator measured in vacuum (V_{DC}=30V).

The plot of the measured phase noise is presented in Fig. 6.3.12. In this case, the close-to-carrier noise is lower than the measured in air conditions mainly due to the higher quality factor. As in the case of the cantilever, the $1/f^3$ noise component is also reduced in vacuum since the use of a lower bias voltage. On the other hand, the noise floor measured is in this case $L(f)$=-101.3 dBc/Hz from the carrier with a power of P_c=-14.7 dBm, resulting a noise value of the sustaining amplifier of -113 dBm/Hz that is quite similar to the value obtained in air conditions since the far-from-carrier noise only depends on the sustaining circuit noise.

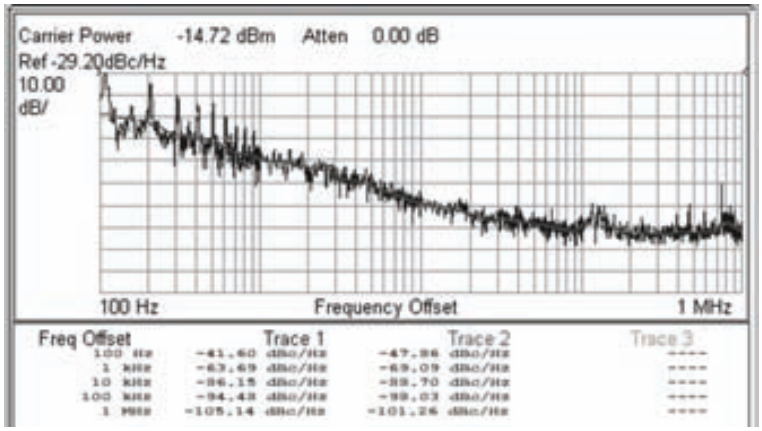

Figure 6.3.12 Measured phase noise versus frequency offset from the carrier of the CC-Beam based oscillator measured in vacuum (V_{DC}=30V).

6.3.3 COMPARATIVE

Table 6.1 summarizes the phase noise performance of the metal CC-Beam and cantilever oscillators designed and measured in this thesis. It is appreciated that in terms of the close-to-carrier phase noise, the best result is achieved with the cantilever oscillator working in vacuum conditions. The CC-beam oscillator is worse in these terms than the cantilever both in air and in vacuum conditions. In this sense, it is expected that the frequency noise or fluctuations of the CC-beam will be higher than the cantilever oscillator. In any case, this assumption would have to be corroborated with experimental measurements of the frequency fluctuation in the time domain (i.e. using a counter).

Table 6.1 Summary of the phase noise performance of the metal MEMS based oscillators.

			$L(f_m)$				
MEMS resonator	V_{DC}	P_C (dBm)	100 Hz	1 kHz	10 kHz	100 kHz	1 MHz
Cantilever (Air)	45	-10.69	-32.08	-55.62	-75.65	-91.58	-9426
CC-Beam (Air)	70	-16.31	-28.68	-53.09	-83.85	-98.07	-100.47
Cantilever (Vacuum)	17	-10.26	-60.71	-68.55	-85.76	-95.00	-95.25
CC-Beam (Vacuum)	30	-14.72	-47.86	-69.09	-88.70	-98.03	-101.26

6.4 CONCLUSIONS

A specific CMOS oscillator circuit adapted to work with two metal resonators (cantilever and CC-beam) has been designed and electrically characterized. The results obtained demonstrate the feasibility of direct on-chip measurements of the resonance frequency of a high-sensitivity resonator by integrating the resonator in a CMOS oscillator circuit. It makes potentially possible to achieve mass resolutions in the attogram range with a completely portable sensor device.

Table 6.2 presents the experimental parameters of the metal cantilever and CC-Beam oscillators presented in this Chapter. The CC-beam needs a higher bias voltage to oscillate than the cantilever that also provides a higher output voltage. With these results and considering that the mass sensitivity of the two devices is similar and taking into account than the CC-beam oscillator seems to be noisier than the cantilever oscillator, the first conclusion is that the cantilever oscillator is superior to the CC-beam oscillator in mass sensing applications. Additional measurements related with the long term stability and temperature dependence of these devices are necessary to demonstrate the superiority of the cantilever in front of the CC-beam.

Finally, a fully integrated mass sensor system may include an on-chip counter in order to measure and digitally code the frequency of the oscillator output signal. This approach is used in quartz crystal microbalance-based sensors [Bee04].

Table 6.2 Experimental parameters of the metal CMOS-MEMS oscillator circuits in air and in vacuum.

Parameter (Air/Vacuum)	**Cantilever**	**CC-Beam**	**Units**
Technology	AMS-C35		––
IC Voltage Supply, V_{DD}	3.3		V
Power Consumption, P	17.8		mW
Layout Area	420 × 150		μm × μm
Resonator Bias Voltage, V_{DC}	45 / 17	70 / 30	V
Oscillation output frequency, f_c	6.32 / 6.44	15.36 / 15.54	MHz
Oscillator output voltage (@ 50Ω)	-10.7 / -10.3	-16.3 / -14.7	dBm
Oscillator noise floor	-102 / -102.5	-113.8 / -113	dBm/Hz
Mass Sensitivity, $\Re^1$	0.9	1.4	ag/Hz
Frequency Fluctuation, $<\delta f_o/f_o>_{\tau=1s}$	0.25 / 0.08	---	ppm
Mass resolution, δM	1.4 / 0.47	---	ag

REFERENCES

[All88] D. Allan, H. Hellwig, P. Kartaschoff, J. Vanier, J. Vig, G. M. R. Winkler, and N. F. Yannoni, "Standard terminology for fundamental frequency and time metrology", in *Proc. 42nd Annu. Freq. Control Symp.*, Jun. 1-3, pp. 419-425, 1988.

[Bat01] F. M. Battiston, J. P. Ramseyer, H. P. Lang, M. K. Baller, Ch. Gerber, J. K. Gimzewski, E. Meyer, H. J. Güntherodt, "A chemical sensor based on a microfabricated cantilever array with simultaneous resonance-frequency and bending readout", *Sensors and Actuators (B)*, vol. 77, pp. 122-131, 2001.

[Bee04] J. M. Beeley, C. Mills, P. A. Hammond, A. Glidle, J. M. Cooper, L. Wang, and D. R. S. Cumming, "All-digital interface ASIC for a QCM-based electronic nose", *Sens. Actutator B*, Chem., vol. 103, pp. 31-36, 2004.

[Bra06] O. Brand, "Microsensor Integration Into Systems-on-Chip", *Proceedings of the IEEE*, vol. 94 (6), pp. 1160-1176, 2006.

[Cle02] A. N. Cleland, M. L. Roukes, "Noise processes in nanomechanical resonators", *J. Appl. Phys.*, vol. 92 (5), pp. 2758-2769, 2002.

[Dür97] U. Dürig, H.R. Steinauer, N. Blanc, "Dynamic force microscopy by means of the phase-controlled oscillator method", *J. Appl. Phys.*, vol. 82, pp. 3641-3651, 1997.

[Kaa05] V. Kaakakari, J. K. Koskinen, and T. Mattila, "Phase Noise in Capacitively Coupled Micromechanical Oscillators", *IEEE Trans. Ultrason. Ferroelectr. Freq. Control* , vol. 52(12), pp. 2322-2331, Dec. 2005.

[Lee01] S. Lee, M. U. Demirci, and C. T.–C., "A 10-MHz Micromechanical Resonator Pierce Reference Oscillator for Communication", in *Proc. of Transducers'01*, June 10-14, pp. 1094-1097, 2001.

[Lee66] D. B. Leeson, "A simple model of feedback oscillator noise spectrum", *Proc. of the IEEE*, vol. 54, pp. 329-330, 1966.

[Lin04] Y. W. Lin, S. Lee, S.-S. Li, Y. Xie, Z. Ren, and C. T.–C. Nguyen, "Series-Resonant VHF Micromechanical Resonator Reference Oscillators", *IEEE J. Solid-State Circuit*, vol. 39 (12), pp. 2477, Dec. 2004.

[Lin05] Y. W. Lin, S.-S. Li, Z. Ren, and C. T.–C. Nguyen, "Low Phase Noise Array-Composite Micromechanical Wine-Glass Disk Oscillator", in *Proc. of International Electron Device Meeting 2005*, pp. 4, Dec. 2005.

[Ngu99] C.T.-C Nguyen and R.T. Howe, "An Integrated CMOS Micromechanical Resonator High-Q Oscillator", *IEEE J. Solid-State Circuits*, vol. 34, no. 4, pp. 440-455, April 1999.

[Ran05] P. Rantakari, V. Kaajakari, T. Mattila, J. Kiihamäki, A. Oja, I. Tittonen, and H. Seppä, "Low Noise, Low Power Micromechanical Oscillator", in *Proc. of Transducers'05*, June 5-9, pp. 2135-2138, 2005.

[Roe98] T.A. Roessig, R.T. Howe, A.P. Pisano, J.H. Smith, "Suface-micromachined 1MHz oscillator with low-noise pierce configuration", in *Proc. of the Solid-State Sensor and Actuators Workshop*, pp. 859-862, 1998.

[Ses02] A.A. Seshia, W.Z. Low, S.A. Bhave, R.T. Howe, and S. Montague, "Micromechanical Pierce Oscillator for Resonant Sensing Application", in *Proc. of 2002 International Conference on Modeling and Simulation of Microsystems*, pp. 162-165, 2002.

[Vit88] E.A. Vittoz, M.G.T. Degrauwe, and S. Bitz., "High-Performance Crystal Oscillator Circuits: Theory and Application", *IEEE J. Solid-State Circuits*, vol. 23 (3), pp. 774-783, 1988.

CHAPTER 7

CONCLUSIONS AND FUTURE WORK

In this Chapter, the general conclusions of this thesis are given. Some indications about a potential design optimization and extensions of this thesis work are commented as well as its application in the RF-MEMS field. Finally, a list of the publications and contributions to main conferences are provided.

7.1 GENERAL CONCLUSIONS

The main contribution of this Ph.D. thesis has been the design and implementation of CMOS-MEMS based mass sensors with ultrahigh mass and spatial resolution. These MEMS are based on a resonant beam structure with electrostatic actuation and capacitive readout performed by means of a monolithically integrated CMOS circuitry.

Some figures of merit were defined for a fair evaluation of the CMOS-MEMS performance both in terms of mass sensitivity and electrical characteristics in comparison with the state-of-the-art mass sensors.

Polysilicon cantilever resonators, with a width down to 500 nm and mass sensitivities of ~4 ag/Hz, have been successfully fabricated on pre-processed 2.5μm CMOS chips (CNM25 technology) using nanofabrication techniques (i.e. DWL or/and EBL) compatible with CMOS, and functionally tested.

A new technique that allows in a very simple manner to implement and integrate MEMS into a CMOS commercial technology has been developed. The structures are completely mechanized during the conventional CMOS process using a standard layer of a commercial 0.35μm CMOS technology (AMS-C35). Only a simple post-CMOS dielectric layer wet etching without any mask is used to release the resonators. In this sense, the complexity and cost of the fabrication process

have been drastically reduced compared with the Nanomass approach increasing also the throughput. 600-nm wide metal beam resonators (cantilevers and CC-beams) showing theoretical frequencies from 6MHz up to 14MHz and mass sensitivities of ~1ag/Hz have been successfully fabricated. In addition, 350-nm wide polysilicon resonators (cantilevers and CC-beams with effective masses of 0.4–1.1 pg) have been also fabricated showing theoretical frequencies higher than 10 MHz and unprecedented mass sensitivities for monolithic CMOS sensors of 65–130 zg/Hz.

High-sensitivity capacitive readout CMOS circuits have been specifically designed to detect and amplify the capacitive current generated due to the resonator displacement in order to measure its resonance frequency. In particular, an interfacing circuit that minimizes the parasitic capacitance at the sense node has been designed showing an equivalent transimpedance gain as high as 120 dBΩ (@ 10 MHz) and an input refereed current noise as low as 18 fA/√Hz (@ 10 MHz). The minimum detection displacement (MDD) has been defined as a figure of merit of the readout system and evaluated for the different CMOS-MEMS devices designed and fabricated in this thesis work. A theoretical MDD value as low as ~10 fm/√Hz have been obtained for the devices developed. In addition, a comparative study of the state-of-the-art, in terms of the MDD parameter, for different readout systems commonly used in MEMS resonators have been also performed. The study has demonstrated that the monolithic capacitive readout system developed in this thesis is superior to other capacitive or piezoresistive readout systems and similar than the best optical readout systems reported with the additional benefit of allowing its use in system-on-chip applications.

An accurate electrical characterization, in air and in vacuum conditions, of the CMOS-MEMS devices have been performed corroborating the ability of the monolithic approach presented in measuring the frequency characteristics of sub-micrometer scale beam resonators. In particular, optimal electrostatic transduction has been obtained measuring frequency responses with high peaks (up to 20 dB or more) and large phase shifts (up to 160º) around the resonance frequency. In addition, measurements showing soft/hard-spring effect and hysteretic performance due to nonlinearities have been also reported for a metal cantilever and a polysilicon CC-beam. On the other hand, the high performance of the monolithic capacitive readout circuit designed in this thesis allows detecting the motion of a resonator, with motional resistances up to 44 MΩ, caused by its intrinsic thermomechanical noise. In particular, the thermomechanical noise has been observed, in air and in vacuum, for a metal cantilever resonator demonstrating the noise-matching between the resonator and the readout circuit.

A calibration of metal resonators has been performed by depositing MgF_2 thin layers. The measured mass sensitivity values were 0.9 ag/Hz and 1.7 ag/Hz for a cantilever and a CC-beam respectively which are in good agreement with the theoretical predicted values. Different time-resolved mass measurement experiments have been also performed by exposing the device to a gold atom flux that is controlled by a shutter. The results obtained indicate a good stability and repeatability of the device on detecting on-line small mass depositions down to ~1 fg.

The best resolution has been achieved for an AMS-C35 polysilicon cantilever being of only ~30 zg/√Hz (equivalent to ~6 pg/cm^2√Hz) in vacuum conditions.

A specific CMOS Pierce oscillator circuit adapted to work with the AMS-C35 metal resonators (cantilever and CC-beam) has been designed and electrically characterized. The cantilever-based oscillator shows an Allan deviation of 2.5×10^{-7} ($\tau = 1$) corresponding with a frequency fluctuation of 1.59 Hz (0.3 ppm) leading to an unprecedented mass resolution for a fully integrated MEMS oscillator of $\delta M = 1.4$ ag.

I also want to indicate a minor contribution for CMOS-MEMS design: the development of an analog HDL model (Verilog-A module) to allow system-level electrical simulations of the mixed CMOS-MEMS using a standard IC CAD environment.

The results obtained in this thesis demonstrate the feasibility of direct on-chip measurements of the resonance frequency of a high-sensitivity resonator by monolithically integrating the resonator in a CMOS oscillator circuit making potentially possible to achieve mass resolutions in the attogram range with a completely portable sensor device.

7.2 DESIGN OPTIMIZATION AND EXTENSIONS

The $1/f^3$ component in the measured phase noise spectrum of the metal resonator based oscillators may degrade the frequency stability of the oscillator and in consequence the mass resolution of sensor. Although the mechanism behind the generation of $1/f^3$ phase noise is not well-established, the group of Prof. Nguyen has experimentally observed that the use of an automatic level control (ALC) circuit in the oscillator design removes the $1/f^3$ component at small offset frequencies [Lee03]. In this sense the new CMOS-MEMS oscillator designs may include an ALC module in order to analyze the improvement on the frequency stability. This module can be included in the oscillator circuit as depicted in Figure 6.1. The ALC module reads the amplitude of the oscillator voltage signal and adjusts the gain of the oscillator loop by controlling the current bias of the sustaining amplifier and in consequence its effective transimpedance gain.

On the other hand, the AMS-C35 polysilicon resonators presented in this thesis shows excellent theoretical mass sensitivities being in the zeptogram range. In addition, the use of the poly1-poly2 capacitor module allows a reduction of the gap improving the electrostatic transduction (higher t/s ratio) which allows operating the resonators with low DC-bias voltages. This good electrostatic transduction has a negative aspect since the resonator presents a hysteretic or nonlinear performance at low driving signals (V_{AC} > -25 dBm). In this sense, in order to operate in the linear regime a clamping amplifier circuit may be added to the oscillator loop as depicted in Figure 7.1. This circuit limits the output voltage swing of the signal applied to the driver electrode, in order to operate the resonator at low oscillation amplitudes. The proposed is reducing the voltage swing in the oscillator loop but not altering the oscillator loop gain.

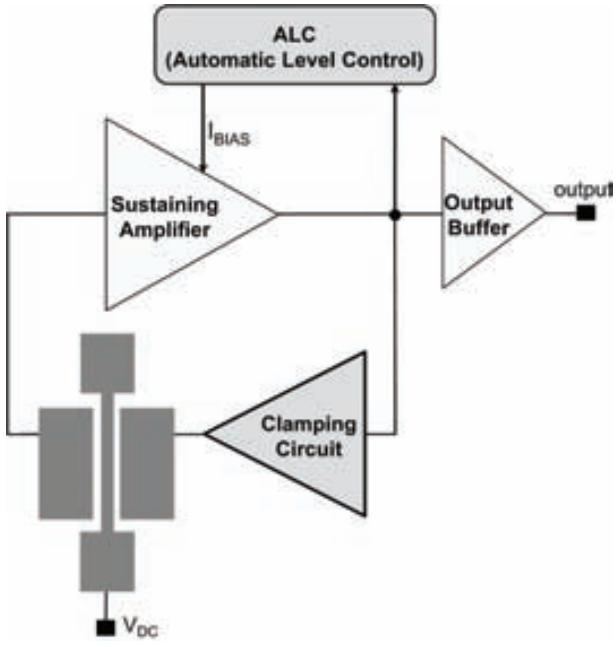

Figure 7.1 Circuit schematic of the MEMS oscillator circuit with an optimization design.

7.3 APPLICATION TO RF-MEMS

Despite the resonators presented in this thesis have been designed and optimized for mass sensing, their performance in RF applications have been also studied. In particular, the operation of the AMS-C35 polysilicon CC-beam resonator as mixer-filter (Mixler) has been demonstrated in down converting signals up to 1 GHz to 22.5 MHz [Ura07].

A figure of merit of the MEMS resonators is the product $Q \times f$ that depends of their mechanical characteristics. Using specific MEMS technology, standalone resonators presenting a $Q \times f$ product higher than 10^{12} Hz have been fabricated as indicated in Figure 7.2. In the case of CMOS-MEMS the $Q \times f$ product is limited by the characteristics of the standard CMOS layers used to fabricate the resonators. In this sense, the best reported $Q \times f$ product for CMOS-MEMS resonators is around two orders of magnitudes lower than for standalone MEMS resonators (see Figure 6.2).

On the other hand, from Figure 6.2 can be observed than the AMS-C35 resonators designed and presented in this thesis work (see Chapter 5) presents a $Q \times f$ product similar or even superior to the state-of-the art of CMOS-MEMS resonators. In particular, the higher $Q \times f$ measured was $3500 \times 11\text{MHz} \approx 4 \cdot 10^{10}$ Hz for the polysilicon cantilever resonator being higher than the best past CMOS-MEMS device.

Moreover, J. Teva have worked on the optimization of the Nanosys fabrication approach presented in this thesis for developing CMOS-MEMS resonators in the VHF and UHF range for RF applications [Tev07]. In particular, a 290-MHz polysilicon CC-beam resonator with only 40nm lateral gap has been fabricated showing a quality factor of ~ 3000 in vacuum conditions which is corresponding with a figure of merit $Q \times f$ as high as $9 \cdot 10^{11}$ Hz that is more than one order of magnitude superior that the best CMOS-MEMS resonator reported.

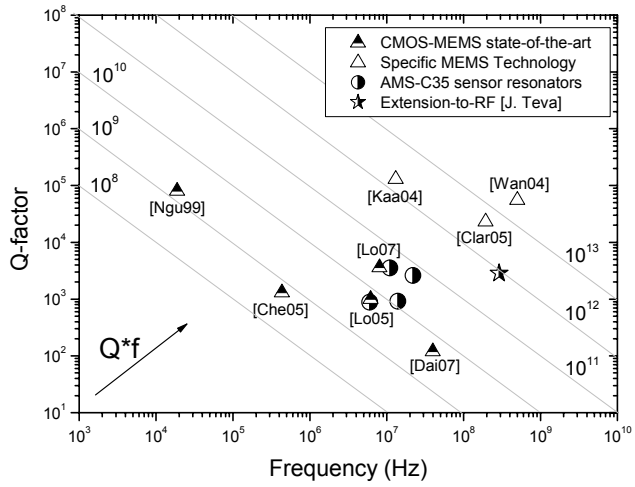

Figure 7.2 State-of-the-art of MEMS resonators from the point of view of the product $Q \times f$.

7.4 CONTRIBUTIONS OF THE AUTHOR

In this section, the contributions of this thesis work as articles published in international journals with ISI index (in inverse chronological order) are listed as well as a selection of the most relevant contributions to international conferences with peer review process.

Articles in international journals

[A1] **J. Verd**, A. Uranga, G. Abadal, J. Teva, F. Torres, J.L. López, F. Pérez-Murano, J. Esteve, N. Barniol, "Monolithic CMOS MEMS Oscillator Circuit for Sensing in the Attogram Range", *IEEE Electron Device Letters*, vol. 29 (2), pp. 146-148, Feb. 2008.

[A2] **J. Verd**, A. Uranga, G. Abadal, J. Teva, F. Pérez-Murano, N. Barniol, "High-Sensitivity Capacitive Sensing Interface for Monolithic CMOS M/NEMS Resonators", *Electronics Letters*, vol. 43, 23, pp. 1274-1276, 2007.

[A3] M. Villarroya, G. Abadal, **J. Verd**, J. Teva, F. Pérez-Murano, E. Figueras, J. Montserrat, A. Uranga, J. Esteve, N. Barniol, "Time resolved evaporation rate of attoliter glycerine drops using on-chip CMOS mass sensors based on resonant silicon micro cantilevers", *IEEE Transactions on Nanotechnology*, vol. 6 (5), pp. 509-512, 2007.

[A4] **J. Verd**, A. Uranga, G. Abadal, J. Teva, F. Torres, F. Pérez-Murano, J. Fraxedas, J. Esteve, N. Barniol, "Monolithic mass sensor fabricated using a conventional technology with attogram resolution in air conditions", *Applied Physics Letters*, vol. 91 (1), pp. 013501, 2007.

[A5] A. Uranga, **J. Verd**, J.L. López, J. Teva, G. Abadal, F. Torres, J. Esteve, F. Pérez-Murano and N. Barniol, "Fully integrated MIXLER based on a VHF CMOS-MEMS clamped-clamped beam resonator", *Electronics Letters*, vol. 43 (8), pp. 452-454, 2007.

[A6] A. Uranga, **J. Verd**, F. Torres, J. Teva, J.L. López, G. Abadal, J. Esteve, F. Pérez-Murano and N. Barniol, "Electrical detection of multiple resonant modes in a CMOS-MEMS cantilever", *Microelectronic Engineering*, vol. 84 (5-8), pp. 1374-1378, 2007.

[A7] M. Villarroya, E. Figueras, J. Montserrat, **J. Verd**, J. Teva, G. Abadal, F. Pérez-Murano, J. Esteve, and N. Barniol, "A platform for monolithic CMOS-MEMS integration on SOI wafers", *Journal of Micromechanics and Microengineering*, vol. 16, pp. 2203-2210, 2006.

[A8] M. Villarroya, E. Figueras, **J. Verd**, J. Teva, G. Abadal, F. Pérez-Murano, J. Montserrat, A. Uranga, J. Esteve, N. Barniol, "CMOS-SOI platform for the monolithical integration of crystalline silicon MEMS", *Electronics Letters*, vol. 42 (14), pp. 800-801, 2006.

[A9] M. Villarroya, **J. Verd**, J. Teva, G. Abadal, E. Forsen, F. Pérez-Murano, A. Uranga, E. Figueras, J. Montserrat, J. Esteve, A. Boisen, N. Barniol, "System on chip mass sensor based on polysilicon cantilevers arrays for multiple detection", *Sensors and Actuators A-Physical*, vol. 132, pp. 154-164, 2006.

[A10] **J. Verd**, J. Teva, J. Teva, J. L. Lopez, F. Torres, J. Esteve, G. Abadal, F. Perez-Murano, N. Barniol, "Integrated CMOS-MEMS with On-Chip Readout Electronics for High-Frequency Applications", *IEEE Electron Device Letters*, vol. 27 (6), pp. 495-497, 2006.

[A11] J. Teva, G. Abadal, F. Torres, **J. Verd**, F. Perez-Murano, N. Barniol, "A femtogram resolution mass sensor platform, based on SOI electrostatically driven resonant cantilever. Part I: electromechanical model and parameter extraction", *Ultramicroscopy*, vol. 106 (8-9), pp. 800-807, 2006.

[A12] J. Teva, G. Abadal, F. Torres, **J. Verd**, F. Perez-Murano, N. Barniol, "A femtogram resolution mass sensor platform, based on SOI electrostatically driven resonant cantilever. Part II: sensor calibration and glycerine evaporation rate measurement", *Ultramicroscopy*, vol. 106 (8-9), pp. 808-814, 2006.

[A13] A. Uranga, J. Teva, **J. Verd**, J.L. López, F. Torres, J. Esteve, G. Abadal, F. Pérez-Murano and N. Barniol, "Fully CMOS integrated low voltage 100 MHz MEMS resonator", *Electronics Letters*, vol. 41 (24), pp. 1327-1328, 2005.

[A14] E. Forsen, G. Abadal, S Ghatnekar-Nilsson, J. Teva, **J. Verd**, R. Sandberg, W. Svendsen, F. Perez-Murano, J. Esteve, E. Figueras, F. Campabadal, L. Montelius, N. Barniol, A. Boisen, "Ultrasensitive mass sensor fully integrated with complementary metal-oxide-semiconductor circuitry", *Applied Phsyics Letters*, vol. 87 (4), pp. 04357, 2005.

[A15] S Ghatnekar-Nilsson, E Forsen, G Abadal, **J Verd**, F Campabadal, F Perez-Murano, J Esteve, N Barniol, A Boisen and L Montelius, "Resonators with integrated CMOS circuitry for mass sensing applications fabricated by electron beam lithography", *Nanotechnology*, vol. 16 (1), pp. 98-102, 2005.

[A16] **J. Verd**, G. Abadal, J. Teva, M. Villarroya, A. Uranga, X. Borrisé, F. Campabadal, J. Esteve, E. Figueras, F. Pérez-Murano, Z.J. Davis, E. Forsen, A. Boisen and N. Barniol, "Design, fabrication and characterization of a submicroelectromechanical resonator with monolithically integrated CMOS readout circuit", *Journal of Microelectromechanical Systems*, vol. 14 (3), pp. 508-519, 2005.

[A17] E. Forsén, SG. Nilsson, P. Carlberg, G. Abadal, F. Pérez-Murano, J. Esteve, J. Montserrat, E. Figueras, F. Campabadal, **J. Verd**, L. Montelius, N. Barniol and A. Boisen, "Fabrication of cantilever based mass sensors integrated with CMOS using direct wrtite laser lithography on resist", *Nanotechnology*, vol. 15 (10), pp. S628-S633, 2004.

[A18] J.Teva, G.Abadal, Z.J.Davis, **J.Verd**, X.Borrisé, A.Boisen, F.Pérez-Murano, N.Barniol, "On the electromechanical modelling of a resonating nano-cantilever-based transducer", *Ultramicroscopy*, vol. 100, pp. 225-232, 2004.

[A19] Z.J. Davis, G. Abadal, B. Helbo, O. Hansen, F. Campabadal, F. Pérez-Murano, J. Esteve, E. Figueras, **J. Verd**, N. Barniol, A. Boisen, "Monolithic integration of mass sensing nano-cantilevers with CMOS circuitry", *Sensors and Actuators A-Physical*, vol. 105, pp. 311-319, 2003.

Abstracts in peer review proceedings

[C1] **J.Verd**, A.Uranga, J.Teva, G.Abadal, F.Torres, J. Arcamone, J.L.López, F.Pérez-Murano, J. Fraxedas, J. Esteve and N. Barniol, "Monolithic 0.35-µm cmos cantilever for mass sensing in the attogram range with self-excitation", in Proc. of *14th International Conference on Solid-State Sensors, Actuators and Microsystems (TRANSDUCERS'07)*, pp. 233-236, June. 2007.

[C2] **J. Verd**, A. Uranga, J. Teva, G. Abadal, F. Torres, F. Pérez-Murano, J. Esteve, N.Barniol, "CMOS Cantilever-Based Oscillator for Attogram Mass Sensing", in Proc. of *IEEE International Symposium on Circuits and Systems, 2007 (ISCAS 2007)*, pp. 3319-3322, May. 2007.

[C3] A. Uranga, **J. Verd**, F. Torres, J. Teva, J. L. López, G. Abadal, J. Esteve, F. Pérez-Murano, N. Barniol, "Electrical detection of multiple resonant modes in a CMOS-MEMS cantilever", in Proc. of *32nd International Conference on Micro- and Nano-Engineering 2006 (MNE'06)*, vol., , pp. -, Sep. 2006.

[C4] M. Villarroya, G. Abadal, **J. Verd**, J. Teva, A. Uranga, F. Pérez-Murano, E. Figueras, J. Montserrat, J. Esteve, N. Barniol, "Dynamics of attolitter glycerine drops evaporation using a CMOS-MEMS mass sensor", in Proc. of *32nd International Conference on Micro- and Nano-Engineering 2006 (MNE'06)*, pp. 137-138, Sep. 2006.

[C5] J.Teva, **J.Verd**, G.Abadal, A.Uranga, F.Torres, J.L.López, J.Esteve, F.Pérez-Murano, N.Barniol, "Fabrication of monolithic MEMS-CMOS devices using a standard 0.35um commercial technology for sensor and RF applications", in Proc. of *32nd International Conference on Micro- and Nano-Engineering 2006 (MNE'06)*, vol., , pp. -, Sep. 2006.

[C6] A. Uranga, J. Teva, **J. Verd**, J. L. López, F. Torres, G. Abadal, J. Esteve, F. Pérez-Murano, and N. Barniol, "CMOS Integrated MEMS Resonator for RF Applications", in Proc. of *IEEE International Symposium on Circuits and Systems, 2006 (ISCAS 2006)*, pp. 2301-2304, May 2006.

[C7] **J. Verd**, G. Abadal, J. Teva, A. Uranga, F. Torres, F. Pérez-Murano, J. Esteve, N. Barniol, "Attogram/Hz Sensitivity Mass Sensor Monolithically Integrated with Capacitive Readout Electronics in a Standard 0.35-um CMOS Process", in Proc. of *International Workshop on Nanomechanical Sensors 2006 (IWNS'06)*, pp. 106-107, May 2006.

[C8] **J. Verd**, G. Abadal, J. Teva, A. Uranga, F. Pérez-Murano, J. Esteve, N. Barniol, "Resonant Metal Cantilever with Attogram/Hz Mass Sensitivity Fully Integrated in a Standard 0.35-um CMOS Process", in Proc. of *19th International Conference on MicroElectroMechanical Systems (MEMS 2006)*, pp. 638-641, Jan. 2006.

[C9] **J. Verd**, J. Teva, G. Abadal, F. Pérez-Murano, J. Esteve, N. Barniol, "Large-signal model of a resonating cantilever-based transducer for system level electrical simulation", in Proc. of *SPIE´s International Symposium on Microtechnologies for the New Millenium 2005*, vol. 5836, pp. 98, 2005.

[C10] **J. Verd**, G. Abadal, J. Teva, A. Uranga, J. Esteve, M. Duch, F. Perez-Murano, N. Barniol, "High-sensitivity capacitive readout system for resonant submicrometer-scale cantilevers based sensors", in Proc. of *IEEE International Symposium on Circuits and Systems, 2005 (ISCAS 2005)*, vol. 5, pp. 4209-4212, May 2005.

REFERENCES

[Che05] F. Chen, J. Brotz, U. Arslan, C-C. Lo, T. Mukherjee, and G.K. Fedder, "CMOS-MEMS resonant RF mixer-filters", *in Proc. of MEMS'05*, pp. 24-27, 2005.

[Cla05] J.R. Clark, W.-T. Hsu, M.A. Abdelmoneum, and C.T.-C. Nguyen, "High-Q Micromechanical Radial-Contour Mode Disk Resonators", *Journal of Microelectromechanical Systems*, vol. 14 (6), pp.1298-1310, 2005.

[Dai07] C.-L. Dai, M.-C. Chiang, M.W. Chang, "Simulation and fabrication of HF microlectromechanical bandpass filter", *Microelectronics Journal*, vol. 38, pp. 828-833, 2007.

[Kaa04] V. Kaajakari, T. Mattila, A. Oja, J. Kiihamäki, and H. Seppä, "Square-Extensional Mode Single-Crystal Silicon Micromechanical Resonator for Low-Phase-Noise Oscillator Applications", *IEEE Electron Device Letters*, vol. 25 (4), pp. 173-175, 2004.

[Lee03] S. Lee, and C.T.-C. Nguyen, "Influence of automatic level control on micromechanical resonator oscillator phase noise", *in Proc. of the 2003 IEEE International Frequency Control Symposium and PDA Exhibition*, pp. 341-349, 2003.

[Lo05] C.-C. Lo, C. Fang, and G.K. Fedder, "Integrated HF CMOS-MEMS square-frame resonators with on-chip electronics and electrothermal narrow gap mechanism", *in Proc. of Transducers'05*, vol. 2, pp. 2074-2077, 2005.

[Lo07] C.-C. Lo, and G.K. Fedder, "On-chip high quality factor CMOS-MEMS silicon-fin resonators", *in Proc. of Transducers'07*, pp. 2449-2452, 2007.

[Ngu99] C.T.-C Nguyen and R.T. Howe, "An Integrated CMOS Micromechanical Resonator High-Q Oscillator", *IEEE J. Solid-State Circuits*, vol. 34, no. 4, pp. 440-455, April 1999.

[Tev07] J. Teva, "Integration of CMOS-MEMS resonators for radiofrequency applications in the VHF and UHF bands", *PhD thesis,* Universitat Autonoma de Barcelona , July 2007.

[Ura07] A. Uranga, J. Verd, J.L. López, J. Teva, G. Abadal, F. Torres, J. Esteve, F. Pérez-Murano and N. Barniol, "Fully integrated MIXLER based on a VHF CMOS-MEMS clamped-clamped beam resonator", *Electronics Letters*, vol. 43 (8), pp. 452-454, 2007.

[Wan04] J. Wang, J.E. Butler, T. Feygelson, and C.T.-C. Nguyen, "1.51-GHz Nanocrystalline Diamond Micromechanical Disk Resonator with Material-Mismatched Isolating Support", *in Proc. of MEMS'04*, pp. 641-644, 2004.

APPENDIX A

VERILOG-A NONLINEAR ELECTROMECHANICAL MODEL

This Appendix presents a nonlinear electromechanical model for electrostatically excited beams that can be used for system level electrical simulations. The model takes into account non-linearities from variable beam-driver electrode gap, fringing field contributions and real deflection profile of the beam. The model is implemented into a Verilog-A module that allows its use in a common IC CAD environment like CADENCE. This compact macro-model allows its simulation of both cantilevers and CC-beams. Finally, small-signal and large-signal simulations of mixed CMOS MEMS are presented.

A.1 INTRODUCTION

To model the interaction of mechanical components with the electronics as well as to predict global performance of the mixed CMOS MEMS system, a system level electrical simulation becomes essential.

As we commented in Chapter 2, the beam-driver system can be represented by an equivalent circuit model (i.e. RLC//C) that allows its use in electrical circuit simulators such as SPICE [3,4]. However, it is a linear small-signal approximation that is only valid for small oscillation amplitudes of the beam. This approach is valid for stiff structures but becomes unrealistic for compliant cantilevers.

In this Appendix, it is presented a non-linear electromechanical model for an electrostatically driven resonating beam that accounts for non-linear effects. For the electrostatic force calculation the model takes into account the real deflection profile of the beam, the contribution to the beam-driver capacitance of the fringing field as well as the third order of nonlinearity in the spring constant.

In previous works [5, 6], we have presented a similar model that need the use of a FEM

simulator (i.e. SUGAR software) in order to obtain the beam deflection profile. In this work, the bema deflection profile coefficients are obtained using analytical expressions that allows its implementation using an analog hardware description language. The model proposed is able to carry out static and dynamic simulations using a common IC CAD environment without the need of any other software. Also, it allows the simulation of non-electrical variables of the structure as the mechanical oscillation amplitude or the beam velocity.

The movement equations of the beam electrostatically excited by a driver electrode are implemented in a single macro-model by using the Verilog-A language in a similar way that in [7]. This macro-model is valid for a clamped-free beams (cantilevers) and clamped-clamped beams (CC-beam). The global performance of the mixed CMOS MEMS system is simulated in an electrical simulator (i.e. SPECTRE) by connecting the behavioural model with CMOS circuitry.

A.2 ELECTROMECHANICAL MODEL DESCRIPTION

The resonant beam structure can be fully characterized by its geometrical, material and configuration parameters. Geometrical factors are cantilever length (l), width (w), thickness (t) and gap distance between the beam and driver (s). Material properties are determined by Young modulus (E) and mass density (ρ). Configuration parameters are referent to Fringing field factor (α) and quality factor (Q).

The model proposed is able to carry out static and dynamic simulations. Previous developed models, considered cantilever linear shape deflection [3, 4]. In this work we present a model that takes into account the real cantilever deflection, fringing field effect for the electrostatic excitation force calculation as well as third-order nonlinearity in the spring constant.

In contrast with the analysis presented in Chapter 2 and for convenience, the beam movement is considered to be in the z-direction for all the analysis presented in this section.

A.2.1 MOVEMENT EQUATION

The mechanical equation of the beam motion, in one dimension for an external force (F_E), with damping and third-order nonlinearity in the spring force is

$$m_{eff}\ddot{z} + D\dot{z} + kz + k_3 z^3 = F_E(z,t)\,. \tag{A.2.1}$$

In this model, the cubic spring coefficient (k_3) has also been added since its effect is important when working with rigid structures like a clamped-clamped beam. In the case of a cantilever, this term becomes irrelevant.

A.2.2 ELECTROSTATIC FORCE

The external forces applied to the beam are considered in the term F_E. Since our system is electrostatically coupled by two driver electrodes (D1, D2), we define the voltage that conforms each driver electrode with the cantilever electrode (C), as:

$$V_1(t) = V_{D1}(t) - V_C(t)$$
$$V_2(t) = V_{D2}(t) - V_C(t) \tag{A.2.2}$$

The term of the external forces F_E takes into account the two main features above presented: the beam real deflection profile and the fringing field correction. This last term, is modelized by an analytical equation that depends only on the beam-driver geometry. That term is inspired from a semi-empirical formulation developed to determine the fringing field contribution to adjacent lines in a CMOS circuitry [5]. Then the total electrostatic force applied to the cantilever can be written as:

$$F_{E-ff}(z,t) = F_E(z,t)\left(1 + \alpha\left(\frac{s}{t}\right)\left(\frac{w}{s}\right)^{0.222}\right), \tag{A.2.3}$$

introducing the fringing field factor (α) in order to adjust this contribution to the beam-drivers transducer.

$$F_{E_{\frac{1}{2}}}(z,t) = \frac{V_{\frac{1}{2}}^{\ 2}(t)}{2}\frac{\partial C_{\frac{1}{2}}}{\partial z}. \tag{A.2.4}$$

A.2.3 BEAM DEFLECTION PROFILE

The analysis of the beam deflection profile is performed using the same approach than Veijola et al. [8] in modeling a CC-beam structure. In this case, the analysis is extended for cantilever structures.

The dynamic displacement of the beam is strongly dependent on the position on the x-axis and in consequence a parallel plate assumption for the beam-driver capacitance is not enough accurate since. In this sense, the analytical solution of the beam deflection profiles is used.

The deflection profile (*z(x)*), between x_a and x_b positions (see Figure A.2.2), of an uniformly loaded beam for x_a<x< x_b are described for the equations A.2.5 and A.2.6, for a clamped-free beam and a clamped-clamped beam respectively [9].

1) Clamped-free Beam:

$$z(x_n) = \frac{x_a - x_b}{2k} W\left[\frac{1}{3}x_n^{\ 3} - \frac{x_a - x_b}{2}x_n^{\ 2}\right] + \frac{W}{24k}(x_n - x_a)^4 \tag{A.2.5}$$

2) Clamped-clamped Beam:

$$z(x_n) = \frac{M_A}{2k}x_n^{\ 2} + \frac{R_A}{6k}x_n^{\ 3} + \frac{W}{24k}(x_n - x_a)^4 \tag{A.2.6}$$

where W is the load, R_A is the reaction force and M_A the momentum, expressed by next equations:

$$R_A = \frac{W}{2l^3}\left[(l + x_b)x_a^{\ 3} - (l + x_a)x_b^{\ 3}\right] \tag{A.2.7}$$

$$M_A = \frac{W}{12l^2}\left[x_a{}^4 - x_b{}^4\right] - \frac{l}{3}R_A \cdot \tag{A.2.8}$$

The normalized deflection profile function *C(x)*, independent of the load (*W*) and the spring constant, is

$$C(x) = \frac{z(x)}{z_{\max}} \tag{A.2.9}$$

where z_{max} is the maximum deflection of the beam. This value is corresponding with *z(l)* and *z(l/2)* for a cantilever and a CC-beam respectively.

A.2.4 FINITE DIFFERENCE MODEL

Despite, an analytical transducer model could be derived from last equations; a finite difference method is used in order to avoid the calculation of tedious integrations. The total capacitance is calculated slicing the beam along its length (*x* direction) into *N* sections, and considering that each sliced beam creates a plane parallel capacitance with the driver. This is illustrated in Figure A.2.2.

The nominal displacement *z* is located at the center of the beam for a CC-beam and at the end free for a cantilever. These points are corresponding with the fictitious effective mass position. The resulting capacitance is

$$C_{\frac{1}{2}} = \varepsilon t \Delta x \sum_{n=0}^{N} \frac{A_n}{s_-^+ C_n z}, \tag{A.2.10}$$

where $C_n = C(x_n)$, $x_n = n \cdot \Delta x + x_a$, Δx is the length of one section and A_n is the weighting coefficient due to the numerical integration. The electrostatic force, distributed between x_a and x_b , is derived from equation A.2.4, resulting

$$F_{E\frac{1}{2}}(z,t) = \frac{V_{\frac{1}{2}}{}^2(t)}{2}\frac{\partial C_{\frac{1}{2}}}{\partial z} = {}_+^- \frac{V_{\frac{1}{2}}{}^2(t)}{2}\varepsilon t \Delta x \sum_{n=0}^{N} \frac{A_n}{\left(s_-^+ C_n z(t)\right)^2} \cdot \tag{A.2.11}$$

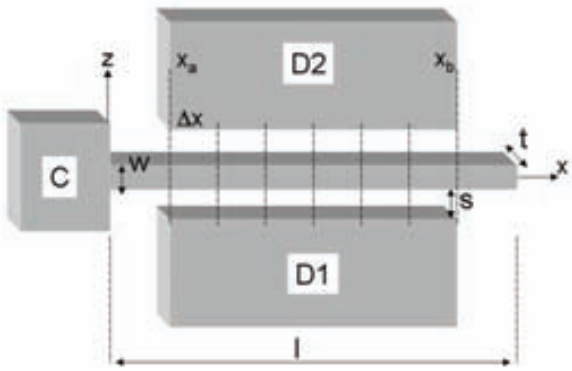

Figure A.2.1 Schematic illustrating the method of finite differences. The beam resonator is sliced in *N* sections (*N*=6 in this case) between positions x_a and x_b.

A.2.5 CURRENT CALCULATION

Finally, the currents generated at each driver-beam interface can be expressed as:

$$I_1(t) = C_1(t)\frac{\partial V_1}{\partial t} + V_1\frac{\partial C_1}{\partial t} \quad . \qquad (12)$$
$$I_2(t) = C_2(t)\frac{\partial V_2}{\partial t} + V_2\frac{\partial C_2}{\partial t}$$

A.3 MODEL INTEGRATION IN AN IC CAD TOOL

By means of the implementation of the equations described in last section with an electrical simulator we obtain an electromechanical model that accounts for nonlinear effects of the mechanical system and thus results more accurate than the simple *RLC* model, only valid for small-signal analysis.

Analog hardware description languages (AHDL) allow us to describe multi-domain systems like MEMS with an IC CAD tool. Therefore, electrical simulations of the mixed CMOS MEMS (mechanical structure plus CMOS circuitry) can be performed by using an electrical simulator. In the context of this thesis, we have developed a very compact macro-model using the Verilog-A description language that implements all the equations and aspects explained in the previous section and allows electromechanical simulations in an analog circuit design environment like CADENCE. The Verilog-A code of this electromechanical model is presented in the Annex I of this Chapter.

The beam-driver model is defined as a three ports system (Figure A.3.1). The ports defined are the two drivers (V_{D1} and V_{D2}) and the beam (V_C). These ports are defined as bi-directional, so the current can flow in any direction depending on the configuration used to excite the beam and to perform the electrical readout.

The main features of this macro-model are next summarized:

- Nonlinear model.
- Real deflection profile of the beam.
- Fringing field factor (α).
- 3 bi-directional electrical ports: driver 1, driver 2 and beam electrodes.
- 2 mechanical output ports: nominal displacement, velocity.
- User can define the driver position (x_a, x_b).
- Valid for clamped-clamped and clamped-free beams.
- Number of beam sections is an input parameter.

The user is able to modify all the input parameters of the macro-model (Fig. A.3.2) that are related with the geometrical dimensions of the beam-driver system, mechanical properties of the structural material (E, ρ), the dielectric constant, Q-factor, number of section (N), fringing field factor (α), cubic spring coefficient (k_3) as well as an integer parameter to select for clamped-free or clamped-clamped beam performance. This macro-model is valid in all analysis modes including AC, DC, transient, noise, PSS, parametric, etc.

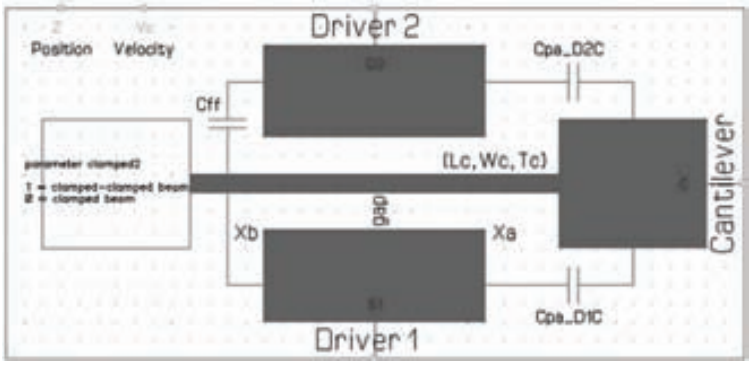

Figure A.3.1 Symbol view of the macro-model developed in CADENCE environment.

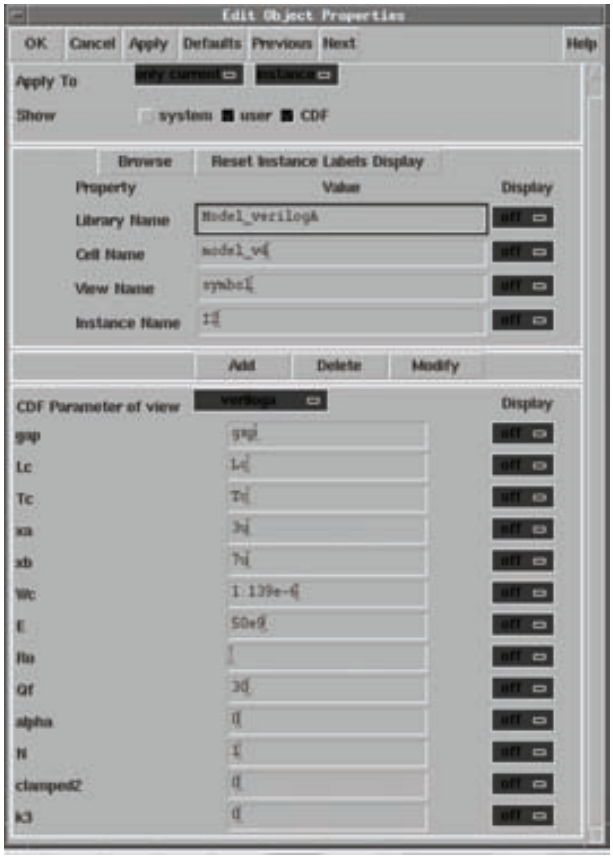

Figure A.3.2 CADENCE window for the edition of the beam parameters.

A.4 SYSTEM LEVEL ELECTRICAL SIMULATIONS

In this section are presented some system level electrical simulations of a mixed electromechanical design that includes both electronics and the Verilog-A electromechanical model. Figure 4.4.1 presents the schematic view of the system showing the symbol view of the macro-model developed connected with a readout CMOS circuit. In this case, the readout circuit is a transimpedance amplifier based on an operational amplifier with resistive feedback. The parameters used in these simulations are: l=10μm, w=500nm, t=925nm, s=750nm, Q=50, E=74GPa, ρ=2700kg/m^3.

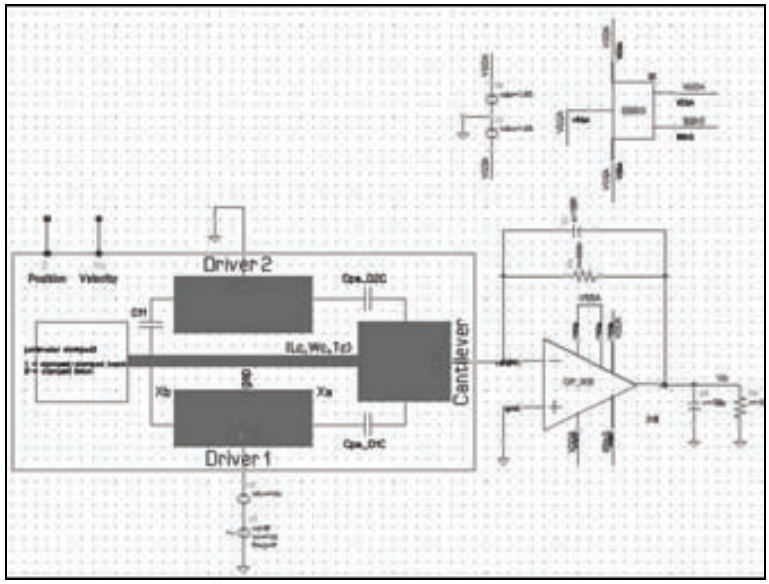

Figure A.4.1 Schematic view of the MEMS showing the symbol view of the macro-model developed connected with a CMOS readout circuit.

As we previously commented, the model proposed allows the simulation of non-electrical variables of the structure. In Figure A.4.2 is presented the voltage magnitude of the frequency response of the mixed CMOS MEMS system as well as the mechanical oscillation amplitude of the beam (cantilever in this case). We can observe the electrical resonance and anti-resonance of the electrical signal as well as the cantilever mechanical resonance. It can be noted the frequency shift between the mechanical resonance frequency and the electrical resonance frequency.

In Figure A.4.3 is presented the magnitude of the frequency response of the system for different DC voltages applied to the driver. In this plot we can observe that the resonance frequency depends on the DC voltage applied in a nonlinear relationship as we explained in Chapter 2.

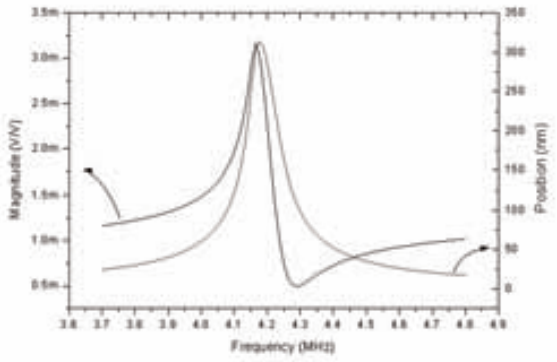

Figure A.4.2 Plot of the magnitude of the mixed CMOS MEMS as well as the mechanical oscillation amplitude of the cantiilever.

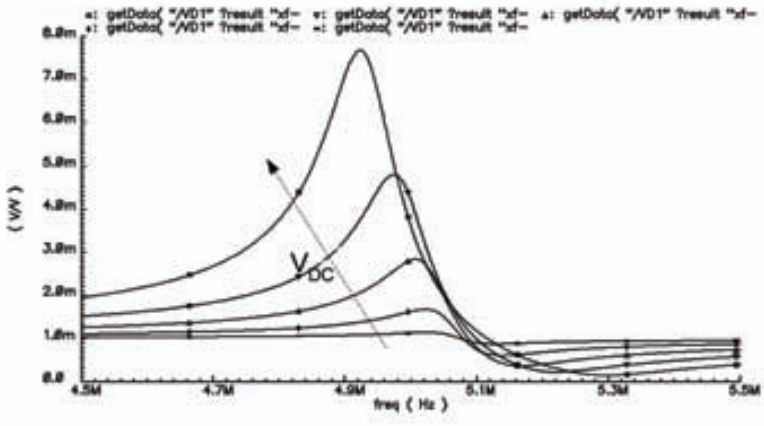

Figure A.4.3 Plot of the magnitude of the mixed CMOS MEMS versus frequency for different resonator bias voltages (10, 20, 30, 40, and 50 V).

A.4.1 DC ANALYSIS

With this type of analysis we are able to determine for example the snap-in voltage of the beam by plotting the beam nominal displacement (z) versus de DC voltage applied to the driver. In Figure A.4.4a we can observe that the snap-in voltage for a cantilever with the dimensions previously indicated is around 550 V since at this voltage the function tends to infinite. In the case of a CC-beam with the same dimensions, the snap-in voltage is over the 1000 V that is the maximum value of the voltage range used in the DC sweep simulation. For this voltage the nominal displacement of the CC-beam is only of 13 nm being the gap of 750 nm.

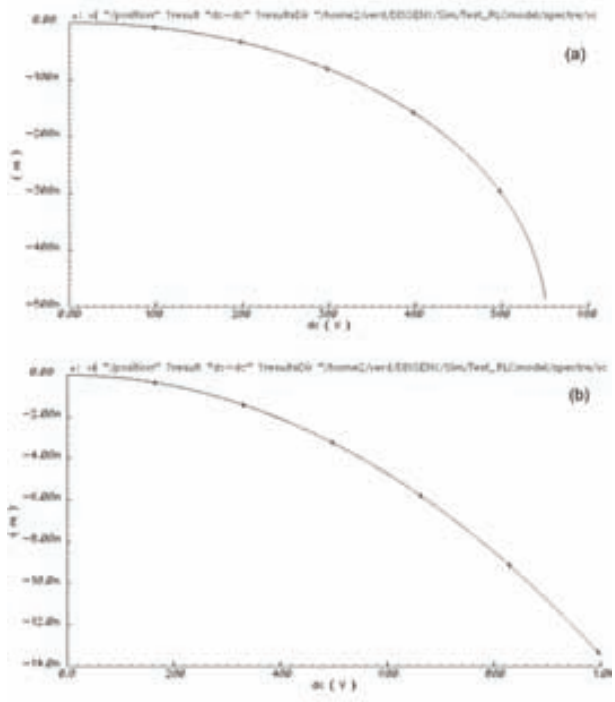

Figure A.4.4 Plot of the nominal resonator displacement versus de DC bias voltage for a cantilever (a) and for a CC-beam (b).

A.4.2 SMALL-SIGNAL ANALYSIS (AC)

A small-signal analysis performs a linearization of the system and therefore, this analysis does not take all the benefits of our model and it is only valid for small beam oscillations (i.e. V_{AC} small). In this case, the results obtained with using the RLC model will be similar than obtained using the nonlinear model for the same parameters.

A.4.3 LARGE-SIGNAL ANALYSIS: PERIODIC STEADY STATE (PSS)

Linear frequency-domain analysis (AC analysis) is not capable of reproducing the nonlinear large-signal characteristics that implements the model presented in this work. On the other hand, a transient analysis (TRAN analysis) handles the nonlinearities, but it is impractical in simulating frequency responses of high-Q resonating structures since for each point in the frequency response, a large number of signal periods are required before the starting transients have died out.

Figure A.4.5 shows the results obtained with a TRAN analysis for two different Q-factors. For a Q of 50, the settling time of the system needed to achieve the stationary state is 20 μs and for a Q of 1000 is 120 μs. On the other hand, the simulation time needed to calculate the steady-state of the system is around 17.5 s and 1m23s respectively.

The Periodic Steady State (PSS) analysis, available in SPECTRE, computes the system steady state in both time and frequency domains, so no linearization is performed with this analysis and it speed up the steady-state calculation for systems having large settling times. Therefore, this analysis is optimal to evaluate the frequency response of the mixed CMOS MEMS system for large oscillation amplitudes of the beam. Figure A.4.6 shows the results obtained with a PSS analysis for a Q of 1000. The simulations time needed in this case is around 9.5 s using the same computer system.

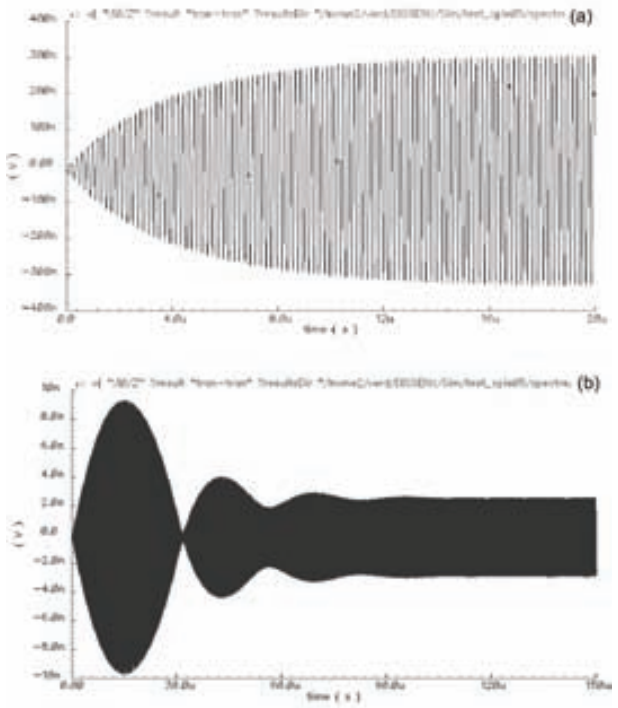

Figure A.4.5 Plots of the output voltage versus time obtained using a TRAN analysis for a beam resonator with a Q of 50 (a) and a Q of 1000 (b).

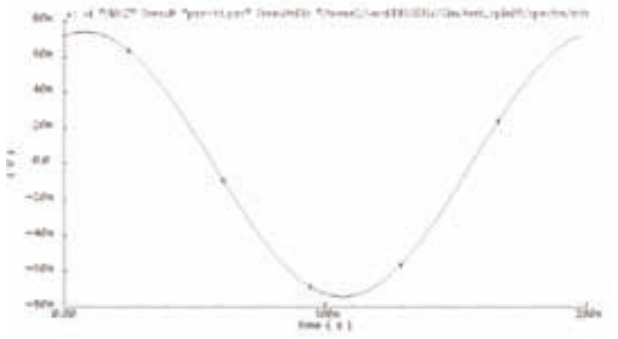

Figure A.4.6 Plot of the output voltage versus time obtained using a PSS analysis for a Q-factor of 1000.

The frequency response of the mixed CMOS MEMS system can be achieved by performing a sweep of PSS analysis at different frequencies in the frequency range desired. For every PSS analysis we measure the 1st harmonic of the variable of interest (output voltage, cantilever position, etc.). We have generated an OCEAN script that executes automatically, using the SPECTRE simulator, these operations by using a "For Loop" structure and generate an output file with the magnitude and phase of the system frequency response. This analysis calculates, in the steady state, the frequency response of the system and thus mimics a spectrum analyzer. This OCEAN script can be found in Annex II.

In Figure A.4.7 is presented the large-signal frequency characteristics of the system obtained using an AC and a PSS analysis. We can observe that the results obtained from an AC analysis differ from the ones obtained from a PSS analysis as we can observe in Figure A.4.7b. This is due to the relative high AC voltage used that induces high oscillation amplitudes of the cantilever producing a nonlinear performance of the electrostatic transduction as explained in Chapter 2. In the other hand, when using small AC voltages, and consequently the cantilever is operating in linear regime, the results of the two type of analysis become the same.

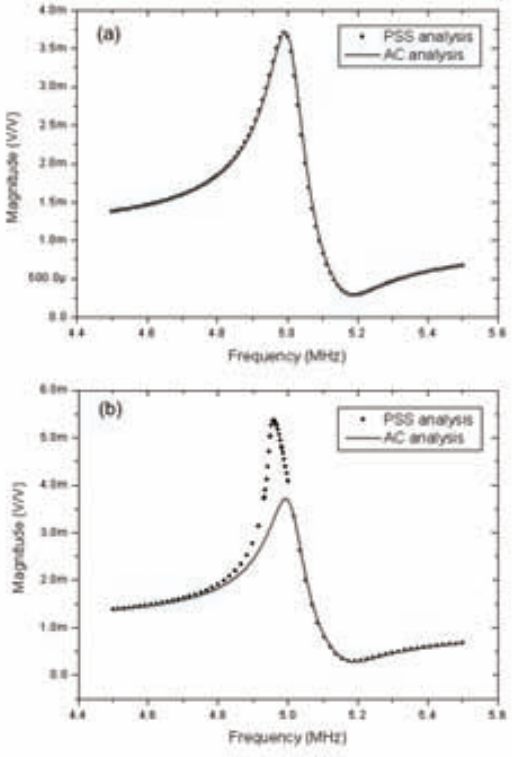

Figure A.4.7. Comparison of the system frequency response obtained from an AC analysis and PSS analysis for different AC excitation voltages V_{AC}= 10 mV (a) and V_{AC}= 10 V (b). V_{DC}=35 V.

REFERENCES

[1] J. Verd et al., "Design, Fabrication, and Characterization of a Submicroelectromechanical Resonator with Monolithically Integrated CMOS Readout Circuit", *IEEE Journal on Microelectromechanical Systems*, vol. 14, no. 3, June 2005, pp. 508-519.

[2] J. Verd et al., "Resonant Metal Cantilever with Attogram/Hz Mass Sensitivity Fully Integrated in a Standard 0.35-um CMOS Process", *Technical Digest of IEEE MEMS Conference 2006*, Istambul, pp. 638-641.

[3] G. Abadal et al., "Electromechanical model of a resonating nano-cantilever for high-resolution high-sensitivity mass detection", *Nanotechnology*, vol. 12, pp. 100-104, 2001.

[4] M. W. Putty, "Polysilicon Resonant Microstructures", *M.S. Thesis*, University of Michigan at Ann Arbor (1988).

[5] J. Teva et al., "On the electromechanical modeling of a resonating nano-cantilever-based transducer", *Ultramicroscopy*, vol. 100, 2004, pp.225-232.

[6] J. Teva et al., "A femtogram resolution mass sensor platform based on SOI electrostatically driven resonant cantilever. Part I: Electromechanical model and parameter extraction, *Ultramicroscopy*, vol. 106, 2006, pp. 800-807.

[7] L. Latorre, V. Beroulle and P. Nouet, "Design of CMOS MEMS Based on Mechanical Resonators Using a RF Simulation Approach", *IEEE Transactions on computer-aided design of integrated circuits and systems,* vol. 23, no. 6, June 2004, pp. 962-967.

[8] T. Veijola, T. Mattila, "Modeling of Nonlinear Micromechanical Resonators and their Simulation with the Harmonic-Balance Method", *Int. J. RF Microw. Comput-Aid. Eng.*, vol. 11 (5), pp. 310-321.

[9] Q. Meng, M. Mehregany and R.L. Mullen, "Theoretical Modeling of Microfabricated Beams with Elastically Restrained Supports," *Journal of Microelectromechanical Systems*, vol. 2, no. 3, Sep. 1993, pp. 128-137.

ANNEX I: VERILOG-A CODE

```
// -------------------------------------------------------------
//
// VerilogA
//
// CANTILEVER-BASED CAPACITIVE TRANSDUCER ELECTROMECHANICAL MODEL
//
//
// J. Verd (2006) - Dept. Enginyeria Electrnica (UAB)
//
// -------------------------------------------------------------

`include "constants.vams"
`include "disciplines.vams"
`define yes 1
`define no 0

module model_v1 (D1, D2, C, Z, Vc);

// Definition of input/output ports ----------------------

inout D1, D2, C;   // Drivers and cantilever
electrical D1, D2, C;

inout Z;      // Nominal displacement
kinematic Z;

inout Vc;       // Cantilever velocity
kinematic_v Vc;

// Cantilever Design Parameters --------------------------

parameter real Lc = 10e-6; // Cantilever Length
parameter real Tc = 925e-9;// Cantilever Thickness
parameter real Wc = 1.139e-6;   // Cantilever Width
parameter real gap = 0.72e-6 ;   // Cantilever-Driver Gap

parameter real xa = 3e-6;  // Driver initial position
parameter real xb = 7e-6;  // Driver final position

parameter real Qf = 300;// Mechanical Q-factor
parameter real E = 50e9;// Young modulus
parameter real Ro = 2.23e3;// Mass density

parameter real k3 = 0;     // Cubic spring coefficient

// Electrical Design Parameters

parameter real alpha = 0;  // Fringing field factor

// Capacitats paràssites

parameter integer N = 6;// # Cantilever sections

parameter integer clamped2 = `yes;


// Nodes declaration -----------------------------------------

   real W, Ra, Ma, k, k1, Meff, Zmax, Zx, D, W0, Cx;
   integer ii, j;
   real dx, Xn;
   real Ci[0:10];     //Array of the Ci coefficients
   real Ai[0:10];     //Array of the Ai coefficients
   electrical Cd1, Cd2, dCd1, dCd2;
   electrical dVd1, dVd2;
   real FF;   // Finging field component
   kinematic Zk3;     // Cubic nonlinearity component
   kinematic FG1, FG2;   // Electrical Forces
```

```
// Parameters calculation -----------------

   analog begin

      @ (initial_step) begin

      if (clamped2 == `yes) begin

         // Clamped-Clamped cantilever ----------------

         k = 16*E*Tc*pow(Wc,3)/pow(Lc,3);   // Stiffness constant
         k1 = 2.365;              // 1st mode constant
         Meff = 12*Ro*Lc*Wc*Tc/pow(k1,4);   // Effective mass
         W0 = pow(k/Meff, 0.5);           // Natural resonance frequency
         D = W0*Meff/Qf;            // Damping factor

         W = 1;                     // Reference force density

         Ra = (W/(2*pow(Lc,3)))*((Lc+xb)*pow(xa,3)-(Lc+xa)*pow(xb,3)); // Force
reaction
         Ma = (W/(12*pow(Lc,2)))*(pow(xa,4)-pow(xb,4))-Lc*Ra/3;   // Moment reaction

         FF = 1+alpha*(gap/Tc)*pow((Wc/Tc),0.222);  // Fringing field contribution


         // Calculation of the Ci and Ai coefficients

         for (ii=0; ii<N+1; ii=ii+1) begin

            dx = (xb-xa)/N;    // section length
            Xn = ii*dx+xa;     // section position

            Ai[ii] = 1;

            // Deflection profile
            Zx = Ma*(pow(Xn,2))/(2*k)+Ra*(pow(Xn,3))/(6*k)+W*(pow(Xn-xa,4))/(24*k);

            // Maximum deflection Z(Lc/2)
            Zmax = Ma*(pow(Lc/2,2))/(2*k)+Ra*(pow(Lc/2,3))/(6*k)+W*(pow((Lc/2)-
xa,4))/(24*k);

            Cx = Zx/Zmax; // Normalized deflection profile

            Ci[ii] =  Cx;
         end
      end
         // -------------------------------------------

      if (clamped2 == `no) begin

         // Clamped cantilever -------------------------

         k = E*Tc*pow(Wc,3)/(4*pow(Lc,3));     // Stiffness constant
         k1 = 1.875;              // 1st mode constant
         Meff = 3*Ro*Lc*Wc*Tc/pow(k1,4);       // Effective mass
         W0 = pow(k/Meff, 0.5);           // Natural resonance frequency
         D = W0*Meff/Qf;            // Damping factor

         W = 1;                // Reference force density

         FF = 1+alpha*(gap/Tc)*pow(Wc/Tc,0.222);    // Fringing field contribution


         // Calculation of the Ci and Ai coefficients

         for (ii=0; ii<N+1; ii=ii+1) begin

            dx = (xb-xa)/N;    // section length
            Xn = ii*dx+xa;     // section position
```

```
            Ai[ii] = 1;

            // Deflection profile
            Zx = ((xa-xb)*W/(2*k))*((pow(Xn,3)/3)-(xa+xb)*pow(Xn,2)/2)+pow(Xn-
xa,4)*W/(24*k);

            // Maximum deflection Z(Lc)
            Zmax = ((xa-xb)*W/(2*k))*((pow(Lc,3)/3)-(xa+xb)*pow(Lc,2)/2)+(pow(Lc-
xa,4)-pow(Lc-xb,4))*W/(24*k);

            Cx = Zx/Zmax;   // Normalized deflection profile

            Ci[ii] =  Cx;
         end
      end
         // -----------------------------------------------

         Ai[0] = 0.5;
         Ai[N] = 0.5;

      end


// ----------   BEHAVIOR DESCRIPTION   -----------------------------------------------
-------------------

      // Cantilever velocity

      Vel(Vc) <+ ddt(Pos(Z));

      // Cubic nonlinearity

      Pos(Zk3) <+ k3*pow(Pos(Z),3);


      // Electrical Force calculation : Fel (x,t)

      for (j=0; j<N+1; j=j+1) begin

         F(FG1) <+ -
((`P_EPS0*dx*Tc/2)*(pow(V(D1,C),2))*Ai[j]/(pow(gap+Ci[j]*Pos(Z),2)))*FF;
         F(FG2) <+  ((`P_EPS0*dx*Tc/2)*(pow(V(D2,C),2))*Ai[j]/(pow(gap-
Ci[j]*Pos(Z),2)))*FF;
      end

      // Movement equation

      Pos(Z) <+ ((F(FG1)+F(FG2))-D*Vel(Vc)-Meff*ddt(Vel(Vc))-Pos(Zk3))/k;

      // Capacity calculation

      for (j=0; j<N+1; j=j+1) begin

         V(Cd1) <+ ((`P_EPS0*dx*Tc)*Ai[j]/(gap+Ci[j]*Pos(Z)))*FF;
         V(Cd2) <+ ((`P_EPS0*dx*Tc)*Ai[j]/(gap-Ci[j]*Pos(Z)))*FF;
      end

      // Current calculation

      V(dCd1) <+ ddt(V(Cd1));
      V(dCd2) <+ ddt(V(Cd2));

      V(dVd1) <+ ddt(V(D1,C));
      V(dVd2) <+ ddt(V(D2,C));

      I(D1,C) <+ V(Cd1)*V(dVd1)+V(D1,C)*V(dCd1);
      I(D2,C) <+ V(Cd2)*V(dVd2)+V(D2,C)*V(dCd2);

   end
endmodule
```

ANNEX II: OCEAN SCRIPT

```
;************************************************************************
;****** LARGE SIGNAL FREQUENCY RESPONSE (BASED ON PSS ANALYSIS) **********
;************************************************************************
;
; ocean script that mimics a Network Analyzer performance by using a large
; signal analysis based on the use of a PSS analysis for each frequency desired
;
; J. Verd (2005) *********************************************************

; *** path of the output file ********************************************

of=outfile("/home2/verd/DISSENY/Sim/test_param/spectre/outputfile.out" "w")

; ************************************************************************


simulator( 'spectre )

; *** pathes of the design netlist and the results directory respectively *

design(  "/home2/verd/DISSENY/Sim/test_param/spectre/schematic/netlist/netlist")
resultsDir( "/home2/verd/DISSENY/Sim/test_param/spectre/schematic" )

; ************************************************************************

modelFile(
'("/home4/llibreries/ams/ams_v3.50/spectre/c35/mcparams.scs" "")
'("/home4/llibreries/ams/ams_v3.50/spectre/c35/cmos53.scs" "cmostm")
'("/home4/llibreries/ams/ams_v3.50/spectre/c35/res.scs" "restm")
'("/home4/llibreries/ams/ams_v3.50/spectre/c35/cap.scs" "captm")

    '("/home4/llibreries/ams/ams_v3.50/spectre/c35/bip.scs" "biptm")
    '("/home4/llibreries/ams/ams_v3.50/spectre/c35/ind.scs" "indtm")
)


; *** Header of the output file ****************
fprintf(of "Frequency \t Magnitude \t Phase \n")
; ***********************************************

;*** Parameters of the logarithmic sweep *****
;** start frequency
Fl = 6.58e6
Fa = Fl
;** stop frequency
Fh = 6.68e6
;**number of points
N = 10
; ***********************************************

; **** Vac : name of the source ac voltage used in the circuit
;
desVar(   "Cpf" 0  )
desVar(   "Cpd2" 0 )
desVar(   "Cpd1" 0.055f )
desVar(   "Vdc" 15 )
desVar(   "ww" 0.650u )
desVar(   "Vac" 1.63  )
desVar(   "tt" 925n   )
desVar(   "ss" 900n   )
desVar(   "ro" 2.46k  )
desVar(   "Q" 500  )
desVar(   "ll" 9.96u  )
desVar(   "knxl" 1.8751 )
desVar(   "fr" 6M  )
desVar(   "epsilon" 8.85e-12  )
```

```
desVar(   "E" 96.5e9 )

envOption(
   'analysisOrder  list("dc" "pss")
)
option( 'gmin  "1e-6"
   'compatible  "spectre"
   'limit  "dev"
   'homotopy  "gmin"
   'reltol  "0.001"
)
; ****** Plot the results in two subwindows (magnitude and phase) ***
newWindow()
addSubwindow()

for( i 1 N

  x = ((i-1)*1.0e0)/((N-1)*1.0e0)
  xx = float(x)
  Fa = Fl*((Fh/Fl)**xx)

;** fr = first frequency name (voltage source)****
  desVar(   "fr"  Fa  )
  analysis('pss ?fund Fa  ?harms "1"  )

  run()

  selectResults('pss_fd)
  magnitude=mag(v("Vo")/harmonic(v("Vin") 1))
  pphase=phase(v("Vo")/harmonic(v("Vin") 1))

  currentSubwindow( 1 )
  plot(magnitude)
  currentSubwindow( 2 )
  plot(pphase)


  ;ocnPrint(mag(v("Vo")/harmonic(v("Vin") 1)))

  one_mag = value(magnitude Fa)
  one_phase = value(pphase Fa)

; ** save data to the file ************************************
  fprintf(of "%12.6e \t %12.6e \t %12.6e \n" Fa one_mag one_phase)
)

close(of)
```

APPENDIX B

SUBMITTED CHIPS LAYOUT

This Appendix presents the layouts and their main specifications of the chips submitted at the different RUNs made in the Nanomass and Nanosys projects.

B.1 NANOMASS - RUN #1995

The chip design was arranged in 2 duplicated quarters. The left half of the chip is corresponding with devices that use BA readout circuits (22+22 devices). The right half of the chip is corresponding with devices that use TIA readout circuits (22+22 devices).

The devices were arranged in rows with 16 connection pads. In addition, some CMOS test devices as well as testing areas was also included in the chip.

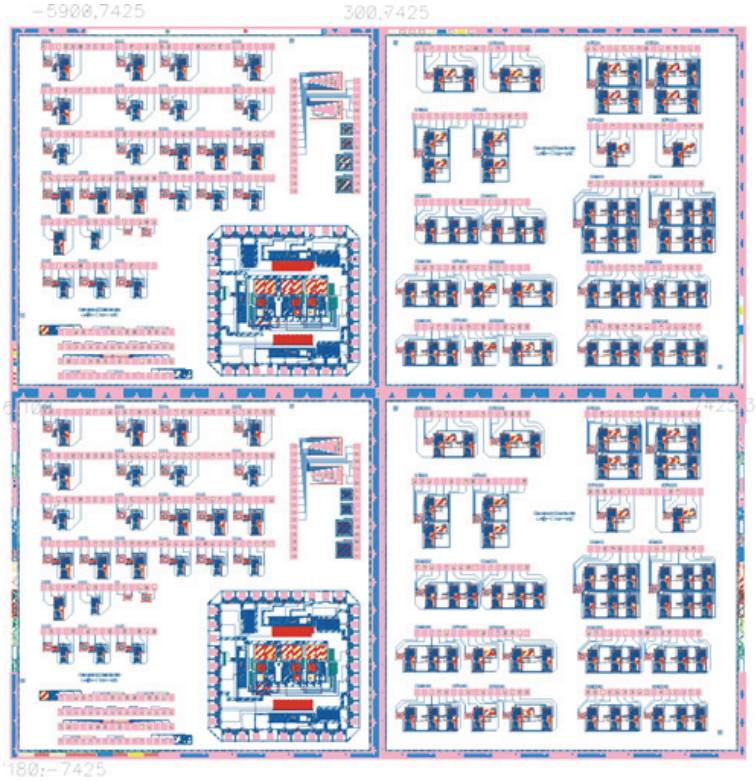

Technology: CNM25.
Chip Size: 15×15 mm^2.
Readout Circuit: BA and TIA.
MEMS devices: "nanoareas" for fabrication of polysilicon 1D-cantilevers and arrays of 2 cantilevers.

B.2 NANOMASS - RUN #2186

In this RUN[1] were defined different devices to fabricate arrays of polysilicon cantilevers. The devices were arranged in rows with 16 connection pads. The readout circuits of the devices are based on the TIA design. In addition, different modules for testing of TIA circuits and other testing circuits were arranged in the middle column of the chip.

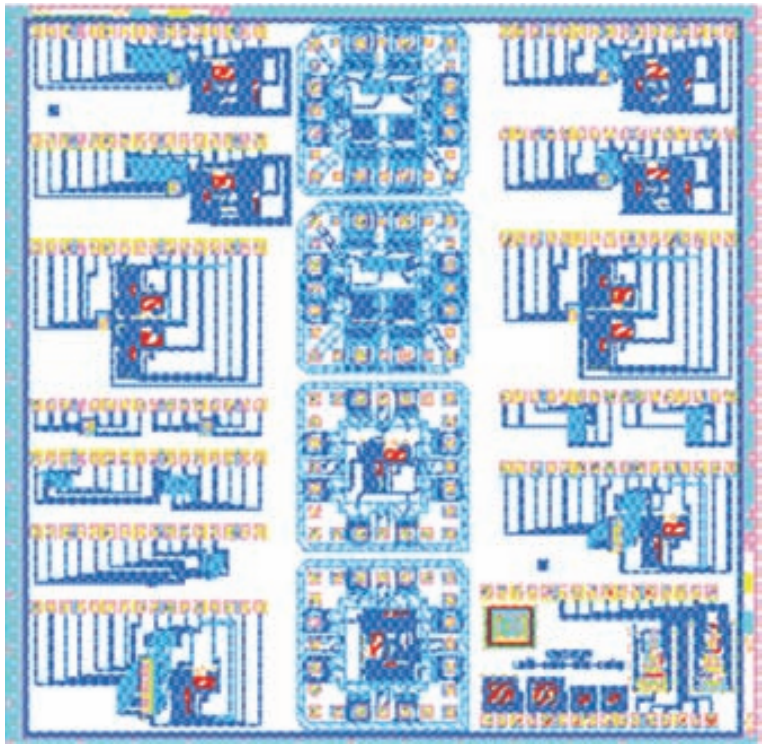

Technology: CNM25.
Chip Size: 7.5×7.5 mm^2.
Readout Circuit: TIA.
MEMS devices: "nanoareas" for fabrication of polysilicon arrays of cantilevers.

[1] *This RUN was designed jointly with M. Villarroya.*

B.3 NANOMASS - RUN #2380

This RUN[2] was designed to integrate CMOS circuits with cantilevers using SOI wafers. In this sense, the MEMS are fabricated on the SOI layer and the CMOS is fabricated on the substrate of the SOI wafer.

The devices were arranged in rows with 16 connection pads. Every chip has 95 "nonoareas" (to fabricate single or arrays of cantilevers) with the readout circuits, some CMOS test and SOI test structures.

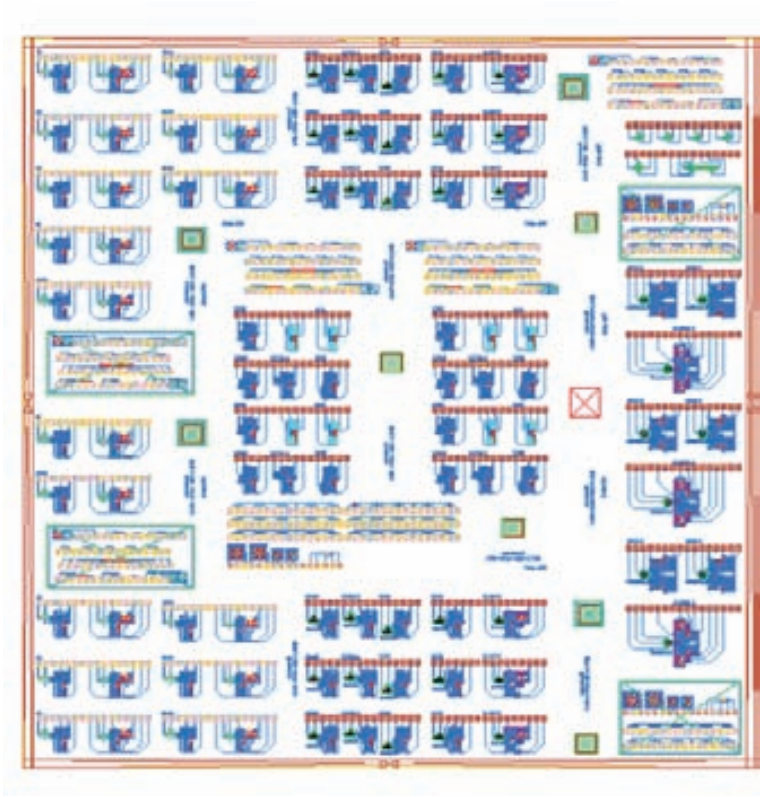

Technology: CNM25.
Chip Size: 15×15 mm^2.
Readout Circuit: TIA and BS_D.
MEMS devices: "nanoareas" for fabrications of SOI single cantilevers and arrays of cantilevers.

[2] *This RUN was designed jointly with M. Villarroya.*

B.4 NANOSYS - RUN #FEB04

It was the first RUN designed to fabricate CMOS-MEMS with a commercial technology at ECAS group. Three different options were investigated to fabricate CMOS metal cantilever resonators: (1) Top metal as structural layer and SiO2 as sacrificial layer (Met3 devices), (2) First metal as structural layer and bulk silicon as sacrificial layer (Met1-Si devices), and (3) First metal as structural layer and polysilicon as sacrificial layer (Met1-Poly devices).

The different devices were arranged in rows with 16 connection pads.

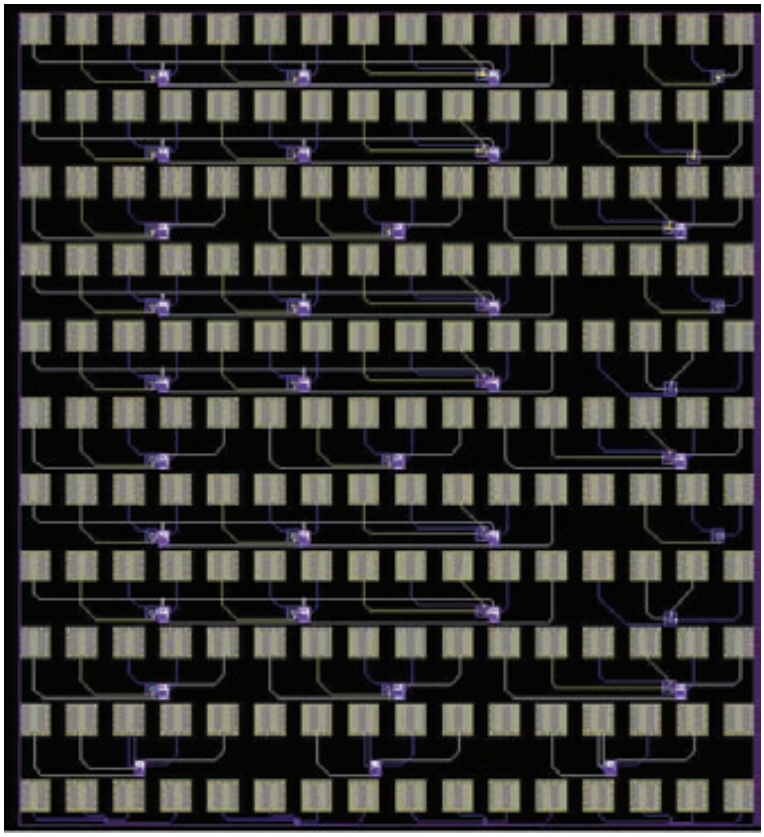

Technology: AMS C35B3C1.
Chip Size: 2345×2595 μm^2.
Readout Circuit: UGB (with polarization diode).
MEMS devices: single cantilevers with 1 and 2 drivers.

B.5 NANOSYS - RUN #MAR05

The same fabrication technology approach developed in the previous RUN was used to design this RUN[3] in order to investigate the success on fabrication of CMOS-MEMS for RF applications.

Since the relative high operation of these designed devices, the connection pads was arranged to be used with 5-tips RF probes.

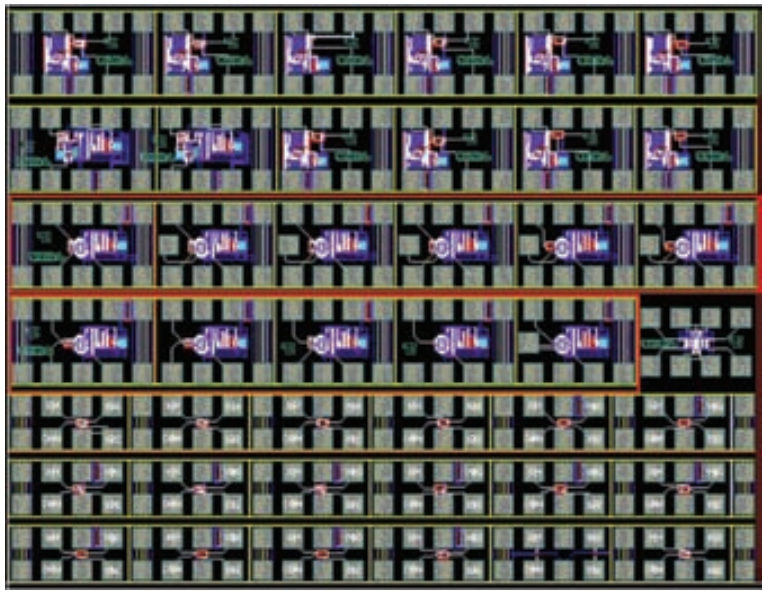

Technology: AMS C35B4C3.
Chip Size: 3598 × 2759 μm^2
Readout Circuit: UGB+B50.
MEMS devices: CC-beams and paddle structures for RF applications (see J. Teva PhD thesis [Tev07]).

[3] *This RUN was designed jointly with J.Teva and A. Uranga*

B.6 NANOSYS - RUN #OCT05

In this RUN[4] were designed metal resonators integrated in a Pierce oscillator circuit for mass sensing applications. In addition, a polysilicon cantilever and a CC-beam to investigate its applicability as a resonator in mass sensing applications.

The connection pads was arranged to be used with 5-tips RF probes.

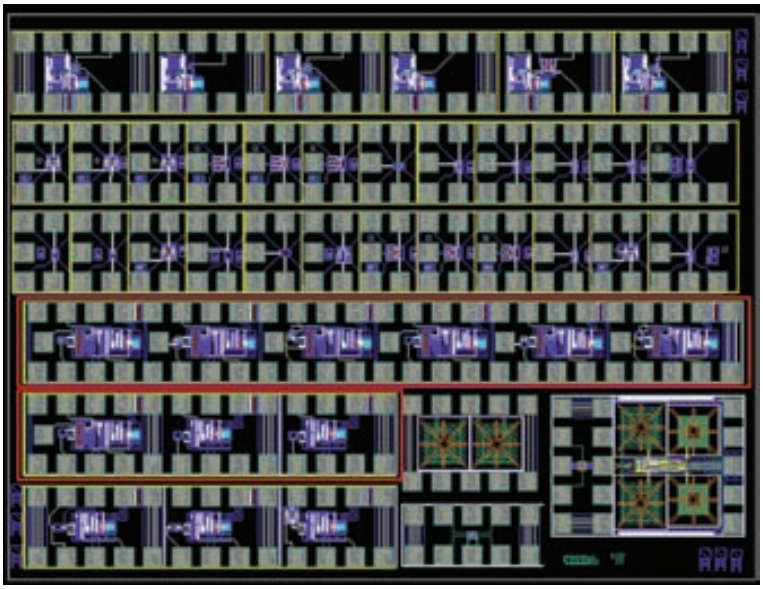

Technology: AMS C35B4C3.
Chip Size: 3690 × 2721mm^2.
Readout Circuit: UGB50 and UGBCA50 in open and closed loop (oscillator).
MEMS devices: Metal cantilevers and CC-beams with 1 and 2 drivers, 1-driver polysilicon cantilever and CC-beam, RF-MEMS.

[4] *This RUN was designed jointly with J.L. Lopez, J. Teva and A. Uranga.*

B.7 NANOSYS - RUN #JUL06

In this RUN[5] were designed 2-driver polysilicon resonators integrated in the UGBCA50 circuit to investigate their future implementation as a self-oscillating resonator for mass sensing applications. In addition, polysilicon structures integrated with the UGBCA50 circuit for RF applications were also included.

The connection pads was arranged to be used with 5-tips RF probes.

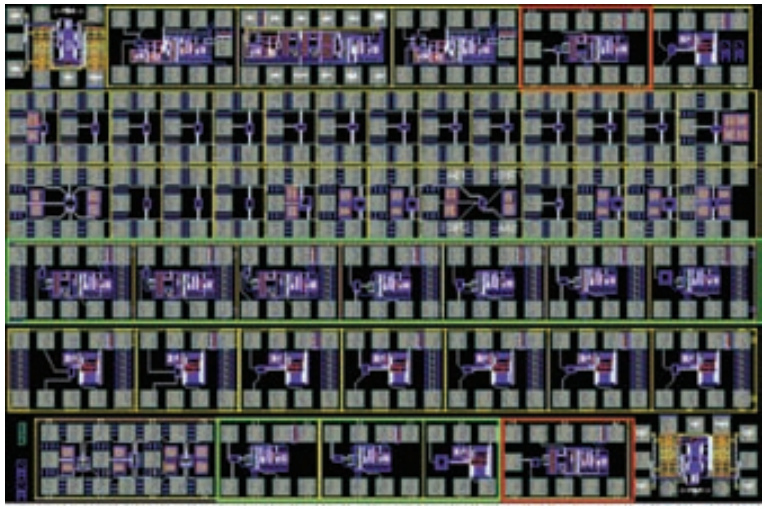

Technology: AMS C35B4C3.
Chip Size: 4250 × 2755 μm^2
Readout Circuit: UGBCA50.
MEMS devices: 2-driver polysilicon cantilever and CC-beam, RF-MEMS.

[5] *This RUN was designed jointly with J.L. Lopez, J. Teva and A. Uranga.*

B.8 NANOSYS - RUN #JUN07

In this RUN[6] were designed a polysilicon cantilever and CC-beam integrated in a Pierce oscillator circuit for mass sensing applications. In addition, a polysilicon cantilever with a smaller gap in open loop configuration was also included.

The connection pads was arranged to be used with 5-tips RF probes.

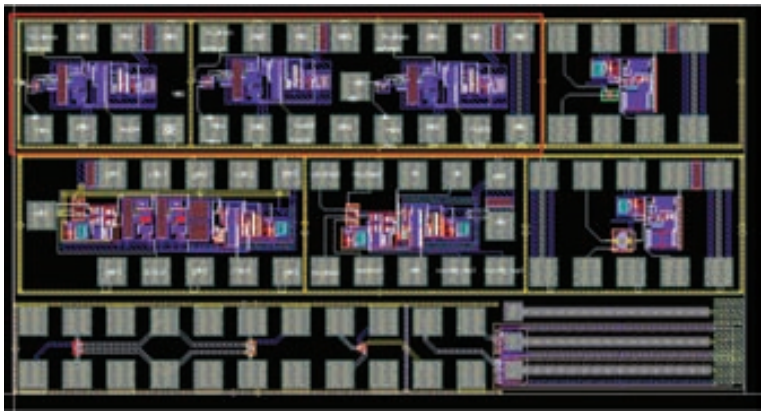

Technology: AMS C35B4C3.
Chip Size: 3690 × 2721 μm^2
Readout Circuit: UGBCA50.
MEMS devices: 2-driver polysilicon cantilevers and a CC-beam, RF-MEMS.

[6] *This RUN was designed jointly with J.L. Lopez, J. Teva, F. Torres and A. Uranga.*

ABBREVIATIONS AND ACRONYMS

ABL	Atom Beam Lithography
AFM	Atomic Force Microscopy
CAD	Computer Aided Design
CMOS	Complementary Metal-Oxide-Semiconductor
DMD	Digital Mirror Device
DWL	Direct Write Laser lithography
EBL	Electron Beam Lithography
ECAS	Electronic Circuits And Systems group (UAB)
FIB	Focused Ion Beam
HF	Hydrofluoric Acid
IC	Integrated Circuit
LCD	Liquid Cristal Displays
MEMS	MicroElectroMechanical Systems
MOEMS	Micro Optical Electro-Mechanical Systems
NEMS	Nanoelectromechanical Systems
NMOS	N-doped MOS transistor
PLL	Phase Locked Loop
ppm	parts per million
QCM	Quartz Crystal Microbalance
RF	Radio Frequency

RIE Reactive Ion Etching

SEM Scanning Electron Microscopy

SoC System on Chip

SOI Silicon on Insulator

SSoC Sensing Systems on Chip

TIA TransImpedance Amplifier

UHF Ultra High Frequency

UVL Ultra-Violet Lithography

VHF Very High Frequency